THE LIBRARY
PHYSICAL RESEARCH LABORATORY
NAVRANGPURA AHMEDABAD-380009
INDIA

STUDIES ON THE DYNAMICS OF THE EQUATORIAL IONOSPHERE

A THESIS

SUBMITTED FOR THE

DEGREE OF DOCTOR OF PHILOSOPHY

OF THE

GUJARAT UNIVERSITY

BY

BODDAPATI GNANA ANANDA RAO

(B. G. RAO)

OCTOBER 1977

043

B8507

PHYSICAL RESEARCH LABORATORY
NAVRANGPURA
AHMEDABAD 380 009
INDIA

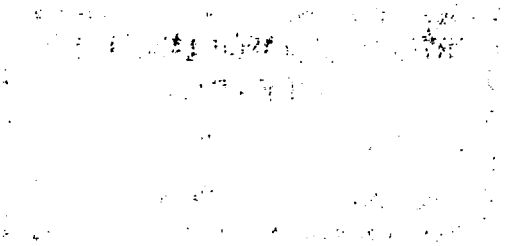

TO

MY MOTHER

C E R T I F I C A T E

I hereby declare that the work presented in this thesis is original and has not formed the basis for award of any degree by any University or Institution.

B.G. Anandarao

(B.G. ANANDARAO)
Author

Certified

R Raghava Rao

(R. RAGHAVARAO)
Professor-in-Charge

STATEMENT

The work presented in this thesis was carried out by the author at the Physical Research Laboratory, Ahmedabad under the guidance of Professor R. Raghavarao.

The Thesis deals with the problems of the dynamics of the equatorial ionosphere. In particular, the studies related to the phenomenon of the equatorial electrojet are presented. Although, extensive investigations were made to understand this phenomenon, there exists still a number of unsolved problems. Besides, the nature of the winds in the upper atmosphere and their possible effect on the equatorial electrojet are still not known very clearly. The author presents in this thesis, experimental and theoretical studies, regarding these problems, made by him.

Two of the important parameters which play a very significant role in the dynamics of the ionosphere are the neutral wind velocity and the electric field. These parameters can be measured very accurately by the technique of release of artificial vapour clouds along the trajectory of a sounding rocket. The author has planned and conducted a number of vapour release experiments during 1972-1976 at Thumba Equatorial Rocket Launching Station (TERLS), Trivandrum situated near the dip equator. The author has also participated in the fabrication of defferential photometric

equipment to track lithium vapour clouds during daytime. This technique enables one to measure the neutral winds in the daytime.

Using the vapour release technique, the author has measured the neutral winds and electric fields over the dip equator. The thesis brings out some important features regarding the neutral winds. It is also shown for the first time, how one can use the electric field measurements to verify the theories of the electrojet. In the light of these experimental results, theoretical investigations are made by the author, to estimate quantitatively the effects of horizontal and vertical winds on the electrojet.

In Chapter I, the author gives a brief account of various phenomena concerning the E region of the ionosphere.

From the experimentally observed wind profiles over the dip equator at TERLS, the tidal and gravity wave components are estimated in Chapter II. Results on the vertical winds and a profile of the vertical wind obtained for the first time over the equator are also presented in this Chapter.

In Chapter III, details of the differential photometric equipment built for the measurement of winds in the daytime are described. Preliminary results obtained by using the equipment are also discussed.

The results of the barium cloud experiments conducted at TERLS to measure electric fields are presented in Chapter IV These results are used to provide the first observational evidence for the validity of theoretical models of the equatorial electrojet.

In Chapter V, the polarization fields generated by the winds of gravity waves at the dip equator are computed by a two-dimensional approach. It is shown that the total electric field produced by these winds in the vertical direction is non-zero and therefore the effects of the gravity wave winds and shears on the electrojet are important. The large scale stratifications in the electron density profiles observed at the dip equator are interpreted by the wind shear theory.

A model equatorial electrojet is developed in Chapter VI which incorporates the effects of neutral winds. Using the model, the effects of zonal, meridional and vertical winds on the electrojet are estimated. It is suggested that the vertical winds could possibly be responsible for the occurrence of counter-electrojet (a phenomenon associated with the electrojet) in afternoon hours.

In Chapter VII are listed the important conclusions of the present investigations and the directions in which the future work is to be done.

(R. RAGHAVARAO)

(B.G. ANANDARAO)

ACKNOWLEDGEMENTS

I take this opportunity to express my deep sense of gratitude to my thesis adviser Professor R. Raghavarao but for whose encouragement, affection and friendship, it would have been hard for me to accomplish my academic pursuits.

I owe a great deal to Professors J.N. Desai and R. Pratap for their interest in my work, for their encouragement and for many helpful discussions.

It is a pleasure to acknowledge the help rendered to me, regarding the numerical analysis by Dr. Rao S. Koneru and Dr. (Mrs.) Suhasini.

I thank M/S. V. Sudhakar, V.V. Babu, R. Aravamudan and G. Padmanabhan and their colleagues at TERLS, Trivandrum for making the vapour cloud release experiments a great success.

The fruitful discussions with Professor G. Martelli of the University of Sussex, Brighton, Dr. C.A. Reddy, Dr. C.R. Reddi and Dr. B.V. Krishnamurthy of V.S.S.C., Trivandrum are gratefully acknowledged.

I am indebted to Professor Satya Prakash, Professor R.P. Kane, Professor T.S.G. Sastry, Professor B.H. Subbaraya, Dr. G. Subramanian and Dr. M.R. Deshpande for their encouragement.

I express my gratitude to M/s. D.V. Subhedar and V.J. Parikh who developed the electronic circuitry for the equipments for measuring the daytime winds.

I thank Miss Ranna A. Patel for her excellent computational assistance and for the painstaking job of preparing the diagrams.

It is with a deep sense of gratitude that I recall my association with my friend, the late Mr. Jayarama Rao, with whom I had had the benefit of many a fruitful discussion.

The encouragement given to me by my friends, particularly by Dr. Prabhakar Sharma, Dr. Vaman Kulkarni, Dr. Vinay Kamble, Dr. Bhupen Goswamy, Dr. Pradeep Chaturvedi Dr. H.S.S. Sinha and Mr. N. Nagesha Rao is gratefully acknoledged.

Mr. K. Ravi typed the thesis very neatly and efficiently. Mr. K.B. Sasidharan typed the first draft of the thesis. Mr. K. Venugopalan typed the first page of the thesis. I am grateful to all of them. My sincere thanks are due to Mr. Ghanshyam Patel who very efficiently cyclostyled the thesis.

The excellent support rendered by the workshop, the computer centre, and Photographic and Documentation section is highly appreciated.

I thank all the members of my family for their affection and encouragement.

CONTENTS

STATEMENT			i
ACKNOWLEDGEMENTS			iv
CHAPTER I		Introduction	
	I.1	Nomenclature	2
	I.2	Ionospheric processes and the ionospheric layers	4
	I.3	E region of the ionosphere	6
	I.4	Neutral motions in the E region	12
	I.5	Turbulence	28
	I.6	Conductivities	34
	I.7	Dynamo theory	40
	I.8	The equatorial electrojet	46
	I.9	Scope of the thesis	52
CHAPTER II		Neutral Wind Measurements by Artificial Vapour Release Technique over the Dip Equator.	
	II.1	Introduction	54
	II.2	Measurement of upper atmospheric winds by artificial vapour clouds	55
	II.3	Observations	68
	II.4	Separation of gravity wave and diurnal tidal wind components from the observed wind profiles	69
	II.5	Vertical winds and turbulence	78
	II.6	Conclusions	85

CHAPTER III	The Technique of Measurement of Winds in the Daytime	
III.1	Introduction	87
III.2	Experimental set-up for the detection of the lithium vapour clouds released in the daytime	95
III.3	Analysis of the data	100
III.4	Results obtained from lithium and barium vapour clouds	105
III.5	Summary	106
CHAPTER IV	Electric Fields in the Equatorial Ionosphere	
IV.1	Introduction	108
IV.2	The technique of artificial vapour release in the upper atmosphere	118
IV.3	Results	129
IV.4	Validity of UNTIEDT'S model of the electrojet	131
IV.5	Conclusions	136
CHAPTER V	Two Dimensional Theory of Electric Fields Generated by Wind Motions at the Equatorial Ionosphere - Application of Wind shear Mechanism to the E Region Electron Density Stratifications	
V.1	Introduction	139
V.2	Electric fields generated by gravity wave winds at the dip equator - KATO'S one-dimensional theory	150

V.3	Two dimensional theory of electric fields engendered by the gravity wave winds at the equatorial ionosphere	152
V.4	Application of the present theory to the observed night-time equatorial E region irregularities	158
CHAPTER VI	A Theoretical Model of the Equatorial Electrojet Incorporating the Effects of Neutral Winds	
VI.1	The observed features of the phenomenon of equatorial electrojet	165
VI.2	The models of the electrojet	179
VI.3	Theory of the model	184
VI.4	Electrojet with no-winds	193
VI.5	Effects of zonal winds and wind shears on the electrojet	198
VI.6	Effects of meridional winds and wind shears on electrojet	207
VI.7	Effects of vertical winds on the electrojet	216
CHAPTER VII	Conclusions	225
APPENDIX I	Numerical Solution of the Partial Differential Equation for the Current Function	A-1
APPENDIX II	Magnetic Field Fluctuations on the Ground Produced by the Electrojet	A-5
REFERENCES		R-1

CHAPTER 1

INTRODUCTION

The study of the dynamics of the equatorial ionosphere has been of great interest in the recent years. Although our understanding of the dynamical phenomena such as the electrojet in the equatorial ionosphere has made new strides in the recent past, there exists still, a number of unsolved problems associated with the equatorial ionosphere.

The electrojet in the E-region, the ionisation anomaly in the F-region are unique to the equatorial ionosphere, by virtue of the horizontality of the geomagnetic field lines. It is known that even the spread F at low latitudes is different in its behaviour from that at other latitudes. Similarly, the E region of the equatorial ionosphere has altogether a special kind of irregularities associated with the electrojet. While the experimental data acquired on parameters (such as electric and magnetic fields; densities and temperatures of the ions, electrons and the neutral gas constituents; and the neutral winds) which govern the various dynamical processes are reasonably sufficient in the middle and high latitudes, there are not many measurements of that kind made at the low latitudes. Further understanding of the phenomena like electrojet, spread F and E region irregularities, requires not only extensive measurements, but in situ measurements of relevant parameters made near-simultaneously.

In the case of the electrojet studies the importance of the measurement of the electric fields and neutral winds along with the electron density can hardly be over-emphasised as these are essential to verify the theory of the electrojet and to investigate the associated problems. An ambitious programme to make such simultaneous measurements is being undertaken by Solar and Planetary Physics Group of the Physical Research Laboratory, Ahmedabad.

The author discusses in his thesis, results of measurements of electric fields, electron density and winds and demonstrates how these can be used to verify the theory of the electrojet. Results of the theoretical investigations carried out on the effects of the neutral winds on the electrojet intensity and distribution are also presented.

In this first Chapter we propose to summarise the current ideas regarding the basic processes involved in the formation of the E layer, the winds and current systems in the E region with special emphasis on the equatorial ionosphere.

I.1 The nomenclature:

The earth's ionosphere can broadly be subdivided into the following regions.

The "lower ionosphere" is the region from about 60 km to about 90 km altitude where mostly the neutral winds and turbulence control the dynamics of both electrons and ions because of their high rate of collisions with the neutral

constituents as compared with their respective gyro-frequencies.

The region from 90 km to about 140 km altitude is called the "dynamo region" wherein the ions and electrons are controlled by different mechanisms. The motion of ions is controlled by the neutral winds whereas that of the electrons is governed by the geomagnetic field. The consequent differential motion between ions and electrons gives rise to polarisation electric fields and electric currents. These fields are communicated to higher altitudes through the highly conducting geomagnetic field lines and cause $\underline{E} \times \underline{B}$ drift of the plasma and is known as the "motor" action.

Above about 150 km, the movements of the ions and electrons are mainly dictated by the geomagnetic field and this region is termed as the "magnetosphere". However, the term magnetosphere is sometimes used in a more restrictive sensefor the region above about 1500 km, where the density of the plasma is predominant over that of the neutral gas (although both decrease with altitude). The earth's magnetic field is enclosed in a cavity called the 'magnetosphere', the boundary of which is known as the 'magnetopause'. The magnetopause is at about 10 R_E (R_E = 6378.16 km, the radius of the earth) on the dayside of the earth and at

a much greater distance on the night side. Above the magnetopause the geomagnetic control over the dynamics of the charged particles is negligible.

In the following section we present the nomenclature according to the distribution of the ionisation.

I.2 Ionisation processes and the ionospheric layers:

In Fig. I.1, is shown a representative distribution of various constituents (neutral as well as charged particles) of the upper atmosphere during the daytime. The ion and electron densities shown here vary greatly with the time and the location of the station.

The ultraviolet (UV), extreme ultraviolet (EUV) and X-radiations of the solar emission, ionise the constituents of the earth's atmosphere by the process of photo-ionisation. Whereas the atmospheric density decreases exponentially, the solar radiation flux increases with altitude. Also, the atmosphere is composed of various kinds of neutral constituents and the rate at which the incoming radiation is absorbed is different for different wavelengths and for different constituents. As a consequence, the rate of production of ionisation, q, shows a maximum at a certain height depending upon the ionising radiations and the density of the absorbing constituents and it then falls off rapidly. The ionised atoms and molecules, interact/recombine with the ambient neutral/charged constituents to become again neutral. Therefore, there is continuous process

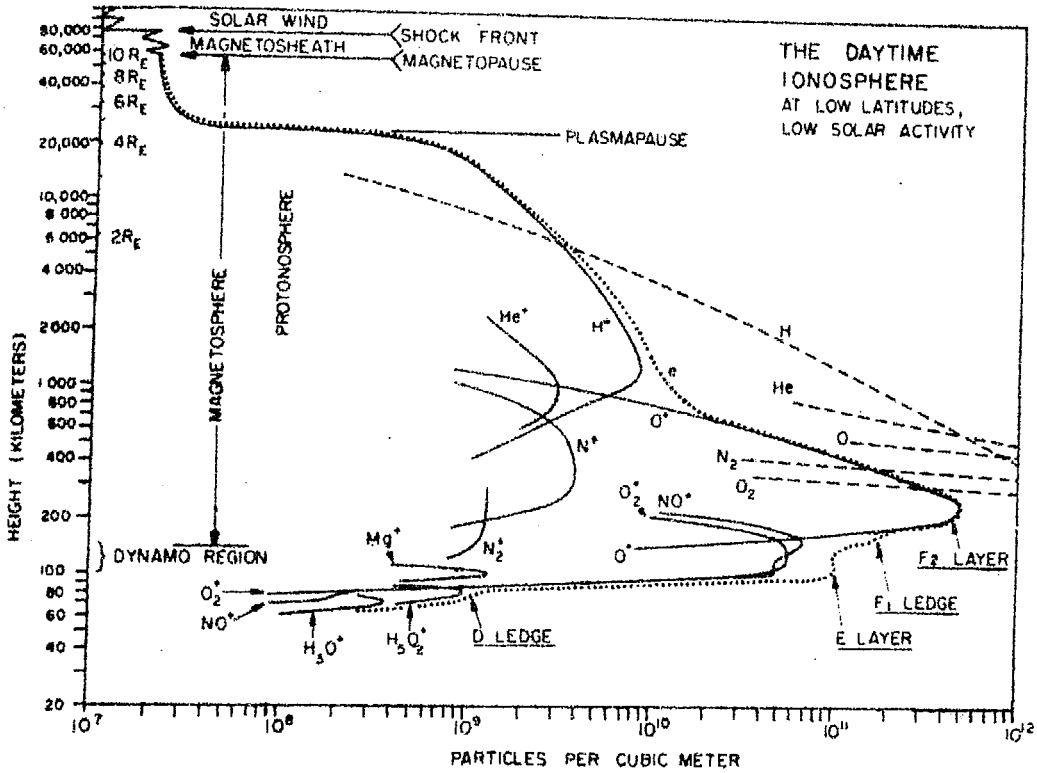

Figure I.1: Altitude variations in the concentration of electrons (e, dotted curve) and various positive ions (solid curves) for an overhead sun at times of low solar activity. Concentrations of the dominant neutral species at the higher altitudes (dashed lines) are also shown. The earth radius (R_E) scale measures the distance from the earth's centre (After, HINES, 1974).

of production and loss of ionisation in the ionosphere. The production due to the direct solar radiation ceases during the night, whereas the loss through the recombination process still remains operative . There are, however, other sources for producing ionisation in the nighttime, as will be discussed later. As a result of these production and loss mechanisms, the ionosphere exhibits a layered structure.

The most important constituents of the neutral gas that are ionised are molecular oxygen (O_2) in the lower ionosphere, atomic oxygen (O) in the upper regions and molecular nitrogen (N_2) throughout. These constituents when they are initially in their lowest state of energy can be ionised by photons at wavelengths equal to or shorter than 1027, 912 and 796Å respectively. Somewhat longer wavelengths are effective only when the neutral particle is initially in an excited state. Nitric oxide (NO), although a minor constituent, is an important contributor to the ionisation at and below E region levels. Its ionising limit is at 1345Å and the line emission H Lyman-Alpha (1216Å), the most intense line of solar emission, ionises it. It thus accounts for the D layer. Ionisation by cosmic rays is important at levels below 75 km.

There are mainly three regions or layers formed by the above processes in the ionosphere. Fig. I.1 shows these regions and their approximate extents. The D region is between about 60-90 km, E region between 90-140 km and above 140 km is the

F region. In the F region there are again two layers, the F_1 ledge and the F_2 layer. The region below the F_2 peak i.e., below the altitude corresponding to the maximum electron density in the entire ionosphere, is called the "bottom-side ionosphere", and the region above it is termed as the "topside ionosphere", where the electron density (i.e., the number density measured in number of electrons per cm^3) decreases with altitude monotonically. However, similar to the F_1 ledge in the bottom-side ionosphere, an abrupt increase in the electron density around 800 km altitude is found especially in the equatorial region during the solar minimum period. This is known as the "Ionisation ledge" in the topside ionosphere.

Lucid descriptions of the basic processes in the ionosphere and magnetosphere are given in the literature elsewhere (for instance, RATCLIFFE, 1960, 1972; RISHBETH AND GARRIOTT, 1969; WHITTEN AND POPPOFF, 1971; BANKS AND KOCKARTS, 1973 a,b; BAUER, 1973). As the problems discussed in the thesis are confined to the equatorial E region only, we now briefly describe the primary mechanisms concerning the E region of the ionosphere.

I.3 E region of the ionosphere:

Major contributions to the daytime ionisation of the E region are made by (i) x-rays in the range $140 \gg \lambda > 8$ Å producing O_2^+, N_2^+ and also O^+; (ii) Lyman β at 1026 Å producing O_2^+ and (iii) the Lyman Continuum at $\lambda < 910$ Å producing O_2^+ and O^+.

Besides these, the intense Lyman α line (1216Å) ionises NO. NO^+ becomes dominant ion along with O_2^+ because of its production by the following charge transfer reactions in addition to photoionization:

$$N_2^+ + O \rightarrow NO^+ + N \qquad (1)$$

$$N_2^+ + O_2 \rightarrow O_2^+ + N_2 \qquad (2)$$

$$O_2^+ + N \rightarrow NO^+ + O \qquad (3)$$

The reactions (1) and (2) are more rapid than (3) and the radiations capable of ionizing N_2 are mostly absorbed above 140 km. At 120 km the life-time of N_2^+ with respect to the formation of O_2^+ (reaction 2) is 0.5 sec while the transformation to NO^+ requires only 0.07 sec. As a consequence, NO^+ becomes the dominant ion along with O_2^+ in the E region.

As has been stated earlier, the ions and electrons thus produced take part in recombination reactions. In the E region, the recombination is mainly the "dissociative" type (BATES AND MASSEY, 1947; BIONDI, 1964). In this type of recombination, a molecular ion combines with an electron to form the neutral constituents, as follows:

$$(XY)^+ + e^- \rightarrow X^* + Y^* \qquad (4)$$

where X and Y represent the atomic constituents and $(XY)^+$ is the molecular ion, e^-, the electron and the asterisk represents an atom in excited state. The recombination can be

characterised by rate coefficient 'α' (in $cm^3 sec^{-1}$) and the rate of recombination then can be expressed as $\alpha N,N$ being the electron density.

The recombination coefficient in the daytime E region is typically of the order of $10^{-7} cm^3 sec^{-1}$ (MITRA, 1968; MITRA AND BANERJEE, 1971), SWIDER (1972, 1975) obtained an empirical formula for the mean recombination coefficient which in most circustances can be equated to the dissociative recombination coefficient pertinent to the E region, as follows:

$$\alpha_M = \alpha_E = 3 \times 10^{-7} (300/T) cm^3 sec^{-1} \qquad (5)$$

for mid-day E region when $\left[NO^+\right] \approx \left[O_2^+\right]$. Here T is the gas temperature (^oK) and the square brackets indicate the concentration (particles/cm^3) or density.

In the nighttime also, the value, $10^{-7} cm^3 sec^{-1}$ is believed to be maintained (e.g., DANILOV, 1970) inspite of the decelerating decay of the ionisation during that time which is not due to a reduction in the recombination rate coefficient, α, but due to the sources (although weak) for producing ionisation in the nighttime. These sources are the scattered flux of Lyman β (SWIDER, 1965) for ionising O_2, scattered Lyman α (SWIDER, 1967) for NO & the electron fluxes in the energy range 1-5 KeV (IVANOV - KHOLODNY, 1965).

In a review article, SWIDER (1972) discussed various sources of ionisation in the nighttime E-region and concluded that equation (5) represents the coefficient very well.

For a simple equilibrium Chapman-layer (CHAPMAN, 1931a,b) in an isothermal atmosphere, the critical frequency is related to the solar zenith angle χ and the maximum production rate q_o as follows (ordinary critical frequency, f_oE):

$$f_o = 9000 \left[(q_o/\alpha)\cos\chi\right]^{\frac{1}{4}} \quad \text{in Hz} \qquad (6)$$

The solar zenith angle χ is defined as the angle made by the sun's rays with the local zenith and is given by

$$\cos\chi = \sin\delta\cos\theta + \cos\delta\sin\theta\cos t \qquad (7)$$

where δ is the declination of the sun, θ, the geographic colatitude of the place in question and t is the local time in angular measure.

The daytime E region is investigated extensively by the ground-based technique, 'the ionosonde' and it has been the best known of the ionospheric layers (RØBINSON 1959). Its maximum electron density $N_{max}E$ is measured routinely by the ionosondes all over the globe. These measurements showed that $N_{max}E$ has quite regular temporal and spatial or geographical variations. $N_{max}E$ depends almost entirely on the zenith angle of the sun and the solar activity and is free from the disturbances so characteristic of D and F regions (VANZANDT, 1967; COHEN, 1967).

The $N_{max}E$ is related to the mean Wolf number $\bar{R}$ (MAEDA, 1971, 1972) which is a measure of the solar activity and the zenith angle, by the following relationship (for the mid-latitudes).

$$N_{max}E(\chi, \bar{R}) = 1.34 \times 10^{5} \left[1 + 0.0106\ \bar{R}\right]^{\frac{1}{2}} \cos^{0.62}\chi \qquad (8)$$

Ionograms showed beyond doubt that there exists a trough or a valley between E and F_1 layers, but gave no indication as to its depth. Only rocket-borne probe experiments such as a Langmuir probe could give the actual depth of the valley and these experiments showed that the daytime valley is quite shallow at mid and low latitudes (JACKSON AND KANE, 1959; PRAKASH ET AL, 1971). However, the night time electron density profiles measured by rocket-borne Langmuir probe showed a broad valley above 120 km (PRAKASH ET AL, 1970) over the dip equator.

Determination of f_oE is, however, not possible on a routine basis in the electrojet region, where the scattering of radio signals by the irregularities in the electron density produced due to the instability mechanisms, shield the normal echoes representing the E layer on the ionosondes. Very few observations on the χ variation of f_oE are available in the region in question. However, $f_{min}F$ is taken to represent f_oE (KRISHNAMURTHY AND SENGUPTHA, 1972) and the formula

$$f_oE \approx f_{min}F = A \cos^{0.33}\chi$$

is observed to fit the data. Here A is a constant.

During the night, the electron density decreases by more than an order of magnitude compared to the daytime values. The recent rocket probe data show that the $N_{max}E$ falls to about $10^3 cm^{-3}$ soon after sun-set and increases to reach a value of about $10^4 cm^{-3}$ at around mid-night while the valley above 120 km altitude deepens with large-scale stratifications becoming prominent (PRAKASH ET AL'S results). As discussed earlier, the sources like the Lyman α, Lyman β emissions scattered by Hydrogen atoms high above in the earth's atmosphere (geocorona), account for the maintenance of the E layer in the nighttime.

Fig.I.2 shows several electron density profiles obtained by the rocketborne Langmuir probe measurements made over the dip equator at Thumba (PRAKASH ET AL'S data). Whereas the daytime profile is relatively clean, the night time profiles show the presence of large scale stratifications or irregularities of electron density. It is also clear from the figure that the electron density rapidly decreases during the senset and increases again by about mid-night.

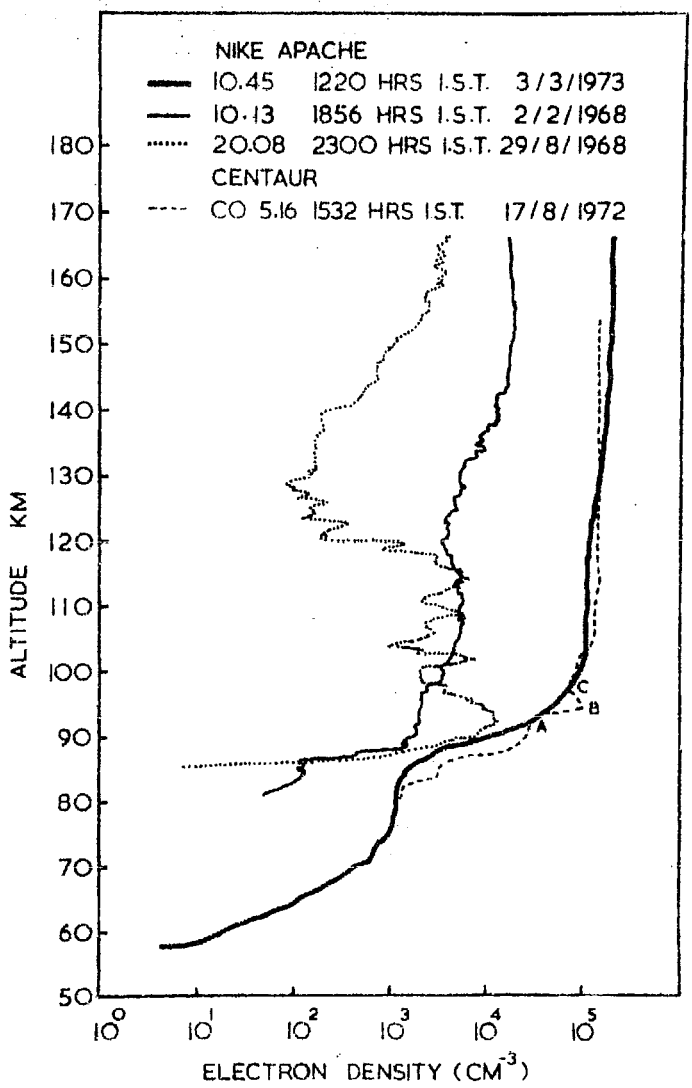

Figure I.2.: Electron density profiles measured by rocket-borne Langumuir probes flown over Thumba on various dates at various local times (Indian Standard Time, IST). These results are obtained and reported in various journals by SATYA PRAKASH and his colleagues. The figure is taken from KANE (1976).

I.4 Neutral motions in the E region:

The equation of motion of the neutral particles can be written as:

$$\frac{d\underline{W}}{dt} - 2\,\underline{\Omega}\times\underline{W} = \underline{g} - \frac{1}{\rho}\nabla p - \nabla\Psi + \frac{\mu}{\rho}\nabla^2\underline{W} - \nu_{ni}(\underline{W} - \underline{V}_i) \quad (10)$$

where $\underline{W}$ is the neutral wind velocity; $\underline{V}_i$ the ion drift velocity; $\underline{\Omega}$, the earth's angular velocity; $\underline{g}$, the acceleration due to earth's gravity; ρ is the gas density; p, the pressure of the atmosphere; Ψ, a scalar potential due to tide raising forces like solar thermal and lunar gravitational forces; μ, the coefficient of molecular viscosity; and ν_{ni} is the neutral-ion collision frequency.

The first term on the left hand side of the above equation represents the inertia term and the operator d/dt can be written as

$$\frac{d}{dt} = \frac{\partial}{\partial t} + \underline{W}\cdot\nabla \quad (11)$$

The term $(\underline{W}\cdot\nabla)$ above, represents momentum transport and renders the equation non-linear. This term is usually neglected to make the solutions of the equation simpler.

The second term on the left is essentially the force due to the rotation of the earth, known as 'Coriolis force'.

The first term on the right of eqn. (10) accounts for the acceleration due to earth's gravity. ∇p is the pressure gradient arising because of the hemispherical temperature differences. The third term accounts for the tidal forces due to solar thermal radiation and lunar gravitational force. The fourth term is a simple form of viscous force in which it is assumed tha

air be incompressible and μ be constant with altitude. In actual circumstances μ varies with altitude through its dependence on temperature and mean molecular mass. The last term is the ion-drag term arising due to the frequent collisional resistance offered by ions on neutral atmospheric motion. The term becomes important above 150 km where ν_{ni} is significant due to the enhanced ion density in the F-region and $\underline{W} - \underline{V}_i \neq 0$.

The equation (10) can be written in a general form as (BEER, 1974),

$$\rho \frac{d\underline{W}}{dt} = \underline{F} \qquad (10)a$$

where $\underline{F}$ represents external force. This fluid dynamical equation makes it possible to choose $\underline{F}$ according to the requirement of the problem or according to one's capacity to solve if the chosen problem is sufficiently complicated. Since the different terms listed above have different spatial and temporal scales it is not necessary to take all the terms at a time. Thus the solutions at any of these scales can be obtained by considering each time only the relevant terms.

The motions in the earth's atmosphere are governed by the following three equations:

(i) the equation of motion, described above.

(ii) the equation of state

$$f(\rho, p, T) = 0 \qquad (12)$$

(iii) the continuity equation or the equation of conservation of mass

$$\frac{\partial \rho}{\partial t} + \nabla \cdot (\rho \underline{W}) = 0 \qquad (13)$$

I.4.1 Prevailing winds:

These are very long period (varying only with season) winds whose associated coriolis force will just balance the local north-south pressure gradient and this gradient is produced in turn by meridional variations in the temperature-height profile. This is known as 'geostrophic approximation'. The geostrophic approximation is mathematically represented by

$$2\Omega W_y \sin\phi = \frac{1}{\rho}\frac{\partial p}{\partial x}$$

$$2\Omega W_x \sin\phi = -\frac{1}{\rho}\frac{\partial p}{\partial y} \qquad (10)b$$

ϕ being the latitude ($\neq 0^\circ$), x and y being toward east and north respectively. These winds, known as 'prevailing winds' because of their definitive nature, are studied extensively (KOCHANSKI, 1955; MURGATROYD, 1957; BATTEN, 1960) in the mesosphere and their distribution and seasonal variations are well established (HINES, 1963). These winds are generally eastward or westward and of magnitudes ranging upto $\sim$ 100 m/sec. There are also meridional components of prevailing winds which are mainly confined to the mesospheric region, 60-80 km.

I.4.2 Thermospheric winds or tidal winds:

The thermospheric winds are driven by pressure inequalities due to daily temperature variations. Because of their basic daily periodicity, these winds could be regarded as tidal in nature.

The sun and the moon exert forces on the earth's atmosphere. These forces are periodic in nature. Whereas the forces are wholly gravitational in the case of the moon, the sun exerts strong thermal force (due to its radiation) and a much weaker gravitational force. The earth's atmosphere responds to these forces in a manner analogous to forced mechanical vibrations and the steady-state responses of the atmosphere to these forces are called atmospheric tides. Naturally, the tides will have periods that are sub-multiples of the solar or lunar day.

Tidal wave winds have dominant periods of 24 hr (diurnal), 12 hr (semi-diurnal) and with lesser amplitude 8 hr (ter-diurnal). Gravity and coriolis forces also play an important role in the generation process of these waves. These are global in extent having large horizontal scale sizes comparable to the radius of the earth. Motions are mainly in the horizontal direction and the vertical motions are usually considered to be negligibly small.

The pertinent ground level measurements are those of pressure. They reveal substantial oscillations with periods

of 12 and 24 solar hours, comparable in magnitude to one another. There are, besides, weaker higher harmonics, and a weak component whose period is 12 lunar hours. The lunar component can be generated only by gravitational force, while the 24 hr solar component is almost certainly due to thermal processes. The 12 hr solar component can be generated by either of these means or by both. A feature of utmost importance to the dynamics of the upper atmosphere is that the amplitude of the tidal velocity increases with altitude. This property is characteristic of internal (or propagating) atmospheric waves. The amplitude enhancement of the internal waves with height results physically from a tendency of the energy flux to remain unchanged despite the decrease of gas density that makes the wave propagate upwards. For, this tendency can be met with only if the amplitude of oscillating velocity vector increases ($\propto \exp\int dz/2H$) with altitude. It is because of this inherent enhancement that tidal oscillations and other internal waves can play a major role in the dynamics of the upper atmosphere.

As a matter of fact, however, the tidal flux does not remain constant with altitude and much of the tidal energy rising from the troposphere is reflected downwards in the middle atmosphere. The upward increase of amplitude is

impeded in the reflecting regions and can even be reversed if the reflection is sufficiently severe. But some fraction of tidal energy can penetrate to the upper atmosphere and there the amplitude of oscillation again increases with height until it is limited by non-linear or dissipative processes such as viscous and ion drag forces. The oscillations that are observed in the upper atmosphere are commonly associated with this leakage of tidal energy from below.

The equation of motion in the case of tides is written as:

$$\frac{d\underline{W}}{dt} - 2\underline{\Omega} \times \underline{W} = \underline{g} - \frac{1}{\rho}\nabla p - \nabla \Psi \qquad (10)c$$

Ψ being the tidal potential function. The ion-drag and viscosity are omitted as a first-order approximation. They become important, however, in the F region altitudes (for example, LINDZEN, 1970; HINES AND HOOKE, 1970; RISHBETH, 1971).

The solar oscillation is written as

$$\chi_s = \sum_m \sum_n R_{mn}(r)\, \Theta_{mn}(\theta) \exp\left[i\left(2\pi t/T_s + \lambda\right)\right] \qquad (14)$$

where λ is longitude, t is time, θ colatitude and r is geocentric distance. T_s is the length of the solar day. The index $m = 1, 2, 3\ldots$ stands for diurnal, semidiurnal, terdiurnal, etc. modes of oscillations. The function $\Theta_{mn}(\theta)$

is known as Hough function and generally expressed in terms of associated Legendre polynomials. 'n' is related to the number of nodes between the poles which is $|n| - m \; (|n| > m)$. Negative values of n are also permitted and the modes are then called 'evanescent'. The eigen values of the equation have the dimension of length and are called the "equivalent depths", h_{mn}, which depend upon the atmospheric parameters. For each mode there exists a wave number k_{mn}, describing the vertical propagation

$$k^2_{mn} = \frac{1}{H h_{mn}} \left[(\gamma - 1)/\gamma + \frac{dH}{dh} \right] - \frac{1}{4H^2} \qquad (15)$$

If k_{mn} is real, the wave is propagating type or internal. If on the other hand, k_{mn} is imaginary (when for instance dH/dh becomes sufficiently negative) the wave is evanescent.

The upward propagation of the tidal energy has been considered among others by BUTLER AND SMALL (1963), KATO (1966 a,b), LINDZEN (1966, 1967). The theory of tides has been discussed in great detail by CHAPMAN AND LINDZEN (1970). According to this theory, the absorption of solar ultra-violet by ozone and water vapour gives rise to heating of the upper stratosphere or lower mesosphere and excites the atmosphere into various modes of oscillation. Since most of the heat input occurs at the low latitudes, those modes having the largest excursions at the equator are preferentially

excited. Oscillations that are in phase at all levels are said to be evanescent and cannot propagate from the level at which they are excited. Such oscillations occur in the thermosphere where they are excited at many levels simultaneously. Propagating or internal modes cause oscillations which are not in phase at different levels and have a vertical wave length determined by the equivalent depth h_{mn} of the atmosphere corresponding to that mode and the scale height H. For an isothermal atmosphere the wave length λ_z for the upward propagating energy is (WEEKES AND WILKES, 1947; HINES, 1964a),

$$\lambda_z \simeq 2\pi H \left(\frac{2}{7} \frac{H}{h_{mn}} - \frac{1}{4} \right)^{-1/2} \qquad (16)$$

The subscripts m, n denote different types of modes. Diurnal mode is denoted by m = 1; semidiurnal, m = 2 and terdiurnal, m = 3.

CHAPMAN AND LINDZEN (1970) have listed the different modes with their equivalent depths. Table 11 gives the various modes with their vertical wave lengths and periodicities. The evanescent modes (for example (1,-2) mode) have very large wave lengths. The propagating semidiurnal (2,2) mode also has a large wave length compared to the other propagating modes.

Theoretically obtained (CHAPMAN AND LINDZEN, 1970) amplitude and phase of the solar diurnal (1,1) and (1,-2)

Table I.1

Values for equivalent depth and vertical scale size (Chapman and Lindzen, 1970)

Diurnal (m = 1)			Semidiurnal (m = 2)			Terdiurnal (m = 3)	
mode	h	λ_z	mode	h	λ_z	mode	h
(1,1)	0.69	24	(2,2)	7.85	103	(3,3)	12.89
(1,3)	0.12		(2,4)	2.11	44	(3,4)	7.66
(1,5)	0.05		(2,6)	0.96		(3,5)	5.09
(1,-2)	-12.03	360				(3,6)	3.62

h and λ_z are in km. λ_z is given only for the important modes.

modes and semidiurnal (2,2) mode are given in Fig.I. 3. The latitudinal variation of the zonal (east-west) and meridional (north-south) functions of the modes (1,1), (1,-2), (2,2) and (2,4) computed theoretically are given in Fig.I. 4.

EVANS (1976) has recently reviewed the dynamical features of the ionosphere and upper atmosphere. He remarked that the experimental evidence indicates that tidal winds in the upper atmosphere appear to be variable and contain contributions from several components. Observations (HINES, 1966; WOODRUM AND JUSTUS, 1968; KOCHANSKI, 1966, 1973) showed that the maximum of the diurnal (1,1) mode occurs at 105-110 km with amplitudes of the order of 30-40 m/s near the equator and falls off toward higher latitudes. Theory (LINDZEN, 1970; LINDZEN AND BLAKE, 1971) also supports this behaviour of (1,1) mode (Fig.I. 3).

Above the level of its maximum, the diurnal wind component as derived from the chemical release data decreases in amplitude upto about 130 km and then begins to increase (KOCHANSKI, 1973) due to the growth of the trapped (1,-2) mode (LINDZEN, 1971; VOLLAND AND MAYR, 1972 , 1974; HONG AND LINDZEN, 1976). Besides the (1,1) and (1,-2) modes, possible higher order propagating modes are also present in the altitude region 110-140 km and these modes interact with each other. Because of the dominance of the semidiurnal mode at these altitudes, the nature of these interactions is not yet fully known (EVANS, 1976).

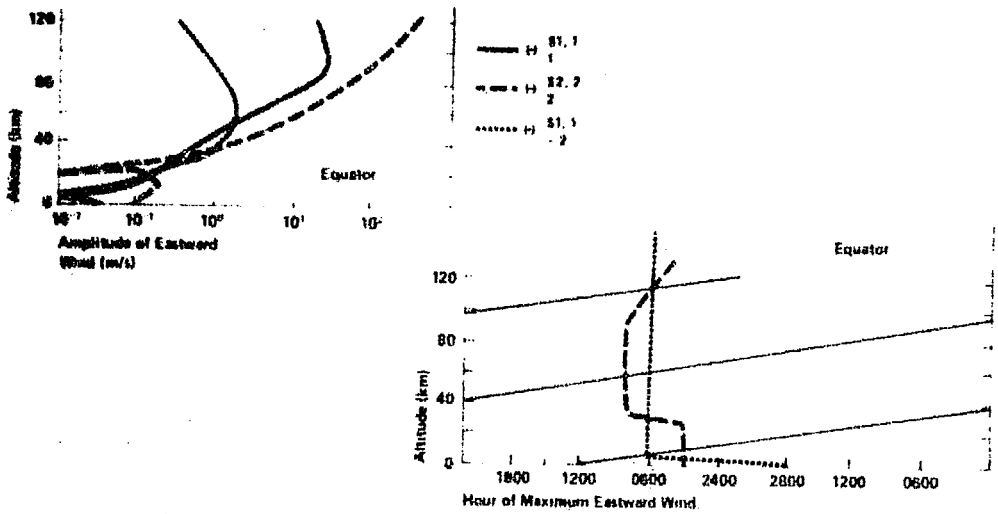

Figure I.3.: Amplitude and phase of the theoretical tidal components of the eastward wind over the equator. Solid curves are for the solar diurnal (1,1) mode. Dashed curves are for the solar semidiurnal (2,2) mode and the dotted curves are for the solar diurnal evanescent (1,-2) mode (taken from BEER, 1974).

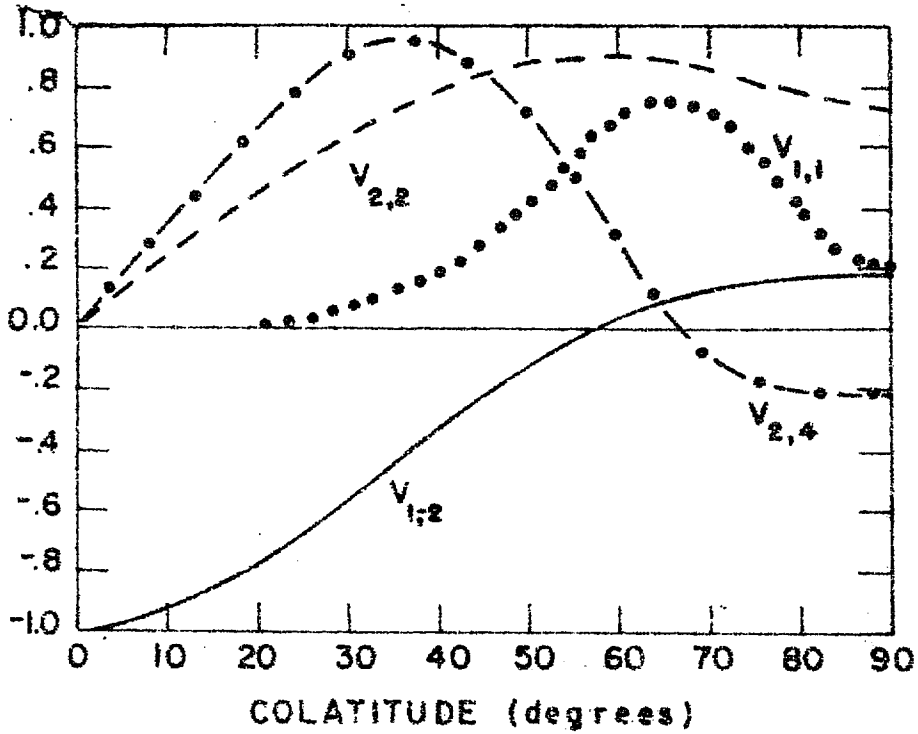

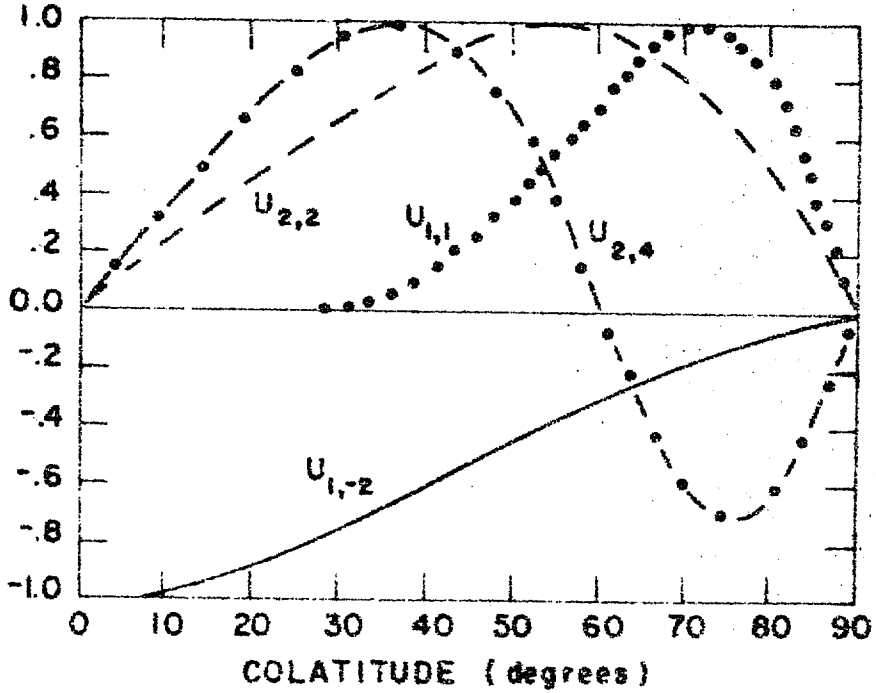

Figure I.4.: Latitudinal variation of the expansion functions for the eastward (V) and southward (U) tidal components - (1,1), (1,-2), (2,2) and (2,4) modes (after, FORBES AND LINDZEN, 1976a). The eastward and northward velocities are functions of the respective expansion functions.

The semidiurnal propagating (2,2) mode is generated strongly in the strato-mesosphere but becomes evanescent in the 60-85 km region and its amplitude is therefore reduced at 100 km altitude. Despite this, the (2,2) mode could be the dominant semidiurnal mode in the lower thermosphere (LINDZEN AND BLAKE, 1971).

The mid-latitude wind measurements by the incoherent scatter radar at Millstone Hill and St. Santin (BERNARD AND SPIZZICHINO, 1971;AMAYENC AND REDDY, 1972; EVANS, 1972; AMAYENC, 1974; BERNARD, 1974 a,b; SALAH AND WAND, 1974; SALAH ET AL, 1975 a,b; EVANS AND SALAH, 1975; EVANS, 1976) and by the meteor radar technique (FELLOUS, 1972; FELLOUS ET AL, 1975; ELFORD, 1973; STUBBS, 1973; GLASS AND SPIZZICHINO, 1974) showed beyond doubt that the wind is predominantly semidiurnal in the E-region altitudes and that the amplitude of the diurnal component must be smaller than that deduced from the dynamo theory. These observations showed the dominance of the (2,4) mode over the (2,2) mode below 130 km, especially in summer. Above this level, the amplitude of the semidiurnal tide grows and reaches a peak at around 170 km and is identified with the (2,2) mode. It has been shown that the dominant diurnal mode above 130 km is the evanescent (1,-2)mode.

A detailed study of the semi-diurnal tide at low-latitudes (Arecibo) is made very recently by WAND (1976). It is found that

the average behaviour of semidiurnal tide at Arecibo, the low-latitude station, is similar to that at the mid-latitudes (WAND AND SALAH, 1974; SALAH ET AL, 1975; WAND, 1976). However, there are differences as to the amplitude and phase at these different latitudes. At the dip equator, REES ET AL (1976) reported that the winds as observed by the vapour trails are predominantly semidiurnal in the altitude region 90-160 km.

The observations of drifts by the spaced receiver technique at low latitudes (excluding the electrojet region) also showed the dominance of diurnal tide (RAGHAVARAO AND RAMANCHANDRA RAO, 1960). However, whether these drifts truly represent the wind motions is debatable (HINES AND RAGHAVARAO, 1968; HINES, 1976). It is not yet known, beyond doubt, as to which mode of the tidal wind is dominant at the E-region altitudes of the equatorial ionosphere.

I.4.3 Gravity waves:

Superimposed on the prevailing and tidal winds at meteor heights are irregular components of magnitude comparable to that of tides and with a time scale ranging from a few minutes to a few hours. The atmosphere of the earth (and any planet) has a characteristic feature as to its density stratifications under the action of gravitational field. Most part of this stratified atmosphere is statically stable, i.e., the potential temperature increases with increasing height. The buoyancy becomes important when the fluid is under these conditions.

Buoyancy waves in the upper atmosphere have probably always been visible to man, through their dramatic effects on the noctilucent clouds (NLC's) which form near the mesopause at high latitudes. The dominant horizontal wavelengths of these waves range from a few kilometers to several hundred kilometers.

They manifest themselves on the meteor trails and the winds derived from observations (visible as well as radio) on the trails reveal irregular fluctuations with time and space (LILLER AND WHIPPLE, 1954; MANNING ET AL, 1950; 1954; ELFORD AND ROBERTSON, 1953; GREENHOW AND NEUFELD, 1959 a,b; 1961; MANNING AND ESHLEMAN, 1959; REVAH, 1969; SPIZZICHINO, 1969 a,b,c; SPIZZICHINO, 1970 a,b). The studies on the winds of upper atmosphere revealed that superposed on the large scale tidal winds and prevailing winds, there are irregular wind fluctuations of much smaller spatial scales and of shorter periodicities. HINES (1960) summarised the properties of such irregular winds, as follows:

(1) The vertical scale sizes of the irregular winds are of the order of a few kilometers; typically the scale size (or wavelength) is 10 km;

(2) horizontal scales exceed the dominant vertical scales by more than an order of magnitude;

(3) temporal variations of scales of many tens of minutes, with a typical period of 200 minutes;

(4) vertical velocities smaller than the horizontal velocities by an order of magnitude or more,

(5) dominant vertical scale sizes increase with increasing height;

(6) amplitude of the dominant irregular winds increasing with increasing height.

These irregular winds are originally thought to be due to turbulence in the lower part of the upper atmosphere (BOOKER, 1956; 1958; BOOKER AND COHEN, 1956). However, the observed distortions in the meteor trains can not be interpreted as due to turbulence (GOSSARD AND HOOKE, 1975, for example).

HINES (1960) was the first to explain satisfactorily the cause and occurrence of these irregular winds. He proposed a theory of internal atmospheric gravity waves and attributed the irregular structure of the observed winds to the propagation of such waves. He argued that the properties (3) through (6) of the irregular winds can be accounted for by the properties (1) and (2) in view of known relationships valid for internal atmospheric gravity waves.

The equation of motion in the case of these waves is,

$$\frac{d\underline{W}}{dt} = \underline{g} - \frac{1}{\rho}\nabla p \qquad (10)d$$

neglecting Coriolis force (because of its longer periodicity than the gravity wave periods), ion drag and viscosity.

The equation of conservation of mass is,

$$\frac{\partial \rho}{\partial t} + \nabla \cdot (\rho \underline{W}) = 0$$

and the equation of state is

$$p \propto \rho^{\gamma}$$

It is assumed that the perturbations in the pressure (Δp) and density ($\Delta \rho$) of the atmosphere and the perturbation velocity ($\underline{W}$), vary as,

$$\frac{\Delta p}{p} \propto \frac{\Delta \rho}{\rho} \propto W_H \propto W_Z \propto \exp i(\omega t - \underline{K} \cdot \underline{r}) \qquad (17)$$

Here H and Z denote the horizontal and vertical components respectively. ω is the wave frequency and $\underline{K}$ is the propagation vector. From these equations, the following dispersion relation (a relationship between the wave number and the wave frequency) is derived (HINES, 1960),

$$\omega^4 - \omega^2 C_s^2 (K_H^2 + K_Z^2) + (\gamma - 1) g^2 K_H^2 + i \gamma g \omega^2 K_Z = 0 \qquad (18)$$

K_H and K_Z, the horizontal and vertical wave numbers cannot both be real. K_H can reasonably be assumed as real and then K_Z can either be (i) purely imaginary or (ii) a complex quantity, $K_Z = k_Z + i/2H$, with k_Z purely real. Case (i) represents the "surface" or "evanescent" waves. Case (ii) represents the "internal" or propagating waves. In case (ii) again, two distinct sequences of waves can propagate; they are

acoustic waves $\omega > \omega_a \equiv \gamma g / 2 C_s$

internal gravity waves $\omega < \omega_g \equiv (\gamma - 1)^{1/2} g / C_s$

For meteor heights,

the sound speed, C_s = 280 m/s

the atmospheric scale height, H = 6.0 km

$\tau_a = 2\pi/(\omega)_a$ = 4.4 min.

$\tau_g = 2\pi/(\omega)_g$ = 4.9 min.

This forms the simple theory of gravity waves formulated by HINES (1960).

However, there are complications too, in the theoretical interpretation, as one has to take into consideration the dissipation due to viscosity, refraction and ducting of the waves because of sharp temperature gradients and non-linear effects (PITTEWAY AND HINES, 1963; TOLSTOY, 1963; EINAUDI AND HINES, 1971; MIDGLEY AND LIEMOHN, 1966; HINES AND REDDY, 1967; KLOSTERMEYER, 1969; HINES AND HOOKE, 1970; HINES, 1974).

Fig. I.5 shows the spectrum of gravity waves derived from the theory. The viscous dissipation and the reflection levels due to the temperature gradients at the mesospheric levels are also shown in the figure.

The winds determined by the optical tracking of the rocket-released chemiluminescent clouds in the region 80-150 km are in conformity with the meteoric train observations and the gravity wave interpretation (MANRING ET AL, 1961; ROSENBERG AND EDWARDS, 1964; ROSENBERG, 1968 a,b; KOCHANSKI, 1964; BEDINGER ET AL, 1968). The

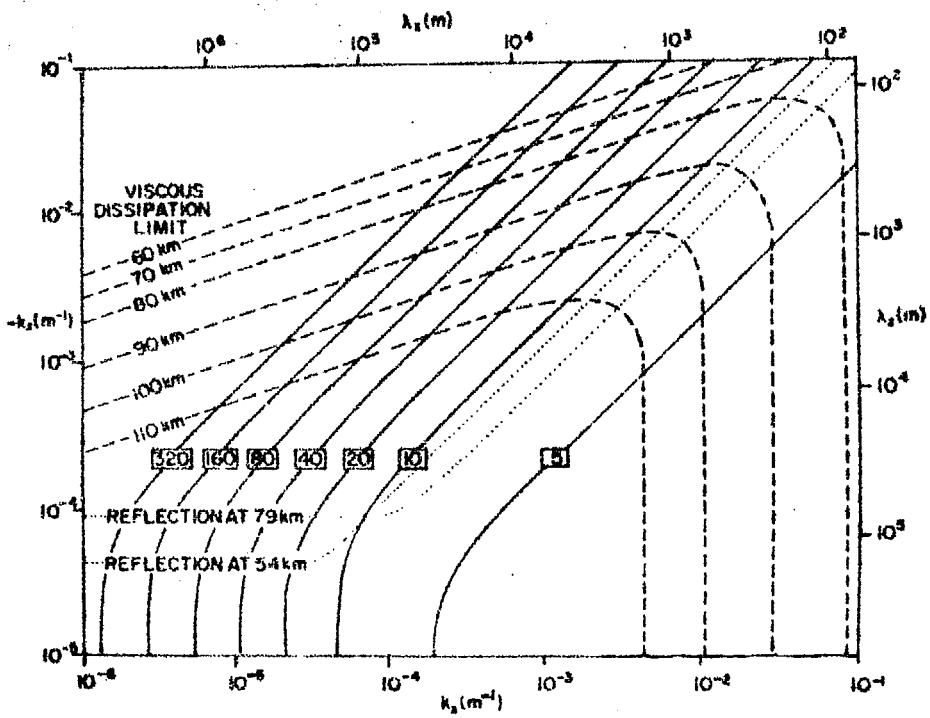

Figure I.5.: The relation between horizontal and vertical wavelengths (λ_x, λ_z) or wave numbers (k_x, k_z) for internal atmospheric gravity waves (solid curves) of various periods (in minutes) given in the boxes on the appropriate curves. The broken curves indicate the 'excluded-permitted' boundary imposed by viscosity; the region above and to the right of these curves being 'excluded'. The intrusion of successive members of this family, as the altitude is raised from 60 to 110 km, indicates the growing importance of viscous damping. The dotted curves represent modes that would be reflected in the mesosphere due to temperature gradients there; the region below and to the right represents the modes that can not penetrate the mesosphere without serious reflection (after HINES, 1960).

incoherent scatter radar observations made at Jicamarca, an equatorial station, also showed the presence of gravity waves (WOODMAN, 1973; RASTOGI AND BOWHILL, 1975).

The existence of gravity waves in the atmosphere is now a confirmed fact. The spectrum of the atmospheric waves (tidal and gravity waves) is derived from the experimental observations for the midlatitudes by SPIZZICHINO (1970) and is reproduced in Fig. I. 6. The figure shows the importance of gravity waves vis-a-vis the tidal winds in the dynamics of upper atmosphere.

The effects produced by gravity wave on the ionosphere have been studied by several workers. The travelling ionospheric disturbances (TID's) are ionisation irregularities observed at the F-region altitudes having horizontal scale sizes, of the order of a few hundred kilometers and vertical scale sizes of the order of a few tens of kilometers and travel very long distances (MUNROE, 1950, 1958; CHAN AND VILLARD, 1962; TITHERIDGE, 1963; THOME, 1964, 1968; GEORGES, 1967, 1968; DAVIS AND DA ROSA, 1969; TESTUD AND VASSEUER, 1969). TIDs are now believed to be produced by the gravity waves (HINES, 1960; 1963; FRIEDMAN, 1966; FRANCIS, 1973; HOOKE, 1968, 1969; DAVIS, 1973).

The temperature profiles, also showed wave like disturbances and are attributed to the gravity waves. The photochemical effects caused by the propagation of gravity waves

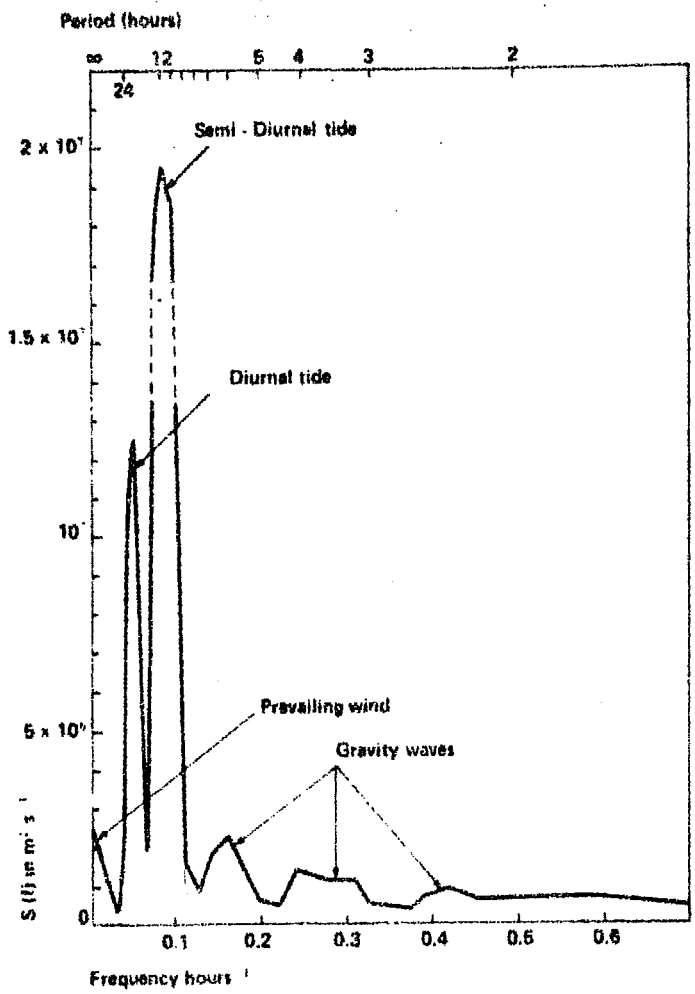

Figure I.6.: Power spectrum S(f) in the frequency domain of the zonal wind in the low E-region observed at a mid-latitude station. The contributions of the prevailing wind (frequency = 0), the diurnal and semi-diurnal winds and of the gravity waves can be seen in the figure (after SPIZZICHINO, 1970).

in the E and lower F-regions are discussed by HOOKE (1968,1969

More recently the electrodynamical effects due to gravity waves in the E-region have been discussed by KATO (1973a) and ANANDARAO ET AL (1977a). They showed that the gravity wave associated irregular winds can produce the electron density stratifications in the E-region through the wind shear mechanism (dealt in detail in CHAPTER V).

I.5 Turbulence:

The turbulence is characterised by the presence of random oscillations of velocity which produce irregularities in the path of a particle. Turbulence can be termed as a sink of energy - just as there are sources of energy. The kinetic energy of the fluid due to the fluctuations in the velocity will subsequently be dissipated as heat. These fluctuations as manifested in velocity are different from the regular wave motions and turbulence grows at the expense of the energy in waves either by breaking them or by extracting energy from the strain rates produced by waves.

For the fluids with kinematic viscosity ν ($= \eta/\rho$, η being the coefficient of viscosity and ρ, the atmospheric mass density). The condition for the occurrence of turbulence is given by the Reynolds number

$$R_g = \frac{U_f L}{\nu}$$

where L is the characteristic scale size of the turbulence

U_f, the fluid velocity. In the case of the earth's atmosphere, the Reynolds number can be expressed as,

$$R_g = \frac{(\omega)_{BV} L^2}{\nu} \qquad (19)$$

Here, $(\omega)_{BV}$ is the Brunt-Vaisala frequency which is the characteristic frequency of the atmosphere. Reynolds number is generally preferred to describe the extinction of turbulence at the small-scale end of the turbulence spectrum.

The persistance of turbulence in a density gradated fluid such as the atmosphere, is characterised by the Richardson number defined as

$$R_i = \frac{(\omega)^2_{BV}}{(\partial W/\partial z)^2} \qquad (20)$$

Here, W is the fluid velocity (or the neutral wind velocity in the case of the atmosphere) and is assumed to be entirely horizontal. $\partial W/\partial z$ represents the destabilisation factor due to the vertical shear in the horizontal motion. The Brunt-Vaisala frequency $(\omega)_{BV}$ represents the stability of the atmosphere. R_i provides a measure of the stabilising influence of gravity modified by temperature gradients in comparison with the destabilising effects of wind shear. The altitude variation of $(\omega)_{BV}$ and the profiles of neutral density scale height H and the molecular viscosity (η) are shown in the Fig.I. 7. The figure shows that $(\omega)_{BV}$ is almost a constant in the E region and therefore it is the wind shear term $(\partial W/\partial$ which controls the Richardson number. The condition for

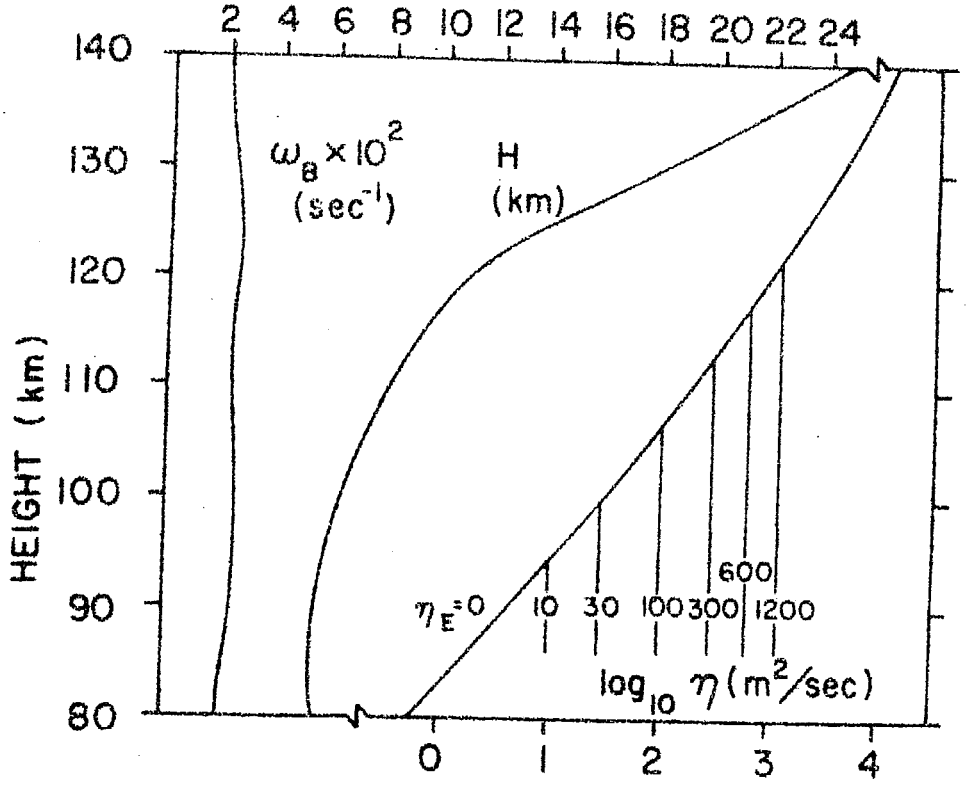

Figure I.7.: Vertical variation of Brunt-Vaisala frequency ω_B and the neutral atmospheric scale height H (upper scale for both) and of kinematic viscosity (lower scale, logarithmic). The $\eta_E = 0$ curve represents the kinematic viscosity η_M due to molecular processes alone, as distinct from turbulent eddy processes. The vertical lines for other values of η_E represent assumed values of eddy kinematic viscosity (after HINES, 1974).

the turbulence to set in is

$$R_i \ll 1.$$

HINES (1971) modified the definition of R_i, by taking into consideration the vertical component of the wind and the shear of the wind in the horizontal direction. He argued that the atmosphere, where the gravity waves are present, the vertical wind and the horizontal shear can be important. HINES redefined R_i as,

$$R_i = \frac{(\omega)^2_{BV}}{(\nabla \underline{W})^2} \qquad (21)$$

$(\nabla \underline{W})^2 = (\nabla W_H)^2 + (\nabla W_Z)^2$. H and Z denote the components in the horizontal and vertical directions respectively. Turbulence occurs if the criterion

$$R_i \leq 1/4$$

is satisfied.

However, in actual circumstances this criterion may not be completely adequate in defining the turbulence (LINDZEN, 1968; LINDZEN AND BLAKE, 1971; BEER, 1974) and the wind shears alone may not be able to account for the occurrence of the turbulence (TCHEN, 1970).

The analysis of turbulence is based on the postulate of the existence of a range of scale sizes of turbulent motion Energy is being continually passed from larger to smaller scale motions. A lower limit is eventually reached when the energy has been passed down to fluctuations that are

too small to permit the formation of still smaller eddies. At this point the energy is directly converted into the random motion of the molecules by viscous forces.

The average properties of small-scale components of any turbulent motion are determined uniquely by the kinematic viscosity of the fluid, ν $(=\eta/\rho)$, and the average rate of dissipation of energy per unit mass of fluid $\bar{\epsilon}$. The largest eddies obtain their energy directly from the wave motions and the smallest eddies convert their energy (derived from large eddies) into heat by viscous interactions. In case of eddies of intermediate sizes with the characteristic velocity (U_T) and diameter (L_T), the average rate of dissipation of energy per unit mass of the fluid is

$$\bar{\epsilon} = \frac{U_T^3}{L_T} \tag{22}$$

This represents the rate at which the energy is converted from the atmospheric motions into heat. The diameter and mean life time of the smallest eddy are given by (for example, KOLMOGOROFF, 1941; BATCHELOR, 1953),

$$L_{min} = (\nu^3/\bar{\epsilon})^{1/4} \tag{23}$$

$$\bar{\tau}_{min} = (\nu/\bar{\epsilon})^{1/2} \tag{24}$$

Rocket-borne mass spectrometer measurements and observations of vapour trail releases in the upper atmosphere

have shown that the atmospheric constituents are thoroughly mixed to a height of 105 $\pm$5 km. It is proved now beyond doubt that the vapour trails do show the ambient turbulence below about 105 km and these effects are not an artifact. The break down from laminar to turbulent flow can easily be recognised by visual inspection of the photographs of the trail taken at different times in a sequence. BLAMONT (1963) has argued that a vapour trail will become turbulent when it reaches a dimension comparable with that of the smallest eddy of the ambient turbulence spectrum. He associated the parameter L_{min} with the onset of turbulence as observed on the vapour trails. He identified that the smallest eddy is of the order of 50 m. BLAMONT AND BARAT (1967, 1968) have shown that below about 100 km, there could exist regions of turbulence and laminar flow. The possible coexistence of laminar and turbulent regions is shown by other workers also (REES ET AL, 1972a ; ANANDARAO ET AL, 1977 b).

REES ET AL (1972a) believe that it is the time elapsed ($\bar{\tau}_{min}$) after deposition of the contaminant that determines the onset of turbulence rather than the dimension of the trail (L_{min}). Around 100 km the time of onset is $\sim$ 20-30 sec. That is, the trail shouldshow up turbulence 20 sec after its release. The time increases with the increase in altitude. Fig.I. 8 shows the plots of $\bar{\tau}_{min}$ and L_{min} versus altitude based on the computations of ROPER (1966) and JUSTUS (1967)

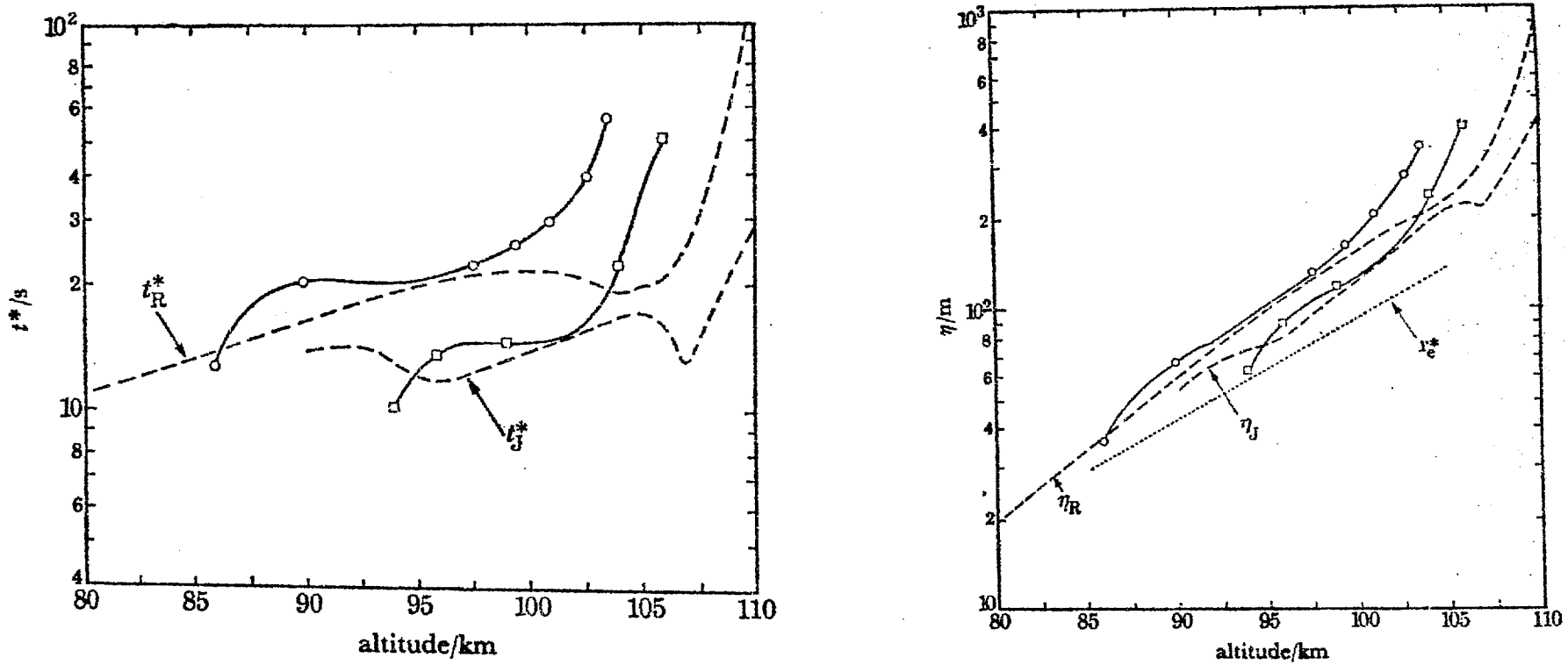

Figure I.8.: Variation with altitude of the time constant of the KOLMOGOROFF microscale t^* (same as $\overline{\tau}_{min}$ used in the text) and that of the KOLMOGOROFF microscale η (same as L_{min} used in the text). The subscripts R and J denote the sources from where the curves are taken, viz. ROPER (1966) and JUSTUS (1967) respectively. The other curves are from the observations on vapour trails taken from REES ETAL (1972 a).

along with the results obtained from the vapour trail releases by REES ET AL (1972a). Upto an altitude of about 105 km, $\overline{\tau}_{min}$ does not show much variation with altitude. Above about 105 km, $\overline{\tau}_{min}$ increases abruptly. In contrast, L_{min} varies almost linearly with altitude with a tendency of abruptness above about 105 km. The results of the vapour trail observations are in good agreement with these profiles (REES ET AL, 1972a). The close similarity in the shapes of the $\overline{\tau}_{min}$ curves (both observed and theoretical) which show a flat region followed by a sharp rise, indicate that the time delay in the onset of turbulence (as observed on the vapour trails) should be related to the time constant of KOLMOGOROFF microscale ($\overline{\tau}_{min}$).

DESAI ET AL (1975), however, have shown by observations on a sodium trail release (over TERLS, Thumba) that the turbulence developed first at 104 km altitude, 30 sec after the release of the trail; and only later at the lower portions of the trail. These observations on the development of turbulence seem to be in disagreement with the plots shown in Fig.I. 8.

The altitude where the turbulence ceases abruptly and the molecular diffusion becomes predominant is known as the turbopause. The level of turbopause is shown to change with season in conformity with the seasonal variation of temperature (ELFORD AND ROPER, 1967). It is found that

the turbopause is at a height of 104 $\pm$2 km (BLAMONT AND BARAT, 1967; REES ET AL, 1972a; DESAI ET AL, 1975). However, on occasion, the turbopause occuring at 93 km is also reported (ANANDARAO ET AL, 1977b). Furthermore, TIETELBAUM AND BLAMONT (1977) have shown that the turbopause undergoes altitude variations during the day.

I.6 Conductivities:

The conductivity of the ionosphere is anisotropic because of the presence of the earth's magnetic field. The expressions for the conductivity can be obtained from the equations of motions of ions and electrons.

The equations of motion of an electron and ion can be written as,

$$\frac{d\underline{V}_j}{dt} = e_j(\underline{E} + \underline{V}_j \times \underline{B}) + m_j \underline{g} + m_j \nu_j(\underline{W} - \underline{V}_j) - \frac{1}{N}\nabla p_j \quad (25)$$

where j represents electrons (e) or ions (i) and $\underline{V}_j$ is the velocity of the charged constituent, m_j is its mass and N is its density. p_j is the partial pressure of the constituents. ν_j is its collision frequency with the neutral particles. $\underline{W}$ is the neutral wind velocity and $\underline{E}$ and $\underline{B}$ are electric and magnetic fields respectively.

In a coordinate system ξ, η, ζ, wherein ζ is along the direction of the magnetic field $\underline{B}$ and η is perpendicular to both magnetic and electric fields, the components of the electron velocity in these directions are given by (e.g. FEJER, 1965),

$$V_{e\xi} = \frac{E'_\xi}{B} \frac{\nu_e \omega_e}{\nu_e^2 + \omega_e^2}$$

$$V_{e\eta} = \frac{-E'_\eta}{B} \frac{\omega_e^2}{\nu_e^2 + \omega_e^2} \qquad (26)$$

$$V_{e\zeta} = \frac{E'_\zeta}{B} \frac{\omega_e}{\nu_e}$$

and similar equations for the ions will be

$$V_{i\xi} = \frac{E'_\xi}{B} \frac{\nu_i \omega_i}{\nu_i^2 + \omega_i^2}$$

$$V_{i\eta} = \frac{E'_\eta}{B} \frac{\omega_i^2}{\nu_i^2 + \omega_i^2} \qquad (27)$$

$$V_{i\zeta} = \frac{E'_\zeta}{B} \frac{\omega_i}{\nu_i}$$

Here $\underline{E}'$ represents the total electric field which is the vector sum of an electrostatic part $\underline{E}$ and the induction part $\underline{U} \times \underline{B}$, where $\underline{U}$ is the relative velocity of the charged particles with respect to the neutrals. Here ω_e and ω_i are the gyrofrequencies of electrons and ions respectively. ν_e and ν_i are the collision frequencies of electrons and ions. Now the current density $\underline{J}$ in the medium is given as:

$$\underline{J} = N(-e\underline{V}_e + e\underline{V}_i) \qquad (28)$$

The components of $\underline{J}$ in ξ, η, ζ directions are.

$$J_\xi = E'_\xi \frac{Ne}{B}\left[\frac{\nu_i \omega_i}{\nu_i^2+\omega_i^2} + \frac{\nu_e \omega_e}{\nu_e^2+\omega_e^2}\right] = \sigma_P E'_\xi \qquad (29)$$

$$J_\eta = E'_\eta \frac{Ne}{B}\left[\frac{\omega_e^2}{\nu_e^2+\omega_e^2} - \frac{\omega_i^2}{\nu_i^2+\omega_i^2}\right] = \sigma_H E'_\eta$$

$$J_\zeta = E'_\zeta \frac{Ne}{B}\left[\frac{\omega_i}{\nu_i} + \frac{\omega_e}{\nu_e}\right] = \sigma_0 E'_\zeta$$

σ_0, σ_P, σ_H being the direct (along the magnetic field line), Pedersen (perpendicular to $\underline{B}$ but parallel to $\underline{E}$) and Hall (perpendicular to both $\underline{B}$ and $\underline{E}$) conductivities.

Conductivity in the presence of crossed electric and magnetic fields (the primary east-west electric field and the earth's magnetic field in the ionosphere) is anisotropic and has the following components.

(i) The conductivity parallel to the magnetic field lines, σ_0, called the direct or parallel conductivity (which would have been the conductivity without the magnetic field) is given by

$$\sigma_o = \frac{Ne}{B}\left[\frac{\omega_i}{\nu_i} + \frac{\omega_e}{\nu_e}\right] \qquad (30)$$

(ii) The conductivity parallel to the primary electric field but perpendicular to the magnetic field, σ_P, known as the Pedersen conductivity, is given by

$$\sigma_P = \frac{Ne}{B}\left[\frac{\nu_i\,\omega_i}{\omega_i^2+\nu_i^2} + \frac{\nu_e\,\omega_e}{\omega_e^2+\nu_e^2}\right] \qquad (31)$$

(iii) The conductivity perpendicular to both electric and magnetic fileds, σ_H, arising due to the crossed electric and magnetic fields, termed as the Hall conductivity is,

$$\sigma_H = \frac{Ne}{B}\left[\frac{\omega_e^2}{\omega_e^2+\nu_e^2} - \frac{\omega_i^2}{\omega_i^2+\nu_i^2}\right] \qquad (32)$$

The difference in the mobilities of the electrons and ions in the direction perpendicular to the electric and magnetic fields ('Hall direction') gives rise to a polarisation field in that direction. As a consequence of this the Pedersen conductivity is modified. The effective conductivity in the direction of the primary electric field known as Cowling conductivity is now given by

$$\sigma_3 = \sigma_P + \frac{\sigma_H^2}{\sigma_P} \qquad (33)$$

In general, the conductivities can be obtained by computing the collision frequencies. The collision frequencie in terms of the known parameters such as the densities of charged and neutral constituents, temperatures and masses of these constituents, are discussed in the literature (CHAPMAN, 1956, 1957; THRANE AND PIGGOTT, 1966; DALGARNO, 1967; BANKS, 1966 a,b; STUBBE, 1968).

Fig.I. 9 shows the altitude profiles of the conductivities σ_0, σ_P, σ_H and the Cowling conductivity σ_3. It can be seen from the figure that σ_0 is about 3 orders of magnitude greater than σ_P and σ_H. σ_P maximises above about 130 km and σ_H is almost a constant in the region of 90 and 120 km. σ_3 has a maximum at 100 km falling steeply above and below the altitude.

The equation (29) can be re-written as

$$\underline{J} = [\sigma] \cdot \underline{E}' \qquad (34)$$

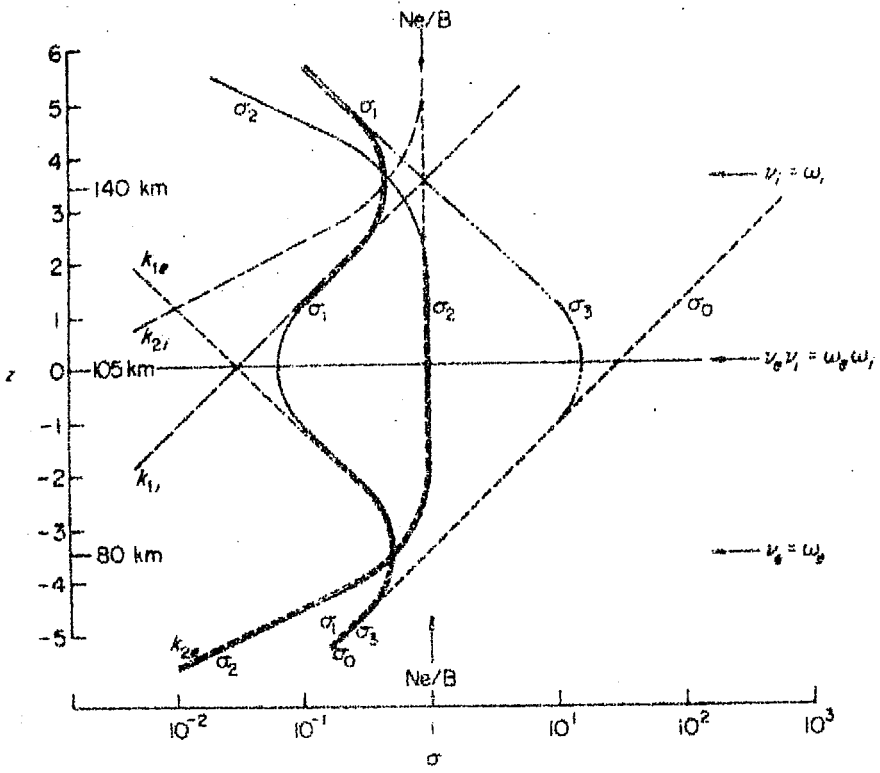

Figure I.9.: Conductivities σ_0, σ_1 (same as σ_P), σ_2 (same as σ_H) and σ_3 per ion pair plotted on a logarithmic scale relative to the value Ne/B, as a function of reduced height z for an idealized isothermal model atmosphere. It is assumed that collision frequency $\nu \propto \exp(-z)$ and gyrofrequency ω is independent of z, for both positive ions and electrons; also that $\nu_i \omega_e / \nu_e \omega_i \simeq 1000$. The zero of z is the level where $\nu_i \nu_e = \omega_i \omega_e$, and the important levels where $\nu_i = \omega_i$ and $\nu_e = \omega_e$ are, situated at $z = \pm 0.5 \ln (1000)$. (after RISHBETH AND GARRIOTT, 1969)

$[\sigma]$ is the conductivity tensor given by

$$[\sigma] = \begin{pmatrix} \sigma_P & -\sigma_H & 0 \\ \sigma_H & \sigma_P & 0 \\ 0 & 0 & \sigma_0 \end{pmatrix} \qquad (35)^a$$

in a coordinate system wherein one of the axes is aligned with the magnetic field direction.

In a geocentric coordinate system r, θ, ϕ where r is radially outwards from the centre of the earth, θ, is colatitude and ϕ is longitude, this becomes

$$[\sigma] = \begin{pmatrix} \sigma_{rr} & \sigma_{r\theta} & \sigma_{r\phi} \\ \sigma_{\theta r} & \sigma_{\theta\theta} & \sigma_{\theta\phi} \\ \sigma_{\phi r} & \sigma_{\phi\theta} & \sigma_{\phi\phi} \end{pmatrix} \qquad (35)^b$$

where

$$\sigma_{rr} = \sigma_0 S^2 + \sigma_P C^2$$

$$\sigma_{r\theta} = \sigma_{\theta r} = (\sigma_0 - \sigma_P) SC$$

$$\sigma_{r\phi} = -\sigma_{\phi r} = -\sigma_H C$$

$$\sigma_{\theta\theta} = \sigma_0 C^2 + \sigma_P S^2$$

$$\sigma_{\theta\phi} = -\sigma_{\phi\theta} = \sigma_H S$$

$$\sigma_{\phi\phi} = \sigma_P$$

C and S are the Cosine and Sine of the dip angle I.

I.6.1 Layer conductivities: BAKER AND MARTYN (1953) have discussed the conductivities in the ionosphere by assuming the ionospheric dynamo region as a thin conducting layer. The thin layer approximation necessitates complete inhibition of the vertical currents resulting in the production of the polarization fields in the vertical direction (Hall polarization fields). Under the assumption that the vertical currents are zero, the conductivity tensor which is originally a 3 x 3 tensor, can be reduced to a 2 x 2 tensor.

$$[\sigma] = \begin{pmatrix} \sigma_{xx} & \sigma_{xy} \\ \sigma_{yx} & \sigma_{yy} \end{pmatrix} \qquad (35)c$$

where $\sigma_{xx} = \sigma_0 \sigma_P / (\sigma_0 S^2 + \sigma_P C^2)$

$$\sigma_{xy} = -\sigma_{yx} = \sigma_0 \sigma_H S / (\sigma_0 S^2 + \sigma_P C^2) \qquad (36)$$

$$\sigma_{yy} = \sigma_P + \sigma_H^2 C^2 / (\sigma_0 S^2 + \sigma_P C^2)$$

Here x is towards magnetic south and y towards east. These conductivities are known as the layer conductivities and at the dip equator (I = 0), they reduce to,

$$\sigma_{xy} = \sigma_0$$

$$\sigma_{xy} = 0$$

$$\sigma_{yy} = \sigma_3$$

σ_3 is the Cowling conductivity defined earlier and is maximum at the equator and at around 100 km (Fig. I. 9).

1.7 The Dynamo Theory:

Even under the quiet sun conditions the geomagnetic field is found to fluctuate during the day. These fluctuations or variations in the magnetic field are known as the "Sq-variations" (Solar quiet variations). BALFOUR STEWART (1882) explained these variations as due to the currents that could be present in the earth's upper atmosphere. According to his hypothesis known as the "dynamo theory", the currents are set up by an induction electromotive force generated by the movement of ionized gas across the main geomagnetic field. These currents cause the observed magnetic field fluctuations on the ground. The ionised gas is moved across the geomagnetic field by the action of the global neutral winds of tidal origin. SCHUSTER (1908) was the first to formulate the dynamo theory mathematically. Subsequently, CHAPMAN (1919) and many others have developed it into its present form. It is believed now, that the Sq variations are indeed a consequence of dynamo action of the tidal winds in the upper atmosphere.

The wind with velocity $\underline{W}$, blowing across the geomagnetic field, induces the Lorentz force $e(\underline{W} \times \underline{B})$. The extent to which the ions and electrons get affected by this force depends upon the ratio of their collision frequencies to their respective gyrofrequencies which in turn is a function of altitude. In a direction parallel to the magnetic field

the wind has no resistance and both ions and electrons are moved in that direction. But in a direction perpendicular to the magnetic field the effect of the Lorentz force depends upon how frequently the electrons or ions collide with the neutral particles compared to their (electrons or ions) gyrofrequencies. In the dynamo region (approximately from 90 km to 140 km), the electron gyrofrequency is much higher than its collision frequency with the neutrals whereas the ion neutral collision frequency is higher than the ion gyrofrequency. Thus in this region, in the presence of a wind, the ions and electrons will have differential motions. As a result, the polarization fields are set up in a direction opposite to the Lorentz force field $\underline{W} \times \underline{B}$. The extent to which the polarization field cancels the $\underline{W} \times \underline{B}$ field depends upon the horizontality of the magnetic field lines. The cancellation is maximum in the region of the dip equator where field lines are horizontal. However, in the mid-latitudes where the magnetic field lines are fairly vertical, the Lorentz field will be quite effective. The polarization fields set up will modify the currents generated initially by the differential motion. The currents developed by the dynamo action can be written as

$$\underline{J} = [\sigma] \cdot \underline{E}' \qquad (34)$$

where, $\underline{E}' = \underline{E} + \underline{W} \times \underline{B}$. $\underline{E}$ is the polarization field assumed to be electrostatic and can be given by,

$$\underline{E} = -\nabla \phi$$

where ϕ is a scalar potential. $[\sigma]$ is the tensor conductivity defined earlier. The currents thus generated are assumed to be non-divergent implying that there is no accumulation of charges ($N_e = N_i = N$). The electrostatic field set up by the charge seperation is considered to be irrotational. Thus we have,

$$\nabla . \underline{J} = 0 \qquad (37)$$

$$\nabla \times \underline{E} = 0 \qquad (38)$$

The equations 34, 37 and 38, along with the equation of motion of the neutral particles (Eq. 10) form the adequate set of equations for the formulation of the dynamo theory. The dynamo calculations are based on the assumed wind and conductivity models. Any uncertainties in these parameters would naturally lead to uncertainties in the estimated Sq field and currents.

The yearly average Sq current system deduced from the magnetic variations recorded at the observatories situated at various latitudes during IGY (1957-58) is shown in Fig.I. 10.

In early attempts to calculate the dynamo effects, HIRONO (1950, 1952), BAKER (1953) and FEJER (1953) started with the pressure variations and computed their electromagnetic effects. They have neglected the diurnal variation of conductivities and obtained only semidiurnal magnetic effects and drifts. MAEDA (1955, 1957), HIRONO AND KITAMURA (1956) and KATO (1956, 1957) have reckoned the ionosphere

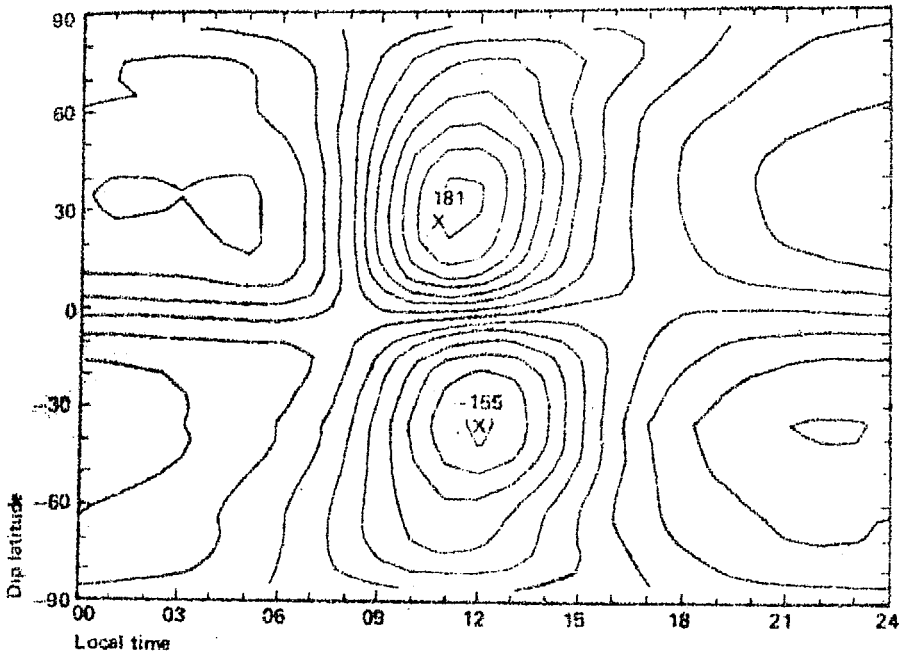

Figure I.10: The average Sq current system deduced from observations during the IGY (1958). The current intensity between two consecutive contours is 2.5×10^4 Amperes. The numbers in the figure give the total current in each vortex in thousands of amperes (after MATSUSHITA, 1968).

as a thin spherical shell (after BAKER AND MARTYN, 1953) and neglected as a consequence, the vertical flow of currents. They have solved the dynamo equations assuming height-independent winds and showed for the first time that the diurnally varying wind system is responsible for the Sq currents. However, observations of meteor trains (GREENHOW AND NEUFELD, 1956) showed that at mid-latitudes the dominant winds are semi-diurnal. KATO (1966 a) showed that the wind responsible for the Sq variations is the diurnal trapped (1,-2) mode as predicted independantly by LINDZEN (1966).

STENING (1969, 1970), TARPLEY (1969, 1970b) and VOLLAND (1970) have studied the efficiency of various symmetric tidal modes to generate electric currents allowing for the height variation of the winds and found that a sufficiently intense solar diurnal trapped mode (1,-2) shown in Fig. I. 11 (MATSUSHITA, 1971) can reproduce the Sq current system fairly well. Besides, they found that the contribution from the solar semidiurnal (2,2) propagating mode is also important. The current generating efficiency of (1,-2) and (2,2) modes is larger than that of the other modes because of the vertical wave lengths of the former modes being larger than those of the latter. The observations on the winds by the incoherent scatter radar at the mid-latitudes (e.g., EVANS, 1976) have shown that the semidiurnal (2,4) winds are dominant in the E region and the amplitude of the diurnal mode used in the

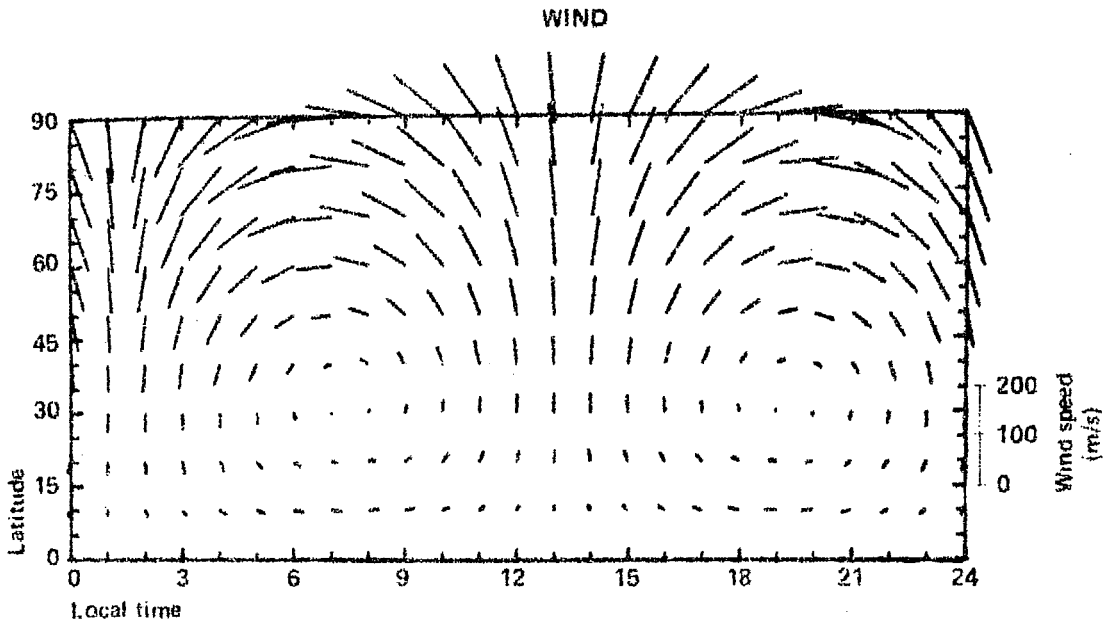

Figure I.11.: Wind vectors for the solar diurnal (1,-2) evanescent mode which give a current distribution very near to the observed Sq current system given in Figure I.10 (after MASTUSHITA, 1971).

dynamo calculations are very high and are unrealistic. KATO (1971), MATSUSHITA (1971 ; 1973) and MURATA (1974) have reviewed the work done on the dynamo theory and concluded that more experimental and theoretical work has to be undertaken in order to assess correctly the dynamo action of tidal winds. These theories on the dynamo effects of the tidal winds are, in general, two-dimensional because it is assumed that the currents along the magnetic field lines (which are almost vertical in the mid-latitudes) are negligible.

Therefore a three dimensional representation of the current system would in fact be more realistic than the simpler two dimensional treatments. MAEADA AND MURATA (1965), MAEDA (1966) and VAN SABBEN (1966) have considered the partial currents along the magnetic field lines which are generally neglected and this problem has since been taken up by FUKUSHIMA (1968), PRICE (1969), COCKS AND PRICE (1969) and STENING (1968, 1969, 1970). These computations however lacked the realistic models of winds. SCHIELDGE ET AL (1973) have attempted to reproduce the global Sq variations allowing for the variation of winds in the vertical direction and also taking the field aligned currents into account. They have shown that more than half of the globally averaged current is produced by the (1,-2) mode, in conformity with the earlier work. However, because of their wind model not being

in accord with the observations; they seem to have over-estimated the contribution due to (2,2) mode (EVANS, 1976).

FORBES AND LINDZEN (1976a) have recently studied the electrodynamic effects of solar tides in the E-region using a three-dimensional model and concluded that there exist still discrepancies of the order of 20% in amplitude and 1 or 2 hrs in phase between the theoretical model and the observations. These discrepancies can be attributed to the uncertainties in the wind and conductivity models. RICHMOND ET AL (1976) have critically assessed the contribution due to the tidal winds, taking more realistic wind models based on the recent observations and neglecting, however, the field aligned currents. They concluded that the (1,-2) mode driving the currents in the upper part of the E-region and the (2,4) mode driving the currents near 115 km are able to reproduce the Sq currents. Furthermore, they have suggested that the day-to-day variations in the currents are due to the short-wavelength semi-diurnal modes in support of the earlier similar conclusions of SCHIELDGE ET AL (1973).

MATSUSHITA (1971, 1972) hypothesised that the primary source of quiet-day ionospheric electric fields, and hence currents, may be originated by the magnetospheric convection driven by the solar wind rather than the ionospheric tidal winds. STENING (1973) and MATSUSHITA (1975) have found observational evidence in support of this hypothesis. But

the recent work of RICHMOND ET AL (1976) shows that it has only secondary importance atleast during the day time, and FORBES AND LINDZEN (1976a) have attributed the discrepancies arising between the dynamo theory and observations to the magnetospheric convection.

I. 8 The equatorial electrojet:

The primary electric field in the dynamo region produced globally by the dynamo action of the north-south winds (poleward during the day at mid-latitudes) is established in the eastward direction during the day and westward during the night. At the dip equator, where the magnetic field lines are entirely horizontal (northward), the conditions in the dynamo region become unique. In this region an intense current known as the "electrojet" is formed during daytime and flows eastward with a noontime maximum current density of about 10 A/km^2 at an altitude of about 106 km.

The primary eastward electric field is believed to be the main source of this intense current in the vicinity of the dip equator. During the day time, the primary electric field produces a vertical drift of the charged particles due to the $\underline{E} \times \underline{B}$ force. However, this drift is mainly experienced by the electrons. The ions do not follow the drift because of their high collision frequency ($\nu_i \gg \omega_i$) with the neutral particles. This causes a charge separation and thus a polarisation field is established in the vertically

upward direction which is known as the Hall polarisation field. The Hall polarisation field, in turn drives the electrons in the westward direction (and the ions do not follow this drift for the same reason as given before) giving rise to a strong eastward current. The Hall polarisation field is strongest over the dip equator because the charge separation is large by virtue of the horizontality of the magnetic field lines. The effective conductivity in the eastward direction is then,

$$\sigma_3 = \frac{\sigma_H^2}{\sigma_P} + \sigma_P$$

known as Cowling conductivity which is maximum at the dip equator and at an altitude around 100 km (Fig.I. 9). σ_3 far exceeds σ_P and σ_H and is comparable to σ_0 at the peak of the electrojet (ONWUMECHILLI, 1967).

Historically, the discovery of the electrojet was made on the basis of the magnetograms recorded at Huancayo, in 1922. The general features of the magnetograms at Huancayo show that the daily ranges of the declination D and the vertical component Z of the geomagnetic field at a station situated near the dip equator are comparable to those of the stations in other geographic latitudes. However, at the equator, daily range of the horizontal component H is found to be abnormally large, being often more than double the value expected. EGEDAL (1947, 1948) has studied the daily variation of H at six equatorial stations and reported

sharply peaked curve symmetrical about the dip equator. GEDAL has suggested that this abromality could be due to varying current sheet of width of about 300 km flowing in very narrow zone over the dip equator.

That the enhancement in the daily variation of H (ΔH) is present at any station situated near the equator has been established by the work done at several other zones (e.g. CHAPMAN 1948, PONTIER, 1950; GIESECKE, 1954; MADWAR; 1953; GULATEE, 1950; PRAMANIK AND YEGNANARAYANAN, 1952; PRAMANIK AND HARIHARAN, 1953). This large variation in H is due to a strong overhead current flowing from west to east. CHAPMAN (1951) named it as the "equatorial electrojet" in analogy with the jet streams occuring at the poles. Figs.I.12 and I.13 show the latitudinal distributions of ΔH and ΔZ obtained by FORBUSH AND CASAVERDE (1961) for the South American zone (longitude 284°E).

The horizontal component ΔH shows an abrupt enhancement at the dip equator. The value at the dip equator is well above the values at other latitudes - a difference of nearly 100γ. The vertical component ΔZ is nearly zero at the dip equator. It maximises at about 3°N (negative maximum) and 3°S (positive maximum).

The electrojet is extensively studied by the ground-based magnetometer giving the daily horizontal (northward) range (ΔH). On a magnetically quiet day the variation of the northward magnetic field ΔH, over the night time

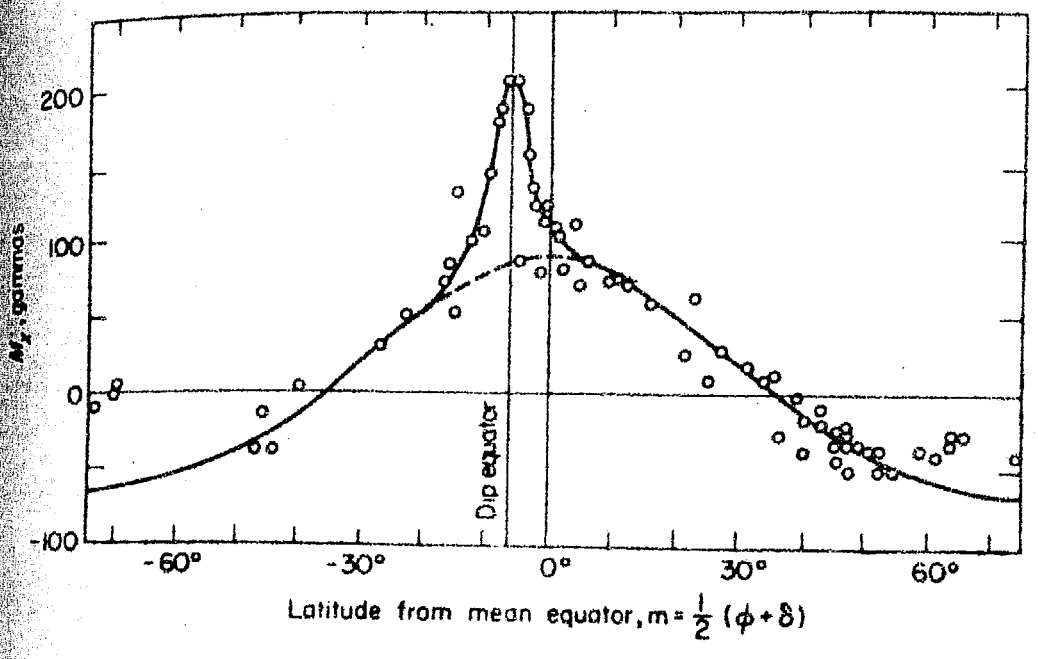

Figure I.12.: Variation of $M_x (\equiv \Delta H)$, the daily range of the horizontal component of geomagnetic field with geographic latitude. The position of the dip equator is for the longitude 284°E (after FORBUSH AND CASAVERDE, 1961).

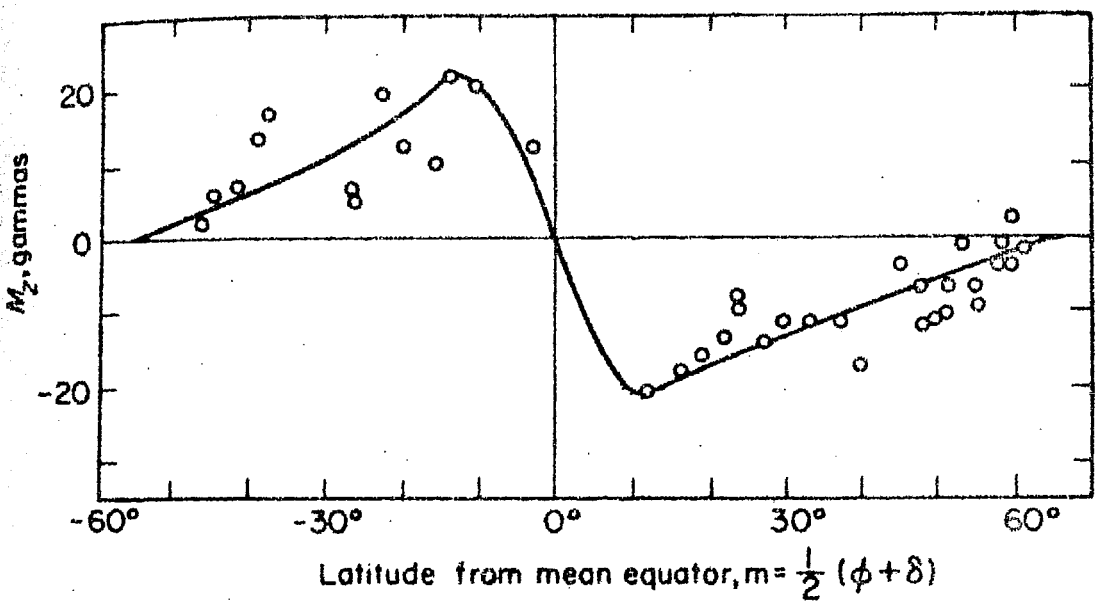

Figure I.13.: Variation of M_Z ($\equiv \Delta Z$) the daily range of the vertical component of geomagnetic field with geographic latitude. The position of the dip equator is for the longitude 284°E (after FORBUSH AND CASAVERDE, 1961).

level (when the currents are practically absent) at a station at or close to the dip equator is composed of the contributions from the Sq currents as well as the electrojet currents. ONWUMECHILLI (1959) and FORBUSH AND CASAVERDE (1961) among others have studied the magnetograms to estimate the jet current variations. As the contribution of the Sq current system does not vary drastically within a few degrees of latitude, the Δ H as recorded at a station outside the electrojet region is usually subtracted from that recorded at a station under the electrojet to estimate the electrojet current strength and its variation at any given time of the day (KANE, 1973).

Rocket-borne magnetometers (VESTINE ET AL, 1947; SINGER ET AL, 1951) have become handy in recent years and till to date many such experiments have been conducted, notably by CAHILL (1959) in the Pacific region (Line Islands); MAYNARD ET AL (1965), MAYNARD AND CAHILL (1965) and SASTRY (1968, 1970) in the Indian zone; and DAVIS ET AL (1967) and MAYNARD (1967) in the South American zone. The results from these experiments have confirmed the presence of the electrojet and have determined important characteristic features of the electrojet, like the height of the peak current density, the thickness, and its vertical distribution. Besides these, other features like the longitudinal variations, and day-to-day variability of the current intensity are also established by rocket experiments (BURROWS, 1970;

BURROWS AND SASTRY, 1976). These variabilities (in ΔH) are also studied by the ground magnetometers (CHAPMAN AND RAJARAO, 1965; VAN SABBEN, 1966; HUTTON, 1967; and KANE, 1973).

Fig.I. 14 (top) shows the contours of the electrojet current density in the altitude-latitude plane based on the observations made by several rocket-borne magnetometers over the South American zone (DAVIS ET AL, 1967). Given in the same diagram is a similar plot obtained theoretically by UNTIEDT (1967). There is fairly good correlation between the two plots. However, the altitude of peak current density in the case of the observations is higher than that obtained theoretically. This discrepancy is thought to be due to the uncertainties in the models of the collision frequencies (e.g. RICHMOND, 1973b). The distortion in the observed contours in contrast with the smooth contours obtained from the theoretical model needs to be explained.

Since the earth also acts like a conductor, the magnetic fluctuations observed on the ground are composed of two parts (i) the external part, due to the current obverhead and (ii) the internal part or induction part, due to an image current inside the earth (CHAPMAN AND BARTELS, 1940). The studies have shown that the internal contribution varies with longitude. Recent studies of FAMBITAKOYE (1973), MAYAUD (1974) and YACOB (1977) have shown that the induced part is very small if not negligible. On the basis of rocket-borne magnetometer survey carried out by SASTRY (Private communication

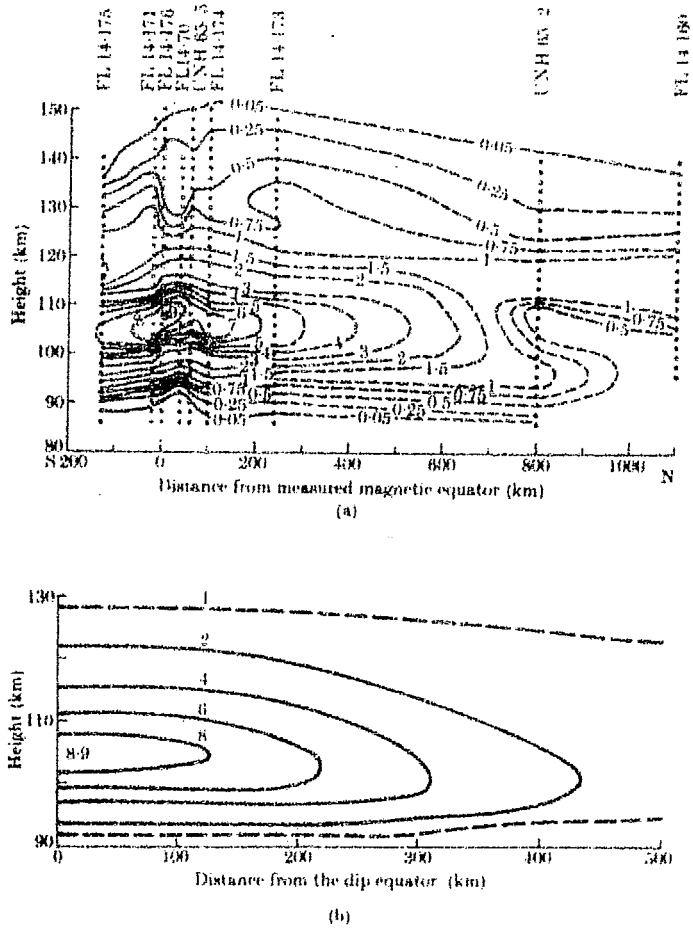

Figure I.14.: (a) The distribution of the equatorial electrojet current constructed by using several rocket observations of the magnetic fields in the South American zone (after DAVIS ET AL, 1967). (b) The theoretical model estimation of the equatorial electrojet current (after UNTIEDT, 1967). The current density is in Ampers/km^2.

the internal contribution is found to be as high as 40% of the external contribution in the Indian zone.

A relatively new phenomenon which is yet to be understood, associated with the electrojet, is the 'counter-electrojet' an unusual westward current during the day time. GOUIN (1962) was the first to observe that on some days the ΔH falls steeply at or around 1400 hrs local time (LT) and goes below the night time minimum and rises again slowly at around 1800 hrs LT. This feature has subsequently been observed by many workers. Such a reversal or decrease of ΔH is thought to be due to a reversal or decrease in the usually eastward current and is known as the phenomenon of counter-electrojet. It is known (GOUIN, 1963) that a similar reversal is observed in the morning hours just before or at the time when normal rise in H is expected to start above the night time level of H. This can happen when the reversal of the electric field from westward to eastward is slightly delayed and thus there is the reversal of the current in the morning hours. But the reversal in the afternoon hours can not simply be explained as above because there is no apparent reason why the primary field should be reversed at that time. The salient features of counter-electrojet are discussed in the Chapter VI where we have examined the neutral wind effects on the electrojet in general, and the effectiveness of the neutral winds (horizontal and vertical) in producing the counter-electrojet, in particular.

I.9 Scope of the Thesis:

In the preceding pages we have discussed a few phenomena concerning the E-region dynamics. It has been pointed out that more experimental and theoretical work is required to understand the equatorial E-region phenomena such as the irregularities and the electrojet. In the next few Chapters we elucidate the results obtained on the neutral winds in the E-region and electric fields in the lower F-region by the vapour cloud release experiments conducted at the Thumba Equatorial Rocket Launching Station (TERLS), Thumba (dip $0^{\circ}.6S$), India.

From the experimentally observed wind profiles over Thumba we bring out the contributions due to the tidal winds and the gravity waves. We also present results on the vertical winds and report for the first time a vertical profile of the vertical winds in the altitude region 90-200 km (Chapter II).

We describe in Chapter III, the details of the differential photometric equipment built for the measurement of the winds in the daytime by tracking the Lithium Vapour clouds released in the upper atmosphere.

The results of the barium cloud experiments conducted at the dip equator (Thumba) are discussed in Chapter IV. These results are used to provide the first observational evidence for the validity of the theoretical model of the equatorial electrojet.

In Chapter V, the polarization fields generated by the winds of gravity waves (through the wind shear mechanism in the equatorial dynamo region) are computed by a rigorous two-dimensional approach. It is shown that the total electric field is non-zero and therefore the effects of the gravity wave winds on the electrojet are of importance. The large scale stratifications in the electron density profiles observed at the dip equator are interpreted by the wind shear theory.

A model equatorial electrojet is developed in Chapter VI which incorporates the effects of neutral winds. The effects of zonal and meridional winds and the vertical shears in these, on the parameters of the electrojet (such as the current intensity, width and thickness) are quantitatively estimated. In addition to these, the effectiveness of vertical winds in altering the electrojet parameters is investigated in view of the experimental evidence (Chapter II) for the existence of such winds. Furthermore, it is suggested that the vertical winds could be responsible for causing the counter-electrojet in the afternoon hours.

The important conclusions of the present investigations and the directions in which the future work is to be done are listed in Chapter VII.

CHAPTER II

NEUTRAL WIND MEASUREMENTS BY ARTIFICIAL VAPOUR RELEASE TECHNIQUE OVER THE DIP EQUATOR

II.1 Introduction

In this Chapter we present some results of winds in the upper atmosphere obtained by means of artificial vapour release experiments at Thumba Equatorial Rocket Launching Station (TERLS). As discussed in the introductory Chapter (Chapter I), winds in the thermosphere are of various periodicities and wavelengths and are termed as (i) prevailing winds; (ii) tidal winds with periodicities 24 hrs, 12 hrs and a weaker component of periodicity 8 hrs and (iii) internal gravity waves with periods of a few minutes to a few hours. Data on winds at the equatorial latitudes are very meagre; while comparatively, the data at mid-latitudes are substantial. The winds at mid-latitudes are found to be predominantly semi-diurnal. In the equatorial region, however, it is not clearly known as to which mode is the dominant one (e.g. MATSUSHITA, 1973). Thus, there is a need to study the available wind data carefully and infer various components like, diurnal, semi-diurnal tidal waves and gravity waves in the equatorial region. Besides the wave motions, it will be interesting to see whether substantial vertical motions exist. This is important because the vertical winds may play a significant role in the physical phenomena such as the generation of electric field in the electrojet region (RAGHAVARAO, 1976). Data revealing

vertical motions are, however, scanty. At mid-latitudes GROVES (1963) and REES (1969) reported vertical winds of amplitudes as large as 30 m/s. At the equator only a few such observations were reported so far (RIEGER, 1974; ANANDARAO ET AL, 1977 b). Careful analysis of the vapour cloud data may reveal substantial vertical motions. For, the errors in the analysis may at times obscure these motions which are small in magnitude compared to the horizontal motions.

We describe in section II.2 the vapour cloud technique which we have used to measure the winds over Thumba. The data on the neutral winds acquired so far, over the dip equator at Thumba, are presented in II.3. In II.4, we describe the methods of extracting the gravity waves and tidal winds (KOCHANSKI, 1966; HINES, 1966) and present the results obtained on the tidal and gravity wave wind components from the measured wind profiles at the equator . In section II.5 we present the results of observation of a barium cloud released at 93 km which revealed vertical motions. We conclude this Chapter by summarizing the results obtained in the investigation

II.2 Measurement of upper atmospheric winds by artificial vapour clouds:

As early as in 1950, BATES suggested that an artificially released cloud of sodium vapour could well be a probe for measuring many an upper atmospheric parameter, like winds, for instance. He discussed both the nighttime and

twilight phenomena which might be observed when the contaminant is released. The visible glow from the contaminant released in the night, results from chemiluminescent reactions between the released vapour and the ambient atmospheric constituents. For a twilight release, the light emitted from the cloud is due to the resonant scattering of the solar radiation by the contaminant particles. Because, during the twilight, the heights at which the vapour is released receive the solar radiation, although the sun is below the horizon for an observer on the ground. Thus it is possible to photograph the released cloud with stars in the background, both during twilight and nighttime. However, during the daytime, photography is not possible as the cloud cannot be seen with naked eye against the bright background sky. The techniques used in measuring the winds in the daytime are discussed separately in Chapter III.

The contaminant cloud is released from a sounding rocket during its flight, along its trajectory at any desired altitude. This requires the trajectory of the rocket be known accurately. Two types of releases are usually employed (i) point release or a 'blob' and (ii) trail release. Point release is ejected out in a 'puff' from the rocket at a prefixed altitude, in a period of less than a second. The rockets that are usually employed have

an apogee altitude of≈160-200 km. They go at a speed of 1 km/s at the altitude of ≈ 100 km. Thus, the point release can be reckoned to represent the conditions at a single level of altitude. Trail release is a continuous release along the path of the rocket (from about 80 km upto its apogee). It, thus, covers a range of altitudes and is useful in the case of determination of altitude profiles of horizontal winds. The determination of vertical winds is very difficult using the trails - because identification of a common point on the trail from the photographs of two or three stations used for triangulation, becomes a difficult task. In the case of point releases, however, the measurement of vertical velocity is possible (if the vertical winds are present!) because one can identify a point which remains, under normal circumstances, to be the same from the tracking station; for instance, the geometrical centre of the cloud.

A trail or a blob, upon release, quickly (in less than a minute) attains the ambient conditions viz., ambient pressure, temperature and motion. The released cloud is illuminated by the sun's rays which are scattered resonantly by the cloud particles emitting their characteristic radiation. The visible cloud is photographed against a background of stars simultaneously from two or more stations equipped with suitable cameras. Generally, the camera stations are away from the rocket launching station. To attain good

accuracies on the results, it is desirable to have the stations separated by distances of 100-200 km for a release at an altitude of about 150 km. The error in determining the position of the cloud is minimum when the distance of the cloud to the base of triangle (formed by the centre of cloud and the two stations) is the same as the base length of the triangle. The cloud positions at different times after release can be obtained from photographs taken from two or more stations. The procedure involved is discussed in a later section.

II.2.1 Selection of material for the release:

A material should satisfy the following criteria before being selected as suitable for the release.

(i) The excitation potential of its atoms should be within the range of energy supplied by the solar radiation. Because any other means of exciting the atoms will be cumbersome.

(ii) The resonance lines of the atoms of the vapour should be in the visible region of the electromagnetic spectrum, so as to facilitate the photography - because photographic method of tracking the cloud is the simplest and accurate as well.

(iii) The time scales of excitation of the atoms should be short enough compared to the diffusion rates. This permits us to have sufficient observational time ($\sim$30 mts.) before the cloud diffuses and disappears.

(iv) Since a chemical technique for the release is used, a low evaporation temperature is highly desirable.

Table II.1 furnishes the strong resonance lines and rates of excitation of various alkali elements that are generally used in the technique.

II.2.2 Thermite payload:

Most commonly used materials for the measurement of winds are sodium, trimethyl aluminium (TMA) and lithium. For the night time releases, TMA is preferable and for the daytime release, lithium is the most suitable. For twilight releases any one of the three can be used.

Sodium thermite payload:- The function of the sodium vaporizers (or, any such vaporizer used in the experiment) is to eject a constant stream of sodium vapour to form a trail from the rocket during its flight. In case of point cloud or a 'blob', the release should be instantaneous. In principle, the method involves in utilizing the heat produced from burning of iron-oxide-aluminium thermite mixture to vaporize the sodium metal. The series of chemical reactions that take place, is as follows,

$$Fe_2O_3 + 2Al \longrightarrow Al_2O_3 + Fe \text{ (exothermic)}$$

$$Fe_2O_3 + 6Na \longrightarrow 3Na_2O + 2Fe$$

$$3Na_2O + 2Al \longrightarrow Al_2O_3 + 6Na \text{ (vapour)}$$

The mixture is tightly packed in a cylindrical steel container which is sealed save for two vent holes

TABLE II. 1

Elements for the vapour cloud release and their properties

Element	Symbol	Resonance emission line (Å)	α_{exc} (s^{-1})	Ionization potential (ev)	Boiling point (^{o}K)
Barium	Ba I	5535	8.40	5.21	1895
	Ba II	4554	C.34		
Calcium	Ca I	4227	0.21	6.10	1760
	Ca II	3933	0.19		
Europium	Eu I	4594	2.30	5.66	1764
	Eu II	4205	0.71		
Lithium	Li	6708		5.38	1609
Sodium	Na	5890		5.13	1165
		5896			
Strontium	Sr I	4607	1.56	5.69	1648
	Sr II	4077	0.09		

through which the vapour jets out (DUBIN, 1964). The rate of burning of the vaporizer can be changed by varying the thermite to sodium ratio of the mixture. The burning rate is also dependent upon the size of the aluminium granules, the packing pressure and the vaporizer configuration. Calculations show that approximately 3.2 grams of thermite is required to vaporize 1 gram of sodium at 1000°C (DUBIN, 1964).

Trimethyl aluminium (TMA):- A mixture of liquid trimythyl-aluminium (80%) and triethylaluminium (20%) is forced by nitrogen under high pressure (10 atmospheres) through an orifice into the atmosphere along the trajectory of the rocket (ROSENBERG ET AL, 1963 a,b). About half of the liquid TMA vaporizes instantly after release forming a glow trail. After the entry into atmosphere, the TMA vapour reacts with the ambient oxygen to form aliminium oxide (AlO) which is chemiluminescent

$$TMA + O \longrightarrow AlO + \text{other products}$$

$$AlO + O \longrightarrow AlO_2^*$$

$$AlO_2^* \longrightarrow AlO_2 + h\nu \quad \text{(pseudo continuum)}.$$

The asterisk represents excited atom or molecule. The continuum emission is in the range of 4500-6500Å and a resultant white glow is seen, upon the release. This happens when the TMA trail or blob is not sunlit, for example, during nighttime.

Aluminium oxide is also capable of scattering the sunlight resonantly (ROSENBERG ET AL, 1964) giving rise to a band spectrum with maximum intensity at 4842Å (bluish green). Besides being useful for the wind measurements, the TMA trails yield valuable information about the neutral temperature of the atmosphere, if tracked with a spectrophotometer (ROSENBERG ET AL, 1964; HARANG, 1964).

Lithium:- The continuum sky background in the daytime is about one half as intense at 6708Å (lithium emission line) as it is at sodium D line or AlO band wavelengths. Thus, lithium is suitable for the release in the daytime. Lithium can also be used in twilight period. The payload consists of a thermite mixture containing copper oxide, lithium metal and barium metal. The reaction is exothermic, and the heat thus generated vaporizes the lithium.

$$Li + CuO + Ba \longrightarrow Cu + BaO + Li \text{ (vapour)}$$

II.2.3 Observation precedure:

The point cloud or trail, after its release, is tracked photographically from two or more ground stations equipped with aerial cameras loaded with high speed film. Clouds can also be tracked by filter photometers as in the case of daytime releases (Chapter III), but the photographic technique yields slightly better accuracies. REES ET AL (1972 b) showed that the photometers yield information as accurate as that obtained by photography. However,

calibration of the look angles of the photometer is rather difficult, whereas stars serve the purpose in the case of photography. Thus, it is convenient to use cameras to track the nighttime or twilight releases. In the present study, the clouds are tracked by K-24 and Hasselblad cameras. The film KODAK 2498 or TRI-X (5" x 5" frames) is suitable to photograph sodium, barium, strontium and TMA clouds. Since these films are not red-sensitive, they cannot be used to photograph lithium clouds. For this reason, KODAK 2485 70 mm film which is more sensitive to red light, is used to photograph lithium clouds. Cameras are operated from two or more ground stations.

II.2.4 Method of analysis:

The method of 'triangulation' is used to reduce the data, to find the position of the clouds with time. SMITH (1963) described a method of reducing the photographic data obtained from 2 or more stations to determine position coordinates of a point on the cloud. We adopt his method to reduce the data. We describe briefly the method of analysis in the following pages.

It may be noted that the two camera-stations should be separated by a distance (base-line) comparable to the altitude of the cloud or lengths of the line of sight of the cloud from each station. Generally distances between 100-200 km are preferable and give good accuracies as to the position of the cloud.

The input data required for the computations are:

(i) the position coordinates (in geocentric latitude and longitude) of the two (or more) camera stations and their vector distances from the launch site, which will be the reference coordinate system;

(ii) the azimuth and elevation angles of the camera axis at each station;

(iii) sidereal time of the day of launch; and

(iv) photographs taken simultaneously from two (or more) stations at known local times.

To start with, common points on the cloud as seen on the photographs from two stations are identified. This common point could, for example, be the centre of the cloud. These points on the photographs are read with respect to 3 or more stars (whose celestial coordinates are known) by means of a travelling microscope. The azimuth and elevation of line of sight of these points on the cloud as seen from the stations are then calculated. A Cartesian coordinate system (x, y, z) is chosen, in which x-axis is towards east, y-axis towards north and z-axis vertically upwards. In this coordinate system, the direction cosines of the point on the cloud from any station can be written as follows. In x, y and z directions respectively,

$$\begin{aligned} \cos\alpha &= \cos E \sin A \\ \cos\beta &= \cos E \cos A \\ \cos\gamma &= \sin E \end{aligned} \qquad (1)$$

Here E is the elevation of the point on the cloud and A, the azimuth measured clockwise from north at any station. In Fig. II.1 is shown schematically the method of triangulation. S_1 and S_2 are the two camera stations whose position vectors $\underline{r}_1$ and $\underline{r}_2$ with respect to any arbitrary point A (the launch pad in the present case) are known. C_1 and C_2 are points on the cloud identified from the photographs taken from the two stations S_1 and S_2 respectively. Ideally, C_1 and C_2 should be one and the same. But it is hard to realize in practice and, accuracy of the measurement lies in obtaining C_1 and C_2 as close to each other as possible. $\underline{R}_1$ and $\underline{R}_2$ are the vectors representing the lines of sight of the points C_1 and C_2 whose magnitudes are not known, and only the direction cosines are known. Our aim now is to find the vector $\underline{R}$, which is $\underline{AC}$, where C is the mid-point of C_1 C_2. It can be shown that (SMITH, 1963) R is given by

$$\underline{R} = \frac{1}{2}(\underline{r}_1+\underline{r}_2) + \frac{1}{2}\frac{1}{|\underline{n}_1\times\underline{n}_2|^2}\Big[\underline{n}_1(\underline{r}_2-\underline{r}_1)\cdot\{\underline{n}_1-\underline{n}_2(\underline{n}_1\cdot\underline{n}_2)\} + \underline{n}_2(\underline{r}_1-\underline{r}_2)\cdot\{\underline{n}_2-\underline{n}_1(\underline{n}_1\cdot\underline{n}_2)\}\Big] \qquad (2)$$

where $\underline{n}_1$ and $\underline{n}_2$ are the unit vectors $\left(\frac{\underline{R}_1}{|\underline{R}_1|}, \frac{\underline{R}_2}{|\underline{R}_2|}\right.$ respectively) along R_1 and R_2. The distance C_1C_2 is given by

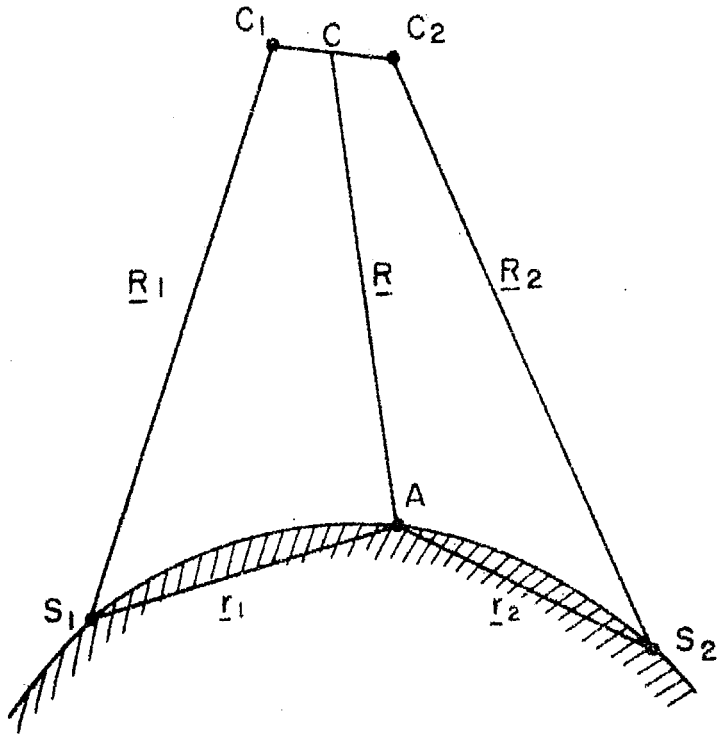

Fig.II.1:- Triangulation procedure. C_1 and C_2 denote the centre of the cloud as seen from the two camera stations S_1 and S_2. C is the mid-point of C_1 C_2. A is an arbitrary point on the surface of the earth with respect to which the spatial coordinates of C are computed (based on SMITH, 1963).

$$C_1C_2 = \begin{vmatrix} x_1 & x_2 & \cos\alpha_1 & \cos\alpha_2 \\ y_1 & y_2 & \cos\beta_1 & \cos\beta_2 \\ z_1 & z_2 & \cos\gamma_1 & \cos\gamma_2 \\ 1 & 1 & 0 & 0 \end{vmatrix} \times K \qquad (3)$$

and $K = \left\{\sum(\cos\beta_1 \cos\gamma_2 - \cos\beta_2 \cos\gamma_1)^2\right\}^{-1/2}$

where $\cos\alpha$, $\cos\beta$, $\cos\gamma$ are the direction cosines along x, y, z axes of the coordinate system whose centre is at A and the suffixes 1 and 2 correspond to the stations S_1 and S_2 respectively. Thus, R for every set of two photographic frames from the two stations at different times is known and the velocity components in x, y, z directions can readily be obtained from the positions at different times.

The method of identification of a common point on the cloud in the photographs taken from the stations needs to be discussed here. (i) In the case of a blob (or point) release, the cloud is spherical or (if wind shears are prominent) ellipsoidal in shape. Identification of the centre of the cloud from each station should not be difficult and it proved to yield good results. (ii) In the case of a trail release, however, the identification of common points is very difficult. By far, the most promising method of the trail analysis seems to be that due to DESAI ET AL (1975). This method is a modified form of SMITH'S (1963) technique and can be briefly described as follows. Trail centres (line

of maximum intensity) are read in the frame of station 1 and corresponding direction cosines are calculated with reference to the star background. The transformation of each trail point from the frameof station 1 to that of station 2 is then done assuming a sequence of values for the slant range from station 1 to the trail point. The locus of these points in the frame of station 2 is a straight line and its point of intersection with the trail as observed from the station 2 gives the corresponding point and the true slant range from station 1. This method obviously avoids the uncertainty involved in identifying a common point.

II.2.5 Errors:

Various sources of errors of the analysis and their estimates have lucidly been described by earlier workers (RAO, 1966; NARAYANAN, 1973). The error in reading the photographs by the microscope are negligibly small. The maximum error in the velocity of the cloud when a good interval of time is spanned ($\geqslant$600 s) is $\sim$ 8 m/s, with a positional error of 2 km. The identification of a common point on the photographs taken from two stations, can sometimes be a major source of error. This error given by the vector $\underline{C_1C_2}$ (in Fig.II.1) can be resolved into x, y, z components to estimate the error in each of the three coordinates.

The direction cosines of the vector $\underline{S_1C}$ (in Fig.II.1) are computed. Then, from the direction cosines of $\underline{R}_1$ and $\underline{S_1C}$, the angle 'δ' between these vectors is calculated. The vector $\underline{S_1C}$ is obtained from the triangle S_1 AC using the relation, $\underline{S_1C} = \underline{R} - \underline{r}_1$. In the triangle S_1CC_1, the angle 'η' between C_1C and S_1C_1 is

$$\text{Sin } \eta = \frac{S_1C \ \text{Sin } \theta}{C_1C}$$

Knowing η, the magnitude of $\underline{R}_1$ is found out from the triangle S_1CC_1. As the direction cosines of $\underline{R}_1$ are known already, the error vector is calculated from the relation

$$\underline{\epsilon} = \underline{C_1C} = \underline{R}_1 - \underline{R}_1'$$

From this the errors in the x, y, z coordinates are calculated

In addition to the above error, which refers to the non-correspondence of the centre points of the clouds on the photographs from two stations, there could be an error due to the possibility that the identified centres may not be same on the successive pairs of photographs. However, on plotting the coordinates of these points against the observed time, they showed very little scatter on the smooth curves and hence the error due to this can be considered negligible.

The errors thus calculated in determining the position of the cloud are taken into account in determining the errors in velocities.

II.3 Observations:

Table II.2 gives the details of the vapour cloud release experiments performed over the dip equator at Thumba between the period 1963-1976. The author carried out the planning and analysis of some of the experiments listed in the table (those with an asterisk in the reference column). Results obtained by the earlier workers (as listed in the table) are also considered for the analysis to extract tidal and gravity wave components. There are in all 14 wind profiles obtained by vapour trails which cover fairly large range of altitudes. The rest are point (or blob) releases which give wind velocity at a single altitude only. The wind profiles are divided into four groups on the basis of time of observation. (1) The dawn releases: There are four profiles available at this time. (2) The daytime releases: Only two profiles are available. (3) The dusk releases: There are 5 profiles. (4) Nighttime releases: Three profiles are available.

Fig.II.2 shows the profiles of speed and azimuth of the wind observed during dawn. Figs. II.3, II.4 and II.5 are similar plots for the wind observed during daytime, dusk and nighttime respectively.

Table II.2

Details of vapour release experiments performed over Thumba

(a) Dawn Releases:

Sr. No.	Date and time (IST)	Type of cloud	Neutral/ ionized	Altitude (km)	Reference
1	12-1-1964 0556	Na trail	Neutral	108-160	BHAVSAR AND RAO (1968)
2	6-11-1964 0538	Na trail	Neutral	106-114 146-170	BHAVSAR AND RAO (1968)
3	10-11-1964 0535	Na trail	Neutral	108-176	BHAVSAR AND RAO (1968)
4	31-3-1968 0537	Ba - Sr 2 Blobs	Neutral& ionized	175,148	NARAYANAN (1973)
5	9-2-1975 0554	TMA trail	Neutral	91-170	REES ET AL (1976)
6	24-3-1975 0535	Ba Blob	Neutral	115	*
7	19-4-1976 0529	Li Blob	Neutral	122	*
		Ba Blob	Neutral	130	*
		Ba Blob	Neutral	138	*
		Li Blob	Neutral	140	*

(b) Daytime Releases:

Sr. No.	Date and time (IST)	Type of Cloud	Neutral/ ionized	Altitude (km)	Reference
8	9-2-1975 1100	Li Trail	Neutral	96-165	REES ET AL (1976)
9	19-2-1975 1420	Li Trail	Neutral	85-150	REES ET AL (1976)

(c) Dusk Releases:

Sr. No.	Date and time(IST)	Type of cloud	Neutral/ ionized	Altitude (km)	Reference
(1)	(2)	(3)	(4)	(5)	(6)
10	21-11-1963 1825	Na trail	Neutral	100-180	BHAVSAR AND RAO (1968)
11	8-1-1964 1845	Na trail	Neutral	104-156	BHAVSAR AND RAO (1968)
12	9-11-1964 1824	Na trail	Neutral	132-172	BHAVSAR AND RAO (1968)
13	28-3-1968 1855	Ba - Sr 4 Blobs	Neutral & ionized	205,174, 152,133	NARAYANAN (1973)
14	30-3-1968 1855	Ba - Sr 3 Blobs	Neutral & ionized	204,180, 152	NARAYANAN (1973)
15	30-3-1968 1855	Ba - Sr	Neutral	100	*
16	19-4-1971 1855	Na trail	Neutral	82-160	DESAI ET AL (1975)
17	4-1-1972 1844	Ba - Sr Blob	Neutral & ionized	155	*
18	6-1-1972 1841	Ba - Sr Blob	Neutral	125	*
19	7-1-1972 1841	Ba - Sr Blob	Neutral & ionized	155	*
20	19-2-1975 1902	TMA Trail	Neutral	80-168	REES ET AL (1976)

(d) Nighttime Release:

(1)	(2)	(3)	(4)	(5)	(6)
21	24-3-1966 2215	TMA trail	Neutral	105-125	NARAYANAN (1973)
22	25-3-1966 0230	TMA trail	Neutral	105-125	NARAYANAN (1973)
23	12-3-1967 2230	TMA trail	Neutral	87-120	NARAYANAN (1973)

* Denotes the experiments in which the author has participated.

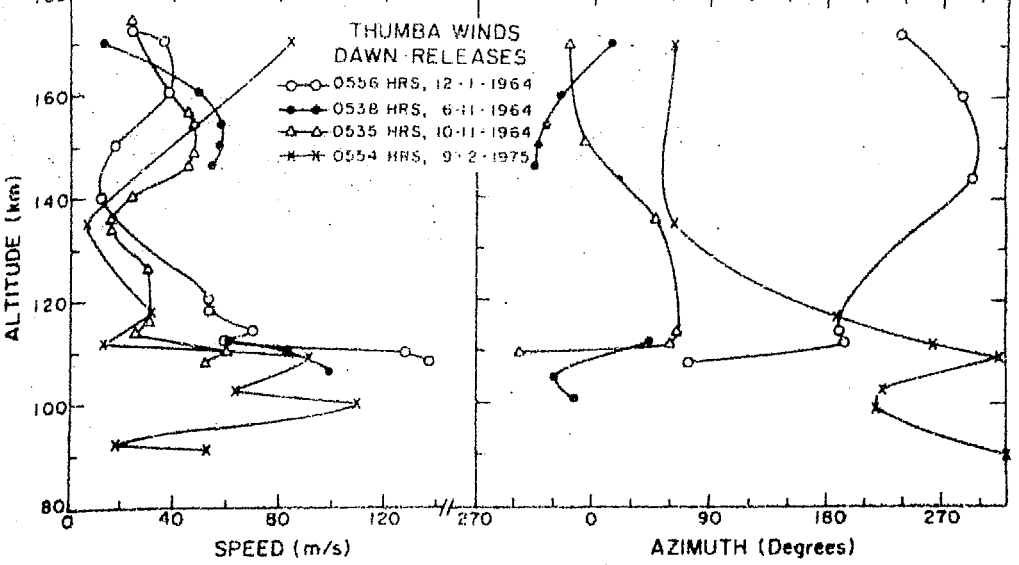

Fig.II.2:- Speed and azimuth of horizontal winds observed by vapour trails at dawn over Thumba. The circles, dots and traingles are taken from BHAVSAR AND RAO (1968). The crosses are from REES ET AL(1976).

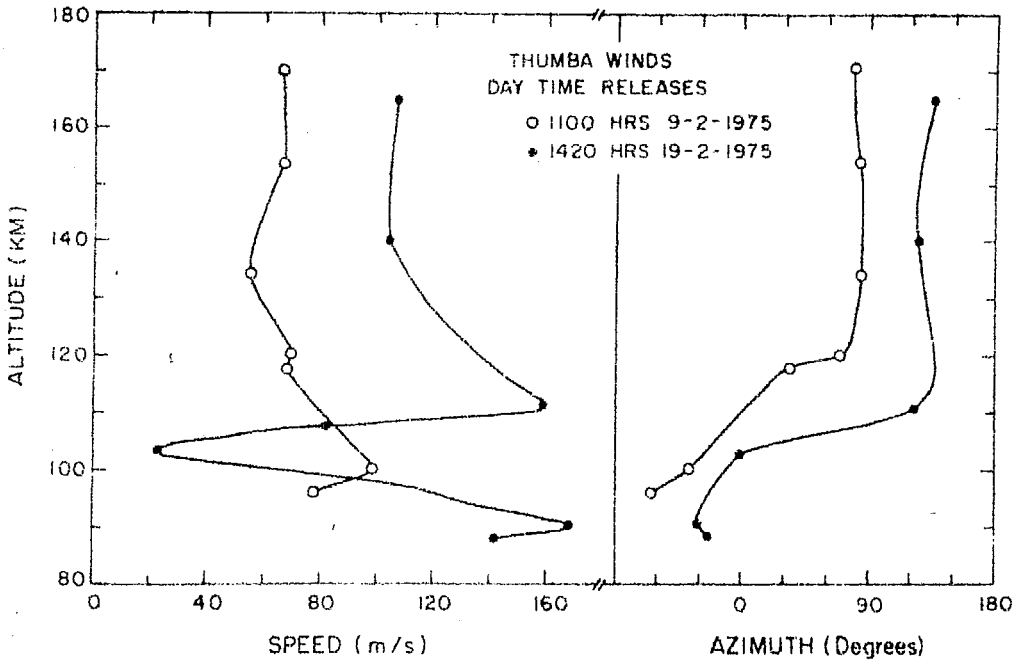

Fig.II.3:- Speed and azimuth of horizontal winds observed by vapour trails during daytime over Thumba. The data are taken from REES ET AL (1976).

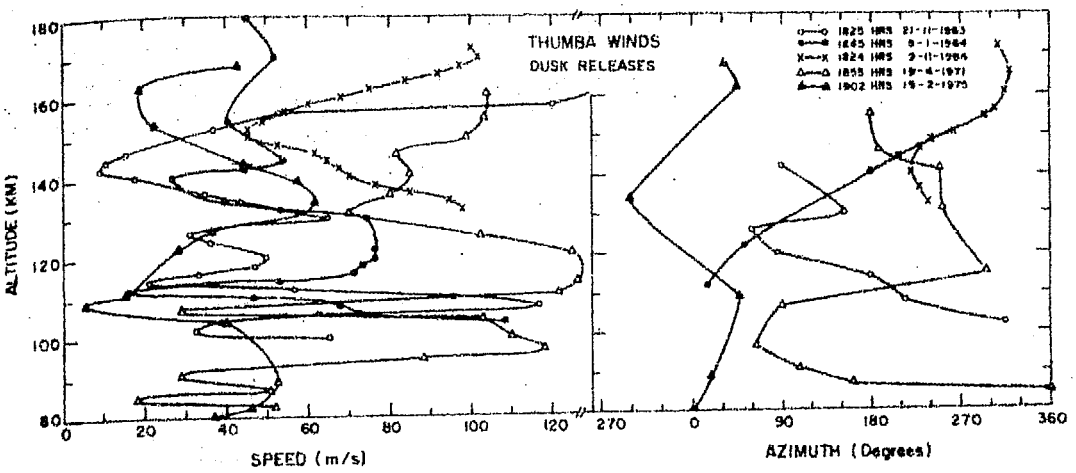

Fig.II.4:- Speed and azimuth of horizontal winds observed by vapour trails at dusk over Thumba. The circles, dots and crosses are taken from BHAVSAR AND RAO (1968); the open triangles from DESAI ET AL (1975); and the closed triangles are from REES ET AL (1976).

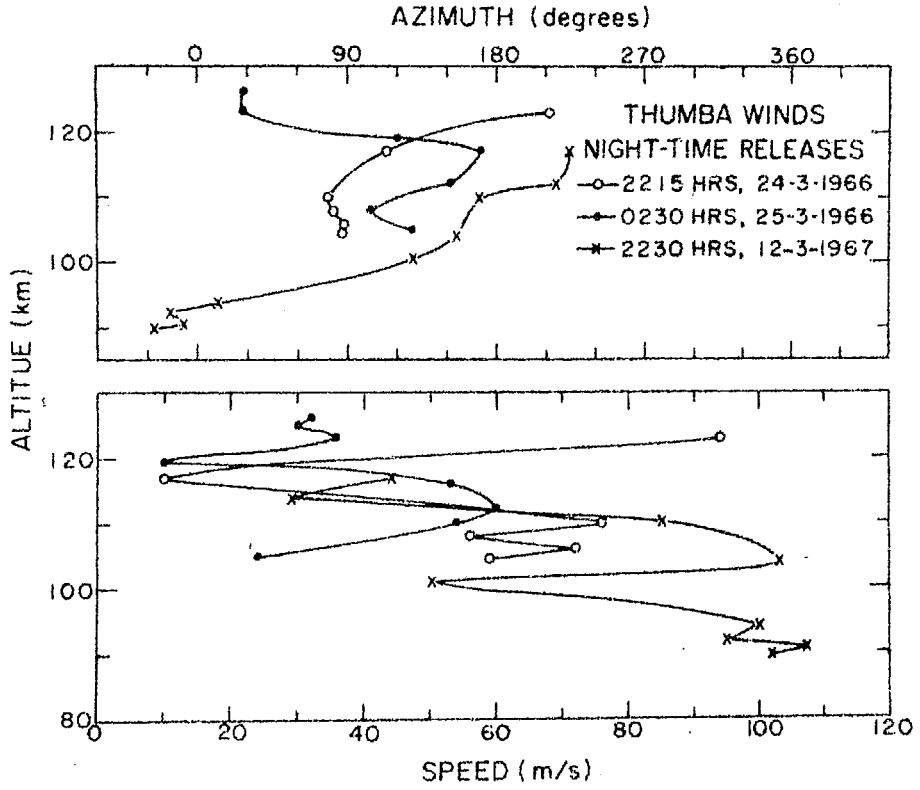

Fig.II.5:- Speed and azimuth of horizontal winds observed by vapour trails during nighttime over Thumba. The data are taken from NARAYANAN (1973).

II.3.1 Wind shears:

Wind shears can be identified in the figures II.2 to II.5 from the sharp gradients in the azimuth profiles. It can be seen that the shears during the daytime are small compared to those observed during dawn and dusk. Whereas the daytime profiles do not show shears above about 110 km, the profiles of dawn and dusk show prominent wind shears above this altitude. In particular the dusk releases showed wind shears throughout the region 80-160 km. These results are in agreement with the earlier results (BHAVSAR ET AL, 1976) in that the shears are most commonly observed in the region 90-110 km at any time of the day. Shears are found in both zonal (east-west) and meridional (north-south) winds. At times, the meridional winds and wind shears are stronger than the zonal winds and wind shears.

II.4 Separation of gravity wave and diurnal tidal wind components from the observed wind profiles:

It is reasonable to assume that the observed motion revealed by the vapour release experiments is composed of three distinct types of motions, viz., (i) the internal atmospheric gravity waves, (ii) the atmospheric tides and (iii) the prevailing winds. Under this assumption, it is possible to separate out from the observed wind motions the irregular or oscillating component due to the gravity waves. The residual motion can then be treated as the sum of prevailing and tidal winds. Furthermore, the removal of diurnal tide

from two sets of data separated in time by $\sim$ 12 hrs can be done without much of subjective error.

From the observed wind profiles shown in the Figs. II.2 to II.5, we first separate the gravity wave component using KOCHANSKI'S (1966) method described later in this section. Then we divide the data into two groups separated by 12 hrs in time -(i) the dawn releases and (ii) the dusk releases. In this grouping we include the results obtained from the observations of point releases also. Following HINES' (1966) technique, we then infer the diurnal component of the wind from these data.

II.4.1 Gravity wave component:

KOCHANSKI (1966) developed a method of extracting the internal gravity wave winds from the observed wind profiles. The method is simple and straightforward and is illustrated in Fig. II.6. The figure shows a typical profile of wind speed. A, B and C in the figure denote the maxima or minima that can be identified on the profile at altitudes h_A, h_B and h_C respectively. The corresponding speeds are W_A, W_B and W_C. The velocity vectors $\underline{W}_A$, $\underline{W}_B$ and $\underline{W}_C$ corresponding to the points A, B and C are shown in the azimuthal plane with centre O (on the top of the figure). The points A, B and B,C are joined in the azimuthal plane. The vectors $\underline{R}$ are obtained by joining the mid-points of AB and BC with the centre O. Now, the gravity wave component at the altitude

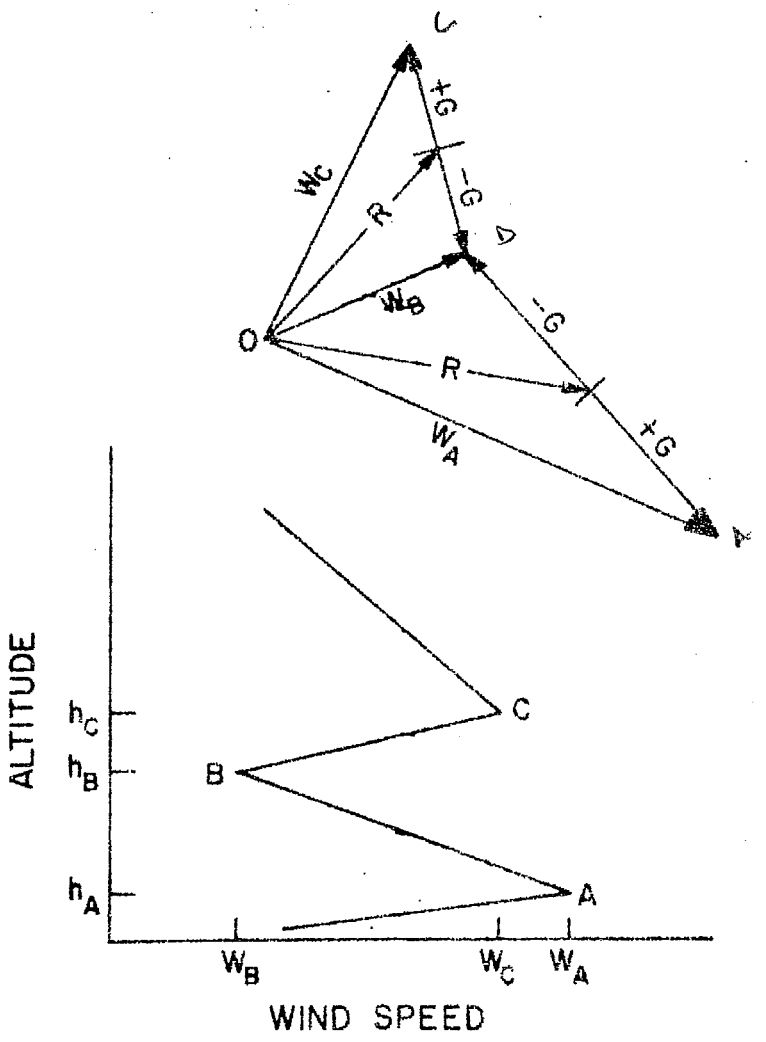

Fig.II.6:- Method adopted to extract gravity wave component from the measured wind profiles. The wind profile shown is only to illustrate the method and is not an observed one. W_A, W_B and W_C are the wind speeds at altitudes h_A, h_B and h_C corresponding to A, B and C respectively. Shown on the top are the wind vectors $\underline{W}_A$, $\underline{W}_B$ and $\underline{W}_C$ on the azimuthal plane. G denotes the gravity wave component and R, the residue (based on KOCHANSKI, 1966).

h_A is $+\underline{G}$ and that at the altitude h_B is $-\underline{G}$ in the vector triangle OAB. Similarly the gravity wave component is found out in the vector triangle OBC. The vector $\underline{R}$ in-side the triangle OAB represents the residual motion at the altitude $(h_A + h_B)/2$. Similarly the vector $\underline{R}$ (not equal to the previous $\underline{R}$) represents the residual motion at the altitude $(h_B + h_C)/2$.

In the wind profiles shown in the figures II.2 to II.5, the maxima and minima of wind speed are identified and using the above method the gravity wave component and the residue are found out.

Figure II.7 shows the profiles of speed and azimuth of the gravity wave component (a) and the residue (b) inferred from the profiles obtained during the dawn time shown in the figure II.2. The gravity wave component and the residue obtained for the daytime, dusk and nighttime profiles (of the figures II.3, II.4 and II.5) are shown in Figures II.8, II.9 and II.10 respectively.

The winds of gravity wave origin obtained from the observed wind profiles seem to be, in general, substantial. From a comparison of the wind profiles (Figs. II.2 to II.5) and the profiles of the gravity wave component at all the 4 periods (dawn, daytime, dusk and nighttime), it appears that the wind shears are caused essentially by the presence of gravity waves. For instance, the sharp gradients in the

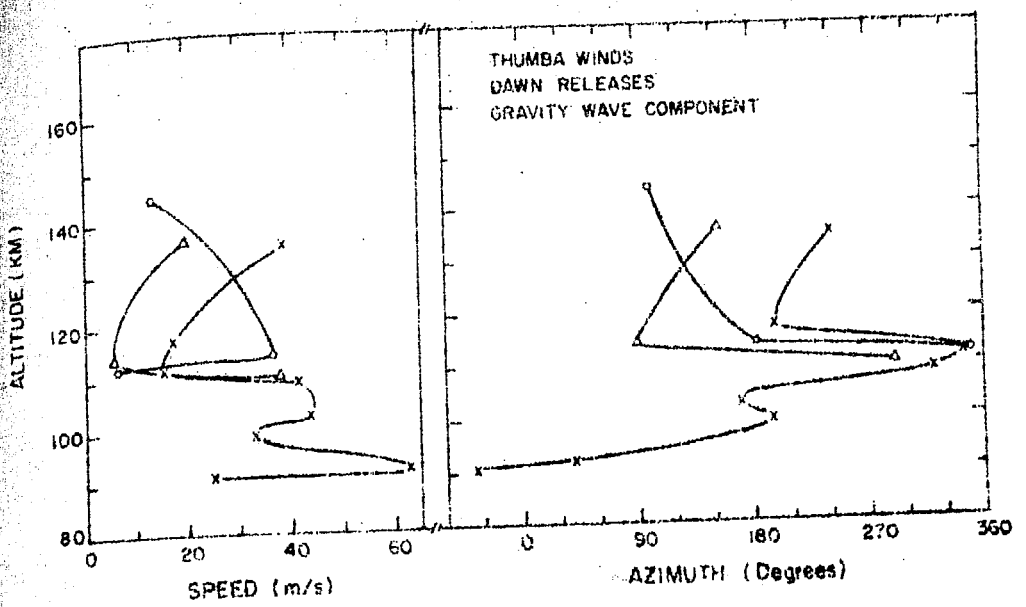

(a)

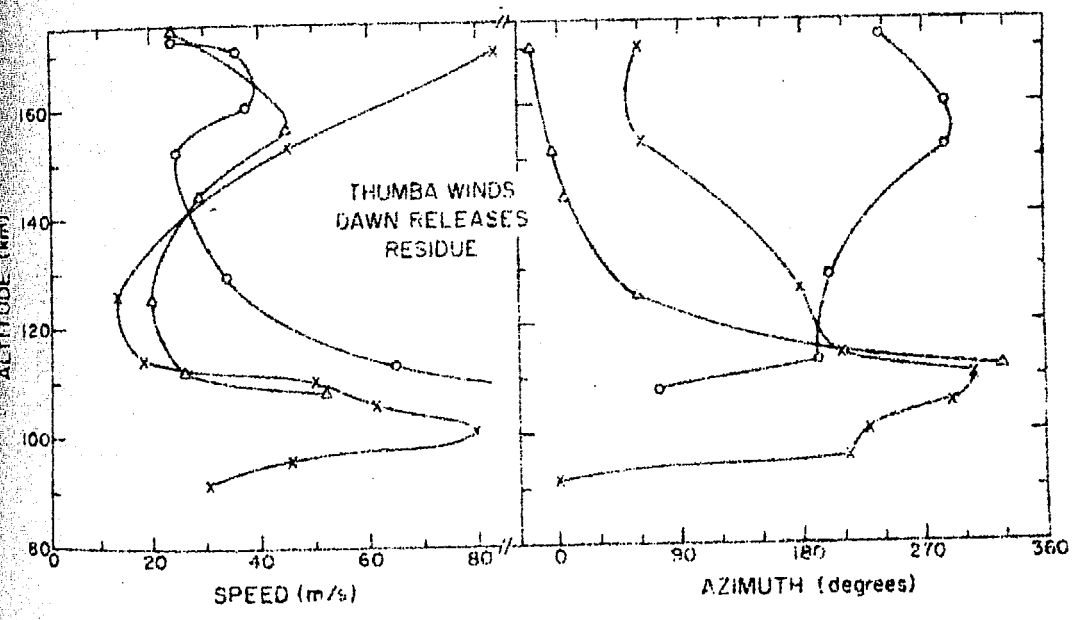

(b)

Fig.II.7:- Speed and azimuth of (a) gravity wave component and (b) residue which consists of diurnal, semi-diurnal and other components, at dawn corresponding to the dawn profiles in Fig.II.2. The circles, dots and traugles here correspond to those in Fig.II.2. The profile with dots in Fig.II.2 is not considered for the analysis.

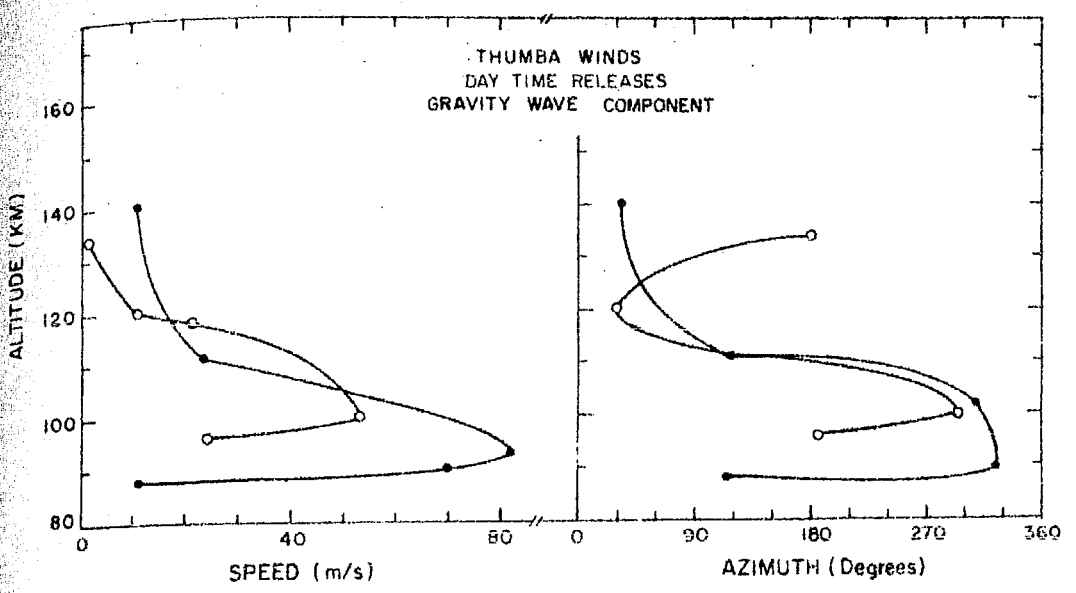

(a)

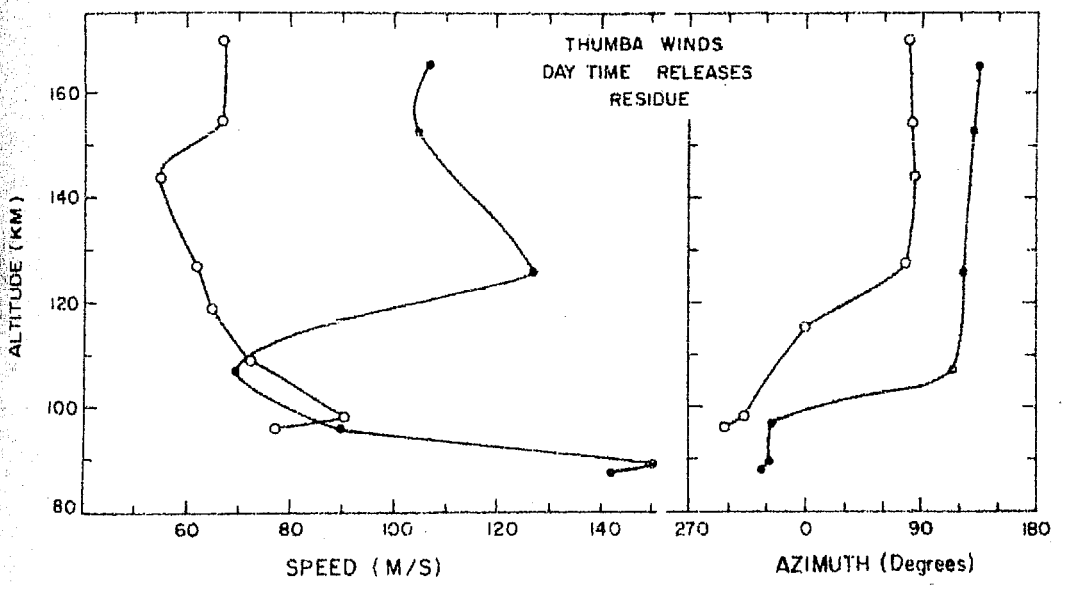

(b)

Fig.II.8:- Speed and azimuth of (a) gravity wave component and (b) residue which consists of diurnal, semi-diurnal and other components during daytime corresponding to the daytime profiles in Fig.II.3. The circles and dots here correspond to those in Fig.II.3.

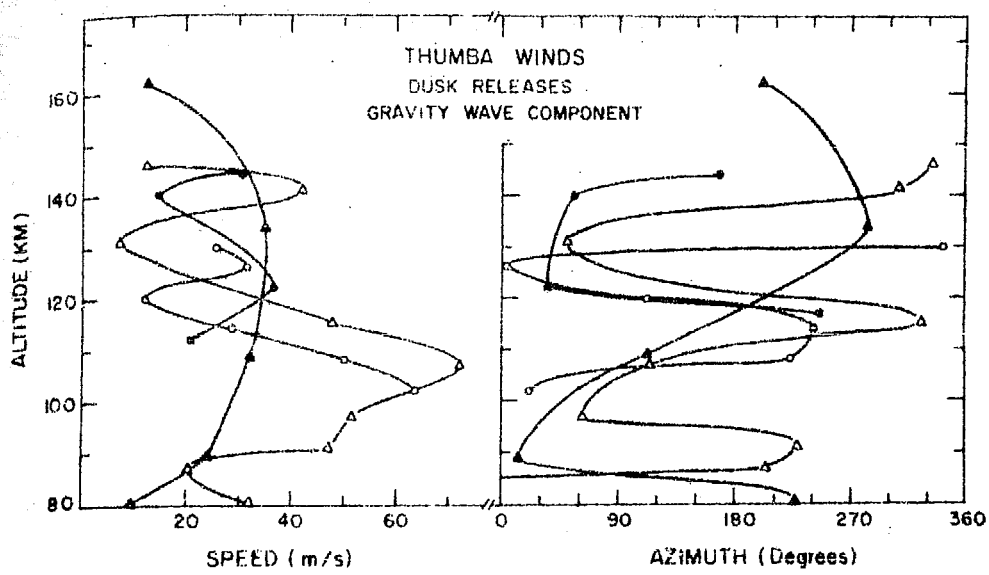

(a)

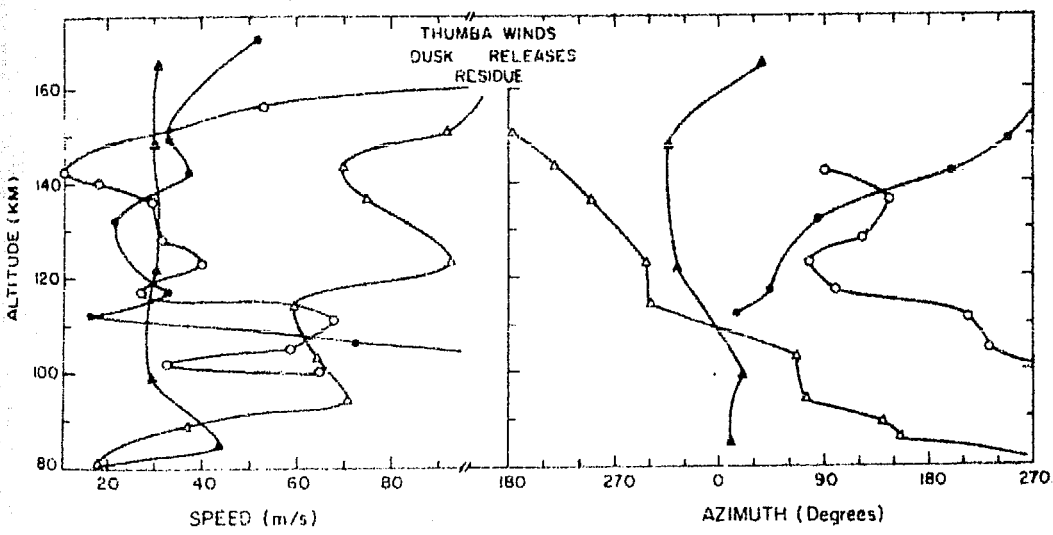

(b)

Fig.II.9:- Speed and azimuth of (a) gravity wave component and (b) residue which consists of diurnal, semi-diurnal and other components at dusk corresponding to the dusk profiles in Fig.II.4. The circles, dots and open and filled triangles here correspond to those in Fig.II.4. The profile with crosses in Fig.II.4 is not considered for the analysis.

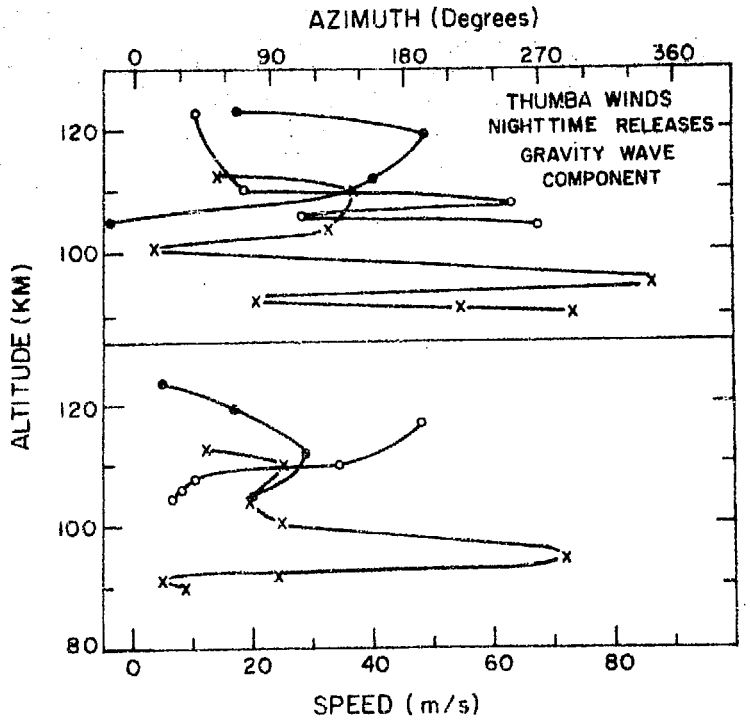

(a)

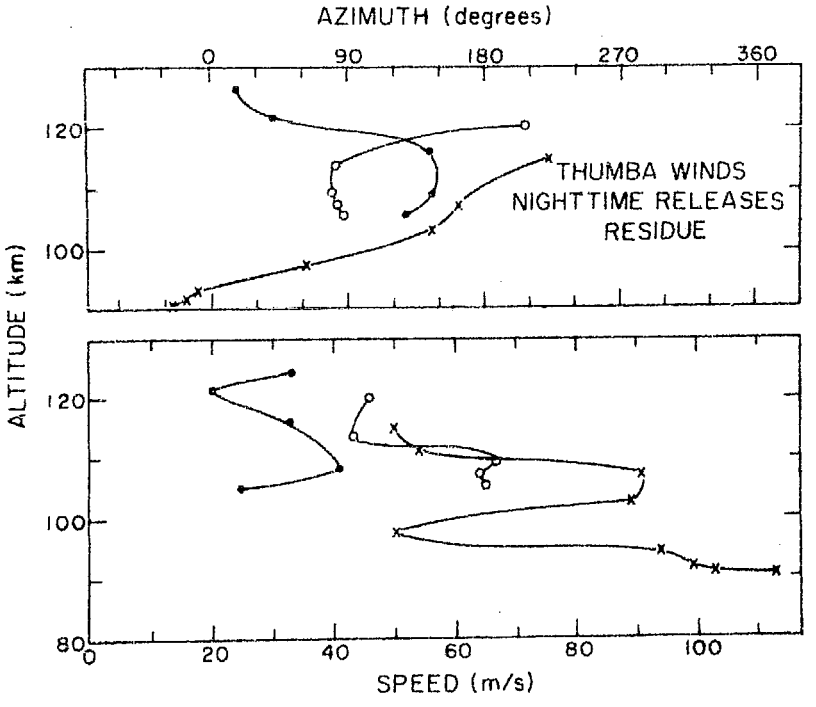

(b)

Fig.II.10:- Speed and azimuth of (a) gravity wave component and (b) residue which consists of diurnal, semi-diurnal and other components during nighttime, corresponding to the nighttime profiles in Fig.II.5. The circles, dots and crosses correspond to those in Fig.II.5.

azimuth profiles at dawn at the altitude 110 km are found in the observed wind profiles as well as in the inferred gravity wave profiles. The maximum speed due to the gravity wave seems to be confined to the altitude region 90-110 km in all the four cases. However, during the dawn and night-time, the altitude of maximum speed of gravity wave winds is found to be below 100 km; while during the dawn and dusk the maximum speed is confined broadly to 90-110 km region. Above about 120 km, the gravity wave wind speeds are rather low ($\sim$20-25 m/s), whereas in the region 90-110 km, the speeds are as high as 60 m/s. The wind speeds due to gravity waves appear to reach maximum ($\sim$80 m/s) during afternoon hours. However, it should be noted that the number of wind profiles available is less and this precludes any conclusion that can be drawn decisively in this regard from these results.

The residue R obtained by this technique is essentially a wind smoothed over vertical intervals of $\lambda_z/2 . \lambda_z$, in the profiles presented here varied from 10 to 20 km in the altitude region 90-120 km. λ_z, however, increased at higher altitudes. It is to be noted that the directions of R and of the observed wind are nearly identical. This is expected because the wave motion adds to and subtracts from R in a nearly random manner and its positive and negative contributions tend to cancel each other.

Finally, it should be pointed out that the method adopted here to extract the gravity wave component relies on subjective identification of the vertical wavelength of velocity oscillations. HINES (1965a, 1966) argued that this technique may underestimate the appearance of wave motions at altitudes greater than about 140 km. However, this technique seems to be adequate for the altitudes below 140 km where the shortest permissible vertical wavelengths are $\lesssim$ 30 km (HINES, 1964a).

II.4.2 Diurnal tide:

HINES (1966) evolved a method by which the diurnal (24 hr) component of tidal motion can be resolved from the observed wind profiles. KOCHANSKI (1966) also pursued this problem independently. KOCHANSKI separated the gravity wave component from the wind profiles before inferring the diurnal component. As mentioned earlier, HINES (1966) argued that KOCHANSKI'S method may fail to identify and extract larger-scale gravity waves. We believe, however, that this danger may not happen below about 140 km where the gravity wave scale sizes are $\lesssim$ 30 km. Moreover, the data available for the present analysis are mostly confined to the altitude region 100 - 150 km. Therefore, we follow KOCHANSKI'S approach.

The method of analysis is again simple. The data (including the point releases) are grouped into two; (i) the dawn and (ii) the dusk releases. Thus, these two groups of

data are separated approximately by 12 hrs in time. Other variations like seasonal variation are not considered. The data are sampled at every 5 km from 90 upto 160 km. The maximum number of observations available at a single altitude during the dusk is seven and in general, atleast, four observations are available at all altitudes in the region 100-150 km. During the dawn, the maximum number of observations available at a single altitude is five and in general, at least, four observation are available at all altitudes in the region 100-150 km. At each level of altitude the corresponding dawn and dusk data are plotted on azimuthal plane and the averages are taken. Fig. II.11 illustrates the method of inferring the diurnal tide. The average dawn (circles) and dusk (dots) wind velocities are shown in the figure at the altitudes 100 km and 110 km. $\underline{OM}$ represents the average dawn velocity and $\underline{OE}$, the average dusk velocity. A is the mid-point of ME. The magnitude of diurnal component of wind is now given by one-half of ME. The vector $\underline{AM}$ represents the diurnal component at dawn and $\underline{AE}$ at dusk. $\underline{OA}$ is the residue composed of semidiurnal and other components.

Fig.II.12 shows the altitude profiles of speed and azimuth of the diurnal component, extracted by the above method, along with the residue. The azimuth of the diurnal component shown in the figure, is for dusk. The portion of the curves in the altitude region $\sim$ 100-150 km is more

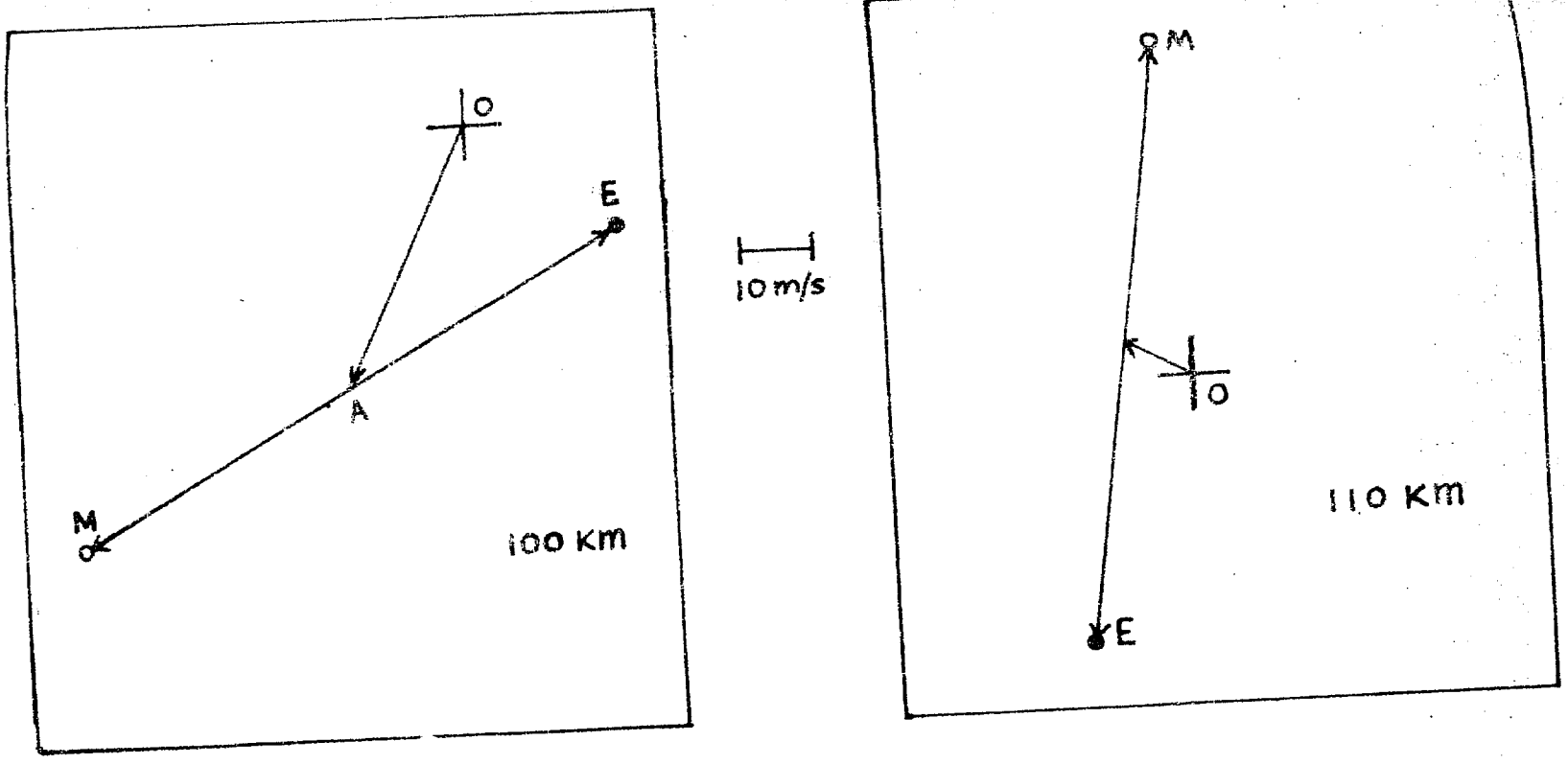

Fig.II.11:- Method of inferring the diurnal component of wind from observed wind profiles. The open and closed circles represent the mean values of the dawn and dusk wind data respectively at a certain altitude and on the azimuthal plane. OM and OE are the mean wind vectors at dawn and dusk respectively. AM and AE are the corresponding diurnal components where A is the mid-point of ME. OA is the residue consisting of semi-diurnal and other components (based on HINES, 1966).

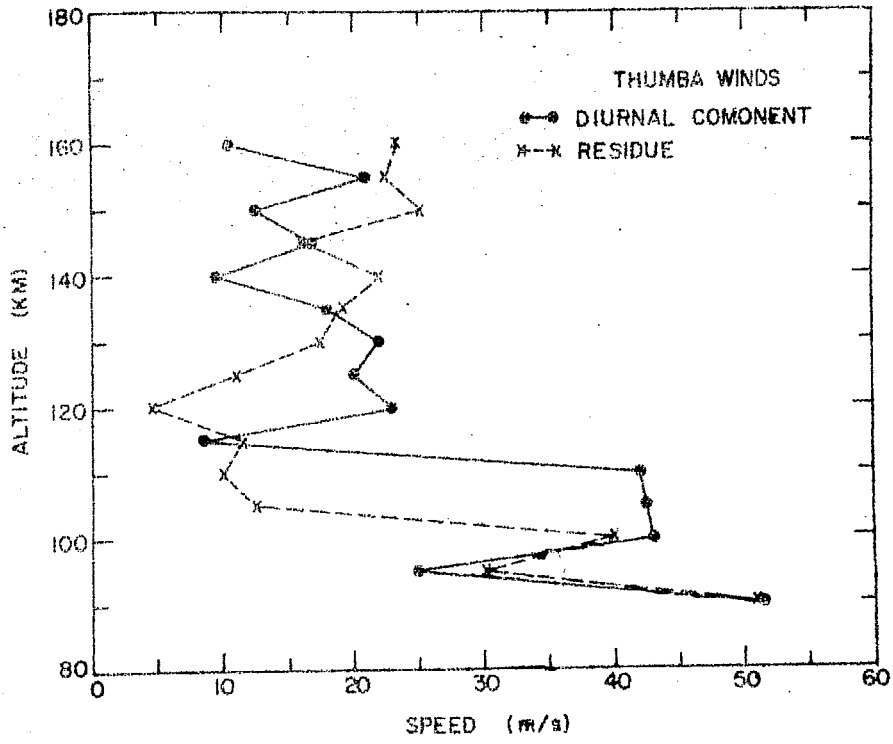

(a)

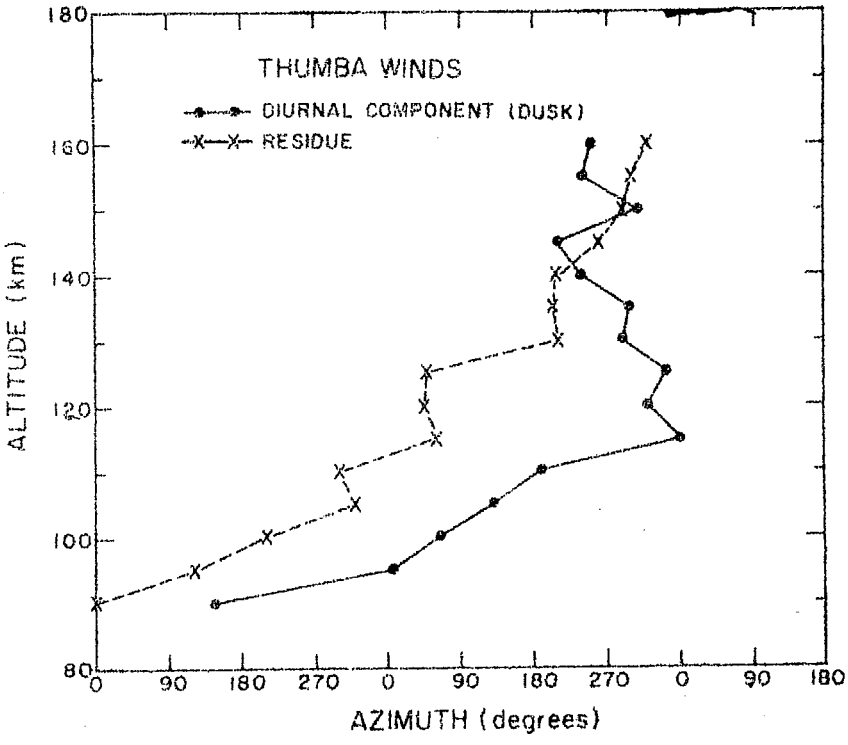

(b)

Fig.II.12:- Speed (a) and azimuth (b) of the diurnal component (dots) and the residue (crosses) inferred from the dawn and dusk data excluding the gravity waves. The azimuth profiles of diurnal component is at dusk.

reliable than that at any other altitude, since the number of observations in that region is more. Despite the limitation that the data are spread over a period of 12 years, it is indeed very interesting to see the consistency of the results and the systematic behaviour of the wind components with altitude.

From the Fig. II.12, it can be seen that the speed of the diurnal wind is about 40 m/s in the altitude region 100-110 km, above which it decreases to a value of 15-20 m/s. These amplitudes are less than those of gravity waves obtained from the individual profiles. The diurnal wind appears to reach a minimum at 95 km below which it shows a tendency of increase. The sharp decrease at 95 km could be related to the possible partial reflection below the altitude of temperature minimum. The increase of the amplitude above about 95 km upto about 110 km can be understood as a consequence of accompanying decrease of gas density. The subsequent decrease of amplitude above about 110 km can be attributed as due to the dissipation of tidal energy effected by the viscosity and thermal conduction.

The azimuth profile of the diurnal wind shows a clockwise rotation with altitude upto about 120 km. This is in conformity with the theory. However, the rate of rotation slowed down above about 120 km. This may be due to a severe damping of the tidal wave energy which results in a suppression of vertical phase variations (HINES, 1966).

The vertical wavelength of the diurnal tide as can be inferred from the figure II.12, is $\approx$ 20 km (between 90 and 115 km wherein the wind underwent a complete rotation of 360^{o}). The dominant diurnal mode at levels below about 120 km is known to be the (1,1) mode (for example, LINDZEN, 1970). From the formula given in eqn. (15) of Chapter I (with h_{mn} = 0.63 for (1,1) mode), the vertical wavelength of this mode at 110 km is found to be around 20 km. Thus, the diurnal component inferred from the present analysis agrees with the theory.

REES ET AL (1976) presented results from 4 lithium trails. Two of them were released at dawn and at 1100 hrs on 9 February, 1975; and the other two at 1420 hrs and at dusk on 19 February, 1975. From these four observations, assuming that they represent winds on a single day, REES ET AL concluded that the dominant winds at the dip equator are semidiurnal. We analyzed their data to extract the diurnal component by the method described earlier and found that their conclusion is erroneous. Fig. II.13 shows the profiles of diurnal wind and residue as inferred from the data of REES ET AL. The figure clearly shows that the diurnal component is dominant certainly below about 105 km and is comparable to the residue (which contains semidiurnal and prevailing components) above about 105 km. Thus, the present results do not support the preliminary results of REES ET AL (1976).

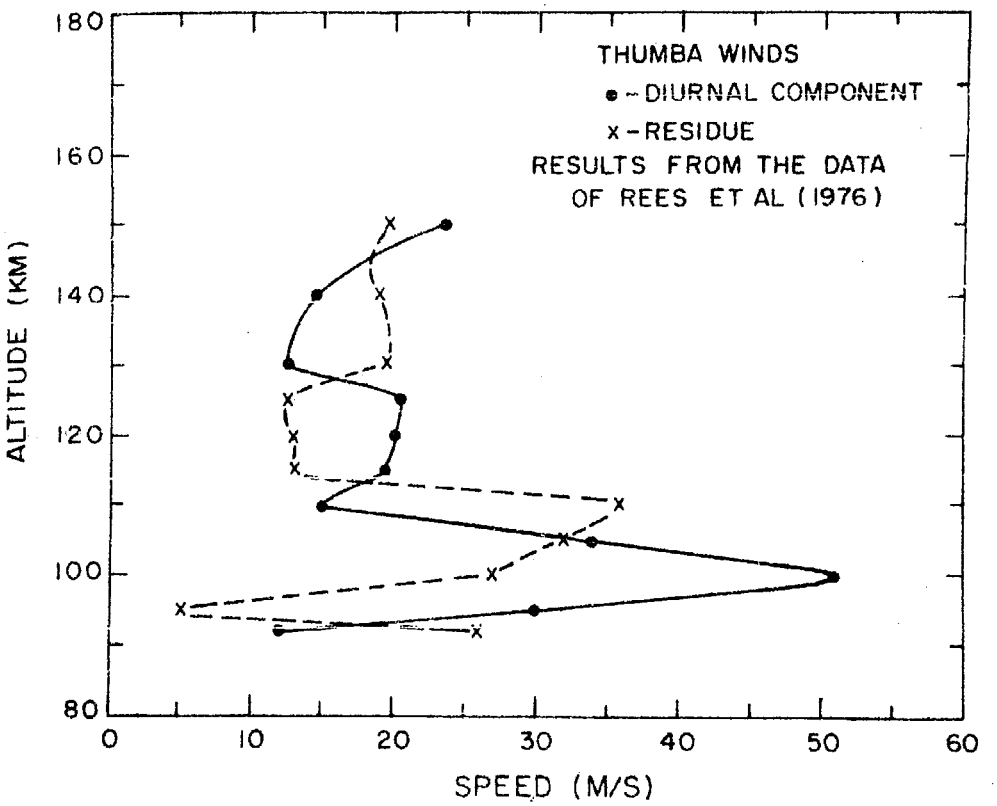

Fig.II.13:- Diurnal component of wind (speed only) obtained by using the data of REES ET AL (1976) on 9 February, 1975 (for dawn) and 19 February, 1975 (for dusk).

The amplitude of the residue shown in Fig.II. 12 is less than that of the diurnal component in general, at all altitudes between 90-140 km and in particular, in the region 100-120 km. The azimuth of the residue also shows a clockwise rotation with altitude. Since the prevailing and semidiurnal components are mixed-up in the residue, it is not possible to comment on the behaviour of these components separately.

So far, the type of analysis to extract the diurnal tide discussed here was not done for the equatorial latitudes. Thus, the present reults provide for the first time, informatio as to the periodicity of winds over the dip equator. We showed that the dominant tidal winds in the region 90-120 km are the diurnal tides.

It should be mentioned here that the results can not be considered very conclusive, in view of the fact that the data used in the analysis are spread over a very long period. Nevertheless, these results are important in that they provide the basis for "interim assessments until more extensive results become available" (HINES, 1966) at the equatorial latitudes. Furthermore, the conclusion that the diurnal tides are predominant over the dip equator is supported even when we considered the data of REES ET AL (1976) which can be safely assumed to represent the winds on a single day.

Fig.II.14:- The barium cloud released at 93 km, 286 s after the release. The points identified on the cloud and their corresponding altitude are also shown. Point 'a' is the tip of the upper loop, point 'b' is the mid-point of the knot in the middle of the entire release which couples the upper and lower loops and point 'c' is the lower most point of the cloud.

after the release, shows three points which can distinctly be identified on a sequence of photographs taken at different times from two camera stations. The point 'a' is the tip of the upper loop, 'b' is the mid-point of the knot-like structure and 'c' is the lower-most point in the cloud below the knot. The upper portion of the cloud between the points 'a' and 'b', remained to be seen very distinctly and clearly all through the period of observation (500 s). However, the lower portion below the knot showed up turbulence at $\approx$ 280 s after release and remained to be turbulent till the end of the observation. The positions of the three points are determined at various stages of observation by the method of triangulation. The correspondence of these points between the photographs from the two stations is checked by the method described by DESAI ET AL (1975) for the triangulation of trail releases.

II.5.2 Results:

Fig.II.15 shows the east-west motion of the points identified on the cloud. The eastward velocity of the points was found to be almost the same (19-25 m/s). The north-south motion of the points is shown in Fig.II.16, which reveals a strong north-south wind shear; the upper part of the cloud (point 'a') moving towards south with a speed of 23 m/s and the lower part of the cloud (point 'c') towards north with a speed of 25 m/s. The distortion of the upper part of the cloud, which appeared as

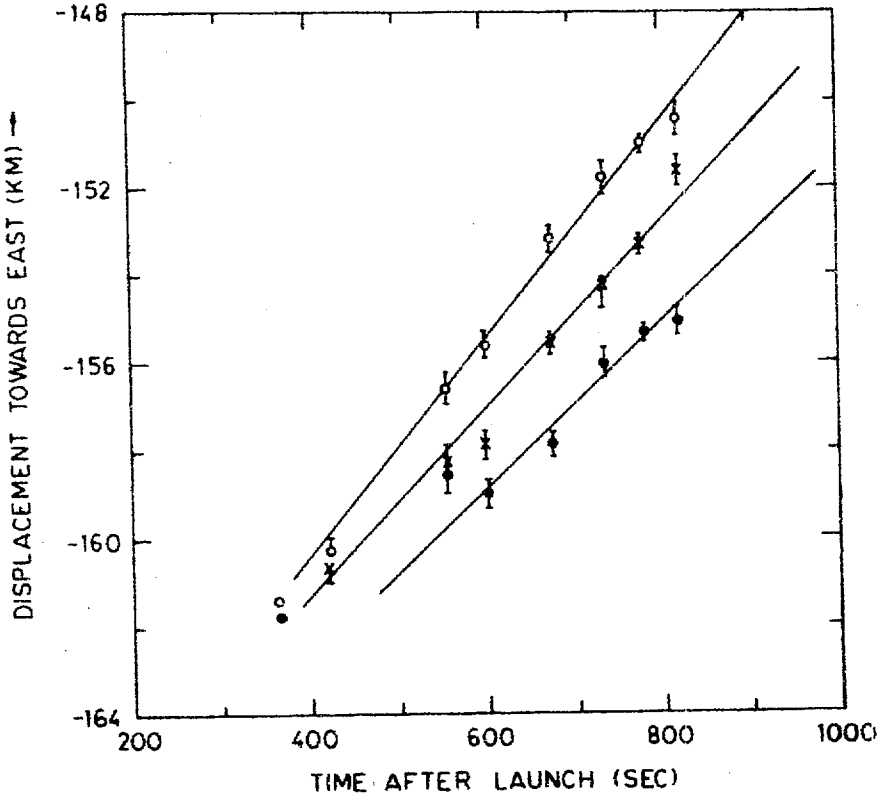

Fig.II.15:- East-west displacement of the points a, b, c represented respectively by circles, crosses and dots with time after launch.

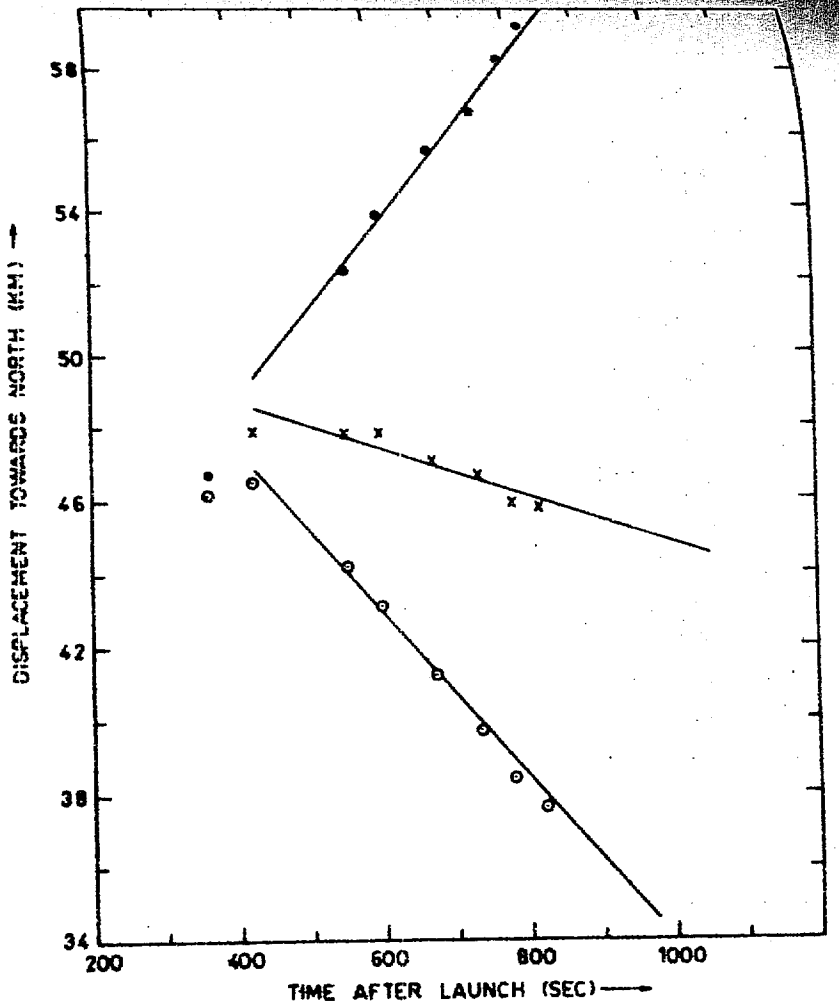

Fig.II.16:- North-south displacement of the points a, b, c represented by the circles, crosses and dots respectively with time after launch.

a circular ring in the initial stages into an elongated loop is mainly due to the wind shear between the points 'a' and 'b'. Fig.II.17 shows the vertical motion of the points on the cloud. It is interesting to note that while the point 'a' moved vertically upwards with a speed of 19 $\pm$ 7 m/s, the point 'c' remained at about the same height. The altitude variation of the vertical and meridional components of the wind velocity reveal variation with time of observation. This is thought to be due to the spatial variation of these components as the cloud parts (a, b and c) moved with time into different positions in space. The velocity components with the corresponding altitudes calculated at 700 s after the rocket launch are taken for constructing the height profiles of the wind components in Fig. II.18. The horizontal winds measured by similar releases by the same rocket at altitudes 150, 176 and 207 km (NARAYANAN, 1973) and the vertical winds at these altitude (RIEGER, 1974) are also shown in the same figure. The data points are then joined by smooth curves to represent the height profiles of the three components of neutral wind velocity viz., eastward, northward and vertically upward. Part of the vertical wind profile shown by dotted curve, reveals reversal of the wind if the observational points were to fit a smooth curve.

The observations shown in Figs. II.15, II.16 and II.17 show the presence of height varying wind components mainly

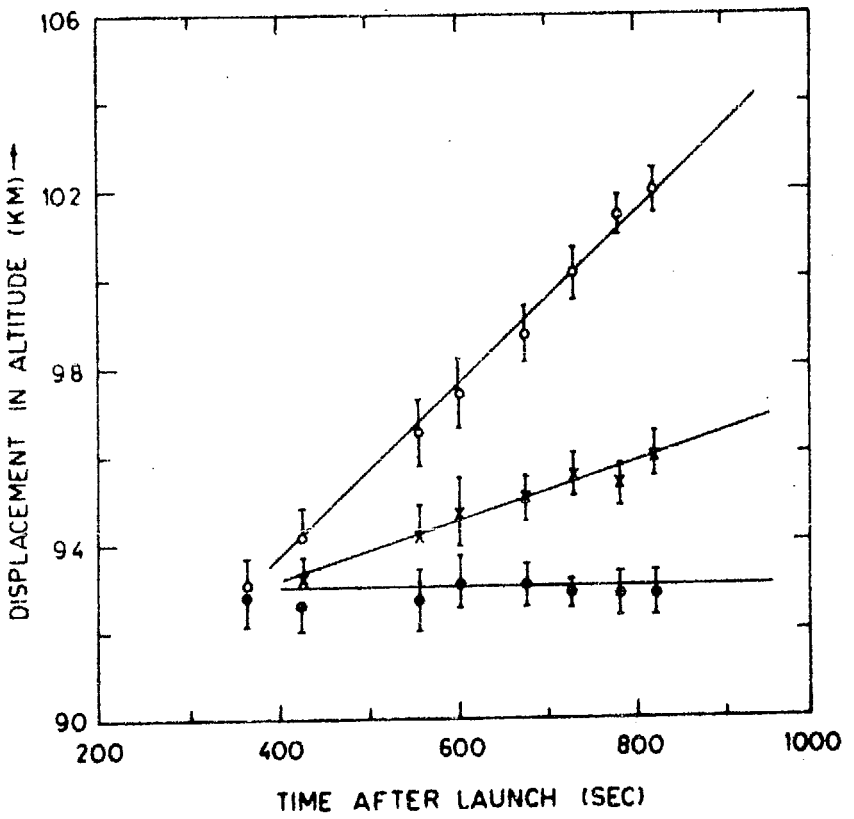

Fig.II.17:- Vertical displacement of points a, b, c represented by the circles, crosses and dots respectively with time after launch.

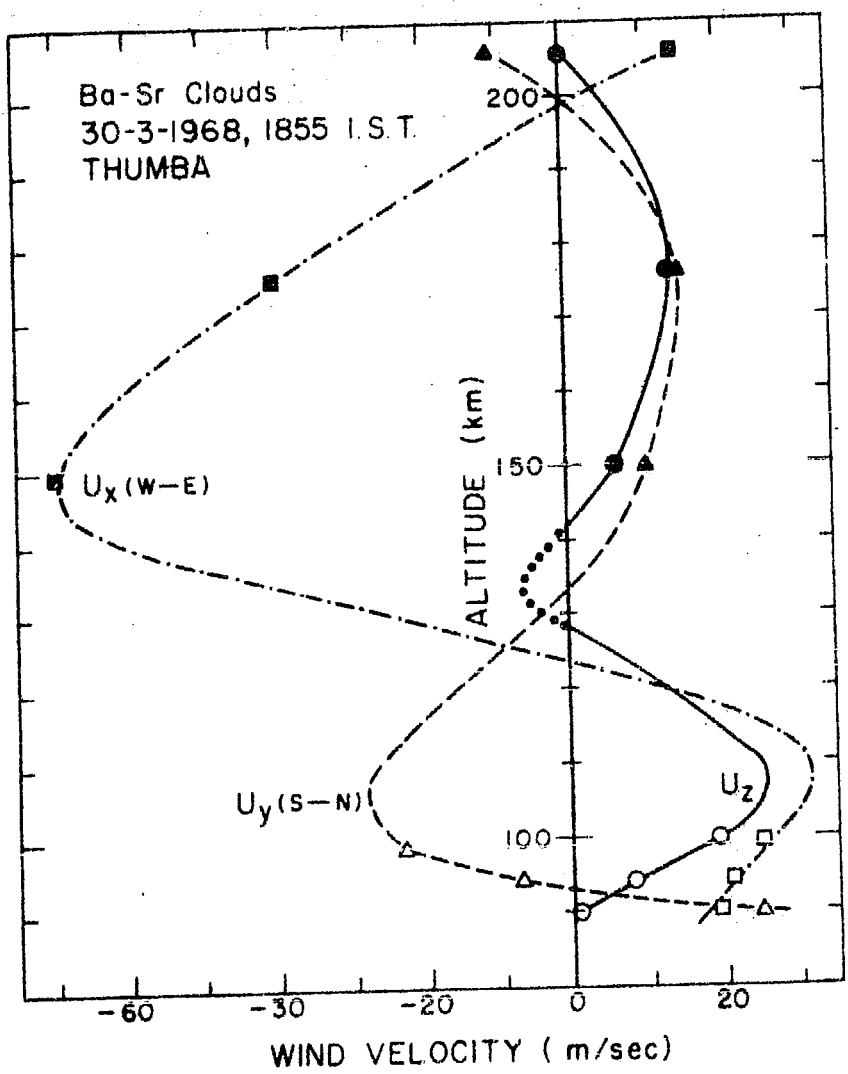

Fig.II.18:- Vertical profiles of the east-west, north-south and vertical components of the neutral wind velocity over Thumba, on 30-3-1968 at 1855 IST. The open squares (east-west velocity, U_x), triangles (north-south velocity, U_y), and the circles (vertical velocity U_z) represent the present results. The filled squares, triangles and circles are the results taken from NARAYANAN (1973) and RIEGER (1974). Smooth curves are drawn joining the observed points. The dotted portion in the U_z profile is to show the uncertainty as to the U_z becoming negative in that region.

in the north-south and vertical directions. The cloud during its expansion in the north-south-vertical (Y-Z) plane has detected the variable wind in that plane. Although the cloud has moved to east during the same time, the eastward velocity is almost uniform in the altitude region of its motion. Fig. II.19 shows the velocity vectors of the points 'a', 'b', 'c' in the Y-Z plane. The positions of these points are taken at every 100 s from the time of the release of the cloud till the end of the observations. The velocity vectors thus represent average values in the duration of 100 s, i.e., for the distance the cloud point moved in the 100 s time. The figure depicts strong gradients in the velocity in the vertical as well as north-south directions.

II.5.3 Discussion:

Turbulence:- The lower part of the cloud (the portion between the points 'b' and 'c' in Fig.II.14)became turbulent 280 s after the release which is rather too long a period to be termed as the delay in the onset of turbulence. The theoretical as well as the observed values of the delay in the onset of turbulence at 93 km is $\approx$20 s only (REES ET AL, 1972 a). The lower part of the cloud moved almost horizontally in the north-east direction to $\approx$ 10 km away from the release point, in 280 s. This shows possibly, an evidence for the co-existence of turbulent and non-turbulent regions as

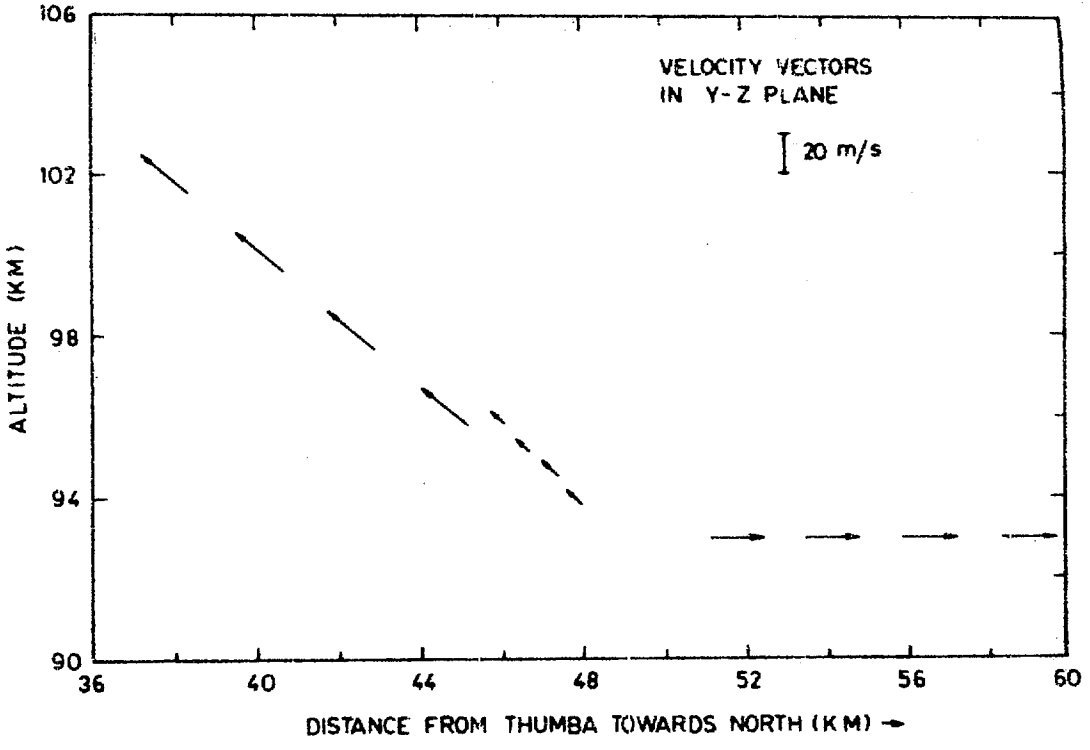

Fig.II.19:- Spatial distribution of velocity vector in the meridional plane of the cloud. The vector represents the velocity component in the plane with the base point indicating the spatial position it corresponds to. The set of four inclined arrows on the left shows the velocity field experienced by the cloud point 'a', the smaller arrows by 'b' and the horizontal arrows on the right are by 'c' at different times during observation.

reported earlier by BLAMONT AND BARAT (1967). The minimum horizontal scale size at 93 km in the present case is inferred to be $\approx$10 km. The upper part of the cloud between the points 'a' and 'b' remained all through in a laminar flow region. As can be seen from Fig.II.19, the gradients of the neutral wind velocity in vertical as well as horizontal (N-S) directions are stronger in the region between the points 'b' and 'c', than those between the points 'a' and 'b'.

The onset of turbulence is often discussed with the aid of what is known as Richardson's criterion (HINES, 1971). HINES (1971) generalised the criterion, taking into account the vertical component of the irregular neutral wind and the gradient of these winds in the horizontal directions also. The modified Richardson's criterion is given by

$$R_i = \omega_{BV}^2 / (\nabla \underline{W})^2 \leq \frac{1}{4}$$

where $(\nabla W)^2 = (\nabla W_x)^2 + (\nabla W_y)^2 + (\nabla W_z)^2$, x, y, z being the Cartesian coordinate axes (eastward, northward and vertically upwards respectively). ∇ denotes the gradient in all the three directions. Taking $\omega_{BV} = 2 \times 10^{-2} \text{sec}^{-1}$, and substituting $(\nabla \underline{W})$ for the lower ('b' - 'c') and the upper ('a' - 'b') portions of the cloud the Richardson numbers are computed and it is found that the R_i value for the lower portion is less than 1/4 upto 280 s after the release time when the turbulence began to appear. If the turbulence were to be present with the

uniform intensity in the region of 93 km altitude, the delay of 280 s in impressing itself on the cloud appears to be too long a time for the 93 km height region. The lower part of the cloud has moved a distance of about 10 km in 280 s where the the turbulence is seen. It appears that the turbulence intensity is not the same at the same horizontal level above which strong wind gradients are present.

The height of turbopause:- The turbopause, in a broad sense, is the level at which the turbulence in the lower thermosphere ceases suddenly and the laminar flow (or the molecular diffusion) becomes predominant. The level of trubopause can be visually seen by releasing a vapour trail. Such experiments in the past revealed the height of turbopause to be 104 $\pm$ 2 km (DESAI ET AL, 1975; REES ET AL, 1972 a; .. BLAMONT AND BARAT, 1967). In the present case the turbopause is found to be at 95 $\pm$ 2 km, which is the height of point 'b' measured at 280 s after the release. These results provide clear evidence for the variability of the level of turbopuse. As these turbopause fluctuations in height are observed in the same season (March-April) they can not possibly be attributed as due to the semi-annual variations in neutral temperatures as in the case of similar fluctuations at mid-latitudes (ELFORD AND ROPER, 1967). It is possible that the significant gradients in the vertical winds could be responsible for the lowering of the turbopause.

Vertical winds:- RIEGER (1974) reported vertical velocities of 6 m/s and 14 m/s at 150 km and 176 km respectively (Fig.II.18) over Thumba which were measured at the same time as that of the present results. The smooth profile in vertical wind in the Fig.II.18 indicates the possibility of reversed or downward wind to be existing in a narrow region between 130 and 140 km. The wind reversal can not be ascertained as there is no measurement in that altitude region. The vertical wind, however, appears to have reached a minimum in that region. The height profiles of the vertical components of wind velocity were shown earlier by REES (1969) for mid-latitudes and the present profile is the first of its kind for equatorial latitudes. The vertical scale sizes (λ_z) of the wave type vertical wind profile of the present results are $\approx$ 50 km at lower altitudes and $\approx$ 80 km above 140 km altitude which are larger than those reported by REES (1969) for mid-latitudes. The amplitudes, however, are of comparable magnitudes. The vertical scale sizes of vertical wind are smaller than those of the horizontal wind (Fig.II.18). This may indicate that physical sources of the two components of neutral wind velocity could be independent. However, additional observations are necessary to ascertain the origin of these winds.

The vertical winds are present during the entire observational time which is longer than the Brunt-Vaisala

periods (τ_{BV}) at these altitudes. For example, the observational time available at 100 km altitude was 10 min during which the length of the cloud loop increased and the Brunt-Vaisala period is only 5 min. At higher altitudes the observational time is much longer (about 45 min at 200 km) while τ_B is only around 10-12 min. Thus the period of the wave-shaped vertical wind profile is longer than τ_B and also the duration of the observations. On this basis as well as the observed vertical wavelengths, the wave-type vertical wind profile can be identified with the presence of an internal atmospheric gravity wave (HINES, 1960) in the equatorial thermosphere. The question then is whether it was triggered by the four barium releases themselves. The amounts of barium released are too small (0.5, 0.5, 0.75 and 2 Kg at 93, 150, 176 and 207 km respectively) to trigger gravity wave in the lower thermosphere. As predicted by RAGHAVARAO (1976), the vertical winds may play a significant role in altering the electric fields in the electrojet region. The effects of vertical winds on the electrojet are discussed in Chapter VI.

II.6 Conclusions:

The important conclusions arrived at in this Chapter are as follows.

1. The gravity wave contribution to the observed winds is prominent in the region 90-110 km. The wind shears

seem to be mainly caused by the gravity waves.

2. The dominant tidal winds over the dip equator seem to be diurnal, particularly in the region 90-120 km. These winds are identified with the (1,1) diurnal tidal mode. These results are in conformity with the theory.

3. Vertical wind velocities are at times as high as 25 m/s over the dip equator. The wave-type vertical wind profile obtained can be identified with an internal gravity wave.

CHAPTER III

THE TECHNIQUE OF MEASUREMENT OF WINDS IN THE DAYTIME

III.1 Introduction:

We described in Chapter II, the technique of measuring the winds in the upper atmosphere by the vapour cloud releases during the twilight and nighttime. Photographic tracking of the releases is possible during these periods, because the releases are visible to the naked eye. During the daytime, however, the background sky brightness is so high that the photography of the cloud from ground is impossible. Attempts have been made to photograph the clouds by cameras fitted with narrow band-pass interference filters (HALL ET AL, 1971) and proved to be futile. Assuming that a vapour release may be photographed if the irradiance produced by it, is 25% of that due to the sky background transmitted by the filter, a satisfactory contrast on the photograph can be attained only by using an interference filter of band width 0.6Å (BEST, 1970 a). The narrowest interference filters have band widths about 2Å, available at a 'reasonable' cost. Nonetheless, since the brightness of the sky reduces substantially at higher altitudes it is possible to photograph the clouds by using cameras with interference filters of band width around 10Å (to have in addition, a reasonably good field of view) from aboard a jet aircraft flying at an altitude of 40,000 ft. (BEDINGER, 1973). Besides being costly, this method also involves somewhat complicated triangulation procedure

to reduce the data. However, BEDINGER (1977) reported a fairly accurate set of results obtained by the technique of on board jet-tracking.

Whatever be the observational technique, lithium seems to be the best element for the daytime release. The daytime sky intensity is highly variable depending upon the spectral region and the position of the sun and that of the observer. Typically the sky intensity is 10 ergs/cm^2/sec/steradian/Å. The maximum observable intensities of the resonance lines of lithium and sodium are 1.5 and 0.07 ergs/cm^2/sec/steradian respectively. In terms of photon intensities these are: for background radiance, 3 x 10^{12} photons/cm^2/sec/str/Å for lithium (6708Å), 5 x 10^{11} photons/cm^2/sec/sterdian; and for sodium (5890Å, 5896Å), 2 x 10^{10} photons/cm^2/sec/str. BEST AND PATTERSON (1962) have analysed the photon intensities of all the alkali metals and showed that rubidium and caesium metals would be as intense as lithium metal. But, rubidium and caesium have resonance lines at 7800Å and 8521Å respectively where the quantum efficiency of the photocathodes of the photo-multiplier tubes (that should be used to amplify the signal from the cloud received through an interference filter) would be very much smaller than at the lithium emission line (6708Å). Furthermore, the solar spectrum near 6708Å is relatively free from absorption features. Thus, lithium seems to be the most desirable candidate for the release in the daytime to measure the winds.

We describe in this Chapter, the equipment fabricated at the Physical Research Laboratory, for the detection of lithium vapour releases during the daytime and present the preliminary results obtained using the equipment.

Various techniques employed by previous workers to detect vapour clouds released in the daytime are briefly discussed in the present section. In III.2, the experimental set-up for tracking the lithium clouds in the daytime, developed at the Physical Research Laboratory, is described. The method of analysis of the data obtained by the technique is described in III.3. In III.4, we present some preliminary results on the neutral winds obtained by using the equipment.

III.1.1 Differential photometers:

BEDINGER (1970) and BEST (1970 a,b) have independently described the use of differential photometry in tracking the lithium cloud against a bright background. The technique essentially involves using a fairly narrow band-pass interference filter (~2.5Å band width) with the peak transmission at 6708Å (the resonance line of lithium) to detect the lithium cloud from the bright sky background. To correct for the background, the difference between the background intensity at a wavelength slightly away from 6708Å and that of the emission from the cloud plus the background emission at 6708Å is taken and amplified. BEDINGER (1970) has employed a rotating mirror which allows a narrow beam of light from the

region of interest in the sky to pass through a very narrow-band interference filter alternately at normal incidence and at a small angle to the normal (this small angle makes the wavelengths of peak transmission to shift to shorter wavelengths than the normal incidence line 6708Å and thus provides a basis for subtracting the background). The signal received by the photomultiplier placed at the back of the filter, is balanced for the light beam incident normally (i.e., 6708Å, lithium line) and at a small angle (i.e., slightly less than 6708Å, for back-ground; assuming that the back-ground intensity is almost the same in the region around 6708Å) when there is no lithium in the sky. In the presence of a lithium source such as a lithium cloud, the balance is disturbed by the very intense emission line from the source. The signal thus obtained, is amplified and synchronously rectified. BEDINGER observed the ratio of the signal from a bright lithium cloud to that received from the daysky, through a filter of band width, 2Å, is 1:10. BEST (1970 a, b) also has used a single filter for both the signal beam and the reference beam. A chopper-wheel makes the light to pass through the filter normally and at an angle. BEST used a tracking system to cover a large field of view, as the field of view for a narrow band filter is very narrow. He employed a scanning mirror driven by a motor in azimuth and elevation. The mirror,

which reflects the light from the sky on to the filter is adjusted manually at the end of each azimuth sweep. The cloud signal information is given to an x-y recorder along with the azimuth (x) and elevation (y) information.

REES ET AL (1972b) have tracked a lithium cloud by a differential photometer device, in principle similar to that used by BEDINGER (1970) and BEST (1970 a, b). A scanning mirror, driven in azimuth and in elevation independently by two motors, reflects the sky signal on to a beam splitter. The beam-splitter splits the on-coming light into two geometrically identical beams which are passed through two filters one tuned to the lithium wavelength, 6708Å and the other at a wavelength 3-4Å away from 6708Å. The filter outputs are amplified by photomultipliers and pre-amplifiers and are coupled by a difference amplifier. HIND AND LLOYD (1973) have discussed the criteria which must be satisfied if the lithium releases are to be observed in the daytime.

III.1.2 Fabry-Perot Interferometer:

BEST (1970 a) has discussed the use of Fabry-Perot interferometer in series with a narrow-band filter to detect the lithium cloud. He used Fabry-Perot (FP) plate of flatnesses $\lambda/50$ and $\lambda/200$ with a free spectral range of 3Å in series with a narrow band filter and found that this technique gives far better resolution. REES ET AL (1972b) also have used this technique to track the lithium clouds. They have used

a 25 mm diameter FP with resolution 0.1Å and free spectral range 10Å, in series with a 3Å band width interference filter and the combination is tuned to the lithium wavelength. This method, however, is costlier than the differential photometric method.

III.1.3 Resonance Cell:

BEST (1970 a) has described a technique to detect sodium clouds in the daytime. The light from the source passed through a 2.5Å filter is directed on to a sodium resonance cell. The scattered light from the cell is directed on to a photocathode. A chopper is used so that the light transmitted by two filters is alternately sent to the resonance cell. One filter isolates sodium D line and the other, a similar range of background only. In theory, only the light within the thermal bandwidth of the vapour in the cell, which is narrower than the bandwidth of the sodium D lines at temperatures above 120 km, should be resonantly scattered. REES ET AL (1972b) have used this technique to detect sodium clouds. They assessed that if technical difficulties of using lithium vapour in the cell arising from the necessity of much higher temperature than for sodium (350-400°C compared to 150°C) could be overcome, the instrument would have appreciable operating advantages over the photometer systems.

NAKAMURA (1974) argued that in the absence of stray reflections, the sodium vapour resonance cell will scatter

radiation only in bands corresponding to the Doppler widths of two sodium resonance lines. In the presence of a magnetic field of 4000 gauss the cell scatters radiation in the components of Zeeman splitting. NAKAMURA developed a Zeeman photometer on similar lines to that of BLAMONT ET AL (1961, 1965) for observing dayglow.

However, the methods employing the sodium cell, suffer from the disadvantage of getting contaminated due to emission from the natural atmospheric sodium (BEST, 1970 a).

III.1.4 Onboard-jet-aircraft tracking:

BEDINGER (1973) successfully photographed lithium and barium clouds released by a rocket, by using narrow band pass interference filters (of 10Å bandwidth) from aboard a jet airliner flying at an altitude of 40,000 ft. Thus, it is possible to photograph the clouds even in daytime by tracking it from a high altitude. BEDINGER (1977) reported results from such an attempt andclaimed good accuracy. This method enables us to track the cloud regardless of weather and logistic restrictions. However, it is fairly costly experiment as it involves hiring a jet aircraft.

From a comparative study of various methods to track the vapour clouds released in the daytime, BEST (1970 a) concluded that the differential photometric technique is adequate enough to track a lithium cloud. Defining signal to noise ratio as the ratio of signal photoelectrons to the square root of the number of continuum photoelectrons with

a bandwidth of 100 Hz, BEST estimated the ratios for the various techniques described above. Table III.1, reproduced from BEST (1970 a), gives the signal-to-noise ratios that can be achieved by various techniques.

Table III.1

Relative performance of possible trail-detectors expressed as signal-to-noise voltage ratio

Trail	Detector	S/N ratio
Li	λ/200 FP interferometer	185
Li	λ/50 FP interferometer	100
Li	2.5Å interference filter	90
Na	Resonance Cell, 20% efficiency	27
Na	2.5Å interference filter	6.6
AlO	2.5Å interference filter	0.8

Eventhough, the FP interferometers have a high S/N ratio, they require temperature controlling systems which complicate the experimental set-up. Besides, the interferometers are costlier than the interference filters used in differential photometry. From the above table it is clear that the interference filters are sensitive enough to detect the lithium vapour releases during daytime. It is also clear that lithium is the most suitable element for the daytime release.

III.2 Experimental set-up for the detection of the lithium vapour clouds released in the daytime:

III.2.1 Description of the set-up:

A scanning mirror, driven by two separate motors in azimuth (this azimuth is same as the conventional azimuth only when the elevation of the mirror is zero and let us call it 'azimuthal' angle) and elevation, tracks a field of view of 30° x 30° in the region of interest in the sky. This tracking is done in 30 horizontal scans in a period of 30 sec from the highest elevation (top) to the lowest elevation (bottom). The tracking is repeated from the bottom to the top at the same speed. The mirror is directed to a pre-determined position corresponding to the predicted release point of the lithium cloud in the sky. Scanning is done with this pre-determined position as the mean position. From this mean position, the mirror is rotated by the motors by $\pm 7^{\circ}.5$ in azimuthal angle and $\pm 7^{\circ}.5$ in elevation so that the field of view scanned in the sky is 30° x 30°. Fig. III.1 shows schematically the optics used in this experiment. The light rays from the sky are reflected by the scanning mirror M on to a collecting lens T which converges the rays at the centre of an aperture (iris aperture) A. The width of the aperture is so adjusted as to allow a light beam of 1° field of view to fall on the collimating lens C. The lens C is placed at a distance equal to its focal length from the centre of the aperture. The collimated 1° wide beam is allowed on to a beam splitter BS

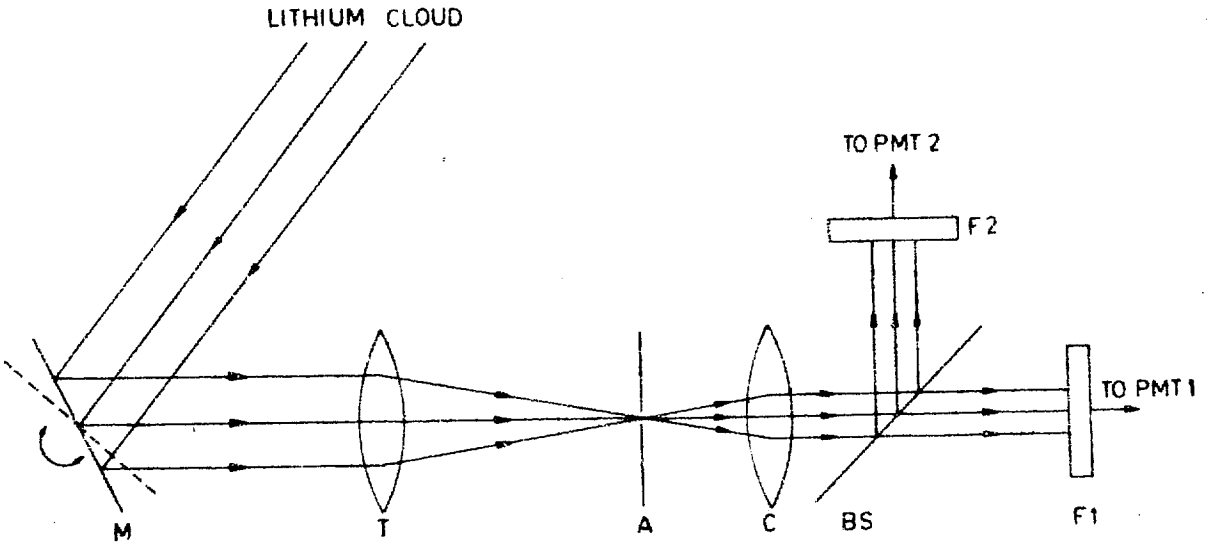

OPTICS OF THE EQUIPMENT FOR
DAY TIME WIND MEASUREMENT

Fig.III.1:- Optics of the equipment for measuring the winds in the daytime. M is a plane mirror rotated vertically and horizontally by two separate motors. T is the collecting lens. A is an iris aperture which can be set at the desired resolution. C is the collimating lens. BS is the beam-spilter. F_1 and F_2 are the interference filters one of which is tuned to the lithium resonance line(6708Å).

which transmits 50% of the incident light and reflects 50% (if there is no absorption). The two beams from the beam splitter are passed through the narrow-band interference filters F_1 and F_2. One of these filters is tuned to lithium emission line, 6708Å and the other to a wavelength about 3Å away from 6708Å. The bandwidth at half peak transmission of the filters is 2.5Å. Two photomultipliers are kept behind the filters to receive the signal at the end of the filters.

Fig. III.2 is the block diagram of the electronics used to detect and record the signals. The current output from each of the two photomultipliers is given to a pre-amplifier, where it is first converted to a voltage signal by a FET input operational amplifier and amplified by another operational amplifier. The difference between the outputs from the two pre-amplifiers is amplified by a difference amplifier (comparator). Prior to the experiment 'balancing' is achieved by scanning the sky with no lithium source. The output of the difference amplifier is given to a chart recorder along with a locally generated 1 pps time code for reference, and the marks at the end of each of the azimuthal and elevation scans. The chart recorder serves as the preliminary data recorder.

The output of the difference amplifier is given to an 8 bit analog to digital (A/D) converter which samples the signals at a rate of 30/sec (corresponding to 1° field of view) and quantises into 8 bit words. The 8 bit word

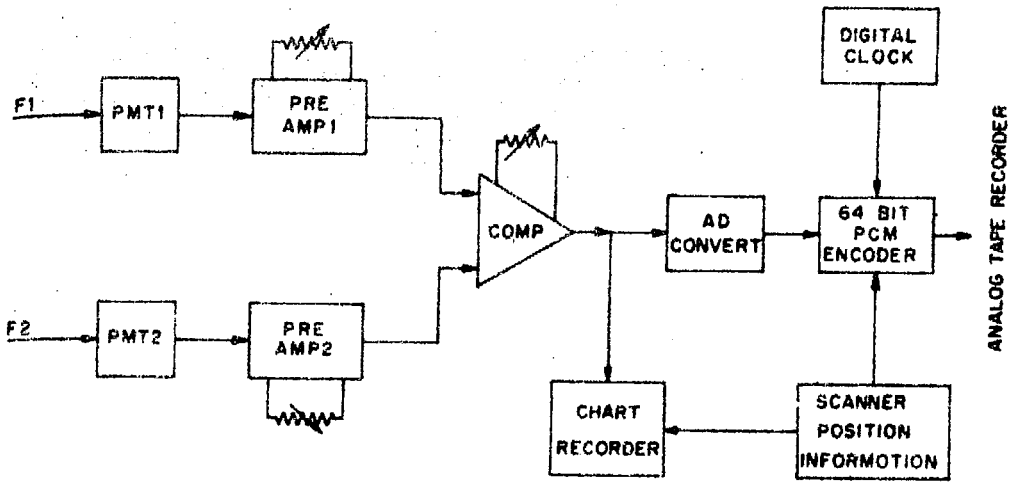

ELECTRONICS OF THE EQUIPMENT FOR DAY-TIME WIND MEASUREMENT

Fig.III.2:- Electronics used to detect and record the signals from the cloud. The outputs of the two photo-multipliers (PMT 1 and 2) are amplified by the pre-amplifiers (PRE AMP 1 and 2). The difference of the outputs of the pre-amplifiers is taken and amplified by the comparator (COMP). The chart recorder serves as the preliminary recorder of the data for on-the-spot analysis.

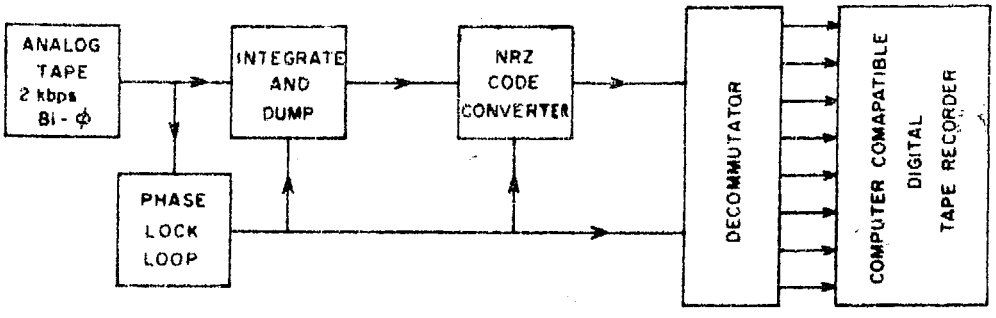

PCM DECODER

Fig.III.3:- PCM (bi-phase) decoding unit.

output along with the reference time and the scanner position (azimuthal angle and elevation) information is multiplexed into a 64 bit Pulse Code Modulation (PCM) frameofeight 8 bit words. The PCM (bi-phase) output is recorded on an analog tape at the rate of 2 kilo bits/sec.

The bi-phase PCM data from the analog tape are decoded at a later date in the laboratory by a PCM decoding unit built to suit the PCM format chosen for the experiment. The decoding unit is shown in Fig. III.3. The 2 kilo bits/sec clock is regenerated (by phase lock loop in Fig. III.3) from the PCM data and is used for the bit detection circuitry ('integrate and dump' in the figure) followed by bi-phase to NRZ (non-return to zero) code converter. The NRZ data are given to the decommutator which searches for the frame synchronization pattern and aligns the 8 bit words serially. The 8 bit words thus obtained on 8 lines (forming one 'character') from the decommutator are recorded on computer compatible digital tape recorder which also has 8 channels for forming a character. The digital tapes thus recorded for two or more ground stations can be analyzed on IBM 360 computer.

III.2.2 Operation of the equipment:

The equipments are operated simultaneously from at least two stations to facilitate triangulation of the position of the cloud. The elevation and azimuth of the scanning mirror at each station are calculated corresponding to the

position of the release point (known from the trajectory of the rocket). The mirrors are set at these pre-determined positions.

Calibration of the position of the scanning mirror:- The initial setting of the azimuth of the scanning mirror is made by fixing the geographic north (approximated to be equal to geomagnetic north) by means of a magnetic compass needle. The azimuth, thus determined is generally in error which cannot be overlooked. Therefore, calibration of the mirror position is needed which can be done by scanning an object whose celestial coordinates are known at a known time in a day. Moon is a possible object. To achieve greater accuracies, we have adopted a slightly different method. Photographic frames are inserted at the focal plane of the lens T (as in Fig. III.1) and the star pictures are taken without disturbing the initial set-up made for the scanning of the cloud. This is done before or after the experiment during the twilight or nighttime. Four pictures are taken, one at each of the four extremities of the scanning mirror. From the known star positions on the photographs, the position of each of the extremities of the mirror can be computed to a great accuracy.

Tuning of interference filters:- Any change in temperature changes in turn the wavelength of the peak transmission of a filter. The bandwidth and the amplitude of transmission of the filter are, however, not changed. The temperature coefficient for most interference filters as found by

BLIFFORD (1966) is between +0.1 to 0.3Å/°C. Also, the wavelength of the peak transmission is changed by a slight tilt, θ, in the path of the light beam incident on the filter from the normal. The relationship between the change in the wavelength of peak transmission and the angle of incidence is given by (for example, BEDINGER, 1973).

$$\frac{\Delta\lambda}{\lambda} = \frac{1}{2}\frac{\theta^2}{\mu^2} \qquad (1)$$

where μ is the refractive index of the layer thickness in the filter. The layers used generally in interference filters are of cryolite ($\mu = 1.35$) and zinc sulphide ($\mu = 2.25$). Since in our equipment there is no temperature control, we tune the filters one hour prior to the experiment (launch time) by allowing light from a lithium discharge lamp to pass through the filters through the whole optical set-up and adjust the gain at each pre-amplifier to the maximum. This can be achieved by tilting the filter slightly. Mechanical arrangements are provided for such adjustments. The spectral composition of the sky brightness changes drastically in a day. It is, therefore, necessary to balance the system before the commencement of the experiment. During the experiment, we can safely assume that the balance is undisturbed. One of the two filters is tuned to Lithium emission line 6708Å with background light within the bandwidth, to get maximum gain at its pre-amplifier output; while the other filter is

tuned slightly off the line 6708Å (for example to 6713Å), to correct for the background. Balancing is achieved by keeping the gain of the difference amplifier at its maximum and adjusting the pre-amplifier gains till the output is zero This adjustment is made so that at any rate the pre-amplifiers do not go to saturation. After achieving the balancing, the gain of the difference amplifier can be adjusted at will to obtain a signal of desirable amplitude in the presence of lithium source. Care is taken so as to see that the output of the difference amplifier is not negative since the A/D converter rejects negative signals.

The equipments are put to operation around one minute before the release time of the vapour cloud. As it is difficult to change the position of the mirror to get the cloud into its field of view (if it is not already), it is very essential that the rocket trajectory be known accurately. The mal-functioning of the rocket, as for example, its failure to reach the predicted apogee, may lead to the failure of the experiment. Nevertheless, since the field of view of the mirror is quite large, slight changes in the path of the rocket are tolerable.

III.3 Analysis of the data:

Position of the Scanning Mirror:- One of the prerequisites for the analysis of the data is the initial position of the scanning mirror. Let us call the initial elevation of the mirror, E_o and the initial azimuthal angle A'_o. The

mirror sweeps a range of 15° between $E_o + 7^{\circ}.5$ to $E_o - 7^{\circ}.5$ in elevation and a range of 15° between $A'_o + 7^{\circ}.5$ to $A'_o - 7^{\circ}.5$ in azimuthal (not the conventional azimuth) angle. Thus, essentially the mirror scans a field of view in the sky of 30° in elevation and 30° in azimuthal angle. The actual azimuth angle of the mirror corresponding to any azimuthal angle is a function of elevation angle also. Fig. III.4 shows the relationship between the 'azimuthal angle' and the 'azimuth angle'. Azimuthal angle is the one that the scanner sweeps in a plane which makes an angle E (the elevation) with the horizontal plane. Therefore, it is a function of elevatio Azimuth angle is the projection of the azimuthal angle on the horizontal plane and is reckoned as the conventional azimuth, measured from north towards east. In Fig. III.4, the plane XX'Y'Y is the horizontal plane and the plane XX'Z'Z is the plane perpendicular to the scanning mirror and it makes an angle E with the horizontal plane. Let us suppose that OP represents the mean position of the azimuthal scan and A' is the angle swept at any particular time. QS is the perpendicular dropped on to the horizontal plane. Now the angle TOS = A is azimuth angle.

In $\triangle$ ORQ, OR = OQ Sin A' and, OR = TS = OQ Sin A'

In $\triangle$ OTS, OT = OQ Cos A' Cos E and $\frac{TS}{OT}$ = tan A

i.e., $$\tan A = \frac{\tan A'}{\text{Cos } E} \qquad (2)$$

It can be inferred easily from the above equation that the field of view covered by the mirror is in the form

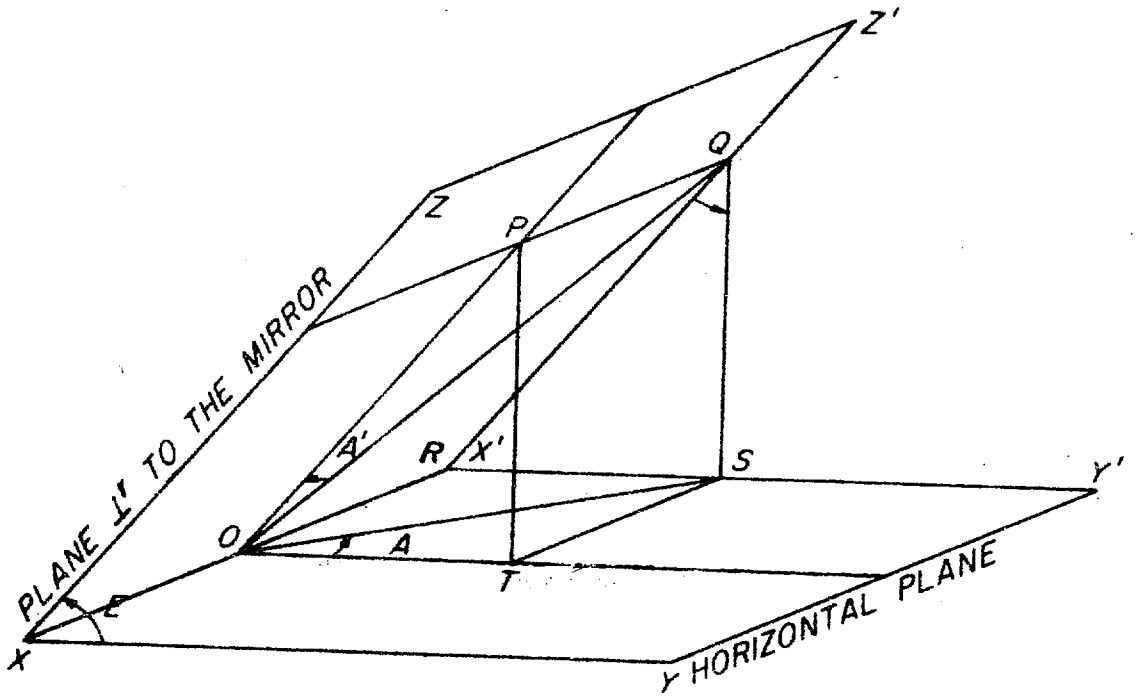

Fig.III.4:- The relationship between the azimuthal angle (A') and the conventional azimuth (A). The azimuth A is measured clockwise from north.

of a trapezium with its narrow side towards the lowest elevation angle.

Analysis of the chart recorder:- The time marks are given o the chart recorder horizontally at every one second. As has already been mentioned the azimuthal sweep (from left to right or right to left of the mirror) is at a rate of one per second and elevation sweep is at a rate of one per 30 seconds (from 'top' to 'bottom'). The actual time of occurrence of the peak (corresponding to the maximum cloud intensity) of the signal can be known from the chart and let it be t seconds (after the release of the cloud). If the initia mean elevation is E_o, then the top most (highest)elevation is $E_T = E_o + 15^o$ and the bottom most (lowest) elevation is $E_B = E_o - 15^o$. E_T and E_B are obtained by the star calibration directly. Now the elevation of the cloud at time t , is computed as follows:

$$E = E_T - \frac{30\ t}{T_o} \quad \text{or} \quad E_B + \frac{30\ t}{T_o} \qquad (3)$$

where T_o is the time taken for a single elevation scan (from top to bottom or vice versa). $T_o = 30\ t_o$, where t_o is the time taken for a single azimuth scan. Generally t_o is one second.

Similarly, the azimuthal angle A' of the centre of the cloud at any time, is given by

$$A' = A'_L - \frac{30\ t'}{t_o} \quad \text{or} \quad A'_R + \frac{30\ t'}{t_o} \qquad (4)$$

where A'_L and A'_R are azimuthal angles when the mirror is at extreme left and at extreme right respectively. t' is the

time taken to reach at the particular position in azimuthal angle from the time it started for a left-to-right or right-to-left scan. The azimuthal angle can be converted to actual azimuth using the eqn. (2). The position of the point of maximum intensity of the cloud is plotted with time in elevation and azimuth. Generally, the plot would yield a straight line. The data from two stations will give the cloud position in (x, y, z) coordinates by the usual method of triangulation (as discussed in Chapter II).

Analysis of digital tapes:- The analog tapes recorded are decoded by means of the PCM decoding unit shown in Fig.III.3. The 2 kilo bits/sec bi-phase data from the analog tape are made into 8 words of 8 bits each in a horizontal frame and recorded on digital tapes - which are computer compatible. The method of analysis is same as the one described in the case of chart data. A computer programme is written and tested which searches the maximum intensity point and computes the spatial coordinates of the cloud. Once the coordinates are known the calculation of the position of any point on the cloud is computed by the usual triangulation method.

Errors and accuracy:- Sources of errors can be several and unless one takes immense care of rectifying them, the results would be in great error. Firstly, the calibration of the mirror position is very important. The azimuth and elevation of the extremities of the mirror should be known accurate upto 1^{o}. Any error in this leads to corresponding error in

the azimuth and elevation of the point on cloud.

The instrumental resolution is 1^{o} in the field of view. This is adjusted before-hand by setting the width of the aperture A properly. The relationship between the width of the aperture and the angle that the aperture allows on to the collimator is given by,

$$\theta(\text{radians}) = \frac{d}{f} \qquad (5)$$

where d is the width of the aperture and f is the focal length of the lens T. The aperture can be set accurately upto about 1 or 2 mm and the error due to this is not significant, since the focal length f of the lens T is very large compared to the width of the aperture.

In the case of the analysis with chart recorder data, reading errors will be unavoidable. The chart speed is adjusted at $\simeq$ 5 cm/sec. This is chosen on the basis of length of paper in a roll and the useful time of recording. In the case of an azimuthal scan, the angle covered in azimuthal direction is around 30^{o}. And a reading error of 1 mm will lead to an error of about $0^{o}.6$ in the azimuthal angle. Similarly in the case of the elevation angle there will be an error of the same magnitude. These reading errors may lead to an error of a few m/s in the velocity of the cloud. The reading errors can be very much minimised in the analysis using the digital computer compatible tapes.

The maximum error is estimated to be of the order of about 10-12 m/s in the computed velocity of the cloud, in the present analysis.

III.4 Results obtained from lithium and barium vapour clouds:

Two lithium point clouds were released at 122 km and at 140 km altitudes by an Indian Centaur rocket during the morning twilight of 19 April, 1976. The reason for conducting the experiment in the twilight is to test the payloads of lithium, their mechanical configuration for release of more than one cloud at pre-determined timings and the performance of the timers as well. The arrangement of payloads and the timers in the rocket body are shown in Fig. III.5. By observing the clouds visually, which is possible only if released in the twilight conditions, we made sure that the payloads and the timers worked satisfactorily. In addition to the two lithium clouds, two barium clouds were also released at altitudes 130 km and 138 km. Since the barium clouds were at altitudes lower than 150 km, they did not show perceptible ionization in them. Lithium clouds were tracked by the equipment described earlier and also photographed by Hasselblad cameras loaded with high speed Kodak 2485 red sensitive film. The barium clouds were photographed by K-24 cameras. The data obtained by the cameras as well as the chart recorders have been analysed to find the cloud velocities.

The results obtained from the photometric and photographic trackings of the releases are in quite good agreement; although the errors in the former case are slightly larger than those in the latter case. Figs. III.6 and III.7 show

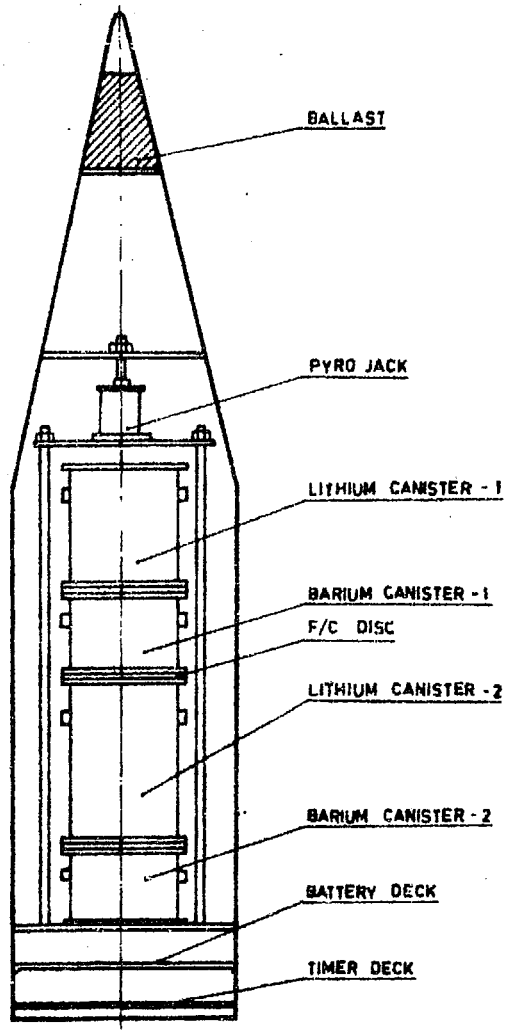

Fig.III.5:- Lithium-barium payload configuration for multiple releases in the body of a rocket (Indian Centaur). The positions of the canisters and timers are shown. This configuration has successfully been used and tested on the morning twilight of 19 April, 1976 at THUMBA.

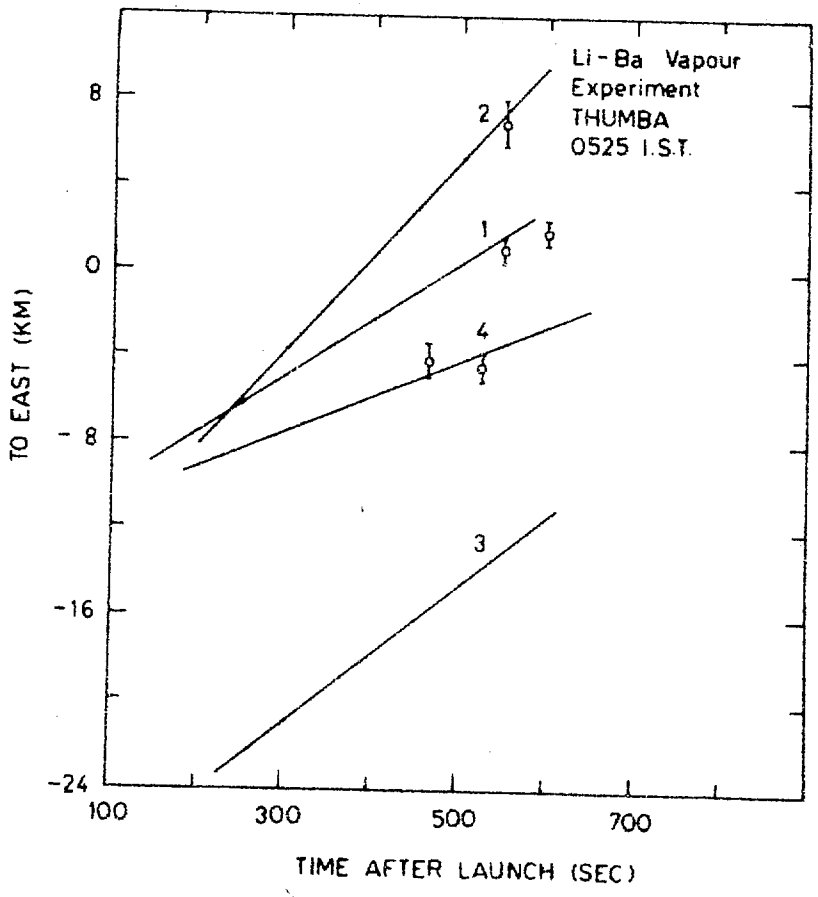

Fig.III.6:- East-west displacement of the lithium-barium clouds. The numbers 1 and 4 correspond to the lithium releases at altitudes 122 abd 140 km respectively. 2 and 3 correspond to the barium clouds released at altitudes 130 and 138 km respectively. Only a few observed points with error bars are shown in the figure.

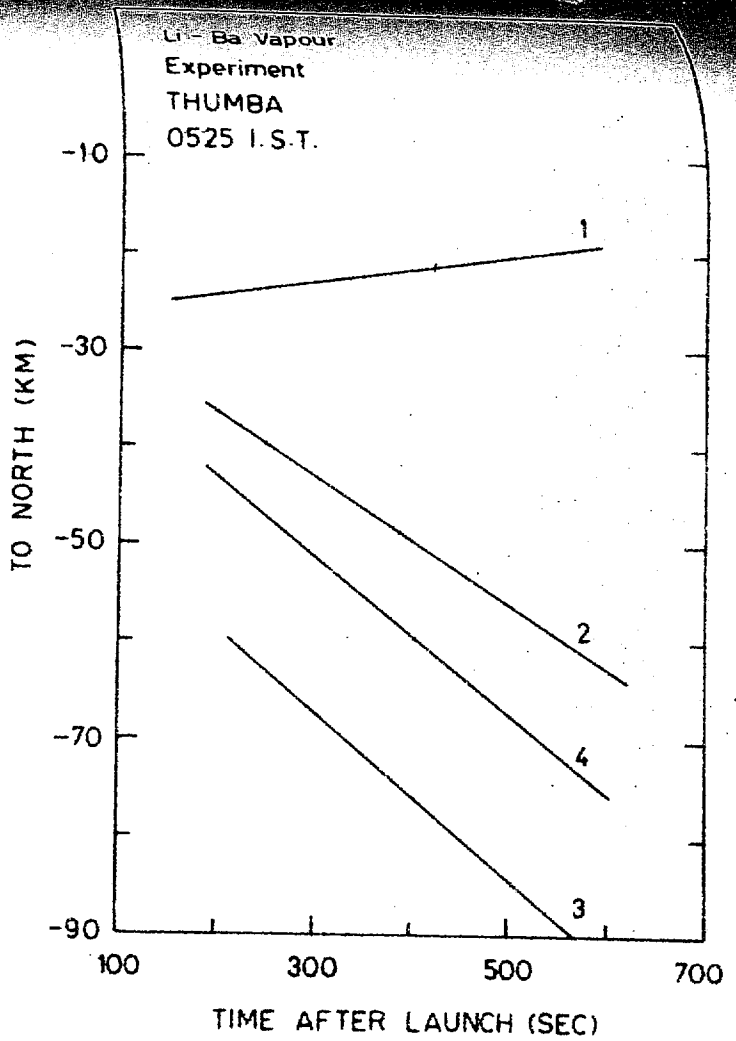

Fig.III.7:- North-south displacement of the lithium-barium clouds. Here the observation points are not shown.

the east-west and north-south displacements of the clouds. The releases 1 and 4 are lithium clouds and 2 and 3 denote the barium clouds. In the case of lithium clouds the positions shown are obtained by averaging the results of the photometric and photographic analyses. Fig. III.8 shows the altitude variation of the zonal (eastward) and meridional (northward) components of the neutral winds in the region 120-140 km. The figure shows a strong north-south wind shear of magnitude $\simeq$ 8 m/s/km at an altitude of 125 km. In general, the north-south winds are stronger than the east-west winds. No appreciable vertical component of the neutral wind velocity is noticed.

III.5 Summary:

The data on winds at low latitudes are meagre; and more so in the daytime. With the development of the daytime lithium cloud tracking equipment and the lithium payloads it is now possible to conduct experiments to find the wind velocities during the day-light hours. As there are theories regarding the possible relationship between vertical winds and the counter electrojet (RAGHAVARAO, 1976) it is now possible to put these theories to test, by measuring winds on days when counter electrojet is in progress and compare with winds when the counter electrojet is not present (as can be observed on the ground magnetometer). The vertical winds of the order of 10 m/s and sometimes as large as 20 m/s

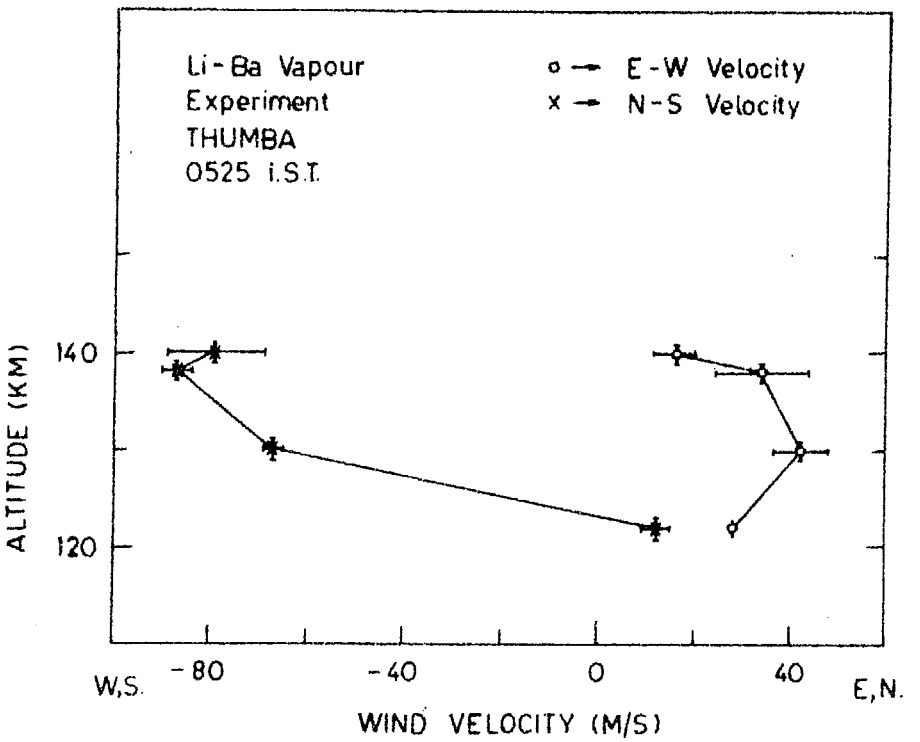

Fig.III.8:- The east-west (circles) and north-south (crosses) components of the neutral winds at 0525 IST on 19 April, 1976.

are observed (ANANDARAO ET AL, 1977b). From the theoretical investigations made by the author on the effect of vertical winds on the electrojet described in Chapter VI, it appears that the vertical (upward) wind of magnitude 20-25 m/s can produce the observed counter electrojet. The equipment used to measure the vertical winds should have error less than 10 m/s in determining the vertical wind. The reason for obtaining considerable error (10 - 12 m/s) in this first attempt described here is that the clouds released contained substantial lithium to saturate the amplifiers used in the experiment. Necessary precautions are being taken for the experiments planned in December 1977 - January 1978 to measure winds as part of the investigations on the cause of the counter electrojet.

CHAPTER IV

ELECTRIC FIELDS IN THE EQUATORIAL IONOSPHERE

IV.1 Introduction

The ionospheric wind systems in mid-latitudes produce electric fields by the dynamo action (HIRONO, 1950; BAKER AND MARTYN, 1953; MAEDA, 1955, 1968; KATO, 1956; MATSUSHITA, 1967; STENING, 1969, 1971; TARPLEY, 1970 a, b; VOLLAND, 1971 a, b). It is thought that the diurnal winds are probably the main contributor to the currents and fields. Recent observations of the winds in the daytime E region showed that the winds are predominantly semidiurnal and that the amplitude of any diurnal component seems to be substantially smaller than that inferred from the dynamo theory. Observations of the electric fields (EVANS, 1972; BEHNKE AND HARPER, 1973; TAYLOR, 1974; BEHNKE AND HAGFORS, 1974; KIRCHHOFF AND CARPENTER, 1975 etc.) are also not in agreement with the theoretical models. MATSUSHITA (1971, 1972) suggested that the primary source of quiet-day ionospheric currents and fields may not be ionospheric winds, but rather magnetospheric convection driven by the solar wind. More recently, RICHMOND ET AL (1976) have reviewed the dynamo theory and have shown that the winds can probably explain the observed middle and low latitude electric fields, if one takes into account the uncertainties in wind pattern and the observed $\underline{E} \times \underline{B}$ drifts. These authors have also concluded that the primary cause of the observed day-to-day variability of electric field on quiet days is probably

the variability in the E region winds. Furthermore, the magnetospheric sources are only of secondary importance for quiet day ionospheric electric fields at mid and low latitudes, atleast during day time.

The primary east-west electrostatic field at the equator is part of the global field distribution which is produced by charge distribution resulting from the global tidal dynamo electromotive force ($\underline{W} \times \underline{B}$) where $\underline{W}$ is the wind velocity and $\underline{B}$ is the geomagnetic field. The east-west field at the equator, produces vertical polarization fields mainly in the E region where the ion-neutral collision frequency is higher than the ion-gyrofrequency which leads to a differential motion between ions and electrons. These polarization fields modify in turn the currents in the horizontal direction. In the vicinity of the dip equator, the primary electric field drives the electrojet current. It is very important to measure the electric fields as these measurements will help in understanding the phenomena like the electrojet, besides knowing the extent of their origin due to winds.

In the early days, the fields have been deduced from the ground magnetic variations (MAEDA, 1955; AXFORD AND HINES, 1961). These results are in great error, naturally because of many an assumption involved in deducing the electric fields. With the advent of sounding rockets and satellites, in the

recent years, in situ measurements of electric fields are made possible. Besides these rocket-borne probes, there are a few ground-based techniques which are also providing invaluable data on the electric fields with great accuracy.

The techniques that are generally employed to measure the d.c electric fields can be devided into two groups.

(i) The techniques under the Group I measure the electric field directly by measuring the potential difference between two electrodes immersed in the ionospheric plasma. These probes are flown on-board a rocket or a satellite into the region in question.

(ii) The techniques under Group II measure the drift velocity of the ionization which is related to the electric field. Thus these are indirect techniques for measuring the electric field. These are generally ground-based; except the barium vapour cloud release technique which involves the usage of space vehicles, like rockets and satellites. However, the tracking of the cloud is done from ground. We discuss here briefly the various techniques for the measurement of the electric fields. The barium vapour cloud release technique which is used by the author is discussed in detail in section 2 of this chapter.

IV.1.1 Group I: Direct measurement of the ionospheric electric fields:

The first attempts to measure the electric field in space was made by GDALEVICH (1964) and IMYANITOV ET AL (1964) by using electrostatic flux meter. However, their measurements

are erroneous and the interpretation is rather doubtful. KAVADAS AND JOHNSON (1964) achieved partial success by measuring the potential difference between two closely spaced electrodes mounted on a rocket. In view of the lack of symmetry in the positioning of the electrodes and also due to their close proximity, the interpretation of their data has many shortcomings. Later, this technique was improved by the development of the double floating probe technique which employs two symmetrical sensors, either spherical (MOZER AND BRUSTON, 1967) or cylindrical (AGGSON AND HEPPNER, 1965) in shape. These sensors are separated by a large distance from each other and placed at a distance from the body of the vehicle.

The potential acquired by a conductor (sensor) with respect to the (ionospheric) plasma in which it is immersed is a function of the properties of the plasma, like the electron temperature, ion and electron currents. To a good approximation, the potential difference between the two sensors (when they are not drawing any current) is proportional to the potential difference in the ionospheric plasma. Because of the presence of the geomagnetic field, there will be induced fields which affect the potential difference, due to the motion of the vehicle viz. $\underline{W}_s \times \underline{B}$ field ($\underline{W}_s$ is the velocity of the vehicle and $\underline{B}$, the geomagnetic field). It is possible to write the equation relating the potential difference of the sensors and the ionospheric fields as

(BOYD, 1967),

$$(V_a - V_s) - (V_b - V_s) = (\underline{E} + \underline{W}_s \times \underline{B}) \cdot \underline{d}$$

$$\therefore \quad V_a - V_b = (\underline{E} + \underline{W}_s \times \underline{B}) \cdot \underline{d}$$

where V_a, V_b and V_s are the potentials of sensor 'a', sensor 'b', and the space vehicle with respect to the background plasma. $\underline{d}$ is the distance between the midpoints of the sensors. Since quantities V_a, V_b, $\underline{W}_s$, $\underline{B}$ are generally known, the electric field $\underline{E}$ can be computed.

The double probe technique is now a fairly well established one, although it has certain shortcomings. Generally, the term $(\underline{W}_s \times \underline{B})$ is of the order of/or even greater than the ambient d.c. electric field. Therefore, the accuracy with which the technique can measure the electric fields depends upon how accurately is $\underline{W}_s$ known. In the auroral region where the fields are of the order of a few tens of millivolt/m, this technique is proved to be reasonably accurate (AGGSON, 1969; MOZER, 1971). SARTIEL (1972) has used this technique to measure the electric field over the dip equator (Thumba) and observed abnormally large values at and above 120 km altitude.

In addition to the uncertainty involved in knowing $\underline{W}_s$ accurately, there are other uncertainties. For example, the floating potentials V_a and V_b are functions of the plasma parameters which/are affected sometimes by the photo-emission resulting from interaction of the solar radiation

with the surface of the vehicle and secondary electron emission from the bombardment of the energetic particles on the surface. Thus, the potentials depend upon the quality of the surfaces of the sensors also. It has been found that it is of great value to use identically shaped sensors made of materials with uniform work function, placed symmetrically about the vehicle (BAUER AND NAGY, 1975).

IV.1.2 Group II: Indirect techniques for measuring the ionospheric electric fields:

The indirect techniques involve the measurement of the drift velocity of the charged particles in the presence of the ionospheric electric ($\underline{E}$) and magnetic ($\underline{B}$) fields. In a collision-less plasma, the drift velocity $\underline{V}_d$, of the ionisation is given by

$$\underline{V}_d = \frac{\underline{E} \times \underline{B}}{B^2}$$

Using this relation, the electric field can be computed since $\underline{V}_d$ is measured and $\underline{B}$ is known. To a first order approximation, these results are in good agreement with the in situ measurements.

IV.1.2.1 VHF radar measurements:

This is a ground based technique and thus a remote sensing technique.

When a radio wave is transmitted, it gets reflected due to the collective behaviour of the electrons in the ionosphere if the ambient plasma frequency matches with the probing radio wave frequency. In the presence of an irregularity in the electron density distribution in a

certain region of the ionosphere, a high frequency wave (high compared to the ambient plasma frequency) gets scattered by the irregularity. The echo received at ground in this case is weaker than that in the case of reflection. The scattering occurs when the wavelength of the probing radio wave is equal to the size of the irregularity. A third kind of echo which is still weaker occurs due to the scattering from individual electrons, known as Thomson scattering or incoherent scattering. The power returned in this case is directly proportional to the electron concentration.

GORDON (1958) discussed the process of incoherent scatter in the ionosphere. He concluded that the incoherent scattering occurs if the electron mean free path exceeds the probing radio wavelength and the scale size of the irregularities. These conditions are valid at meter wavelengths at altitudes above about 100 km.

Ionosphere is known to contain irregularities of various scale sizes embedded in the background ionization. There exists a number of small scale (compared to the ambient ionization scale heights) irregularities in the ionosphere at almost every level. Detection of the irregularities is possible by their ability to scatter the radio waves. Since the irregularities are drifting because of the $\underline{E} \times \underline{B}$ force, measurement of the Doppler shift in the

frequency of the scattered echoes gives information regarding the drift velocity.

BAILSLEY (1965, 1969b) and CARRU ET AL (1967) measured the Doppler shift in the frequency of echoes received by a very high frequency (VHF) radar and deduced the electron drift velocities in the ionospheric E and F regions respectively, whereas the previous workers (BOWLES, 1960; BOWLES AND COHEN, 1962; COHEN AND BOWLES, 1963a) used the VHF radar technique to measure the intensity of the irregularities only. BAILSLEY AND WOODMAN (1971) have derived an empirical relationship between the measured east-west drift velocity of electrons and the east-west electric field based on the observations at Jicamarca,

$$E_x \simeq -6 \times 10^{-6} V_e$$

where V_e is the electron drift velocity in m/s and E_x, the electric field in V/m, both measured in the eastward direction.

The results of electric field measurements obtained over the years in the equatorial region have recently been reviewed by BAILSLEY (1973). This techique has also been used at mid latitudes by EVANS (1972), BEHNKE AND HAGFORS (1974), BEHNKE AND HARPER (1973), TAYLOR (1974) and KIRCHHOFF AND CARPENTER, (1975).

WOODMAN AND HAGFORS (1969) have measured the vertical drifts in the F region by the measurement of Doppler shift in the frequency of echo returned by the (incoherent scattering

electrons. Under this condition, the spectral width of the incoherently scattered signal is sufficiently narrow to determine the vertical component V_z of the plasma drift. WOODMAN (1970) has shown that the eastward electric field, E_x in the F-region is related to the vertically upward drift velocity, V_z (based on the observations) as follows,

$$E_x \simeq 2.5 \times 10^{-5} V_z$$

where E_x and V_z are measured in V/m and m/s respectively.

WOODMAN (1972) has also measured the east-west plasma drift velocity as a function of local time in the F-region which agrees fairly well with the theoretical profile of MAEDA (1963).

IV.1.2.2 Fading method of measuring the drift of the ionizatic

MITRA (1949) suggested a technique to measure the drift velocity of irregularities in the ionosphere. The technique uses a transmitter operating at high frequency (a few megahertz) and three receivers, forming triangle (the apexes of which are about one wavelength apart) to record the amplitude fluctuations (fadings) of the received signal from the ionosphere. The 'fading' in the amplitude is usually attributed to the presence of the irregularities situated near the height of reflection. By choosing suitable radio frequencies, it is possible to study the motion of the irregularities in the daytime E layer and

nighttime E_s layer and the F-region (BRIGGS ET AL, 1950; BRIGGS AND SPENCER, 1954; PHILLIPS AND SPENCER, 1955; SHIMAZAKI, 1959; RAO AND RAO, 1960; BOWHILL, 1961; BRIGGS, 1962; RAWER, 1963, etc.).

There has been much discussion regarding the interpretation of the results from these experiments as to, (i) whether the measured drifts represent the real motions of the ambient plasma, and (ii) what is the role of neutral motions in affecting the drifts? CLEMMOW AND JOHNSON (1959) and KATO (1965) have shown that a field aligned irregularitiy moves under the influence of an electric field. In the E region the neutral winds and ionization drifts are related, whereas in the F region, because the ion-neutral collisions are negligible, the neutral winds do not have any effect on the ionization drifts. BAILSLEY (1973) has compared the VHF radar observations of the drift velocities (averaged seasonally) at Jicamarca with the seasonally averaged drift velocity measurements obtained (MISRA AND RASTOGI, 1971) by the spaced receiver technique at Thumba. He found a general agreement of the drift direction, albeit there are difficulties in the interpretation of the drift experiment results (HINES AND RAGHAVARAO, 1968; FEDOR AND PLYWASKI, 1972). Magnitudes are, however, found to be different. This difference may be attributed to the longitude difference of the stations chosen for conducting the two experiments.

Hitherto, we have discussed various techniques for measuring the ionospheric electric fields. We now describe (in IV.2) the technique of barium cloud release for measuring the electric fields. In IV.3 the results obtained from the barium cloud release experiments conducted at TERLS (Thumba) are presented and compared with the earlier observations made at the dip equator. The electric field model as described by the self-consistent models of the equatorial electrojet is discussed in IV.4 in order to interpret the experimental results. We conclude the Chapter by summarising the important results of the investigation in IV.5.

IV.2 The technique of artificial vapour release in the upper atmosphere:

BIERMANN (1957) deduced the solar wind parameters from the ionized cometary tails which point almost radially away from the sun. Thus the ionized cometary tails can be used as natural probes of the solar wind. Later, it was proposed to use artificial plasma clouds to probe the space, since comets are rare events and cometary ions (generally CO^+ and N_2^+) have low oscillator strengths in the visible band systems.

BATES (1950) suggested that optical tracking of artificial vapour contaminants ejected from the rockets could yield valuable information about the upper atmospheric

parameters. He discussed both the nighttime and twilight phenomena which can be observed when sodium vapour is released. On one hand the technique of these artificial vapour releases is being used to measure the atmospheric winds which is discussed in detail in Chapter II, while on the other hand, the measurement of electric fields is possible by this, using appropriate elements which can be ionised by solar UV radiation.

A material (either in atomic or molecular form) in the upper atmosphere should have the following characteristics (i) the resonance lines of the ions of the elements must be in the visible range in order to be seen and photographed during twilight, (ii) the time scales for excitation of the resonance lines of ions and the time scales for the photoionization of the neutral atoms by the solar radiation must be sufficiently short and (iii) since a chemical technique for the release is to be used, the evaporation temperature of the element should be as low as possible.

For the reasons mentioned above, the promising elements are Caesium (Cs), Barium (Ba), Europium (Eu) and Ytterbium (Yb). These elements have resonance lines in the visible spectrum both for the neutral and the ionized atoms. The required quantity of the vapour to be released is low and well within the limits of the normal payload weight of a sounding rocket. The photoionization efficiencies are high for these elements. The solar radiation (in UV and EUV)

is sufficient to ionize the atoms when one of them like Ba is released in the vapour form.

FOPPL ET AL (1965, 1967), in West Germany, were the first to develop the technique of making the barium vapour payload and later such payloads were developed in different countries including India (COMMEN ET AL, 1976).

The barium vapour cloud can be generated by (i) utilising the exothermicity of the reaction between part of barium and a suitable oxidizer (CuO) to vaporise the rest and (ii) converting the entire quantity of barium into vapour through a shock wave produced by detonation of a high explosive (shaped charge technique). The first method follows according to the chemical reaction

$$(n + 1)\ Ba + CuO = BaO + nBa\ (vapour) + Cu$$

There are several other types of reactions, but the reaction given above seems to be the most efficient one (HASER, 1967; FOPPL ET AL, 1967). The reaction is exothermic and the heat thus released vaporizesa considerable part of the excess barium. The heat released in the reaction is ≈ 96.3 K cal/gm mole at $25^{\circ}C$. Cupric oxide is chosen as the oxidizer because of its low heat of formation ($\simeq 37.1$ K cal/gm mole) and thus gives more exothermicity. The rate at which the reaction proceeds can be controlled by the use of a binder in which the chemicals are imbedded. The mixtures are pressed into steel containers (canisters) equipped with timers and igniting devices. The size, weight

and shape of the canisters to be used for a release, depend upon the rocket used, number of releases required and the height of release. The above reaction gives about 10 to 20% efficiency - i.e. from the volatile barium about 10 - 20% barium atoms could be observed.

The barium vapour thus released in the ionosphere resonantly scatters the solar radiation at 5535Å. The intensity of neutral barium resonance line (5535Å) is found then to decrease with a time constant $\approx$100 seconds. This is due to the loss of barium atoms by any of the following processes. (i) Ionization by solar UV radiation. The typical time scale of ionization is $\approx$ 20 sec. The ionization occurs definitely above about 150 km. The whole of barium vapour gets ionized except the impurity like strontium which remains unionized and provides a visible (at 4607Å) neutral part of the cloud. (ii) Oxidation by the atmospheric Oxygen. This is important for the barium clouds released below about 150 km, where the rate of oxidation exceeds the rate of ionization of a barium atom. Thus below 150 km the lower the cloud is released, the lesser will be the ionization produced in it.

Using spectrographs with powerful optics (Camera f/0.75) and highly sensitive film together with greatly increased brightness , HASER (1967) studied the spectra of the neutral and ionized barium. He concluded that the ionization takes place in two steps (i) resonance absorption (5535Å) and subsequent population of a metastable level by spontaneous

transitions and (ii) photo-ionization by absorption of UV radiation (3266Å) in the metastable state (a one electron jump). Photo-ionisation of barium from the ground state seems to be less probable because it needs more energy (2380Å) and needs a two electron jump (HASER,1967).

A typical barium vapour release has two distinct phases. (i) The initial phase in which the barium vapour expands with a speed of about 1.2 km/sec until the vapour reaches equilibrium with the ambient atmosphere after a few seconds and (ii) diffusion phase in which further expansion of the cloud is governed by the process of diffusion. The ionization process sets in during the transition phase of the cloud from the initial rapid (thermal) expansion to the diffusion dominated expansion.

The experiment is performed in the twilight period (dawn or dusk) only. During the twilight period the solar radiation is still present at the ionospheric heights and some of the bright stars are visible in the sky. Thus it is possible to photograph the vapour clouds during the twilight against a star back-ground which serves as a reference frame to compute the position of the clouds. During the nighttime, the ionisation of the barium vapour is not possible because of the absence of direct solar radiation. The clouds can not be seen with naked eye against a very bright background sky in the daytime; and only with spectrophotometers of very high resolution it is possible

to detect the clouds. The technique of detecting Lithium (neutral) clouds during the daytime is discussed in Chapter III. So far the barium (ion) clouds are not released and tracked during the daytime because of the complications involved in detecting the cloud. Thus the barium cloud experiment for measuring the electric fields is limited to only twilight periods.

IV.2.1 Observation technique:

The barium vapour clouds are tracked by means of ground-based cameras fitted with appropriate wideband optical filters to improve the photographic resolution. The K-24 aerial cameras loaded with KODAK TRI-X or 2498 high speed film are employed to track the clouds photographically. The vapour clouds are photographed simultaneously from two or more ground stations. 3 to 5 exposures of short-duration (3 to 10 sec) per minute in the initial stage of the release and 2 to 3 exposures of long-duration (10 to 20 sec) in the later stages are taken. The position of the centre of the cloud is computed by the method of triangulation described in Chapter II.

As has been mentioned already, the strontium (Sr) impurity in the barium mixture provides a visible neutral cloud. At and above about 150 km (where the barium-strontium clouds are released usually), the neutral motions do not govern the motion of the ionization completely ($\because \nu_i \leq \omega_i$).

Therefore, usually the cigar-shaped ion (Ba) cloud and the spherical neutral (Sr) cloud are separated from each other. The determination of ion drift velocity as well as the neutral wind velocity is thus possible.

The theory of electric field measurement due to HAERENDEL ET AL (1967) is discussed in the following section. This enables us to compute the electric fields from the observed ion drift velocity and the neutral wind motion.

IV.2.2 Theory of electric field measurement:

HAERENDEL ET AL (1967) developed a theory for calculating the electric fields in the ionosphere from the drift motion of a cylindrical irregularity of ionization by taking appropriate models of magnetic field, neutral wind and the ionospheric conductivity. In what follows is given a brief description of their theory. The equation of motion of the charged particles can be written as

$$m_j N_j \frac{d\underline{V}_j}{dt} = -\nabla p_j + m_j N_j \underline{g} + N_j e_j \left[\underline{E} + \underline{V}_j \times \underline{B}\right] - \sum_{l=e,i} m_j N_j \nu_{jn} (\underline{V}_j - \underline{W}) \quad (1)$$

Here, m_j is mass; N_j, the number density; $\underline{V}_j$, the velocity; p_j, the pressure; e_j, the charge of electrons (j = e) and ions (j = i). $\underline{W}$ is the neutral wind velocity. $\underline{E}$ and $\underline{B}$ are the electric and magnetic fields respectively.

Under quasi-static conditions and for irregularities of dimension smaller than the atmospheric scale height, the above equation can be written as

$$0 = -\nabla P_j + N_j e_j \left[\underline{E} + \underline{V}_j \times \underline{B}\right] - \sum_{p=e,i} m_j N_j \nu_{jn} (\underline{V}_j - \underline{W}) \quad (2)$$

It is assumed further that the processes are isothermal, so that $T_e = T_i = \text{Constant } (T)$

$$P_j = N_j \, kT$$

Also, it is assumed that the charge neutrality is valid in the ionosphere (i.e., $N_i = N_e = N$) and the electric field is static.

Thus we have

$$\nabla \cdot \underline{J} = 0 \quad (3)$$

$$\nabla \times \underline{E} = 0 \quad (4)$$

Here $\underline{J}$ is the current density and $\underline{E}$ is the electrostatic field to be determined.

In a frame of reference which is moving along with the neutral particles with a velocity $\underline{W}$, the eqn. (2) can be written as

$$\underline{V}_j' + \frac{1}{R_j^2} \frac{\underline{B}}{B} \times \frac{\underline{V}_j' \times \underline{B}}{B} = \frac{1}{R_j} \underline{U}_j + \frac{1}{R_j^2} \frac{\underline{U}_j \times \underline{B}}{B} \quad (5)$$

where, $\underline{V}_j' = \underline{V}_j - \underline{W}$

and $R_j = \nu_{jn}/\omega_j$, ratio of the collision frequency of the charged particle with the neutrals to its gyrofrequency.

$j = e$, for electrons and $j = i$, for ions.

$$\underline{U}_j = \frac{1}{B} \left(\underline{E}' - \frac{kT}{e} \frac{\nabla N}{N} \right) \quad (6)$$

with $\underline{E}' = \underline{E} + \underline{W} \times \underline{B}$

The components of $\underline{V}_j'$ perpendicular and parallel to the magnetic field $\underline{B}$, are respectively,

$$\underline{V}'_{j\perp} = \frac{R_j}{1+R_j^2}\underline{U}_{j\perp} + \frac{1}{1+R_j^2}\frac{(\underline{U}_j \times \underline{B})_\perp}{B} \qquad (7)$$

and $\underline{V}'_{j\parallel} = \frac{1}{R_j}\underline{U}_{j\parallel}$

Due to the difference in the mobilities of ions and electrons, polarisation fields are set up within the inhomogeneity. $\frac{kT}{e}\frac{\nabla N}{N}$ represents the polarization field and is very small compared to the ionospheric electric fields.

The theory of motion of ionospheric irregularities, developed by MARTYN (1953), CLEMMOW ET AL (1955), DUNGEY (1958), KATO (1963, 1964) and many others, applies closely to the motion of the ion cloud in the ionosphere. These theories, however, deal with irregularities of infinite extent along the field lines in a homogeneous medium while the Ba ion cloud is an irregularity of finite extent, above the region of maximum Hall and Pedersen conductivities. DOUGHERTY (1959) has pointed out that the polarization field within the cloud can be short-circuited by the currents flowing along lines of force and closing in the E and F regions. Thus there is an abrupt change in the electric field at the boundary of the irregularity which is determined only by the ratio of integrated conductivity along the line of force through the cloud and out-side (BOSTROM, 1964; PIDDINGTON, 1964).

The ion cloud is represented by a homogeneous cylinder of finite length with electron density which is λ times the electron density of the ambient ionosphere. The parallel component of the electric field $\underline{E}$ is neglected in comparison with the perpendicular component, because the magnetic field lines are equipotentials.

The current $\underline{j}$ flowing in the inhomogeneity (the ion cloud) is written as

$$\underline{j} = [\Sigma] \cdot \underline{E} \tag{8}$$

where $[\Sigma]$ is the two-dimensional conductivity tensor obtained by disregarding σ_0, the parallel conductivity and integrating the Pedersen (σ_P) and the Hall (σ_H) conductivities along the magnetic field lines.

From the eqns. (7) and (8), the perpendicular component of the electric field can be shown to be

$$\underline{E}_\perp = \frac{B}{D}\left[a(\underline{V}_\perp - \underline{W}_\perp) + b\left(\frac{\underline{B}}{B} \times \underline{V}_\perp\right) + (b-D)\left(\underline{W}_\perp \times \frac{\underline{B}}{B}\right)\right] \tag{9}$$

where $D = a^2 + b^2$

with $a = \alpha\gamma - \beta\delta$

and $b = \alpha\delta + \beta\gamma$

The parameters α, β, γ and δ are given by

$$\alpha = \frac{2(1+\lambda^*)}{(1+\lambda^*)^2 + (1-\xi)^2\zeta^2} \quad ; \quad \beta = \frac{2(\xi-1)\zeta}{(1+\lambda^*)^2 + (1-\xi)^2\zeta^2}$$

$$\gamma = \frac{R_i}{1+R_i^2}\,\frac{\lambda-\lambda^*}{\lambda-1} \quad ; \quad \delta = \frac{R_i}{1+R_i^2}\left(\frac{1}{R_i} + \frac{\xi-1}{\lambda-1}\,\zeta\right)$$

with $\lambda^* = \Sigma_{P_C}/\Sigma_{P_I}$; $\zeta = \Sigma_{H_C}/\Sigma_{H_I}$; $\xi = \Sigma_{H_C}/\Sigma_{P_I}$

σ_P and σ_H are the integrated Pedersen and Hall conductivities along the field lines. C and I denote the cloud and the ionosphere.

For altitudes above about 150 km, $R_i \ll 1$ and the eqn. (9) can be simplified (HAERENDEL ET AL, 1967) as

$$\underline{E}_\perp \approx \frac{1+\lambda^*}{2}\left[\underline{B}\times\underline{V}_\perp + R_i(\underline{V}_\perp - \underline{W}) + \frac{\lambda^*-1}{\lambda^*+1}\,\underline{W}_\perp \times \underline{B}\right] \quad (10)$$

Thus the theory demands, in addition to the velocity of the ion cloud, the measurement of the neutral winds and the electron densities inside and outside the cloud.

The theory formulated by HAERENDEL ET AL (1967) is applicable to the F region of the ionosphere where the inequality $R_i \ll 1$ holds good. For E region altitudes, however, the theory becomes complicated involving many parameters, the values for some of which are difficult to obtain. In practice, therefore, the electric fields in the E region cannot be obtained by the above theory.

GILES AND MARTELLI (1971) have applied the theory of motion and structure of inhomogeneities in a magnetoactive plasma, developed by GUREVICH AND TSEDILINA (1966, 1967), to the barium plasma cloud. GILES AND MARTELLI (1971) identified three distinct features of the clouds, one, two or all the three of which are seen generally in the actual releases

(WESCOTT ET AL, 1969; GILES ET AL, 1970);(i) the neutral part of the cloud, (ii) ionized cloud which is field-aligned and (iii) another part of the ionized cloud which expands in a direction perpendicular to the magnetic field. The neutral cloud generally gets separated from the ion cloud unless the ion-neutral collisions are predominant, as in the case of E region. The breaking up of ion cloud into two 'maxima' - one along the field line and the other perpendicular to it - also is rarely seen. Furthermore, the barium cloud released in the E region ($\lesssim$ 150 km) gets oxidized quickly, because the oxidation time scales are shorter than those of ionization (HASER, 1967).

IV.3 Results:

Two barium-strontium clouds were released from TERLS, at an altitude of $\sim$ 155 km on the 4 and 7 Jan. 1972 (hereafter referred to as flights 1 and 3 respectively). A third barium cloud (flight 2) released at $\sim$ 126 km on the 6 Jan.,1972 did not get ionized and the the neutral wind velocities obtained from the release are reported already in Chapter II. By applying the method of triangulation the positions of the ionized barium and the neutral strontium clouds are calculated. The details of the method of triangulation and the nature of the errors involved in the analysis are discussed earlier (in Chapter II). Figs. IV.1, IV.2 and IV.3 show the eastward, the northward and the vertical displacement of the clouds (flights 1 and 3) with time. From these plots

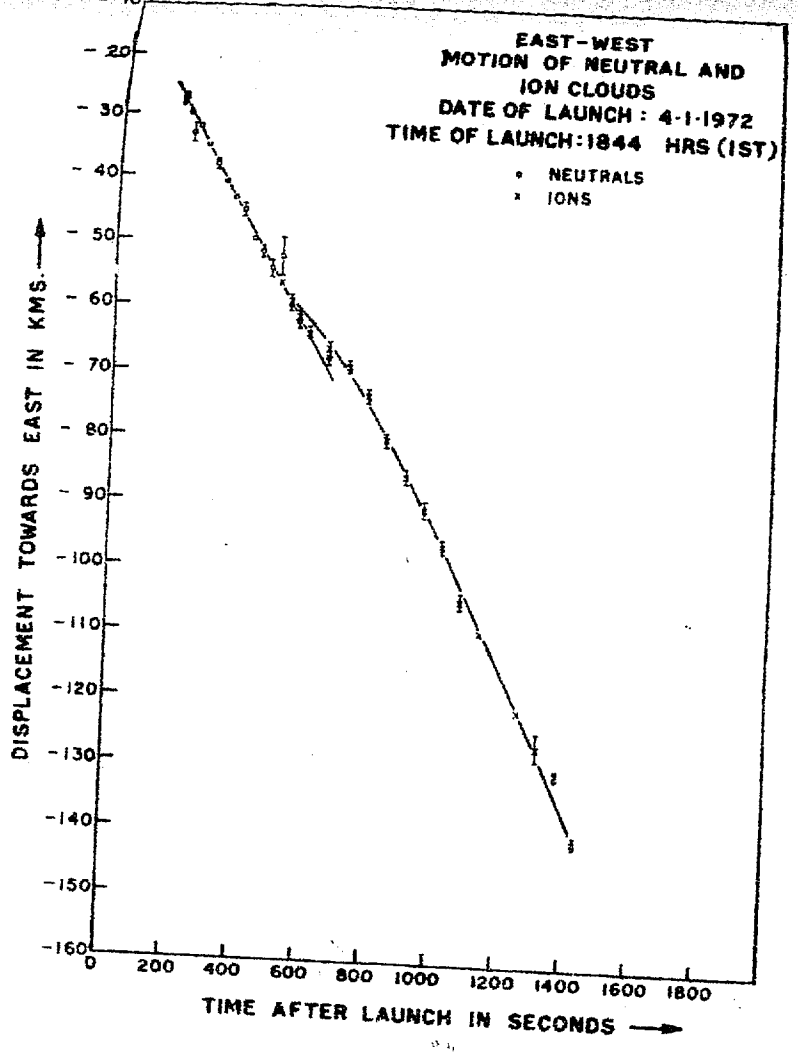

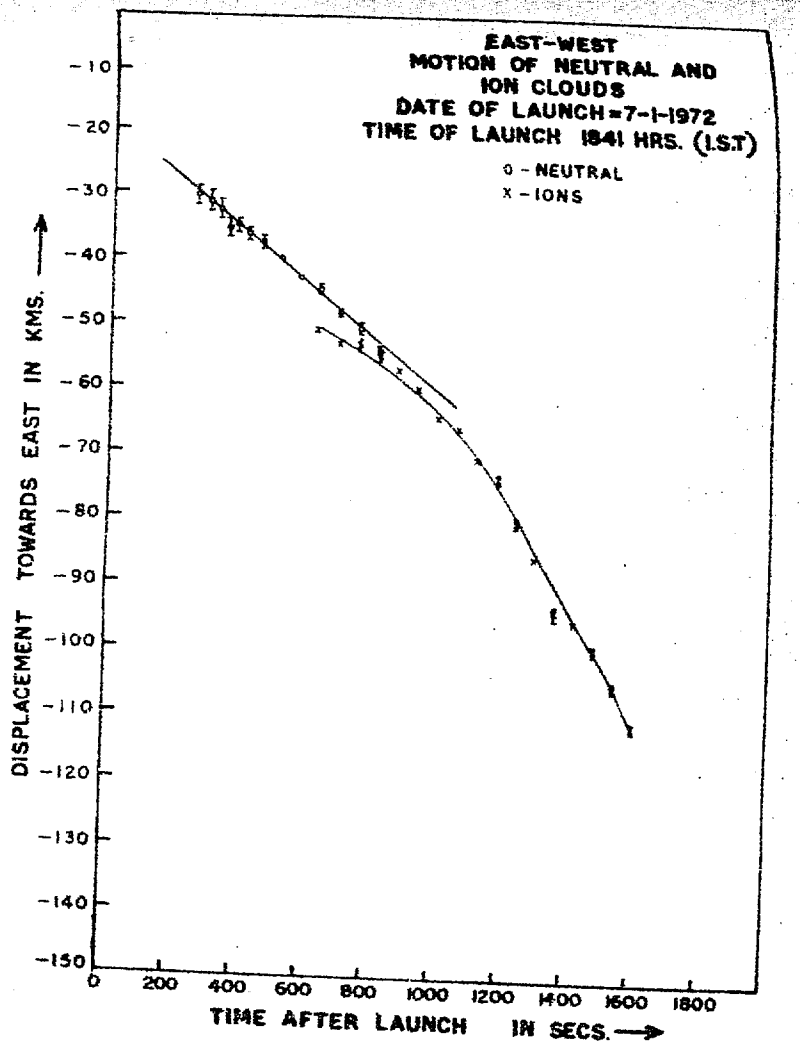

Fig. IV.1:- East-west displacement of the neutral and ion clouds with time after the rocket launch for flights 1 (left) and 3 (right). The velocities are obtained by averaging the displacements over the entire observation time.

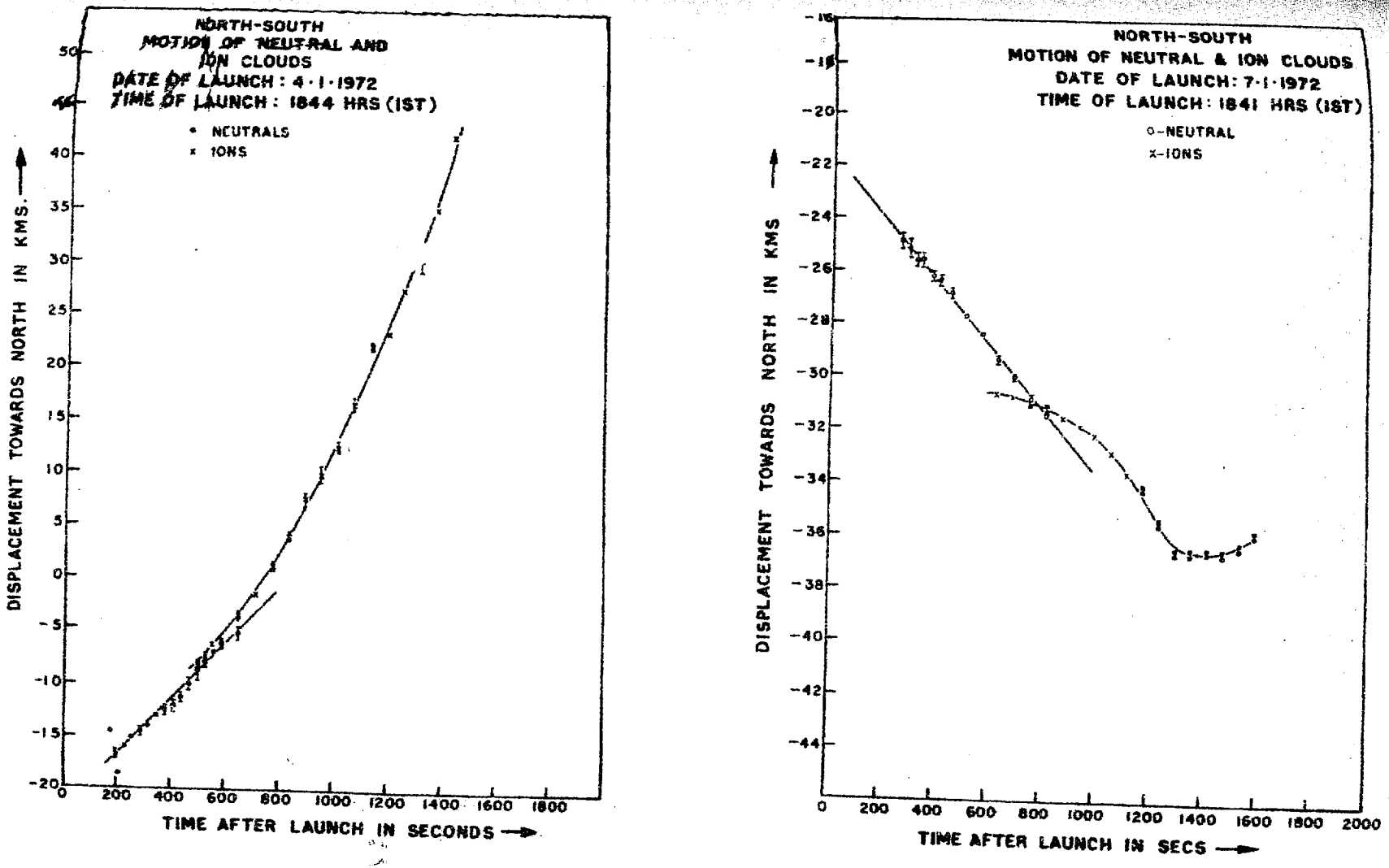

Fig. IV.2:- North-south displacement of the neutral and ion clouds with time after rocket launch for flights 1(left) and 3(right). The velocities are obtained by averaging the displacements over the entire observation time.

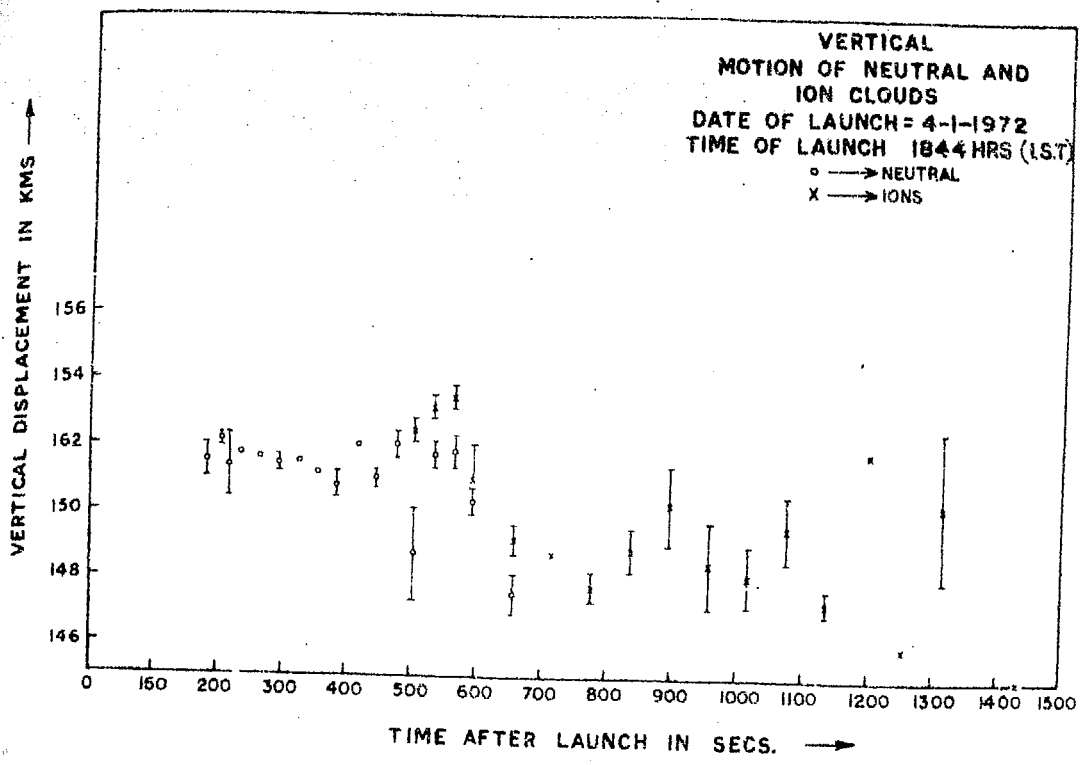

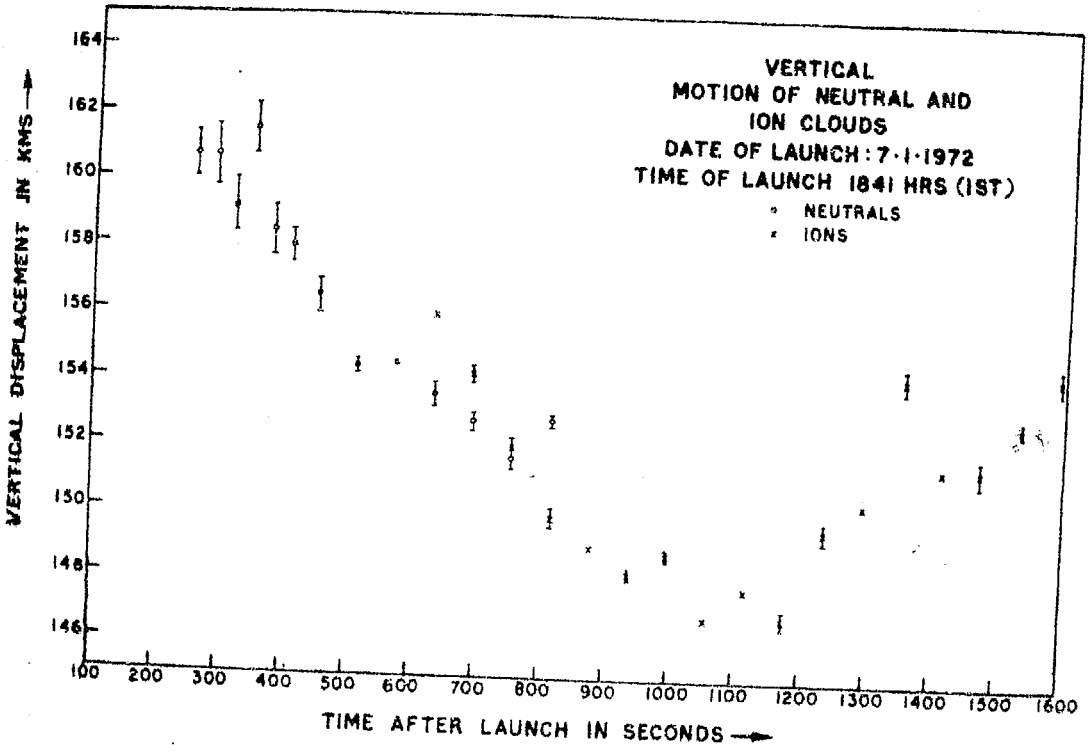

Fig.IV.3:- Vertical displacement of the neutral and ion clouds with time after the rocket launch for flights 1 (top) and 3 (bottom). The velocities are obtained by averaging the displacements over the entire observation time.

the components of the velocities are computed. Under the assumption that $\lambda^* \simeq 1$ (i.e., the integrated Pedersen conductivity inside the cloud is equal to that in the ambient ionosphere). The eqn. (10) can be simplified as

$$\underline{E}_\perp = \underline{B} \times \underline{V}_\perp + {}^{B}R_i(\underline{V}_\perp - \underline{W}_\perp) \qquad (11)$$

Thus the measurements are in error to the extent that λ^* is not exactly known. However, the clouds of moderate released quantity (0.5 to 2.5 kg of the thermite mixture below 300 km) attain the ambient conditions as quickly as in 20 sec. after the release. The electric field components in the eastward (E_x) and vertically upward (E_z) directions are obtained from the cloud motions. In Table IV.1 are listed the electric field components E_x and E_z and also the ratio $F = E_z/E_x$. RIEGER (1971) has reported results from four barium vapour release experiments (one at dawn and three at dusk) performed at the dip equator over Thumba, in rch 1968. Table IV.1, includes the values of electric field components and the ratios, F, from these results (flight numbers 36 to 39 in Rieger's paper). It is clear from the table that the ratio E_z/E_x (=F) is greater than 1, even at heights above 150 km. We now examine what the theoretical models would predict the ratio to be.

TABLE IV.1

Flight Number	Date	Time of launch (I.S.T.)	Height range (km)	E_x (mV/m) positive towards East	E_z (mV/m) positive vertically upwards	$F = E_z/E_x$
1	4-1-72	1841	155-160	0.22±0.07	3.7±0.7	16.8±5.3
3	7-1-72	1844	155-160	0.21±0.09	2.5±0.2	11.9±5.1
36	28-3-68	1855	150-180	1.20±0.08	3.5±0.3	2.9±0.4
			180-210	1.00±0.07	3.2±0.2	3.2±0.4
			210-240	0.82±0.07	2.7±0.2	3.4±0.4
37	30-3-68	1855	150-180	1.00±0.11	3.3±0.3	3.3±0.4
			180-210	1.50±0.15	3.5±0.3	2.3±0.2
			210-240	1.20±0.14	2.7±0.3	2.3±0.2
38*	31-3-68	0537	180-210	-2.60±1.30	-2.5±1.3	1 ±0.6
39**	31-3-68	1745	155-230	0.45	2.5	5.56

* This morning release is included for completeness.

**This value is not shown in the Fig.IV.5, because of the large height range.

IV.4 Validity of UNTIEDT'S model of the electrojet:

The problem of how the conductivity tensor affects the electric field distribution and the currents in the equatorial ionosphere has been investigated by a number of authors. The models of the electrojet proposed till todate are reviewed in Chapter VI. RICHMOND (1973a)pointed out that some information about the various mechanisms controlling the equatorial ionosphere can be obtained from an inspection of the ratio F of the electric field component perpendicular to the magnetic field in a vertical plane, E_z, (which becomes exactly vertical above the geomagnetic dip equator) to that in the east-west direction, E_x. Thus, the model proposed by SUGIURA AND CAIN (1966) indicates that F should be equal to the ratio

$$R = \sigma_H / \sigma_P \qquad (12)$$

where σ_H and σ_P are the Hall and Pedersen conductivities.

UNTIEDT (1967) has shown that the electrojet model of SUGIURA AND CAIN (1966) is not self-consistent as it violates the assumption that $\nabla \cdot \underline{J} = 0$ which is valid in the ionosphere. We now derive an expression for the ratio F from this basic assumption.

In geomagnetic polar spherical coordinates (r, θ, ϕ), the equations of a magnetic surface and of a magnetic equipotential for a dipole field are given by

$$r = \alpha \sin^2\theta \quad ; \beta = \cos\theta / r^2 \qquad (13)$$

The surfaces of constant α, ϕ and β define an orthogonal curvilinear coordinate system (α, ϕ, β). In this coordinate system, the transverse meridional, the east-west and the parallel components of $\underline{E}$ are respectively E_α, E_ϕ and E_β. Our aim is to calculate the ratio E_α/E_β ($\simeq E_z/E_x$) under the assumption of an infite parallel conductivity.

To this end we note that the integral of the current density $\underline{J}$ over a closed surface S is zero by virtue of the equation of continuity. It is convenient to choose S to be the surface formed by the base of the conducting region AA'CC' (Fig. IV.4), the sector AA'BB'CC' of the surface α = constant generated by a field line, and two meridional plane ABC and A'B'C' separated by a small angle $\delta\phi$.

As AA'CC' lies in the non-conducting region, it makes no contribution to the integral. In addition, the contributions from the two meridional planes ABC and A'B'C' cancel because the longitudinal component of the current is assumed to be constant. In reality this condition may not be rigorously fulfilled at sunset, but it appears to be adequate for the present purpose. Hence we are left with the contribution from AA'BB'CC', giving

$$\delta\phi \int_{-\beta_1}^{\beta_1} J_\alpha(\alpha,\beta)\, h_\beta h_\phi \, d\beta = 0 \qquad (14)$$

where β_1 is the coordinate of the point where the field line α = constant intersects the non-conducting layer

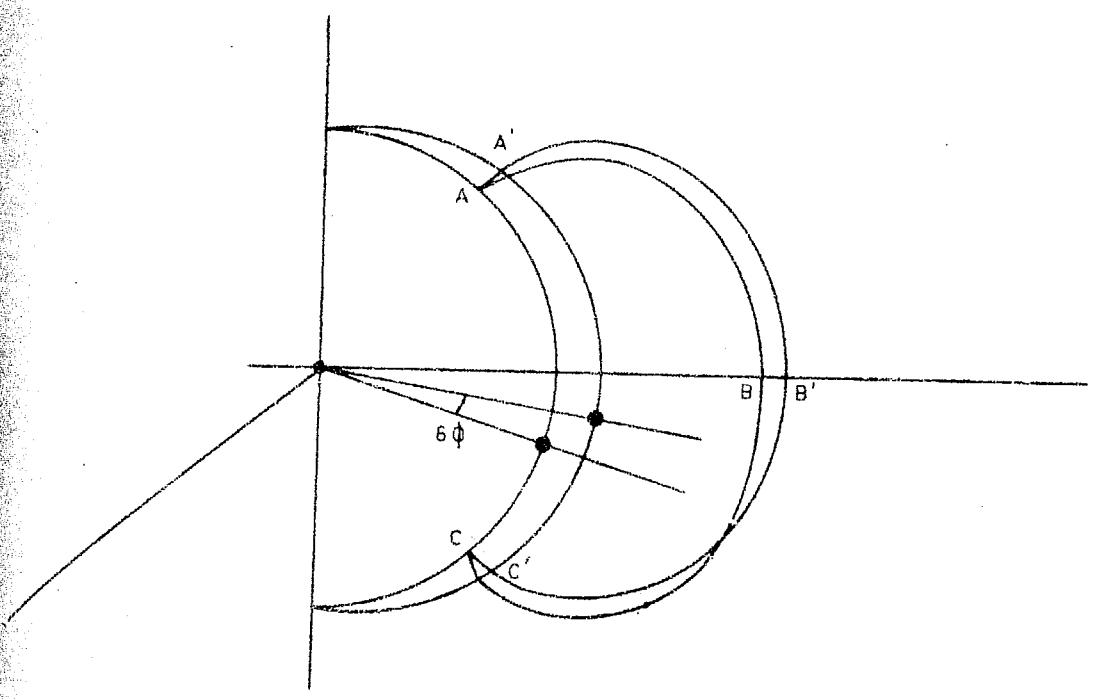

Fig.IV.4:- Volume over which div $\underline{J}$ = 0 is integrated.

$r = R$, and the scale factors h_α, h_β and h_ϕ are given, to a high degree of approximation, by

$$h_\alpha = \chi(\alpha,\beta) \; ; \; h_\phi = \alpha \chi^{3/2}(\alpha,\beta) \; ; \; h_\beta = \alpha^3 \chi^{5/2}(\alpha,\beta)$$

and an element of length along a field line by

$$dl = \alpha^3 \chi^{5/2} d\beta \quad \text{with} \quad \chi(\alpha,\beta) = \left(1+3\beta^2 R_e^4\right)\Big/\left(1+4\alpha\beta^2 R_e^3\right)$$

where R_e is radius of the earth.,

and, $\beta_1 = \left[(\alpha - R)/\alpha R_e^4 (4R - 3R_e)\right]^{1/2}$

Now the transverse meridional current is given by

$$J_\alpha = \sigma_P E_\alpha - \sigma_H E_\phi \qquad (15)$$

Also, since curl $\underline{E} = 0$, we have

$$h_\phi E_\phi = \text{constant} \qquad (16)$$

and when $E_\beta = 0$,

$$h_\alpha E_\alpha = \text{function of } \alpha . \qquad (17)$$

On substituting eqn. (15) in eqn. (14) and making use of eqns. (16) and (17), we obtain the desired result, namely,

$$R' = E_\alpha / E_\phi = (h_\phi / h_\alpha) \int_{-\beta_1}^{\beta_1} \sigma_H h_\beta d\beta \Big/ \int_{-\beta_1}^{\beta_1} \sigma_P \frac{h_\phi h_\beta}{h_\alpha} d\beta \; , \qquad (18)$$

In the region of interest $\chi \approx 1$ and we can therefore approximate eqn. (18) by

$$E_\alpha / E_\phi = E_Z / E_X = \int_0^{\theta_{max}} \sigma_H d\theta \Big/ \int_0^{\theta_{max}} \sigma_P d\theta \qquad (19)$$

where θ_{max} is the latitude of the point where the field line intersects the base of the conducting layer.

It is well known that at electrojet heights the ratio R has a maximum R_m of the order 25 to 30. For altitudes larger than 110 km, R decreases rapidly and at, for instance, 200 km, is smaller than 10^{-1}. The value of R, and thus of R_m, is obviously independent of the local electron density N and is, therefore, expected to vary little with local time. The altitude dependence of R is primarily controlled by ν_e and ν_i which are functions of atmospheric density, composition and temperature so that, for any realistic atmospheric model, at altitudes above 130 km the value of R is already smaller than unity.

On the other hand the ratio R' defined above depends on the electron density N measured along a magnetic field line. Because of lack of sufficient experimental electron density profiles at various latitudes near the equator, we have assumed that N as a function of altitude h, is latitude independent over the latitude range spanned by the extremes of integration. Fig. IV.5 compares the height profiles of the ratios R and R'. The ratio R' is calculated over the range 80-250 km above the equator, at every two-kilometre intervals, and the integration is carried out along each field line from the magnetic equator ($\theta = 0$) to the appropriate latitude θ. For the present calculations we have used the electron density profiles measured simultaneously with the Barium release experiments, reported by RIEGER (1971) around 1855 IST. Similar measurement

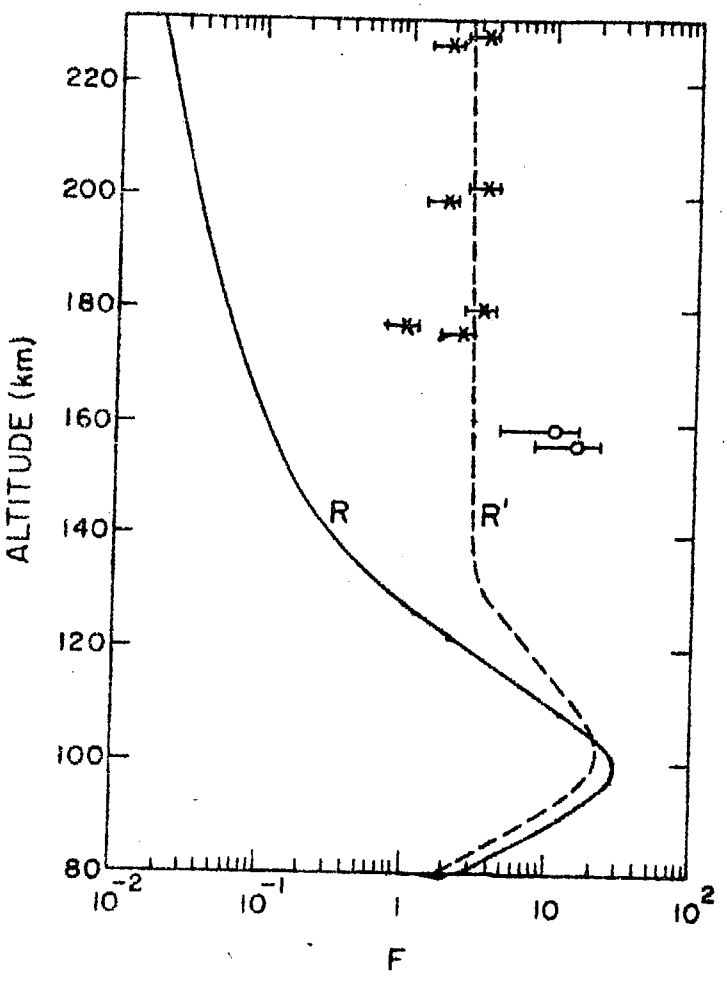

Fig.IV.5:- Ratio of conductivities versus altitude. The solid curve shows the ratio of the Hall conductivity (σ_H) to the Pedersen conductivity (σ_P). The dashed curve shows the ratio of the integrated Hall and Pedersen conductivities. The circles represent the values of $F = (E_Z/E_X)$ computed from the data obtained by the author and the crosses are taken from RIEGER (1971).

for the Barium release experiments performed in 1972 are not available. Although in our computations we have assumed values of θ_{max} corresponding to the latitude where a field line intersects a circle of radius R_e + 80 km (R_e being the earth's radius), the ratio R' is very insensitive to the choice of N(h) upto 100-110 km, and therefore to the precise choice of θ_{max}.

Upto 110 km the curve R' follows quite closely the behaviour of R. Above 110 km, however, the value of R' begins to differ markedly from that of R and at 150-160 km can be greater than R by a factor of 10-30 or more, according to the particular vertical profile chosen in the integration.

Table IV.1 and Fig.IV.5 show the ratio F for flight 1 and 3 (open circles), together with the values of F deduced from the results published by RIEGER (1971) at different altitude (crosses). We observe a reasonable agreement between our values and Rieger's within the errors and, although our experimental values are on the high side of the computed curve R', they are removed from the ratio R by two orders of magnitude.

Computations have shown that a decrease of N(h) above 110 km results in an increase of R'. It may well be that at the time of our release the electron density trough (i.e. the depletion of electron density) above 110 km was much deeper than at the time of Rieger's experiments.

In this case we would expect the values of R' above 110 km to be larger than those shown in Fig. IV.5, which have been calculated using the N(h) measured at the time of Rieger's experiments. Furthermore, the components $\underline{V}$ and $\underline{W}$ used to calculate F in our experiments have been deduced from measurements taken during the last 400 sec or so of observation, i.e., when N(h) is expected to decrease with time. Since no electron density measurements were performed during the flight of our two rockets, we cannot quantify this argument further, although the relative high value of $\underline{E}$ ($\sim$3 mV/m) and the negligible electrojet current are consistent with a reduction of at least one order of magnitude of N(h) at electrojet altitude and above.

The computations were done for the apex of the lines of force at the altitude of the relaase. The correction to the computed value of R' is very sensitive to the relative position of the measured point and the apex of the line of force, and the ion clouds were about 50 km long towards the end of the observation period.

IV.5 Conclusions:

The analysis of results from ion cloud release performed to date over the geomagnetic equator gives strong evidence in favour of the electrojet model proposed originally by UNTIEDT (1967) and subsequently elaborated by SUGIURA AND POROS (1969) and RICHMOND (1973a). In particular, the ratio

of the vertical to the east-west electric field components in the equatorial ionosphere can be derived from the ratio of the integrated Hall and Pedersen conductivities.

It is worth noting that the fairly high value of E_z, measured in all these experiments indicates that the absence of currents at the time of the releases is caused not so much by a reduction of the electric field, as by a decrease of the individual conductivities associated with a decrease of N(h) after sunset.

While the barium cloud technique can not be used at the electrojet altitudes, it is difficult to measure the east-west electric field by the double-probe technique and only the vertical electric field (which is much greater than the east-west field at the electrojet altitudes) can be measured by the latter technique. The profile of the vertical electric field measured over the dip equator at any local time can be compared with the profile of R' computed by taking an electron density profile at the same local time. From these two profiles it is possible to obtain the profile of the east-west electric field on the basis of the theory discussed in IV.4. However, we have not considered here, the neutral wind effects which may be important under certain conditions. It is shown in Chapter VI, how the neutral winds and wind shears affect the electric fields.

In future, it is necessary to measure simultaneously the electric field (even if it is only the vertical component), electron density and neutral winds in order to assess experimentally the wind effects on the electrojet parameters.

CHAPTER V

TWO DIMENSIONAL THEORY OF ELECTRIC FIELDS GENERATED BY WIND MOTIONS AT THE EQUATORIAL IONOSPHERE - APPLICATION OF WIND SHEAR MECHANISM TO THE E REGION ELECTRON DENSITY STRATIFICATIONS

V.1 Introduction:

It is generally believed that the source of the ionospheric electric currents at the magnetic equator is a primary electrostatic field in the eastward direction generated by charge distribution due to the dynamo action of the global tidal winds in the non-equatorial region. In the E region of the ionosphere, the ions tend to be carried with the neutral wind motions and the electrons are tightly bound to the geomagnetic field lines as discussed earlier. In the presence of an eastward wind of velocity $\underline{W}$, the ions move (i) eastwards with a velocity $\underline{W}$ and (ii) vertically upwards due to the Lorentz force with a velocity

$$\frac{R_i}{1 + R_i^2} \quad \frac{\underline{W} \times \underline{B}}{B},$$

R_i being the ratio of ion-neutral collision frequency to the ion-gyrofrequency. This results in the development of polarization field in a direction opposite to the ion motion. Ions are always slowed down in the horizontal direction by the combined action of the vertical polarization field and the geomagnetic field (by $\underline{E} \times \underline{B}$ drift). Thus, essentially the wind $\underline{W}$ causes the ions to move upwards by the Lorentz force. The electrons, on the other hand, are constrained to move along the geomagnetic field lines to neutralize the space charge set up by the ion motion and thus to quench the polarization field.

This neutralization process is very effective where the magnetic field lines are almost vertical as, for instance, in the mid-latitudes. The vertical field lines enable the electrons to move from one altitude to the other. If the neutralization process is complete, then the winds govern the dynamical behaviour of ionisation. If, in contrast, the neutralisation cannot take place as in the case of horizontal field lines (presumably at the dip equator), the polarization field cancels the Lorentz field completely and the winds do not play a major role in controlling the ion motion.

However, if the curvature of the geomagnetic field lines is taken into account, even at the equator, the cancellation of the wind induced (Lorentz) fields may not be complete (KATO, 1973 a).

Fig.V.1 shows the effect of the Lorentz field $\underline{W} \times \underline{B}$ on the ionization in the case of a wind with a shear (gradient in the vertical direction). The figure (reproduced from HINES, 1964 b) shows a special case of a wind reversing its direction with altitude. The Lorentz force moves the ionization up and down for the eastward and westward winds respectively and therefore the ionisation accumulates at the centre of the shear to form a layer. This mechanism, commonly known as "the wind shear mechanism" accounts for the production of ionization irregularities in the mid-latitudes (WHITEHEAD, 1961; AXFORD, 1963).

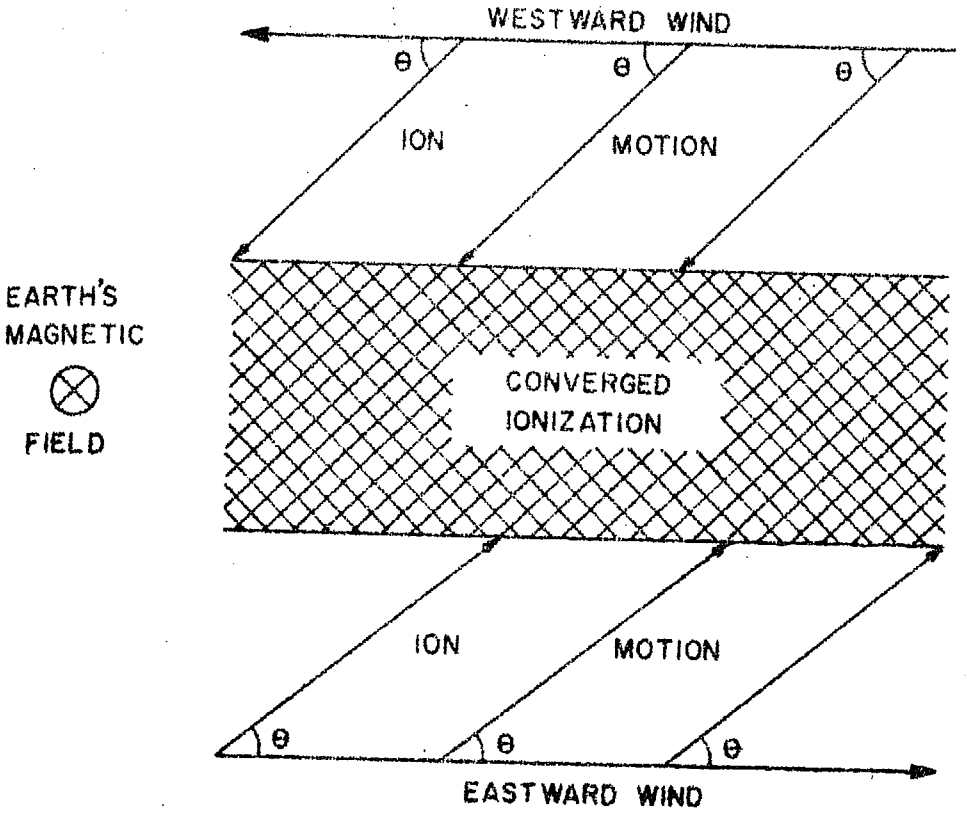

Figure V.1.: Wind-shear mechanism in the E-region. The plane of the diagram represents an east-west vertical plane at the magnetic equator, seen from the south. The arrows show the ion motion due to the combined action of the east-west winds and geomagnetic field. The electrons are constrained by electrostatic forces to follow the ion motion, so that ionization accumulates within the shear. The angle Θ is given by tan Θ = ω_i/ν_i which increases with altitude (after HINES, 1964b).

In this Chapter, we develop a two dimensional theory of the electric fields generated by winds in the equatorial ionospheric E region taking the curvature of the field lines into consideration and show how well can the wind shear mechanism explain the observed electron density stratifications. The mid-latitude E region irregularities (stratifications) and their production by the wind shear theory are briefly discussed in section V.1.1. The various types of irregularities in the equatorial E region and the theories which explain their formation are presented in V.1.2 and V.1.3 respectively. In V.2, the one-dimensional theory of electric fields generated by gravity wave winds at the dip equator put forward by KATO (1973 a), is discussed and the necessity for a two-dimensional treatment is brought out. The two-dimensional theory of electric fields generated by winds of gravity wave origin in the equatorial ionosphere developed by the author is presented in V.3. Application of this theory to the irregularities observed in the nighttime equatorial E region is discussed in V.4.

V.1.1 Sporadic-E irregularities at mid-latitudes:

EDWARD APPLETON (1930), using the frequency change method of ionospheric sounding, detected abnormal layers in the E-region of the ionosphere at night which he termed as "abnormal E". These layers are very dense (several times higher than the normal E layer densities) occuring at altitudes

around 100 km. They are patchy and partially transparent to radio waves reflected from higher layers. They occur randomly with time. Sometimes, these layers appear in sheets which completely hide or 'blanket" the overlying F layer - blanketing E (KNECHT AND MCDUFFIE, 1962; COHEN AND BOWLES, 1963 b; BANDYOPADHYAY AND MONTES, 1964). Extensive experimental studies, have shown that this abnormality, now known as "sporadic E" (Es) occurs both day and night and is a world wide phenomenon. The phenomena and the causative mechanisms as such are different for the equatorial sporadic E (Es - q), the mid-latitude (temperate - latitude) sporadic E and the auroral sporadic E (SMITH, 1957, 1967).

As early as 1956, DUNGEY (1956) suggested that a north-south shear in the north-south wind could accumulate the ionization by forcing it up and down the magnetic field lines by the process of ambipolar diffusion. As the ion mobilities along (direct) and perpendicular to (Pedersen) the field line are comparable in the E region, the ambipolar diffusion is not very effective. WHITEHEAD (1961) showed that the Lorentz force due to a wind $\underline{W}$, having a strong gradient in height could converge the ionization very effectively (Fig. V.1) to produce the observed stratifications in electron density in the E region viz. the sporadic E (Es). HINES (1964 b) has clarified some confusion about the "signs" in the original equations given in the theory of WHITEHEAD. Ever since

WHITEHEAD proposed the preliminary theory of wind shear mechanism, there has been a series of theoretical papers each one stimulating further advances and improvements over the earlier ones. LAYZER (1964 a, b) has pointed out some difficulties in the theory of WHITEHEAD, as to the low recombination coefficient demanded by the theory and as to the lack of correlation of the altitude of thepeak electron density with that of the wind shear. He also showed that while the observed peak electron densities are several times higher than the back-ground, the minimum densities do not seem to be lower than the background as predicted by the theory. WHITEHEAD (1964) and AXFORD (1964) tried to clarify these objections. Extensive theoretical studies have been made, incorporating various aspects like the effects of diffusion (STOREY AND HERSE, 1963), recombination (AXFORD, 1963), vertical gradient of ion-neutral collision frequency (MACLEOD, 1966), variation of recombination coefficient in the case of a mixture of ions (AXFORD AND CUNNOLD, 1966; AXFORD ET AL, 1966; WHITEHEAD, 1966), meteoric ionization (CUCHET, 1966), vertical gradients of electron temperature (WHITEHEAD, 1966), superposed electric field with a gravity wave motion (KATO ET AL. 1968) etc., to explain different observed features of the mid-latitude sporadic E. Now it is believed that the meteoric ionization, which has low recombination coefficient, plays a significant role in the formation of the sporadic E. Among

several theories to explain the sporadic E layers, the one involving the wind shear mechanism provides probably the best explanation (SMITH, 1966, 1967; WHITEHEAD, 1970).

V.1.2 The equatorial E region irregularities:

The equatorial sporadic E (Es - q) is a different phenomenon, distinguishable from the mid-latitude sporadic E. This is mainly due to the unique feature that characterizes the ionosphere over the dip equator viz. the nearly horizontal magnetic field across which a highly intense current, "the electrojet", flows. The association of the Es - q with the equatorial electrojet and hence with the variation of the northward component of the earth's magnetic field ΔH on the surface of the earth was found by MATSUSHITA (1951). In contrast, the mid-latitude sporadic E has little correlation with the variation in H (RISHBETH AND GARRIOTT, 1969). The altitude of the electrojet which is at $\approx$ 106 km, is close to the height of occurrence of the sporadic E irregularities. The structure and movement of the irregularities have been studied by the VHF radars transmitting radio frequencies in the range 50-150 MHz. The results from these experiments have revealed that, (i) the irregularities are embedded in the electrojet, (ii) the irregularities are of scale sizes ranging from less than a metre to hundreds of metres, (iii) there is a temporal correlation between the occurrence of the irregularities and the strength of the electrojet and that (iv) the irregularities are highly field aligned

(BOWLES ET AL, 1960; EGAN, 1960; COHEN ET AL, 1962; BOWLES ET AL, 1963; COHEN AND BOWLES, 1963 a, b; COHEN, 1967). BALSLEY (1965, 1969 a, b) has studied these irregularities at Jicamarca by means of a VHF radar and identified distinctly two types of irregularities in the electrojet. The type I irregularities which occur only when the electric field (and hence the electron drift speed) exceeds a certain minimum threshold value. These irregularities are plane wave structures moving with the ion-acoustic speed ($\approx$360 m/s). They are found to be prominent and most frequent in occurrence during 0900-1100 hrs LT (BALSLEY, 1969 b) although they are observed both during day and night. The second type of irregularities, called the type II, are originated by weaker electric fields. These are at times stronger than the type I. They move with a velocity, approximately equal to the electron drift velocity. These irregularities appear only near the top and bottom edges of the electrojet where the gradients in background electron density are sharp. They occur even in the night time (COHEN AND BOWLES, 1963 b).

PRAKASH ET AL (1970) have flown Langmuir probes on-board several rockets and detected three types of night time irregularities, distinguishable by their size. The smallest size is 1-15 m having small amplitudes. The second type is in the range of scale sizes 30-300 m and having

amplitude a few percent of the ambient electron density. The third type are large scale structures or stratifications in the electron density profile, shown in Fig. V.2 and are generally observed only in the nighttime (PRAKASH ET AL, 1970). It is clear from the figure that the stratifications are consistently observed during both ascent and descent of the trajectory of the rocket. The horizontal separation at 100 km altitude between the ascent and descent is about 60 km, indicating that the horizontal sizes of these large-scale irregularities (the third type) are $\gtrsim$ 60 km. The vertical scale sizes of these irregularities are $\approx$ 10 km, as can be inferred from the figure.

In a daytime experiment, PRAKASH ET AL (1971 a, b) have detected the above mentioned small scale irregularities along the positive gradient of the electron density but the large scale irregularities were absent.

The blanketing type sporadic E is found to be confined to only the temperate latitudes and their occurrence sharply diminishes at equatorial latitudes (PIGGOTT AND RAWER, 1961; REDDY AND MATSUSHITA, 1969; KNECHT AND MCDUFFIE, 1962; COHEN AND BOWLES, 1963 b; BANDYOPADHYAY AND MONTES, 1964). However, REDDY AND DEVASIA (1973) have observed blanketing type sporadic E layers at the dip equator over Thumba($0^{o}.6$ S). The detailed studies of structure and character of the irregularities mentioned above have led to some important theoretical investigations. We now discuss briefly the theories explaining the formation of these irregularities.

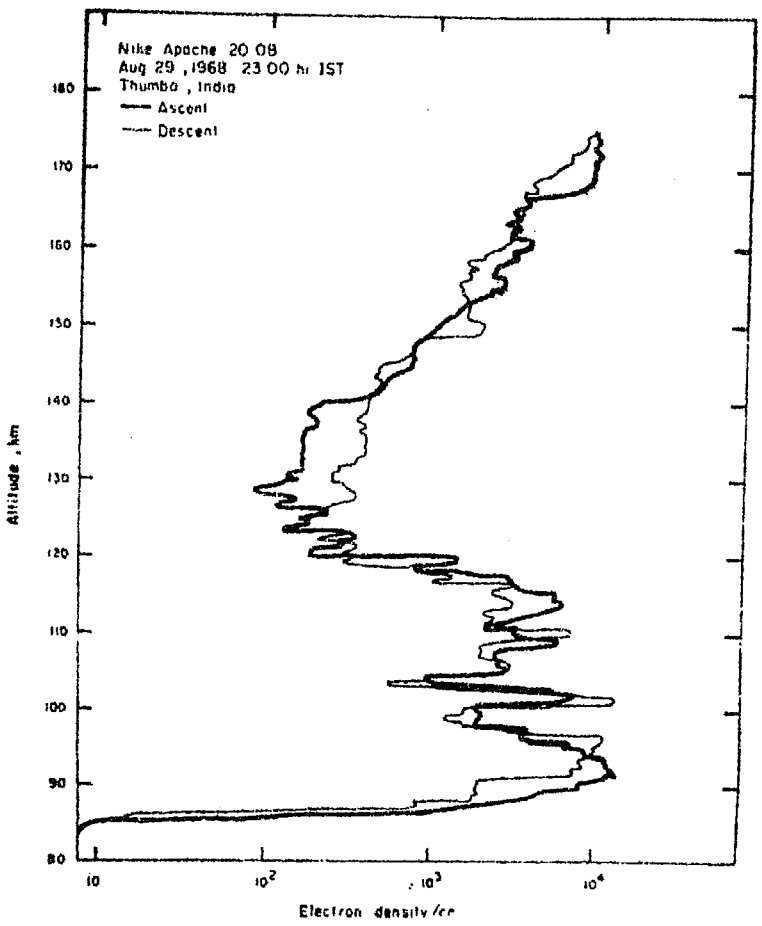

Figure V.2.: Electron density profile obtained by a rocket-borne Langumuir probe flown over Thumba, the dip equator at 2300 IST. The heavy line represents the ascent and the light line marks the descent of the rocket flight (after PRAKASH ET AL, 1970).

V.1.3 Theories of the equatorial E-region irregularities:

V.1.3.1 Two-stream instability:

In a magneto-active, weakly ionized plasma, if the electron drift velocity exceeds the ion-acoustic speed, an instability namely "the two-stream instability" sets in (FARLEY, 1963). Thus it depends on the magnitude of the electric field only and it can occur either during day or night. ROGISTER (1971) and SATO (1972) have considered the non-linear effects in the theory and accounted for the irregularities of scale sizes smaller than 3 m. The two-stream instability mechanism, in general, explains the observed features of the type I irregularities as reviewed by KATO (1973 b).

V.1.3.2 Cross-field instability:

This instability demands a gradient in the unperturbed background electron density distribution N in a direction perpendicular to the geomagnetic field $\underline{B}$. Besides, the electric field should be in the same direction as that of the gradient in N. Under these conditions, the cross-field instability occurs and produces the ionization irregularities. MARTYN (1959) laid the foundations to this mechanism when he discussed the growth of irregularities that are responsible for spread-F. SIMON (1963) developed the theory of cross-field instability and proved that this instability grows in a vertically bounded laboratory plasma. TSUDA ET AL (1966) applied the mechanism to the ionospheric plasma to explain

the sporadic E formation. KATO (1972) has explained the production of the electrojet irregularities as due to the cross-field instability. SATO (1971), ROGISTER (1972), SUDAN ET AL (1973) and ROGNLIEN AND WEINSTOCK (1974) have considered the non-linear aspects of the theory. The cross-field instability mechanism explains in general the formation and structure of the type II irregularities in the equatorial ionosphere where the gradient in N and the electric field are predominantly in the vertical direction (FARLEY AND BAISLEY, 1971; KATO, 1973 b). Though the small-scale irregularities observed by rocket-borne probes (PRAKASH ET AL, 1970, 1971 a, b) can be accounted for by the cross-field instability theory, it is not clearly known whether these are identical to the type II irregularities detected by the VHF radar (KATO, 1973 b). Similarly, rocket experiments have yet to be made to identify the type I irregularities.

V.1.3.3 Horizontal shears of the horizontal winds:

REDDY AND DEVASIA (1973) detected blanketing type sporadic E layers over the dip equator. These authors proposed a wind shear mechanism (similar to DUNGEY'S (1956) original mechanism) for the formation of the blanketing sporadic E in which the convergence of the ionization is forced by a north-south shear in a north-south wind. Internal gravity waves of 'short' periods and horizontal scale sizes $\approx$ 50 km are invoked to help the convergence along the field line.

KATO'S (1973 a) objection to this theory as to the validity of non-zero divergence of the internal gravity waves ($\nabla . \underline{W} \neq 0$) does not seem to be a serious one. For, it is known from HINES' (1960) original theory of gravity waves, that for short period internal gravity waves the divergence of their velocity could be non-zero (i.e., those waves are not completely 'transverse'). Nevertheless, observational evidence is required for asserting that such shears are present. The physical basis for the generation of small scale gravity waves that produce these shears is yet to be investigated.

V.1.3.4. Wind-shear mechanism at the dip equator:

It has been argued that the wind-shear theory (hereafter by wind-shear, we mean, the vertical shear in the horizontal wind in east-west direction in contrast with the shear discussed in V.1.3.3) does not apply at the dip equator because the geomagnetic field lines are horizontal. Nonetheless, KATO (1973 a) showed that if one takes the curvature of the field lines into account, then one gets a non-zero total electric field because of the winds, i.e., $\underline{E}' = \underline{E} + \underline{W} \times \underline{B} \neq 0$. He argued that the wind shear mechanism should be applicable at the dip equator also which is shown to account for the large scale irregularities observed by PRAKASH ET AL (1970). He solved the problem for a one-dimensional case, in which the horizontal wave number ($K_H = 2\pi/\lambda_H$) is neglected in comparison with the vertical wave number ($K_z = 2\pi/\lambda_z$).

The importance of the horizontal wave number is stressed by REDDY AND DEVASIA (1973). ANANDARAO ET AL (1977a) considered the two-dimensional aspect of the problem and showed that one could explain the formation of large irregularities by the wind-shear theory at the equator.

V.2 Electric fields generated by gravity wave winds at the dip equator - KATO'S one dimensional theory:

As mentioned earlier in this chapter, the polarization field set up by the charge separation does not cancel completel the Lorentz force field $\underline{W} \times \underline{B}$ induced by the winds of gravity waves even at the dip equator, if the curvature of the magnetic field lines is taken into account. KATO (1973 a) considered an eastward wind of speed 100 m/s at 100 km altitude due to a gravity wave of vertical scale size 10 km and horizontal scale size 50 km and calculated the electric field generated at the dip equator by solving the equation for the current density along with the condition that div $\underline{J} = 0$. He obtained the following equation for the electric field components at the dip equator,

$$E_z\left[\sigma_P(ik + H^{-1}) - 2\sigma_0/a\right] - E_\phi\left[\sigma_H(ik + H^{-1})\right] + BW_\phi\left[\sigma_P(ik + H^{-1})\right] = 0 \qquad (1)$$

where E_z and E_ϕ are the vertical and eastward components of the polarization field; W_ϕ, the eastward wind; k, the vertical wave number; H^{-1}, the reciprocal of the electron density scale height; B, the geomagnetic field assumed to

be a dipole field; and a is the radius of the earth. σ_0, σ_P and σ_H are the direct, Pedersen and Hall conductivities respectively. The term $(2\sigma_0/a)$ in the coefficient of E_z accounts for the curvature of the field line.

Under the assumption that

$$\frac{E_z}{E_\phi} = \frac{\text{Horizontal wavelength}}{\text{Vertical wavelength}} \gg 1,$$

he neglected the second term in the eqn. (1). He then defined an efficiency parameter,

$$R = \frac{E'_z}{W_\phi B} = \frac{-2(\sigma_0/a)}{(ik + H^{-1}) - (2\sigma_0/a)} \qquad (2)$$

which is a measure of the relative strengths of the total electric field $\underline{E}'$ and the wind induced field $\underline{W} \times \underline{B}$. $|R| = 1$, when the polarization field is zero. $|R| = 0$, when the polarization field is just sufficient to balance the wind induced field. As one of the most important conclusions of his work, KATO asserts that if the curvature of the field lines is considered $\underline{E} + \underline{W} \times \underline{B} \neq 0$, i.e., $R \neq 0$; and therefore, the wind shear mechanism to produce E region electron density stratifications is effective even at the dip equator.

However, at the altitude of 100 km, $\sigma_H \simeq 30\ \sigma_P$ and hence the second term cannot be neglected when compared to the first term of the eqn. (1), for the vertical wavelength

10 km and horizontal wavelength 50 km. If we consider the second term also into account, the efficiency parameter will be decreased. Therefore, it is essential to formulate the two-dimensional treatment of the problem and examine whether the wind shear mechanism will still be efficient at the equator.

V.3.1 Two dimensional theory of electric fields engendered by the gravity wave winds at the equatorial ionosphere:

We choose a Cartesian coordinate system with **x**-axis towards magnetic south, **y** towards east and **z**-axis vertically upwards. The earth's magnetic induction vector $\underline{B}$ which lies in the x-z plane makes an angle I (the dip angle) called the 'dip', with the x-axis.

Assumptions made in the present theory are:

(a) The magnetic field $\underline{B}$ is assumed to be a dipole field.

(b) The variation of all the parameters with the eastward coordinate y is neglected: $d/dy = 0$.

(c) The conductivity components $\sigma_0, \sigma_P, \sigma_H$ are assumed to be undisturbed by the wind $\underline{W}$. But the variation of these parameters due to the variation in the electron density is taken into account. It is also assumed that the conductivities vary only with altitude and not in **x** and **y** direction.

The current density in terms of the conductivities and the electric field is

$$\underline{J} = \sigma_0 \underline{E}_{\parallel} + \sigma_P \underline{E}'_{\perp} + \sigma_H \frac{\underline{B} \times \underline{E}'_{\perp}}{B} \qquad (3)$$

with the condition

$$\nabla \cdot \underline{J} = 0 \qquad (4)$$

which is valid in the ionosphere.

The total electric field $\underline{E}'$ is composed of two parts, the polarization field generated by the charge separation due to the wind of gravity wave origin, $\underline{W}$ and the wind induced field (Lorentz field) $\underline{W} \times \underline{B}$; i.e.,

$$\underline{E}' = \underline{E} + \underline{W} \times \underline{B} \tag{5}$$

The polarization field is assumed to be the gradient of a potential

$$\underline{E} = -\nabla \phi \tag{6}$$

and $\underline{W}, \phi \propto \exp\left(i(k_x x + k_y y + k_z z)\right)$ (7)

In the configuration of the coordinate system chosen, the geomagnetic (dipole) field is given by.

$$\underline{B} = B\left(-\hat{a}_x \operatorname{Cos} I - \hat{a}_z \operatorname{Sin} I\right) \tag{8}$$

where I is dip angle and $\hat{a}_x$ and $\hat{a}_z$ are unit vectors along x and z axes respectively.

The dependence of horizontal and vertical components of the wind velocity W_H and W_Z, due to a non-divergent ($\nabla \cdot \underline{W} = 0$) gravity wave wind system is related to its wave numbers k_H and k_Z in the respective directions and is given by the asymptotic relationship (HINES, 1960)

$$W_Z / W_H \simeq - k_H / k_Z \tag{9}$$

Therefore,

$$\left.\begin{aligned} W_H &= \frac{W}{k} k_Z \\ \text{and} \quad W_Z &= -\frac{W}{k} k_H \end{aligned}\right\} \tag{10}$$

$$\left.\begin{aligned} W^2 &= W_H^2 + W_Z^2 \\ \text{and} \quad k^2 &= k_H^2 + k_Z^2 \end{aligned}\right\} \tag{11}$$

The three components of $\underline{J}$ can be written down as

$$J_x = \sigma_0 E_{\parallel B} C + \sigma_P E_{\perp B} S + \sigma_H E_y S - \sigma_P W_y B S + \sigma_H B W_{\perp B} S$$

$$J_y = (\sigma_P E_y - \sigma_H E_{\perp B}) + B(\sigma_P W_{\perp B} + \sigma_H W_y) \quad (12)$$

$$J_z = \sigma_0 E_{\parallel B} S - \sigma_P E_{\perp B} C - \sigma_H E_y C + \sigma_P B W_y C - \sigma_H B W_{\perp B} C$$

where, $E_{\parallel B} = E_x C + E_z S$; $E_{\perp B} = E_x S - E_z C$

$W_{\perp B} = W_x S - W_z C$, with, $C = \cos I$, $S = \sin I$.

The condition div $\underline{J} = 0$ yields the following:

$$ik_x J_x + \sigma_0 E_{\parallel B} \frac{\partial C}{\partial x} + \sigma_P E_{\perp B} \frac{\partial S}{\partial x} + \sigma_H E_y \frac{\partial S}{\partial x} - \sigma_P B W_y \frac{\partial S}{\partial x} + \sigma_H B W_{\perp B} \frac{\partial S}{\partial x} + ik_y J_y + ik_z J_z + H_z J_z = 0 \quad (13)$$

where,

$$H_z = \frac{1}{N} \frac{\partial N}{\partial Z}$$

is the reciprocal of the electron density scale height.

We now examine the variation of the dip angle I with x. For ionospheric heights $h \ll a$, the earth's radius; and for the geomagnetic latitudes in the vicinity of geomagnetic equator, we can realize the following relation,

$$\frac{x}{a} = \tan \theta$$

where x is the north-south distance and θ is the magnetic latitude. We also have (e.g., CHAPMAN, 1964), $2 \tan \theta = \tan I$,

$$\therefore \quad \frac{dS}{dx} = \frac{2C^3}{a}$$
$$\frac{dC}{dx} = -\frac{2C^2S}{a} \qquad (14)$$

From eqns. (6) and (7), $E_x = 0$, since we have taken the wind to be east-west and vertical only. And also

$$E_y = \frac{E}{k} k_H \qquad (15)$$

and similarly, $E_z = \frac{E}{k} k_z$

Substituting the results obtained in eqns. (10), (14) and (15) in the eqn. (12), we get, after some rearrangement,

$$\frac{-i\phi k}{BW} = \frac{i(B_1 k_H + B_2 k_z) + (B_2 H_z + B_3)}{i(A_1 k_H + A_2 k_z) + (A_2 H_z + A_3)} \qquad (16)$$

$$\therefore \frac{E}{BW} = \left[\frac{(B_1 k_H + B_2 k_z)^2 + (B_2 H_z + B_3)^2}{(A_1 k_H + A_2 k_z)^2 + (A_2 H_z + A_3)^2} \right]^{1/2}$$

where,

$$A_1 = \sigma_P k_H + \sigma_H k_z C$$
$$A_2 = \sigma_0 k_z S^2 + \sigma_P k_z C^2 - \sigma_H k_H C$$
$$A_3 = (\sigma_0 - \sigma_P) k_z \frac{\partial SC}{\partial x} - \sigma_H k_H \frac{\partial S}{\partial x} \qquad (17)$$
$$B_1 = \sigma_P k_H C + \sigma_H k_z$$
$$B_2 = \sigma_P k_z C - \sigma_H k_H C^2$$
$$B_3 = \sigma_P k_z \frac{\partial S}{\partial x} - \sigma_H k_H \frac{\partial SC}{\partial x}$$

From eqn. (16) we get the polarization field E and the components of $\underline{E}$ can be obtained from eqns (15). Then the components of $\underline{E}'$ can be computed from eqn. (5). Defining the efficiency factor,

$$R = E'_Z / (\underline{W} \times \underline{B})_Z \qquad (18)$$

R is computed for different values of $k_H (= 2\pi/\lambda_H)$ and $k_Z (= 2\pi/\lambda_Z)$; at different altitudes (in region 80 - 140 km, the E region) and at latitudes 0° and 5°.

V.3.2 Comparison of the two dimensional theory with KATO'S one dimensional theory:

The comparison is done by computing R, for the equatorial case, I = 0, at the altitude of 100 km. The horizontal wavelength λ_H is taken to be 50 km (as in KATO'S work) and the values of R for the vertical wavelength λ_Z = 5, 10, 15, 20 km are calculated. Fig. V.3 shows the plot of λ_Z versus R. It includes the results obtained by KATO also (figure 1 of his paper). The solid curve is for the case $H_Z = 0$, i.e., the vertical gradient of electron density is zero. The dashed curve is for the case $H_Z = -k_Z$ (H_Z here corresponds to H^{-1} in KATO'S work). It is seen in the figure that in the case of $H_Z = 0$, the efficiency parameter R increases and reaches an asymptotic value of 0.52 at λ_Z = 20 km. The corresponding value obtained by KATO in his one-dimensional treatment is 0.97 which is thus an over-estimate by a factor of about 2. The difference between the two treatments increases when we consider lower values of λ_Z. Similarly,

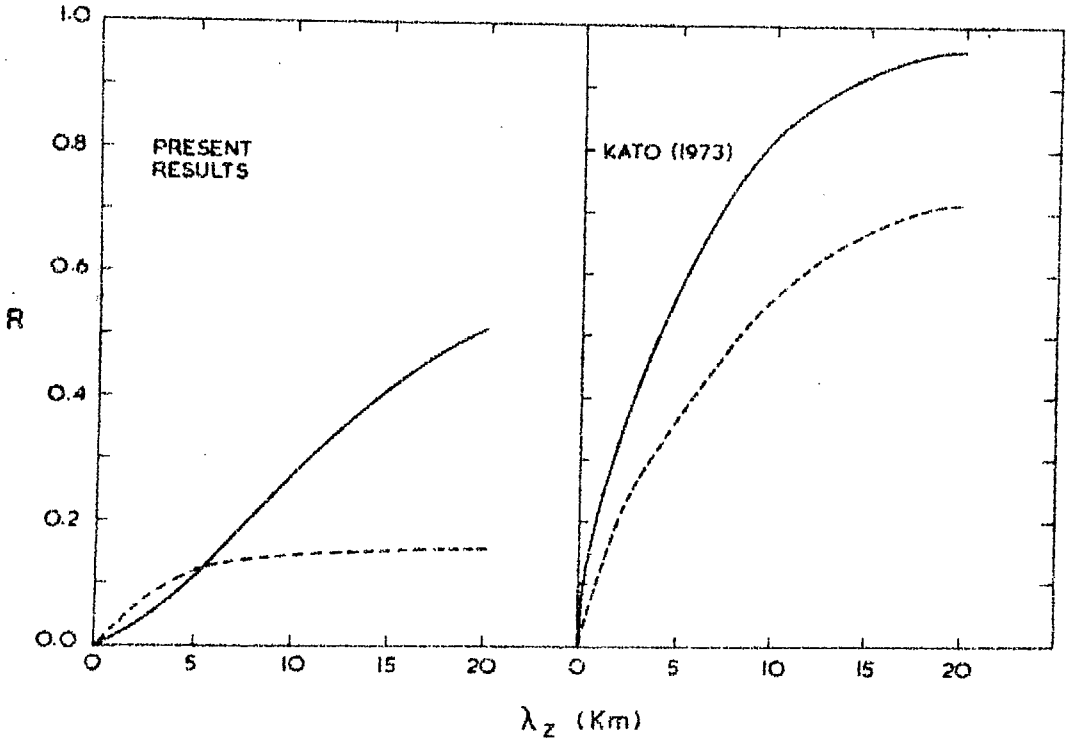

Figure V.3.: The plot of the efficiency factor R versus λ_Z for λ_H = 50 km at 100 km. Solid curve is for the case $H_Z = 0$ and dashed curve is for $H_Z = -k_Z$. On the right is shown the Figure 1 of KATO (1973) for comparison.

for the case $H_z = -k_z$ the asymptotic value of R is 0.15 and the corresponding value obtained in the one-dimensional treatment is 0.72 - an over-estimate by a factor of 5. It is clear now that one should consider the horizontal wave number in comparison with the vertical wave number as seen in the case of $\lambda_H = 50$ km.

V.3.3 Discussion of the results of the two dimensional theory:

The present study emphasizes the importance of the horizontal wavelength. The dependence of R on the horizontal wavelength is shown in Fig. V.4. For the condition $H_z = 0$, the value of the efficiency parameter R reaches a maximum when $\lambda_H \geq 50$ km, for all λ_z. On the other hand, R reaches the maximum value rather slowly at $\lambda_H \geq 200$ km when, $H_z = -k_z$. In the latter case the values of R are slightly greater for $\lambda_z < 10$ and smaller for $\lambda_z > 15$ km, than the values of R in the former case. The author's study shows that the small scale gravity wave winds are not very effective in providing significant values of the efficiency parameter R which, as will be shown later in this chapter, plays an important role in the convergence of the ionization.

Fig. V.5 shows the variation of R with altitude at the dip equator for various λ_z. The horizontal wavelength λ_H is kept at a constant value, viz. 50 km and H_z is assumed to be zero. In this case it is found that the variation of R with λ_H (≥ 50 km) is not appreciable. Thus, the figure represents the altitude variation of R at $\lambda_H \geq 50$ km. The

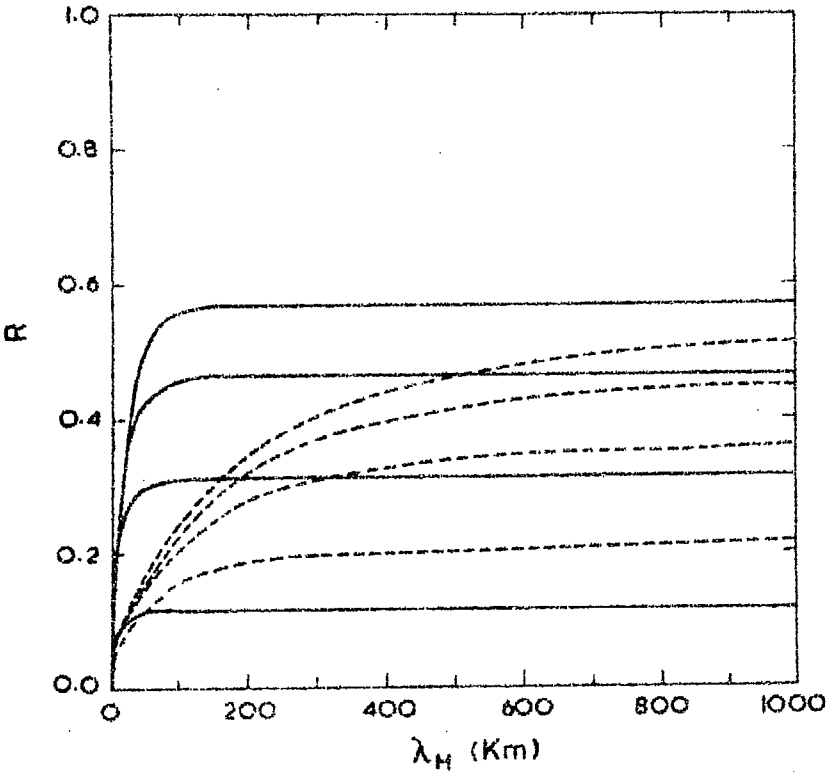

Figure V.4.: The efficiency factor R versus λ_H at 100 km. The set of solid curves is for the case $H_Z = 0$ and that of the dashed curves is for $H_Z = -k_Z$. The four curves in each set are for $\lambda_Z = 5$, 10, 15 and 20 km, starting from bottom to the top of the diagram respectively.

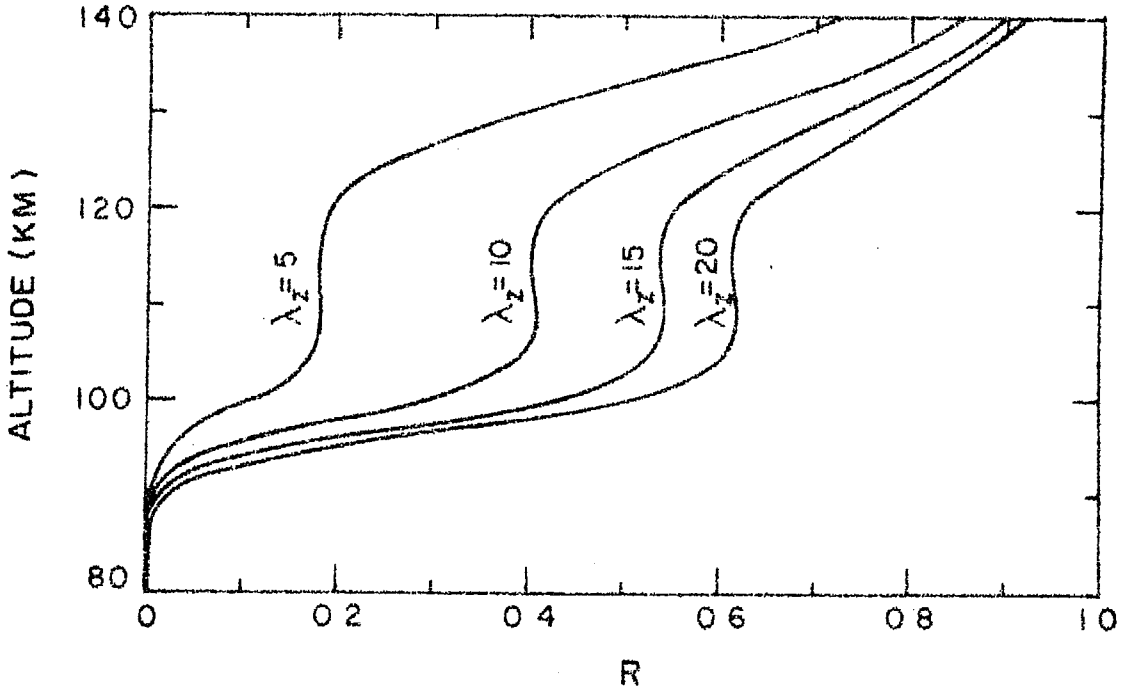

Figure V.5.: The altitude variation of the efficiency factor R at the dip equator, for different vertical wavelengths λ_Z, and for $\lambda_H \geq 50$ km. Hz is taken to be zero.

efficiency parameter R seems to be constant in the region 100-120 km above which it steeply rises and approaches unity. However, the vertical shears in the horizontal winds are rather rarely observed at altitudes above 120 km. They are observed usually in the 90-120 km altitude region.

The efficiency parameter R at low latitudes: The variation of R with altitude, at 5° dip angle is shown in Fig. V. 6. The curve steeply rises and reaches almost unity at 100 km and thereupon remains constant. The variation with λ_z or λ_H is not significant in this case. This shows the effectiveness of the mechanism for regions away from the dip equator. Figs. V.7 and V.8 are the altitude profiles of R for λ_H = 50 km and 200 km respectively. H_z is taken to be equal to $-k_z$ in these cases. It is clear from a comparison of Figs. V.6 and V.7, that the condition $H_z = -k_z$ gives lower efficiencies than the condition $H_z = 0$ which seems to be the prevailing condition for the background electron density N at 100 km. A comparison of Figs. V.7 and V.8 shows that the parameter R increases in general for λ_H = 200 km as compared to the one for λ_H = 50 km.

V.4 Application of the present theory to the observed nighttime equatorial E region irregularities:

Large-scale electron density irregularities with horizontal scale sizes $>$ 60 km and vertical scale sizes $\sim$10 km have been detected in the equatorial E region by PRAKASH ET AL (1970) using a rocket-borne Langmuir probe. These irregularities which are likely to occur in the nighttime

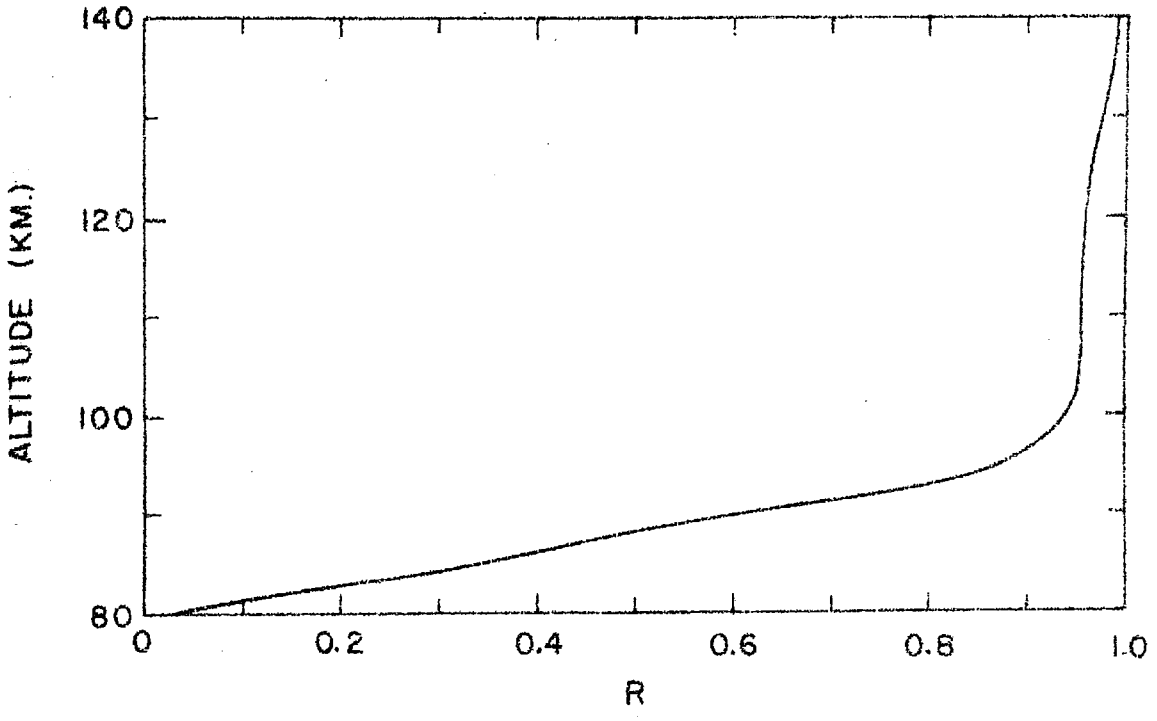

Figure V.6.: The altitude variation of the efficiency factor R at the dip angle 5^{0}. H_Z is taken to be zero. It is to be noted that there is no appreciable variation of the profile of R with λ_Z or λ_H.

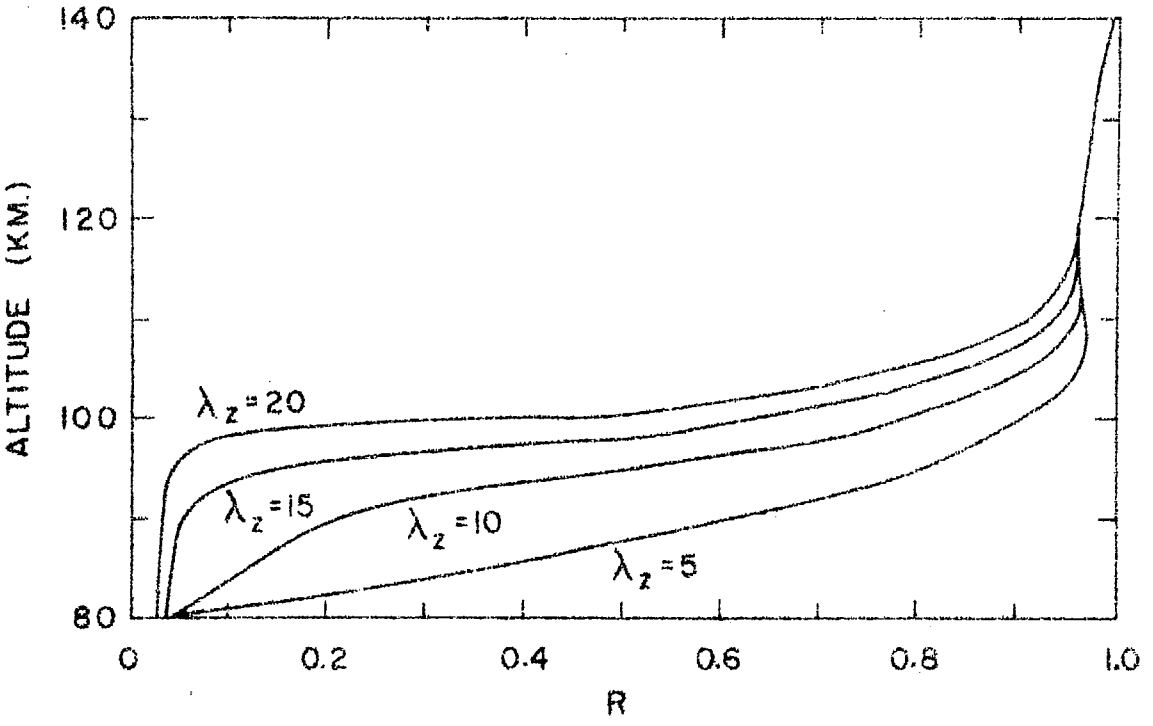

Figure V.7.: Altitude variation of the efficiency factor R at dip angle 5° for different λ_Z and for $\lambda_{H_K} = 50$ km. H_Z is taken to be equal to $-K_Z$.

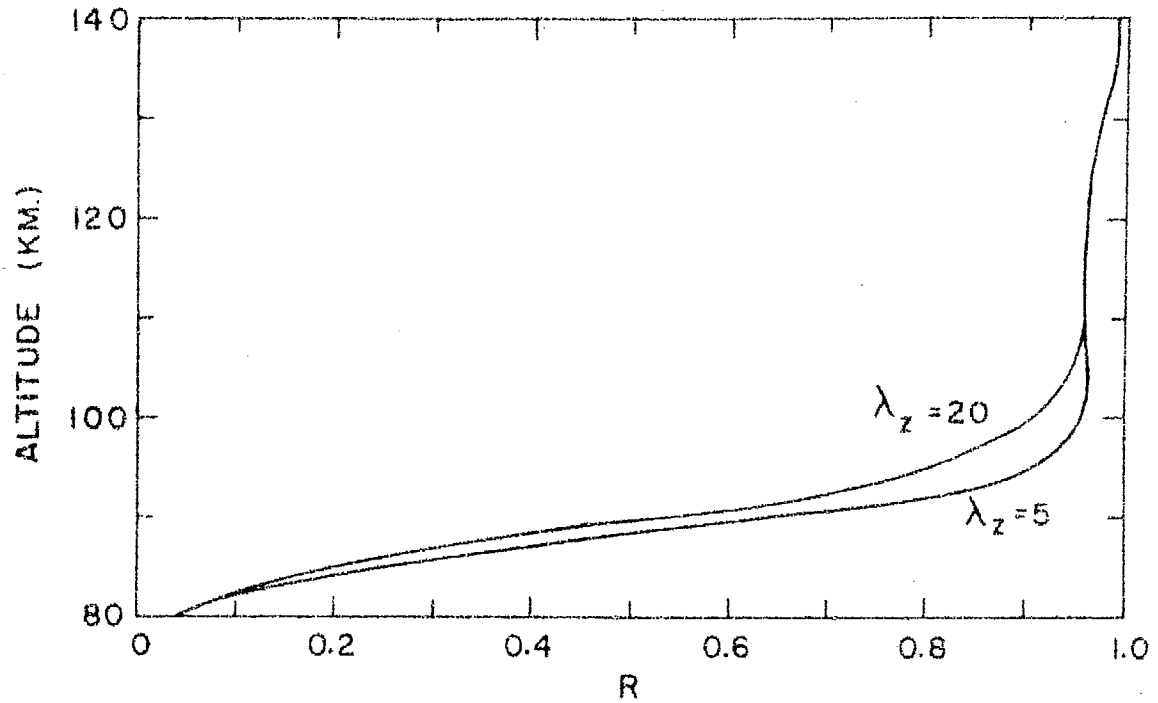

Figure V.8.: Altitude variation of the efficiency factor R at dip angle 5^0 for different λ_Z and for λ_H = 200 km. Hz is taken to be equal to $-k_Z$.

ionosphere are prominent in 90-120 km region. Fig. V.2 shows nighttime electron density profile observed by PRAKASH ET AL (1970).

Although KATO developed one-dimensional theory to explain the formation of these large scale irregularities, his theory suffers from the difficulties pointed out earlier. Therefore, we discuss the interpretation of the large scale irregularities or stratifications in the electron density in the light of the results obtained by the two-dimensional theory and bring out the importance of the horizontal wavelength of the wind in controlling the convergence rates of the ionisation at the E region altitudes. The ion velocity is given by (KATO, 1965),

$$\underline{V_i} = \frac{R_i}{1+R_i^2}\frac{\underline{E'}}{B} + \frac{1}{1+R_i^2}\frac{\underline{E'}\times\underline{B}}{B^2} + \underline{W} \qquad (19)_a$$

where $R_i = \nu_i/\omega_i$, the ratio of the ion collision frequency to the ion gyrofrequency. At the altitude of 100 km, $R_i \geq 10$. Thus, the second term in eqn. $(19)_a$ is negligible, because of the term R_i^2 being in the denominator.

$$\therefore \quad \underline{V_i} \simeq \frac{\underline{E'}}{R_i B} + \underline{W} \qquad (19)_b$$

Taking the divergence

$$\nabla\cdot\underline{V_i} = \frac{\nabla\cdot\underline{E'}}{R_i B} + \frac{\underline{E'}}{B}\cdot\nabla\left(\frac{1}{R_i}\right) + \nabla\cdot\underline{W}$$

For the gravity wave winds, the condition $\nabla . \underline{W} = 0$ is valid (HINES, 1960).

$$\therefore \nabla \cdot \underline{V_i} = \frac{\nabla \cdot \underline{E'}}{R_i B} + \frac{E'_z}{B} \frac{d}{dz}\left(\frac{1}{R_i}\right)$$

(ν_i is a function of neutral particle number density)

We may assume that R_i varies with height only through the collision frequency ν_i.

$$\frac{d(1/R_i)}{dz} = -\frac{1}{R_i}\left(\frac{1}{\nu_i}\frac{d\nu_i}{dz}\right)$$

We can neglect the variation of ω_i with height as the variations of B and the average mass of the ion with height are very small.

$$\therefore \nabla \cdot \underline{V_i} = \frac{k_H E'_y + k_z E'_z}{R_i B} - \frac{E'_z}{B R_i}\frac{1}{\nu_i}\frac{d\nu_i}{dz}$$

$$\frac{1}{\nu_i}\frac{d\nu_i}{dz} \approx -\frac{1}{H}$$

where H is the neutral scale height. As $k_H E'_y \ll k_z E'_z$, the convergence rate of ionisation

$$G = |\nabla \cdot \underline{V_i}| = \left(2\pi R W_y/\lambda_z R_i\right) - \left(R W_y/R_i \nu_i\right)\frac{d\nu_i}{dz} \quad (20)$$

The factor $\frac{1}{\nu_i}\frac{d\nu_i}{dz}$ in the second term on the right hand side is typically about $-0.17 \times 10^{-3} m^{-1}$ at the altitude of 100 km. It can be seen that the magnitude of $\frac{1}{\nu_i}\frac{d\nu_i}{dz}$ decreases slowly with the increase in altitude. Therefore, for a rigorous computation, one has to allow for the variation

of R_i with altitude. It is important to note here that MACLEOD (1966) has taken the collisional gradient term into account in his theory of mid-latitude sporadic E.

Table V.1 shows the rates of convergence, G, for $\lambda_H = 50$ km, and $\lambda_z = 5$, 10, 15, 20 km. H_z is taken to be zero and for the sake of comparison, the values obtained from the present analysis as well as those obtainable from KATO'S work are given in the table. The variation of R_i is not taken into account which,nevertheless, gives a positive contribution to the convergence. We will now see how much could be the contribution from this term. From Fig.V.3 we take the value of R corresponding to $\lambda_z = 20$ km and $H_z = 0$ and substitute in the eqn. (2.0). The value of the first term is $1.5 \times 10^{-3} sec^{-1}$ and that of the second term is $0.9 \times 10^{-3} sec^{-1}$. Thus, the total convergence rate is $2.4 \times 10^{-3} sec^{-1}$. As the second term is contributing substantially, its neglect is hardly justifiable. ANANDARAO ET AL (1977a)have not taken this term into account, because their main aim was to stress the importance of the two-dimensional theory over the one-dimensional theory. Nevertheless, their conclusion, that the rate of convergence mainly depends upon the shear in the wind viz. W_y/λ_z, is still valid. An important feature that deserves to be mentioned is, that the convergence G is almost the same for different values of λ_z when $H_z = 0$ and $\lambda_H \geq 200$ km, since R increases almost linearly with λ_z. On the other hand

Table V.1

Efficiency parameter R and Convergence rate G for λ_H = 50 km and H_z = 0 at different λ_Z. Comparison with the results obtained from KATO (1973 a).

λ_Z (km)	KATO (1973 a)		Present results	
	R	G x 10^3 (s^{-1})	R	G x 10^3 (s^{-1})
5	0.58	7.0	0.11	1.3
10	0.82	4.9	0.28	1.5
15	0.92	3.7	0.41	1.6
20	0.96	2.9	0.50	1.5

Table V.2

Efficiency parameter R and Convergence rate G for λ_H = 50 and 200 km at different λ_Z. H_Z is taken to be equal to $-k_z$. Variation of R_i with altitude is also taken into account.

λ_Z (km)	λ_H = 50 km		λ_H = 200 km	
	R	G x 10^3 (s^{-1})	R	G x 10^3 (s^{-1})
5	0.12	1.6	0.19	2.6
10	0.15	1.2	0.28	2.2
15	0.15	0.9	0.32	1.8
20	0.15	0.8	0.35	1.3

when $H_z = -k_z$, the convergence rates do not differ much for different λ_z. Table V.2 gives the rates of convergence computed from the curves of Fig. V.4, for the case $H_z = -k_z$, for different λ_z and λ_H. While the convergence rates are in general smaller in the latter case ($H_z = -k_z$) than the former ($H_z = 0$); they appear to have an inverse relationship with λ_z. This indicates that the convergence is mainly governed by the wind shear (W_y/λ_z). Nevertheless, when the altitude variation of R_i is taken, the value of the convergence rate increases while the effect of wind shear still prevails. Typically the convergence rate is about $2.4 \times 10^{-3} sec^{-1}$, for a gravity wave of horizontal wavelength 200 km and vertical wavelength $\sim$10 km and when $H_z = 0$. The ionization thus accrued is lost by the loss processes in the ionosphere, mainly due to the recombination. The recombination coefficient at 100 km is $\alpha = 10^{-7} cm^3 sec^{-1}$ (MITRA AND BANERJEE, 1971). The typical value of the electron density N at 100 km is 3 to 7 $\times 10^3 cm^{-3}$ (from Fig. V.2). Thus, the recombination rate is αN = 3 to 7 $\times 10^{-4} sec^{-1}$ which is an order of magnitude less than the rate of convergence obtained by the wind shear mechanism. It is thus possible that the vertical shears of the horizontal (east-west) winds due to gravity waves of large horizontal scale sizes can cause electron density stratifications in the evening hours when the ionization is low. It can be proposed that different

vertical scale sizes revealed by the electron density stratifications in the height region 90-120 km may be attributed to the vertical structure of the wind system in that region of the ionosphere. It may also be noted that the wind shear mechanism is likely to be effective during the daytime as the recombination rates are higher or at best equal to the convergence rates. This is borne out by the observations that the daytime electron density profiles reported by PRAKASH ET AL (1971 a, b) do not reveal any stratifications.

WHITEHEAD AND HOOKE (1971) showed the importance of vertical wind velocity in computing the ion convergence. The vertical winds of only a few meters per second may be as effective in converging the ionization as the large horizontal winds. It is to be noted that in the present calculations of the efficiency parameter R, the effects due to the vertical wind are also considered. It is interesting that the ion convergence is proportional to the vertical wind velocity and not to its gradient ($\partial W_z/\partial z$) for winds of gravity waves with long period ($\omega \ll g/c$) but small vertical wave length ($k_z^2 \gg \frac{1}{4H^2}$).

CHAPTER VI

A THEORETICAL MODEL OF THE EQUATORIAL ELECTROJET INCORPORATING THE EFFECTS OF NEUTRAL WINDS

The vapour release experiments performed over Thumba as discussed in Chapter II showed that the wind shears are usually strong in the region 90-110 km. Furthermore, a few observations identified the presence of vertical winds of magnitude $\sim$ 20 m/s at the electrojet altitudes. We propose to study the effects of neutral winds (both horizontal and vertical) on the electrojet in this Chapter.

A summary of the observed features of the equatorial electrojet is given in section VI.1. In the same section, we also give an account of the phenomenon of counter-electrojet (C-EJ, hereafterwards). We review in VI.2, the models of the equatorial electrojet proposed earlier. We develop a model of the electrojet in VI.3, following the procedure adopted by SUGIURA AND POROS (1969) and incorporating the effects of neutral winds. The structure and distribution of the electrojet with no winds obtained by the present model are discussed and compared with the earlier models in VI.4. The effects caused by the zonal, meridional and vertical winds on the electrojet as computed from the model are discussed in the sections VI.5, VI.6 and VI.7 respectively. In these sections we interpret some of the observed features of the electrojet and C-EJ.

VI.1 The observed features of the phenomenon of equatorial electrojet:

VI.1.1 Normal electrojet:

The electrojet is characterized by a very large range of solar daily variation of the northward component of the geomagnetic field (EGEDAL, 1947; CHAPMAN, 1951). Studies using the data from the ground-based magnetometers established a fairly consistent picture of the latitudinal structure of the electrojet (ONWUMECHILLI, 1967; HUTTON, 1967) as well as its variations with longitude (RASTOGI, 1962; CHAPMAN AND RAJARAO, 1965). Numerous rocket-borne magnetometer measurements (SINGER ET AL, 1951; CAHILL, 1959; MAYNARD AND CAHILL, 1965; MAYNARD, 1967; DAVIS ET AL, 1967; SASTRY, 1970; BURROWS, 1970; BURROWS AND SASTRY, 1976) confirmed that currents in the daytime ionosphere between 90 - 140 km are sufficient to explain the ground-level magnetic variations. These experiments (using ground-based and rocket-borne magnetometers) established the following features of the quiet-day electrojet.

(a) The maximum electrojet current density occurs at an altitude of 106 $\pm$ 2 km (DAVIES ET AL, 1967; SASTRY, 1970).

(b) The maximum current density occurs at around 1100 hrs I.T and is about 10 A/km^2 over the Indian zone. The corresponding ground-level range of northward magnetic field (ΔH) at Thumba is around 100γ (SASTRY, 1970).

(c) The strength of the electrojet increases with sunrise to a maximum around 1100 hrs LT and falls off rather slowly in the afternoon (compared to its rise in forenoon) to its near zero value by about local sunset. On a quiet-day, the electrojet current strength during the night is negligible (ONWUMECHILLI,1959; SASTRY,1970).

(d) The half-width of the electrojet, defined as the latitude on any side of the dip equator at which the current strength falls to one-half of the value at the dip equator, is $\sim 2^{\circ}.5$ for the Indian zone (YACOB AND KHANNA, 1963) and $\sim 3^{\circ}.0$ for the American zone (FORBUSH AND CASAVERDE, 1961).

(e) The thickness of the electrojet, defined as the extent of the region between the altitudes where the current strength falls to one-half of the value at the altitude corresponding to the maximum current strength, is around 15 km at 1100 hrs and becomes broader during the afternoon (SASTRY, 1970).

(f) The electrojet strength and other parameters like the width, thickness etc. vary with longitude. However, the altitude of maximum current strength does not seem to vary with longitude (RASTOGI, 1962; MAYNARD, 1967).

(g) The strength of electrojet and its width and thickness vary from day to day (FORBUSH AND CASAVERDE, 1961; OSBORNE, 1962, 1964; MAYAUD, 1967; BURROWS, 1970;

KANE, 1971; BURROWS AND SASTRY, 1976). These changes are not in correlation with the changes in ΔH at several degrees away from the dip equator.

(h) The width and thickness undergo variations on a single day also (SASTRY, 1970).

(i) Although a major part of the daily variation in H follows the sun, some part of its variation has a lunar tidal origin (BARTELS AND JOHNSTON, 1940; ONWUMECHILLI, 1963, 1964).

(j) The electrojet often displays noticeable asymmetry about the magnetic equator and the degree of asymmetry changes with season, from day-to-day and in the course of an individual day (ONWUMECHILLI, 1959; OSBORNE, 1962; YACOB, 1966).

(k) The intensity of the electrojet was found to be more in solar maximum period than in solar minimum (ONWUMECHILLI, 1967). It also appears that the electrojet is narrower during high solar activity.

VI.1.2 Counter-electrojet during daytime:

GOUIN (1962) reported a case in which the daily variation in the northward component H of the earth's magnetic field at the dip equator was reversed around midday hours. GOUIN AND MAYAUD (1967), HUTTON AND OYINLOYE (1970), ONWUMECHILLI AND AKASOFU (1972), SASTRI AND JAYAKAR (1972) and many others showed examples of similar depressions

during day time. RASTOGI (1974) described many observational characteristics of the phenomenon. In Fig.VI.1 are shown a few examples of H magnetograms at the equatorial stations where significant depression of H field are seen during afternoon hours. The decrease of the H component in the afternoon hours on certain days reach below the nighttime value. It is then called full-counter-electrojet. If the excursion (decrease) in H is present but not strong enough to cross the nighttime level, it is called partial-counter-electrojet .

The latitudinal variations of ΔH and ΔZ during the days of normal electrojet and C-EJ are shown in Fig.VI.2. It is important to note that the latitudinal variation of ΔH on a normal EJ day slowly decreases from the time of maximum (around 1100 hrs LT).

The base of the curve (the level at which the ΔH rises with latitude) gradually increased to a maximum sometime between 1100 and 1200 hrs LT starting from 0700 LT and decreased to zero level by 1800 hrs LT. This increase or shift in the profile can be construed as Sq variation (at low latitudes) with time which is positive throughout the day. On C-EJ day, the latitudinal profile of ΔH decreases much faster, with time of the day, than during the normal EJ day. The profile reverses showing the negative ΔH values

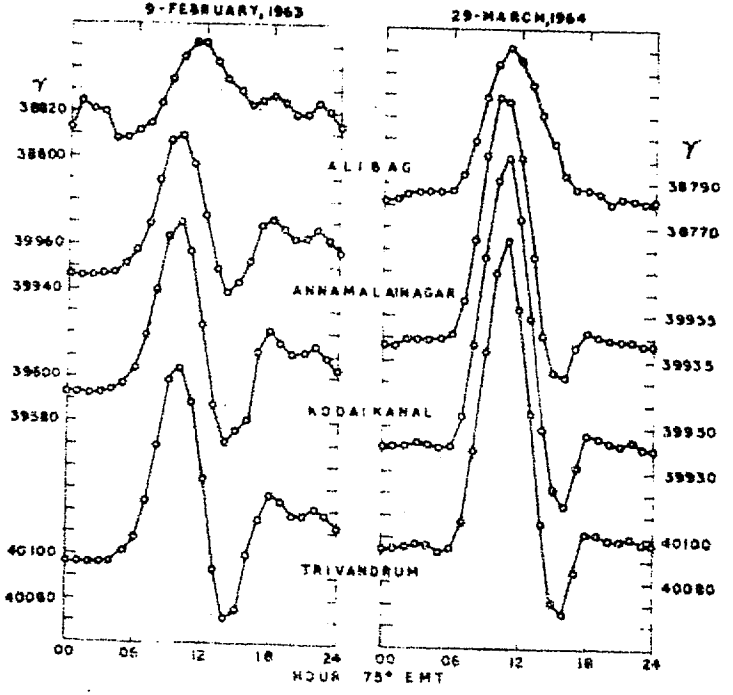

Fig.VI.1:- Daily variations of the H field at geomagnetic stations in India showing evening depressions in H (after RASTOGI, 1974).

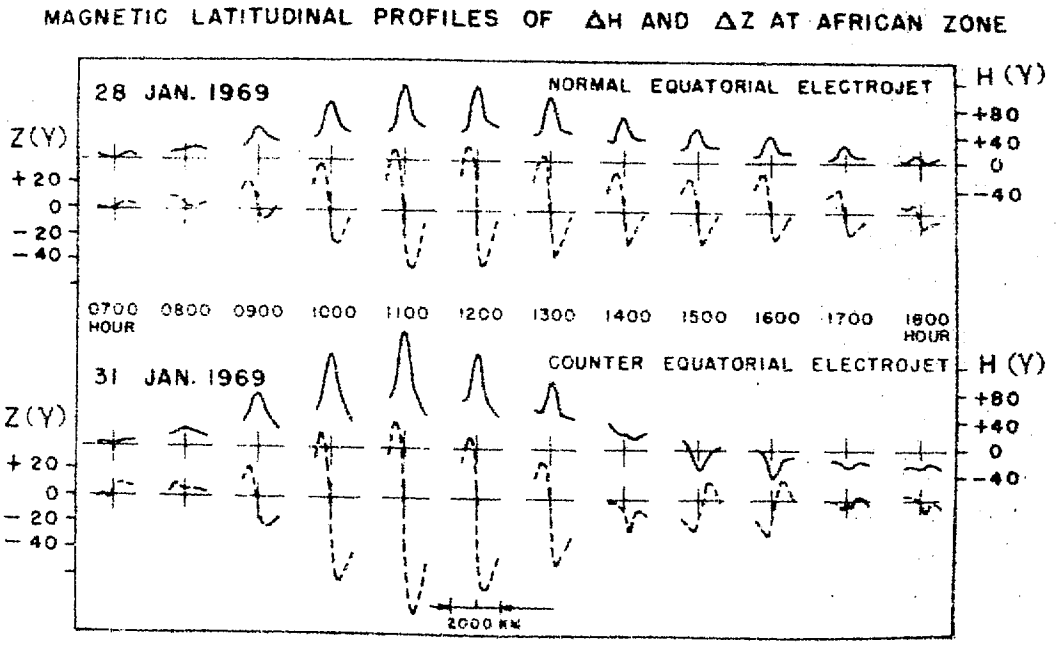

Fig.VI.2:- The latitudinal variations of ΔH and ΔZ at different hours of a day of normal eletrojet and of a day of counter electrojet currents for the African zone (after RASTOGI, 1974).

to occur first (around 1500 LT) in the vicinity of the electrojet and later extending to substantial part of the low latitude region. The extent of the low latitude region showing negative ΔH is different for different C-EJ days. On some occasions of C-EJ the ΔH variation with latitude returns to the +ve values before or at local sunset.

The latitudinal variation of ΔZ on a normal EJ day shows a variation in magnitude (-ve on the north and +ve on the south of dip equator) with the time of the day (increasing till around 1200 hrs LT and then decreasing). During the C-EJ time the pattern reverses and becomes the mirror reflection of its normal profile (-ve on the south and +ve on the north of dip equator).

The salient features of the quiet-day counter-electrojet (C-EJ) occuring during afternoon hours are the following:

(a) The maximum depression in ΔH occurs usually at places close to the dip equator and the effect decreases rapidly with the dip latitude. It is generally believed that counter electrojet is confined to the very narrow region of the normal electrojet (RASTOGI, 1974).

(b) Although the occurrence of C-EJ can be on isolated days, usually the C-EJ occurs on a sequence of days with different values of reduction in ΔH (RASTOGI, 1973).

(c) The occurrence of the C-EJ has some dependence on the lunar phase. It occurs most frequently around new and

full moon days (SASTRI AND JAYAKAR, 1972).

(d) The phenomenon of C-EJ sometimes occurs in a limited longitude zone only. The C-EJ is most common in the longitude zone having weakest normal electrojet currents (RASTOGI, 1974).

(e) The occurrence probability of C-EJ (in the afternoon hours) is maximum during the solar minimum years (GOUIN AND MAYAUD, 1967; HUTTON AND OYINLOYE, 1970).

(f) It is observed that the sporadic E at the equator (E_{s-q}) disappears at the time of the counter-electrojet (KRISHNAMURTHY AND SENGUPTA, 1971, 1972).

(g) The equatorial anomaly, as observed by the daytime trough in the daily variation of the critical frequency of F_2 layer (foF2) at any equatorial station, reveals that the foF2 increases as soon as the C-EJ starts developing. It is then inferred that the upward drift responsible for the trough in foF2 near the dip equator, is inhibited by the decrease of the eastward electric field not only in E region but above E and at F region altitudes as well.

Fig.VI.3 depicts the features mentioned in (e) and (f). It is important to note from the figure that the critical frequency of the F_2 layer (foF2) increases and the height of the layer (hpF2) decreases as the electrojet current (and hence H) decreases. The reverse happens when the H again increases near local sunset before it falls to the near zero night level. The disappearance of E_{s-q} and the

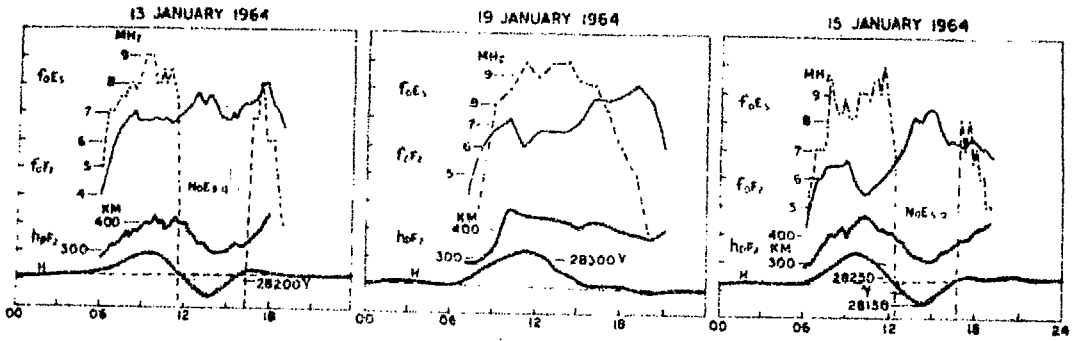

Fig.VI.3:- The variations of the height of peak electron density in the F region (h_pF_2), critical frequencies of the q type E_s (f_oE_s) and of the F_2 region (f_oF_2) at Huancayo on a normal electrojet day (January 19, 1964) and on counter electrojet days (January 13 and 15, 1964). Reproduced from RASTOGI, 1974.

reversal of the drift direction in E region indicate (although indirectly) that the upward electric field in the electrojet decreases and sometimes reverses producing a westward current during C-EJ.

Similarly, the changes in the F region parameters during C-EJ indicate that the daytime eastward electric field in the low latitude dynamo region, either decrease substantially or reverse in order that $\underline{E} \times \underline{B}$ drift (responsible for effectively maintaining the ionization anomaly) is inhibited or reversed. The strong correlation of the variations in the foF2 and hpF2 with that of H during the C-EJ can be explained by such a hypothesis. RASTOGI AND WOODMAN (1977) showed that there is such a reversal of upward drift in the F2 region. The data of vertical and horizontal drifts (in the F and E regions respectively) for a few days, published by BAILSLEY AND WOODMAN (1971), contained one clear example of C-EJ (12 Dec. 1968) where the vertical drift in F2 region shows reversal during C-EJ. Such a reversal in E region drift is not possible to measure even-though it is present, as the irregularities, necessary for coherent backscatter technique to be operative, disappear when the electric field reverses during daytime at these heights where only upward gradient in the electron density is present.

VI.1.3 Correlation of counter electrojet with the ionization ledge in the topside ionosphere:

Ionization ledge formation in the equatorial topside ionosphere was first observed by KING ET AL (1964) as a 'cusp' on the topside ionograms obtained from the Alouette-1 satellite. The ledge is essentially an enhancement over the normal, almost exponentially decreasing electron density profile in the topside ionosphere.

It is essentially a daytime phenomenon and it occurs around 1130 LT above hpF2 over the dip equator and with time moves upward for a few hours. RAGHAVARAO AND SIVARAMAN (1974) satisfactorily explained the formation of the ledge by envisaging an anomaly in the neutral temperature and density in the equatorial ionosphere which is developed by the ionization anomaly. Such an anomaly in N_2 and O densities at F region altitudes was detected by the neutral mass spectrometer on board OGO-6 satellite (HEDIN AND MAYR, 1973). The effect of the neutral anomaly is to inhibit the downward plasma diffusion (which is inversely proportional to the temperature and density of the neutral particles) along the field line on which the crests of neutral temperature and density are located. This results in excess ionization on the top of the field tube which passes through the anomaly crests as compared to the neighbouring field line tubes.

Recent observation on the ledge (RAGHAVARAO ET AL, 1977a;RAGHAVARAO ET AL, 1977b)revealed the following features

which are similar to those of the phenomenon of counter-electrojet. A fairly good correlation was found between the occurrence of the ledge and that of the C-EJ (RAGHAVARAO ET AL, 1977a). The important common features are:

(a) The lunar age dependence of the ledge occurrence is similar to that of counter electrojet (SHARMA, 1976).

(b) Both phenomena occur in the afternoon hours and predominantly during solar minimum period.

(c) The ledge occurs, occasionally, in a limited longitude zone like the occurrence of C-EJ.

VI.1.4 A new mechanism for the cause of counter electrojet:

RAGHAVARAO (1976) proposed a mechanism that can explain satisfactorily the afternoon reversal of the electrojet.

According to his mechanism, the presence of the neutral anomaly leads to excess pressure ridges in the neutral atmosphere on either side of the dip equator. These pressure cells produce winds in the meridional plane which blow toward the equator from both hemispheres, causing an upwelling at and near the equator. This results in vertical winds at the equator. These vertical winds in turn would so act as to inhibit or reverse the electric field causing the decrease or reversal in the current density. A brief description of this mechanism is given in the following pages.

RAGHAVARAO (1976) computed the latitudinal distribution of the exospheric neutral temperature following the

method of HEDIN AND MAYR (1973) from the observed latitudinal distribution of $N_{max}F2$ (from topside ionograms of ISIS-satellites) at 1240 hrs LT when the ledge was present and the counter electrojet was in progress on 6 Oct. 1972. The distribution of $N_{max}F2$ and the exospheric temperature T_∞ are reproduced in Fig.VI.4. The neutral pressure at altitudes above the lowest boundary, 90 km, of the pressure ridges at any particular latitude are generated with the latitudinal profile of T_∞ given in Fig.VI.4. The model atmosphere given in JACCHIA (1970) was used for this calculations. The isobars at fixed altitudes on one side of the dip equator are shown in Fig.VI.5. The maximum pressure bulge occurs between the altitudes of 100 and 160 km. The excess pressure at a particular altitude is then calculated at each latitude.with respect to the value at the magnetic equator. These excess pressure contours are shown in Fig.VI.6 (1 unit = 1.3×10^{-5} dynes/cm^2). The altitude is shown in units of $\log_{10}(P_o/P)$ where P_o is the gas pressure at 90 km and P at any higher altitude. The maximum value of the pressure, 100 units, occurs around 110 km. The horizontal arrows represent the force term $-\frac{1}{P}\frac{dP}{dx}$ that generates the winds.

In the region above 200 km, the neutral flow due to each ridge is essentially in the horizontal direction. The winds are equatorward in the latitude zone 0^o-15^o. From 15^o

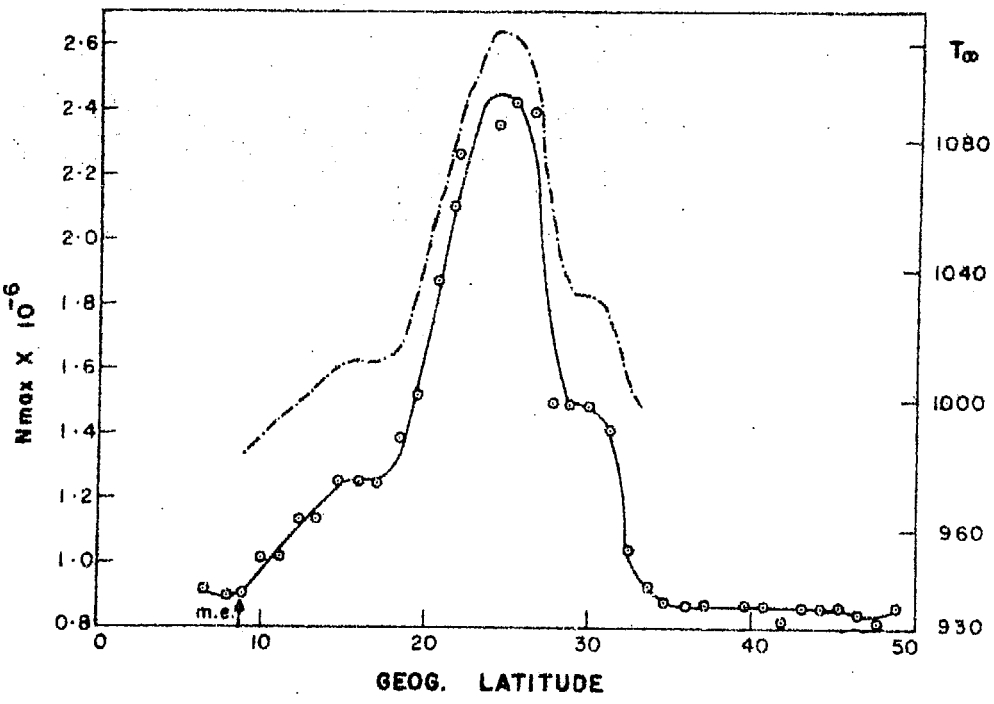

Fig.VI.4:- Latitudinal distribution of $NmaxF_2$ (full curve) obtained by means of ISIS-2 satellite on October 6, 1972, 1240 hrs LT and the calculated exospheric temperature (dot-dashed curve). Reproduced from RAGHAVARAO (1976).

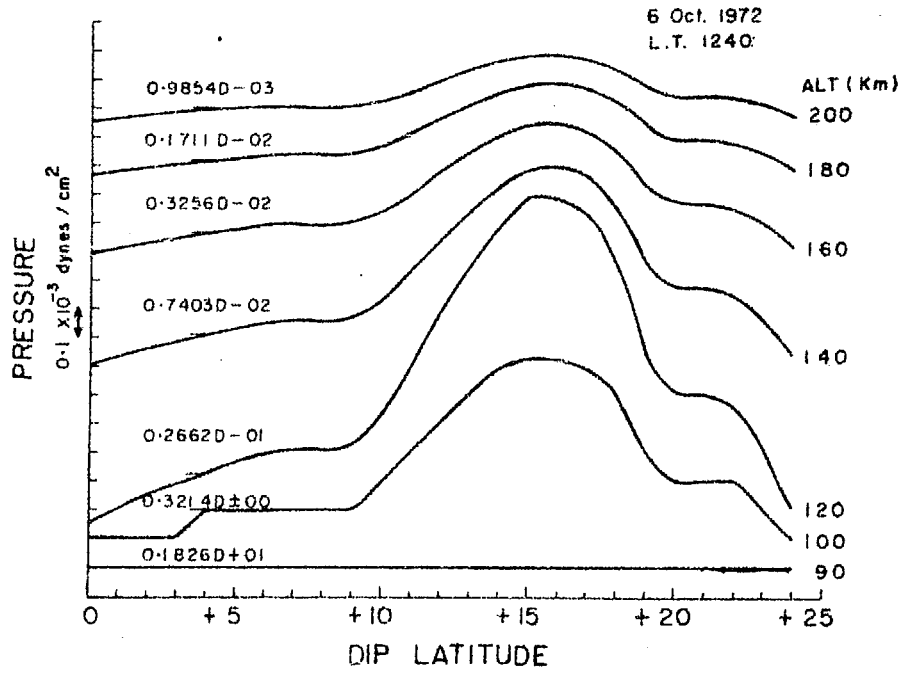

Fig.VI.5:- Latitudinal distribution of pressure at various fixed altitudes on October 6, 1972, for the exospheric temperature profile shown in Fig.VI.4 (after RAGHAVARAO, 1976).

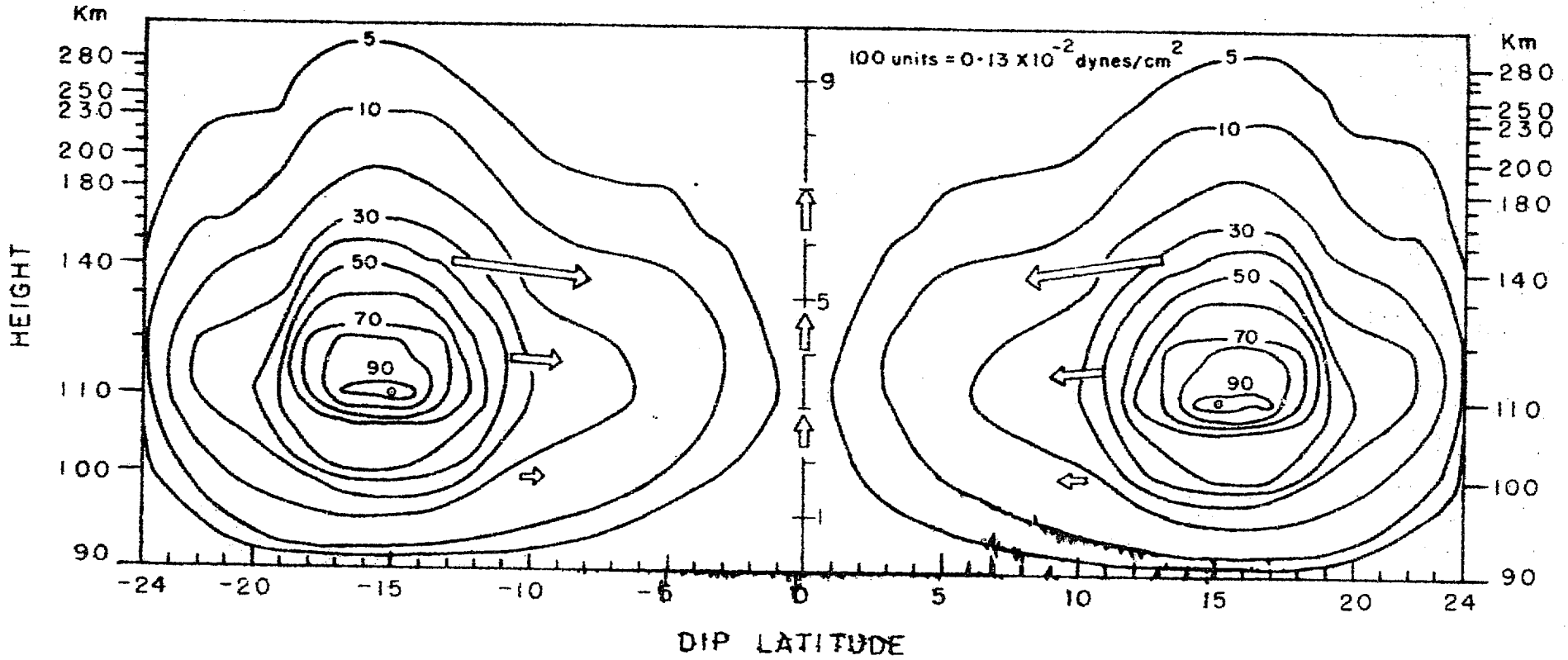

Fig.VI.6:- Excess pressure contours obtained from the distribution shown in Fig.VI.5. The contours on the southern dip latitudes are drawn by assumed symmetry of the anomaly (after RAGHAVARAO, 1976).

and away, the winds are poleward. The wind speed and its spatial variation are controlled by the pressure gradient and the kinematic viscosity; the former drives the winds while the latter opposes the gradients in the wind velocity. The ion-drag force prevents or inhibits substantiall the wind motion perpendicular to the magnetic field (RISHBETH, 1971, 1972).

In the lower part of the thermosphere where the effects due to ion-drag and kinematic viscosity are very small, the excess pressure ridges are likely to set up internal atmospheric gravity waves with a typical period of 5 hrs. The neutral winds would flow towards the equator with a small downward velocity component in the zone of 2^{o}-14^{o} dip latitude on both sides of the equator with maximum wind amplitude around 10^{o} dip latitude. This results in an upwelling in the narrow zone of $\pm 2^{o}$ on either side of the equator giving rise to vertically upward winds. The horizontal (north-south) wave number of the gravity wave thus generated (of a periodicity $\approx$ 5 hours) is inferred to be $k_x = 2.0 \times 10^{-6} m^{-1}$.

The region in which the maximum pressure perturbations occur is however in the lower thermosphere as can be seen in Fig.VI.6 which is a non-isothermal region. The conditions to be satisfied for the propagation of gravity waves in this region are (EINAUDI AND HINES, 1971) that (i) $\alpha > \beta$ and (ii) $\dot{\alpha}/k_x < \sqrt{\alpha/\beta}$. Here $\alpha = \gamma H k_x$ and

$\beta = \omega^2/gk_x$. $\dot{\alpha}$ is variation of α with altitude. H is atmospheric scale height. As these conditions are found to be satisfied, the value of the vertical wave number in the lower thermosphere is taken as $k_z = 3.14 \times 10^{-5} m^{-1}$ (or $\lambda_z = 200$ km).

Applying the asymptotic relationship for the gravity waves (HINES, 1960),

$$\frac{k_x}{k_z} = -\frac{W_z}{W_x} = \frac{1}{16.6}$$

Taking $W_x = 330$ m/s, the sound speed, which is the upper limit of the speed of the gravity waves, W_z is found to be 20 m/s.

Alternatively, one can solve numerically the equations of momentum, continuity, hydrostatic state and thermodynamics and obtain the wind pattern (ROBLE AND DICKINSON, 1970). RAGHAVARAO AND SUHASINI (private communication) calculated the atmospheric motions by numerically solving the equations mentioned above for the region bounded by the neutral anomaly. By this method, they obtained confirmation of RAGHAVARAO'S earlier prediction that the vertical winds are confined to a narrow latitude region around the dip equator. These winds arise essentially to satisfy the nondivergence of the wind system generated as a consequence of the neutral anomaly.

In conformity with the above theoretical prediction, ANANDARAO ET AL (1977 b) reported a wave type vertical profile of vertical winds with a speed of 20 m/s at 100 km altitude by barium vapour releases at 95, 150, 176 and 210 km altitudes over Thumba during the evening twilight hours of 30 March 1968. On the basis of the diurnal variation of the intensity of the ionization anomaly observed by BROWN (1973) and RASTOGI (1966) by the latitudinal variation of foF2 at fixed local times in solar maximum and minimum periods, RAGHAVARAO (1976) expects by his mechanism such a wave-type vertical winds to be present at the evening twilight hours during solar maximum period and in the afternoon hours (1400-1600 hrs LT) during solar minimum period.

RAGHAVARAO (1976) then examined the effect of vertical wind on the Hall polarization field in the electrojet region. The equation of motion for the electron and ion at the E region altitudes can be written as:

$$-e\left[\underline{E} + \underline{V}_e \times \underline{B}\right] - m_e \nu_e \left(\underline{V}_e - \underline{W}\right) = 0 \qquad (1)$$

$$e\left[\underline{E} + \underline{V}_i \times \underline{B}\right] - m_i \nu_i \left(\underline{V}_i - \underline{W}\right) = 0 \qquad (2)$$

Here, $\underline{E}$ and $\underline{B}$ are electric and magnetic fields respectively. $\underline{V}_e$ and $\underline{V}_i$ are the electron and ion velocities, and $\underline{W}$ is neutral wind velocity. It is assumed that the forces due to the partial pressure gradients of the electrons and ions

are negligible. He assumed that vertical currents in the vicinity of the centre of the electrojet are zero which is a close approximation to the realistic situation. This gives

$$V_{ez} = V_{iz}$$

where V_{ez} and V_{iz} are the vertical components of the electron and ion velocities respectively. From the above equation the following relationship between E_z and W_z is obtained.

$$E_z = \frac{\sigma_H}{\sigma_P} E_y - \frac{Ne}{\sigma_P} W_z \left[\frac{1}{R_i^2+1} - \frac{1}{R_e^2+1}\right] - BW_y \quad (3)$$

Here, σ_H and σ_P are Hall and Pedersen conductivities and R_e and R_i are the ratios of the gyrofrequency to collision frequency of electrons and ions respectively. In the electrojet region $R_i \ll 1$ and $R_e \gg 1$, and the eqn. (3) can be simplified as

$$E_z = \frac{\sigma_H}{\sigma_P}\left(E_y - BW_z\right) - BW_y \quad (4)$$

It can be readily seen that a vertical wind of 13 m/s can annul the eastward field, E_y = 0.5 mV/m at the centre of the electrojet for B = 0.38 gauss at 100 km altitude. Also, the vertical wind W_z is σ_H/σ_P ($\simeq$30 at 100 km) times more effective than the eastward wind W_y in reducing the electric field.

The important criterion for the counter electrojet to occur is that the IA crest strengths should attain a sufficient magnitude (>150%) by local noon hours when the

zonal motion of the neutrals reverses from west to east and the ion drag force becomes effective in producing neutral anomaly. It is important to note that the ionisation ledge formation starts around 1130 hrs LT (SHARMA, 1976) and the depression in H associated with the counter electrojet can be construed to begin a few minutes after the maximum in H at around 1100 hrs LT.

VI.2 The models of the electrojet:

BAKER AND MARTYN (1953) obtained the electric field of the ionosphere under the assumption that the vertical currents are zero and the dynamo region is a thin sheet. They have shown that the vertical polarization electric field is maximum in a narrow strip at the equator with a half-width of 3° in latitude and centered at an altitude of about 100 km. Later on, SUGIURA AND CAIN (1966) brought out for the first time the observed longitudinal differences in the electrojet in their numerical model derived from the equations of BAKER AND MARTYN (1953). SUGIURA AND CAIN (1966) assumed that (i) the vertical flow of currents is inhibited and (ii) the north-south electric fields are negligible. These assumptions lead to a very simple equation

$$J_y = \sigma_{yy}(x, y)\, E_y$$

where y is towards east, and x towards magnetic south, σ_{yy} is the layer conductivity and at the dip equator it reduces to the cowling conductivity. σ_{yy} is computed, in this model as a function of x and z. E_y, the primary electric

field, is taken to be a constant and the east-west current density J_y (electrojet) is calculated as a function of x and z. Using a spherical harmonic expansion for the geomagnetic field, they reproduced the general features of the vertical profile of the electrojet as well as the longitudinal differences in the electrojet strength.

UNTIEDT (1967) criticised the above model and proved that it is not self-consistent in that it gives rise to a strongly divergent current system, whereas it is well-known that the ionospheric currents are non-divergent, i.e., $\nabla \cdot \underline{J} = 0$. As an alternative, UNTIEDT (1967) put forth a two-dimensional self-consistent model. Allowance was made for meridional currents and a northward electric field at the magnetic equator, in his model. Inclusion of these meridional currents (which become vertical in the vicinity of the magnetic equator) nearly doubles the magnetic variation obtained from the thin-shell dynamo model (as, for example, in SUGIURA AND CAIN, 1966). This doubling effect relaxes the need for very large wind speeds required to generate the east-west polarization fields (TARPLEY, 1970 b) to reproduce the Sq current system. This happens because the electrojet current sheet broadens both vertically and in north-south direction as well, when one allows for the meridional flow of the currents. UNTIEDT considered a dipole field to represent the geomagnetic field and computed the

electrojet currents by solving a partial differential equation. This model resulted in stronger currents and larger width of the electrojet which are closer to the values derived from the magnetic field (N-S component) variations than those predicted by the σ_{yy} model which neglects the meridional currents. Nonetheless, the σ_{yy} model gives the peak current density to an excellent approximation. UNTIEDT discussed the wind effects on the electrojet though he did not solve the equations including a wind system. He concluded that the east-west winds do not have significant influence on the jet current whereas the north-south winds of large scale sizes may cause the observed asymmetry of the electrojet with respect to the magnetic equator.

SUGIURA AND POROS (1969) considered the spherical harmonic expansion to represent the geomagnetic field and solved for a two-dimensional current system. SUGIURA AND POROS succeeded in reproducing the inequalities in the electrojet current strength at different longitudes. They obtained negative current densities (the main electrojet is eastward and these currents are westward) at about 7^{o}-8^{o} on eitherside of the dip equator. However, the models proposed later by RICHMOND (1973 a,b), ANANDARAO (1976), FORBES AND LINDZEN (1976 b) do not show any such feature. One contention (ANANDARAO, 1976) is that these negative currents were obtained because of larger grid size in solving the equations numerically and hence they are an artifact.

RICHMOND (1973 a,b) examined in detail the physical features of the equatorial electrojet with the aid of a numerical model which includes neutral winds and two-stream instability. He found that the model currents and resultant magnetic variations are not very much affected when the parallel conductivity, σ_0 is assumed to be infinite. This result is important, because the assumption viz. $\sigma_0 \to \infty$, simplifies the mathematical complexities in formulating the model; besides, it means physically that the fields and currents at an altitude are dependent on the conditions over the entire field line passing through the altitude. ANANDRAO ET AL (1977 c) discussed the implications of this result and presented an experimental verification (details of which are given in Chapter IV). Furthermore, RICHMOND (1973 a) showed, considering (1, 1) mode diurnal tidal winds at the equator, that the effect of these winds on the current strength of the electrojet is not very significant at the dip equator. He indicated that the north-south winds cause currents to flow across the equator, but are relatively uninfluential on the eastward currents. He suggested that the day-to-day variations observed in the electrojet parameters can be attributed to the variations in the neutral winds. Changes in various upper atmospheric parameters like temperature, electron and neutral densities, magnetic field strengths, and charged particle collision frequencies with neutrals are tested in

the model to illustrate how the electrojet is sensitive to these changes.

In a recent paper, FORBES AND LINDZEN (1976 b) solved the electrojet for a three-dimensional case. They considered diurnal, semidiurnal and terdiurnal modes of winds away from the equator and studied their effects on the current strengths. The midday flow structure obtained from their model corresponds closely to that predicted by UNTIEDT (1967), SUGIURA AND POROS (1969) and RICHMOND (1973 a). The double peaked structures in the electrojet current profile observed by MAYNARD (1967) near the dip equator, are explainable as being due to local winds (RICHMOND, 1973 a; FORBES AND LINDZEN, 1976 b). FORBES AND LINDZEN (1976 b) could simulate the counter-electrojet effects around 0600 hrs and 1800 hrs by varying the phases of the tidal winds within allowable limits. But the counter electrojet is known to occur during 1400-1600 hrs LT.

VI.2.1 The necessity for the present model:

The vapour release experiments performed over the years at the Thumba Equatorial Rocket Launching Station, India, revealed strikingly regular features regarding the structure of the neutral winds at the E region heights. One of these features is the presence of wind shears, i.e., sharp vertical gradients in the horizontal velocity of the wind. The presence of the wind shears is more common in 90-110 km

region than in any other region of the upper atmosphere. Besides, a few observations revealed the existence of vertical winds (RIEGER, 1974; ANANDARAO ET AL, 1977 b). These observations showed vertical winds of magnitudes as large as 20 m/s at 100 km. At the dip equator, ANANDARAO ET AL (1977b) obtained a vertical profile of vertical winds (Fig. VI.8).

Although, the neutral wind effects were taken into account in the earlier models (e.g. RICHMOND, 1973a; FORBES AND LINDZEN, 1976 b), the effects of wind shears have not been studied in detail. Furthermore, the effects of vertical winds on the electrojet were shown to be important (RAGHAVARAO, 1976). BEDINGER (1977) stressed the importance of north-south winds in the models. We study here the influence of zonal meridional and vertical winds on the equatorial electrojet. After examining critically the effects of shear in the horizontal winds and those of the vertical winds on the electrojet, we identify the nature of winds that can effectively produce the counter electrojet and explain many observed characteristics listed in sections VI.1.1 and VI.1.2. We now present the description of the theory of the model.

VI.3 Theory of the model:

The basic equations are the following:

$$\underline{J} = \sigma_0 \underline{E}_{\parallel} + \sigma_P \underline{E}'_{\perp} + \sigma_H \frac{\underline{B} \times \underline{E}'_{\perp}}{B} \qquad (5)$$

With the condition

$$\nabla \cdot \underline{J} = 0, \tag{6}$$

which is a necessary condition and is imposed in the region of interest. And we assume

$$\nabla \times \underline{E} = 0 \tag{7}$$

which means that the phenomenon we consider here is in a quasi-steady state. In these equations

$$\underline{E}' = \underline{E} + \underline{W} \times \underline{B} \tag{8}$$

where $\underline{E}$ is the polarization field produced by the electrodynamical effects due to the wind $\underline{W}$. σ_0, σ_P, σ_H are the direct, Pedersen and Hall conductivities. $\underline{B}$ is the geomagnetic field.

We choose a geocentric coordinate system (r, θ, ϕ), where r is the radial distance of any point from the centre of the earth, θ is the colatitude and ϕ is the longitude. The variation of the ionospheric parameters involved in the model calculations with respect to ϕ is neglected. RICHMOND (1973 a) estimated the error due to the above assumption to be about 14% in the electrojet current, if the fields and conductivities are varying in ϕ direction with typical scale lengths of 6490 km (or 1 radian in ϕ).

The condition in eqn. (6) will yield, when $d/d\phi = 0$

$$\underline{J} = \nabla \times \underline{A}$$

Let A_ϕ be the component of vector potential $\underline{A}$ in ϕ direction and a be the radius of the earth. The above equation

in components is written as

$$J_r = -\frac{a}{r^2 \sin\theta}\frac{\partial}{\partial\theta}(r\sin\theta A_\phi)$$

$$J_\theta = \frac{a}{r\sin\theta}\frac{\partial}{\partial r}(r\sin\theta A_\phi)$$

$$\psi = r\sin\theta A_\phi$$

$$J_r = -\frac{a}{r^2\sin\theta}\frac{\partial\psi}{\partial\theta}\ ;\ J_\theta = \frac{a}{r\sin\theta}\frac{\partial\psi}{\partial r} \qquad (9)$$

ψ is a current function

From eqn. (7) we have

$$\frac{\partial}{\partial\theta}(E_\phi \sin\theta) = 0$$

$$\frac{\partial}{\partial r}(r E_\phi) = 0$$

$$\frac{\partial}{\partial r}(r E_\theta) - \frac{\partial}{\partial\theta}E_r = 0 \qquad (10)$$

by neglecting $\partial/\partial\phi$. It is clear from the first two equations of (10) that E_ϕ can be represented by

$$E_\phi = f_r \cdot f_\theta$$

where f_r and f_θ are functions of r and θ respectively. Substitution of the above equation in the first two equations in (10) yields,

$$\frac{d}{d\theta}(f_\theta \sin\theta) = 0\ ;\ \frac{d}{dr}(r f_r) = 0$$

$$f_\theta = \alpha / \sin\theta \; ; \; f_r = \beta / r$$

where α and β are two constants. At the equator Sin $\theta = 1$ and $r \approx a$. The constants are given by

$$\alpha\beta = a\, E_{\phi 0}$$

$$E_\phi = f_r f_\theta$$

$= a\, E_{\phi 0}/r$, at the equator and at any other location

$$E_\phi = \frac{a\, E_{\phi 0}}{r \sin\theta} \qquad (11)$$

$E_{\phi 0}$ is a constant and it is the primary eastward electric field to be furnished as an input to calculate the current function,

The components of $\underline{J}$ from eqn. (5) in r, θ, ϕ directions are:

$$\begin{aligned}
J_r &= (\sigma_0 S^2 + \sigma_p C^2)\left[E_r + (\underline{W} \times \underline{B})_r\right] \\
&\quad + (\sigma_0 - \sigma_p)\left[E_\theta + (\underline{W} \times \underline{B})_\theta\right] SC - \sigma_H \left[E_\phi + (\underline{W} \times \underline{B})_\phi\right] C \\
J_\theta &= (\sigma_0 - \sigma_p)\left[E_r + (\underline{W} \times \underline{B})_r\right] SC \\
&\quad + (\sigma_0 C^2 + \sigma_p S^2)\left[E_\theta + (\underline{W} \times \underline{B})_\theta\right] + \sigma_H \left[E_\phi + (\underline{W} \times \underline{B})_\phi\right] S \\
J_\phi &= \sigma_H \left[E_r + (\underline{W} \times \underline{B})_r\right] C - \sigma_H \left[E_\theta + (\underline{W} \times \underline{B})_\theta\right] S \\
&\quad + \sigma_p \left[E_\phi + (\underline{W} \times \underline{B})_\phi\right]
\end{aligned} \qquad (12)$$

The following equations for E_r and E_θ can be obtained easily.

$$E_r = -(\underline{W} \times \underline{B})_r + \frac{\sigma_H}{\sigma_P}\left[E_\phi + (\underline{W} \times \underline{B})_\phi\right] C + J_r(\rho_0 C^2 + \rho_P S^2) - J_\theta(\rho_0 - \rho_P) SC \qquad (13)$$

and,

$$E_\theta = -(\underline{W} \times \underline{B})_\theta - \frac{\sigma_H}{\sigma_P} S\left[E_\phi + (\underline{W} \times \underline{B})_\phi\right] - J_r(\rho_P - \rho_0) SC + J_\theta(\rho_P S^2 + \rho_0 C^2) \qquad (14)$$

where $\rho_0 = 1/\sigma_0$ and $\rho_P = 1/\sigma_P$

S = Sin I and C = Cos I

Substituting the eqns. (13) and (14) along with the eqn.(9) in the last eqn. of (10) we get the following partial differential equation

$$f_1 \frac{\partial^2 \Psi}{\partial r^2} + 2f_2 \frac{\partial^2 \Psi}{\partial r \partial \theta} + f_3 \frac{\partial^2 \Psi}{\partial \theta^2} + f_4 \frac{\partial \Psi}{\partial r} + f_5 \frac{\partial \Psi}{\partial \theta} + f_6 = 0 \qquad (15)$$

This is a second degree elliptic partial differential equation - "elliptic" because, the discriminant $(f_2^2 - f_1 f_3)$ is negative. The coefficients f_1 to f_6 are functions of r, θ and the ionospheric conductivities. These are given by,

$$f_1 = \rho_P S^2 + \rho_0 C^2$$

$$f_2 = \frac{1}{r}(\rho_P - \rho_0) SC$$

$$f_3 = \frac{1}{r^2}(\rho_P C^2 + \rho_0 S^2)$$

$$f_4 = \frac{\partial}{\partial r}(\rho_P S^2 + \rho_0 C^2) - \frac{1}{r} \cot\theta\,(\rho_P - \rho_0) SC + \frac{1}{r} \frac{\partial}{\partial \theta}(\rho_P - \rho_0) SC \qquad (16)$$

$$f_5 = \frac{1}{r} \frac{\partial}{\partial r}(\rho_P - \rho_0) SC - \frac{1}{r^2}(\rho_P - \rho_0) SC - (\cot\theta / r^2)(\rho_P C^2 + \rho_0 S^2) + \frac{1}{r^2} \frac{\partial}{\partial \theta}(\rho_P C^2 + \rho_0 S^2)$$

The last coefficient f_6 is composed of two terms (i) f_{6o} which is equal to f_6 when winds are not considered and (ii) f_{6W}, arising due to winds. These are

$$f_{6o} = -E\phi_o\left[\frac{1}{r}\frac{\partial}{\partial\theta}\left(\frac{\sigma_H}{\sigma_P}C\right) - \frac{1}{r}\frac{\sigma_H}{\sigma_P}C\cot\theta + \frac{\partial}{\partial r}\left(\frac{\sigma_H}{\sigma_P}S\right)\right] \quad (17)$$

and wind-contribution

$$\begin{aligned} f_{6W} = \frac{\sin\theta}{a}\Bigg[& -\frac{\sigma_H}{\sigma_P}(\underline{W}\times\underline{B})_\phi\left\{S + \frac{rS}{\sigma_H/\sigma_P}\frac{\partial(\sigma_H/\sigma_P)}{\partial r} + \frac{C}{(\sigma_H/\sigma_P)}\frac{\partial(\sigma_H/\sigma_P)}{\partial\theta} + \frac{\partial C}{\partial\theta}\right\} - (\underline{W}\times\underline{B})_\theta \\ & - \frac{\sigma_H}{\sigma_P}\left\{rS\left(W_r\frac{\partial B_\theta}{\partial r} - W_\theta\frac{\partial B_r}{\partial r}\right) + \left(B_\theta\frac{\partial W_r}{\partial r} - B_r\frac{\partial W_\theta}{\partial r}\right)rS \right. \\ & \left. + C\left(W_r\frac{\partial B_\theta}{\partial\theta} - W_\theta\frac{\partial B_r}{\partial\theta} + B_\theta\frac{\partial W_r}{\partial\theta} - B_r\frac{\partial W_\theta}{\partial\theta}\right)\right\} \\ & - r\left(W_\phi\frac{\partial B_r}{\partial r} - W_r\frac{\partial B_\phi}{\partial r} + B_r\frac{\partial W_\phi}{\partial r} - B_\phi\frac{\partial W_r}{\partial r}\right) \\ & + W_\theta\frac{\partial B_\phi}{\partial\theta} - W_\phi\frac{\partial B_\theta}{\partial\theta} + B_\phi\frac{\partial W_\theta}{\partial\theta} - B_\theta\frac{\partial W_\phi}{\partial\theta}\Bigg] \end{aligned} \quad (18)$$

The eqn. (15) is solved for ψ numerically using the method of "successive over-relation" (described in Appendix-I). After obtaining ψ (r, θ), the components of the current density J_r and J_θ are computed using the eqn (9). J_r and J_θ are used then to compute E_r and E_θ from eqns. (13) and (14). Finally, J_ϕ, the electrojet current density is computed using the last of the eqn. (12).

Neutral atmosphere model:- The neutral atmospheric parameters relevant for the computation of conductivities are the neutral temperature, density and mean molecular weight.

These are calculated from the model atmosphere described by JACCHIA (1971) for solar minimum period. This model gives the parameters at and above 90 km only. But we changed the lower boundary to 80 km, assuming that the temperature does not vary between 80 and 90 km.

Table VI.1 gives these parameters in the altitude range of 80-200 km. It is assumed that the electron temperature is equal to the gas temperature.

Geomagnetic field model:- The geomagnetic field is assumed to be,

$$\underline{B} = -\nabla V \tag{19}$$

where, V is a scalar potential.

$$V = a \sum_{n=1}^{\infty} \left(\frac{a}{r}\right)^{n+1} \sum_{m=0}^{n} P_n^m(\cos\theta)\left[g_n^m \cos m\phi + h_n^m \sin m\phi\right] \tag{20}$$

Here, r is the radial distance increasing outward, θ is the colatitude increasing southward, and ϕ is the longitude increasing eastward. $P_n^m(\cos\theta)$ is a modified form of associate Legendre Polynomial known as the Schmidt function of degree n and order m. a is the radius of the earth. When $n = 1$ and $m = 0$, $P_1^0 = \cos\theta$ and the magnetic field will be that of simple dipole. This is independent of ϕ, the longitude. In order to take the longitudinal variation of the magnetic field into account, the higher order multipoles are included in the eqn. (19) (CAIN ET AL, 1965). The geomagnetic field represented by 48 coefficients (CAIN ET AL, 1965) is taken for the present computation.

TABLE VI. 1

The neutral atmospheric parameters and the electron density profile at 1100 hrs.

Altitude (km)	Neutral gas density n(part./cm^3)	Electron density N(part./cm^3)	Neutral gas temperature T(^{o}K)	Mean Molecular Mass M
80	0.4316E+15	0.2466E+04	0.1830E+03	0.2883E+02
90	0.7224E+14	0.6918E+05	0.1830E+03	0.2883E+02
100	0.1199E+14	0.1294E+06	0.1941E+03	0.2764E+02
110	0.2251E+13	0.1472E+06	0.2431E+03	0.2655E+02
120	0.5758E+12	0.1648E+06	0.3336E+03	0.2545E+02
130	0.2076E+12	0.1762E+06	0.4437E+03	0.2447E+02
140	0.9722E+11	0.2168E+06	0.5465E+03	0.2363E+02
150	0.5390E+11	0.2805E+06	0.6318E+03	0.2289E+02
160	0.3330E+11	0.2805E+06	0.6957E+03	0.2222E+02
170	0.2208E+11	0.2805E+06	0.7509E+03	0.2162E+02
180	0.1536E+11	0.2805E+06	0.7921E+03	0.2106E+02
190	0.1107E+11	0.2805E+06	0.8251E+03	0.2055E+02
200	0.8191E+10	0.2805E+06	0.8520E+03	0.2009E+02

Electron density profiles:- The electron density profiles measured by the rocket-borne Langmuir probes at 1100 hrs (REES ET AL, 1976), 1420 hrs (SUBBARAYA ET AL, 1972) and 1532 hrs (PRAKASH ET AL, 1976) are used in the computation of the conductivities. It is assumed that within the boundaries ($\pm$ 10^{0} dip latitude) of the region of present interest, the electron density does not change appreciably and thus the profiles are assumed to be latitude independent.

Collision frequencies and conductivities:- The expressions used for the computation of the collision frequencies are as follows (CHAPMAN, 1956)

Electron - neutral collision frequency

$$\nu_{en} = 5.4 \times 10^{-10} n T^{\frac{1}{2}}$$

Electron - ion collision frequency

$$\nu_{ei} = 34 + 4.18 \log_{10}(T^3/N)\ NT^{-3/2}$$

Ion - neutral collision frequency

$$\nu_{in} = 2.6 \times 10^{-9} n\ M^{-\frac{1}{2}}$$

Here n and N are the neutral and electron number densities respectively (given in particles/cm^3). T is the gas temperature and M, the mean molecular mass. Then the conductivities are computed using the formulas given in the section I.6.

Recent work on the collision processes (BANKS, 1966a,b; PACK AND PHELPS, 1961; STUBBE, 1968; MASON, 1970) is more commonly used now to compute the collision frequencies. These

formulas need the knowledge of electron temperature and other parameters. However, we believe that the simpler formulas given by CHAPMAN (1956) are adequate for the present purpose. Furthermore, RICHMOND (1973 a) estimated the change in the ground-level ΔH corresponding to a change of 10% in ν_i to be $\lesssim$10% at the equator and still smaller outside the equator. A change of 10% in ν_e would lead to a change of $\lesssim$2% in ΔH at the equator. As the uncertainties are always present in the collision frequencies, it was thought that the CHAPMAN'S formulas serve the present purpose. Fig.VI.7 shows the profiles of the direct, Pedersen, Hall and Cowling conductivities at 1100 hrs LT and for solar minimum period.

Boundary conditions:- The boundary conditions used are $\psi = 0$ at 80 km$\lesssim r \lesssim$200 km* and $80^\circ \lesssim \theta \lesssim 100^\circ$. The step sizes in r and θ viz. h_r and h_θ are 2 km and $0^\circ.5$ respectively.

Physical validity of the numerical solutions:- The physical validity of the numerical solutions obtained is checked by the following tests. (i) The boundaries of the region in which we seek the solutions are changed to 70 km and 350 km in r and 78° and 102° in θ. (ii) The boundary conditions are changed. (iii) The step-sizes in r and θ are changed to 1 km and $0^\circ.25$ respectively. (iv) The number of reliable significant digits (the accuracy) of the solutions is increased. On the basis of these tests it is concluded that the boundary conditions

* Here r does not include the earth's radius.

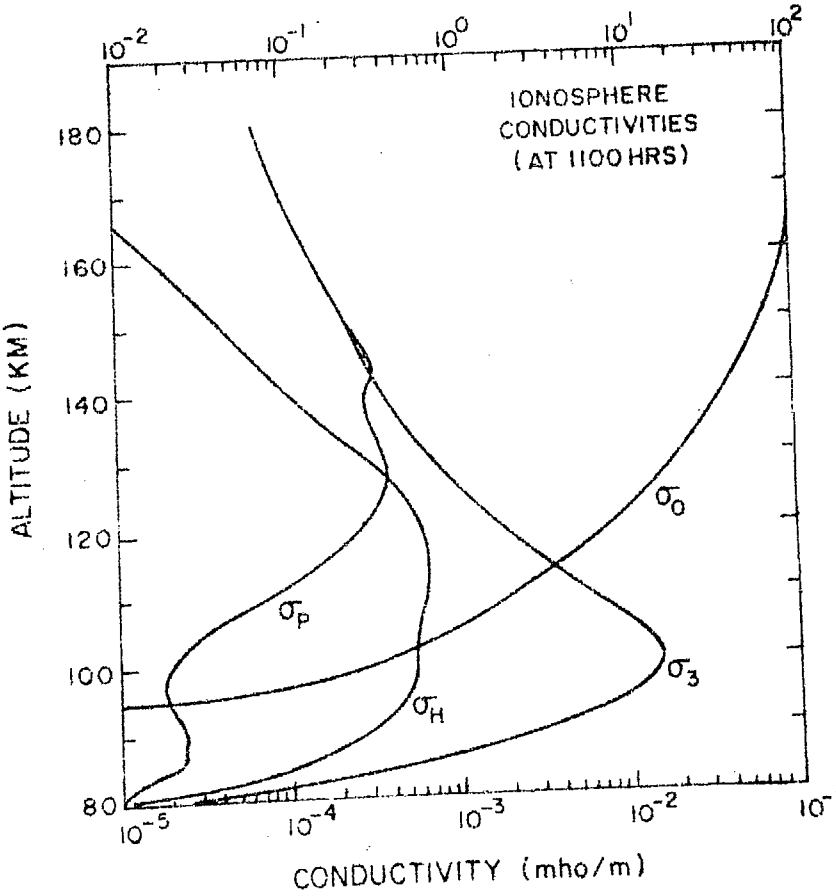

Fig.VI.7:- Profiles of the direct (σ_0), Pedersen (σ_P), Hall (σ_H) and Cowling (σ_3) conductivities computed by using Jacchia (1971) model for the neutral atmosphere (Table VI.1) and an observed electron density profile at 1100 hrs IST. The scale on the top of the figure is for σ_0. The scale on the bottom is for the other three conductivities.

$\psi = 0$ at 80 km $\leq r \leq$ 200 km and $80^{\circ} \leq \theta \leq 100^{\circ}$; the step sizes h_r = 2 km and $h_\theta = 0^{\circ}.5$; and the accuracy of 0.5×10^{-3} (which means the solutions are reliable upto the third significant digit) give fairly good and physically valid results.

VI.4 Electrojet with no-winds:

It is pertinent here to examine how f_{60} (with no winds) varies with altitude and latitude. f_{60} is given by(eqn. 17).

$$f_{60} = -E_{\phi_0}\left[\frac{1}{r}\frac{\partial}{\partial\theta}\left(\frac{\sigma_H}{\sigma_P}C\right) - \frac{1}{r}\frac{\sigma_H}{\sigma_P}C\cot\theta + \frac{\sigma_H}{\sigma_P}\frac{\partial S}{\partial r} + S\frac{\partial(\sigma_H/\sigma_P)}{\partial r}\right]$$

The dominant term in the coefficient f_{60} is the last term. From the profile of σ_H/σ_P (as shown in Fig. IV.5) it can be seen that the vertical gradient of σ_H/σ_P is positive below about 100 km and negative above that altitude. Therefore, the coefficient f_{60} is negative below the altitude of 100 km and positive above it in the northern hemisphere. This polarity of the coefficient reverses in the southern hemisphere. At the equator the coefficient is very small compared to that at other latitudes.

The eqn.(15) is solved for ψ first without introducing winds. The electron density profiles measured at 1100 hrs and 1420 hrs IST by the rocket-borne Langmuir probes from TERLS are used to calculate the conductivities

at these local times.

Fig.VI.8 shows the vertical profile of the eastward current density (the electrojet) J_ϕ at 1100 hrs LT. The profiles are given at 0°, 2° and 4° magnetic latitudes (same as dip-latitude). The current density maximizes at an altitude of about 100 km and falls steeply above and below this altitude. The altitude of the maximum current density seems to be decreasing with increase in latitude. The profiles of the vertical electric field E_r shown in Fig.VI.9 follow closely the J_ϕ profiles. E_r reaches an asymptotic value above about 130-140 km and this result is in conformity with the profile of F ($=\int\sigma_H ds / \int\sigma_P ds$) in the Fig.IV.5 of Chapter IV. Fig. VI.10 shows the profiles of the vertical current density J_r at 1100 hrs LT. The vertical current density J_r is larger at the equator than at 2° or 4°. J_r reaches a maximum of about 0.3 A/km^2 at an altitude of 120 km over the equator. In general, J_r is quite small compared to the eastward current density J_ϕ. The profiles of the meridional current density J_θ at 1100 hrs LT are shown in Fig.VI.11. At the equator J_θ is negligibly small. A few degrees away from the equator, J_θ becomes comparable to J_ϕ and at higher altitudes J_θ is greater than J_ϕ. The maximum (positive) of J_θ at 2° and 4° occurs at about 100 km. Fig.VI.12 and VI.13 show the

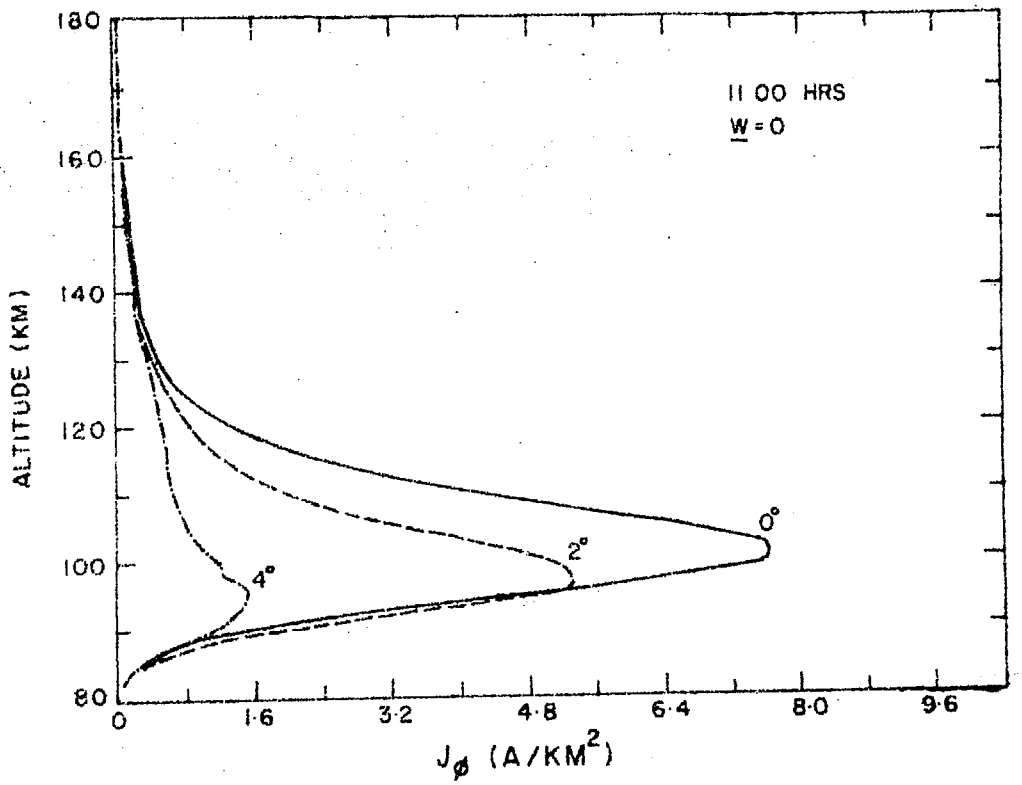

Fig.VI.8:- Vertical profiles of eastward (+ve) current density $J\phi$ (in Amperes/km^2) at 0° (dip equator), 2° and 4° magnetic latitude at 1100 hrs LT. The profiles are for no-wind case ($\underline{W} = 0$).

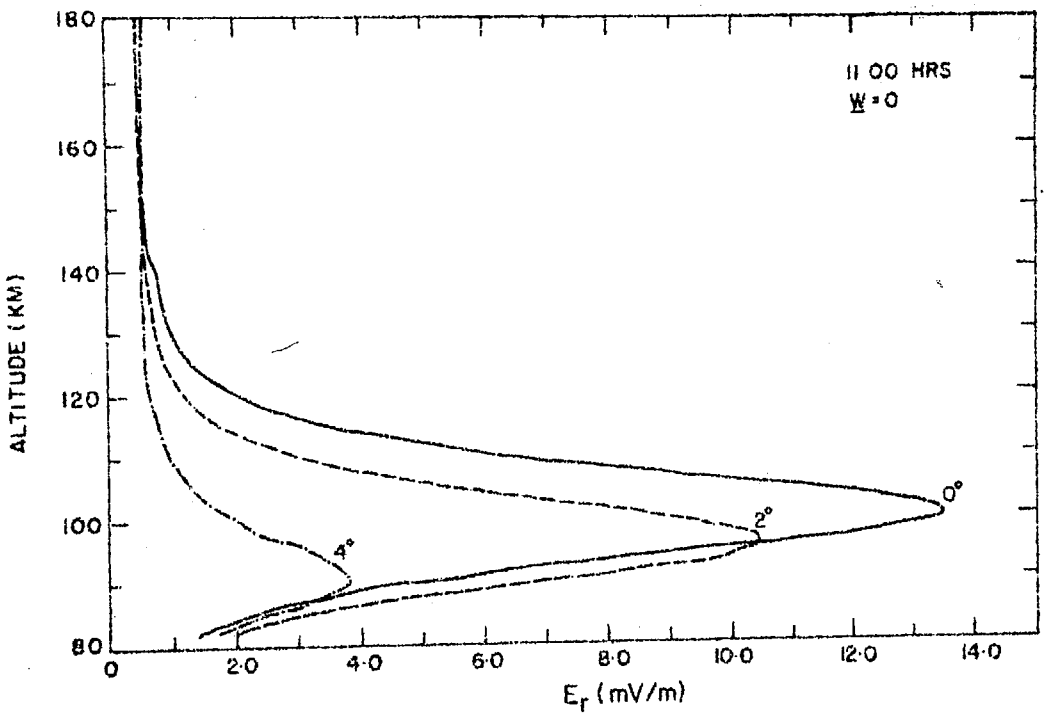

Fig.VI.9:- Vertical profiles of vertical (+ve upward) electric field E_r (in milli volts/meter) at 0°, 2° and 4° magnetic latitudes at 1100 hrs LT. The profiles are for no-wind case.

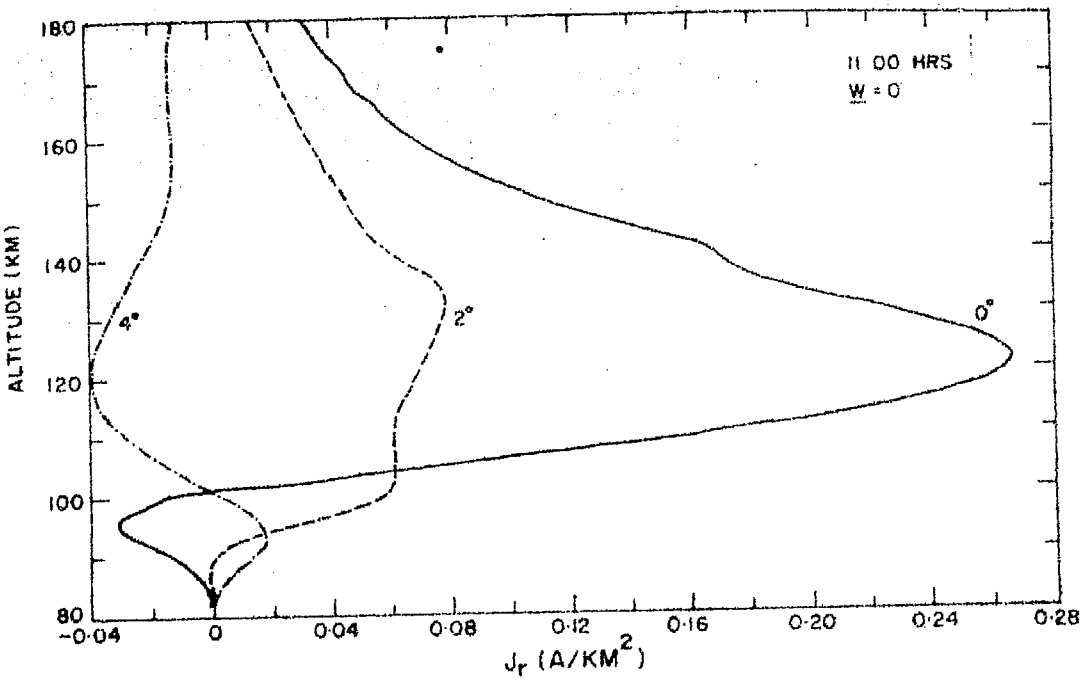

Fig.VI.10:- Vertical profiles of vertical current density Jr at 0°, 2° and 4° magnetic latitude. The profiles are for 1100 hrs LT and for no-wind case.

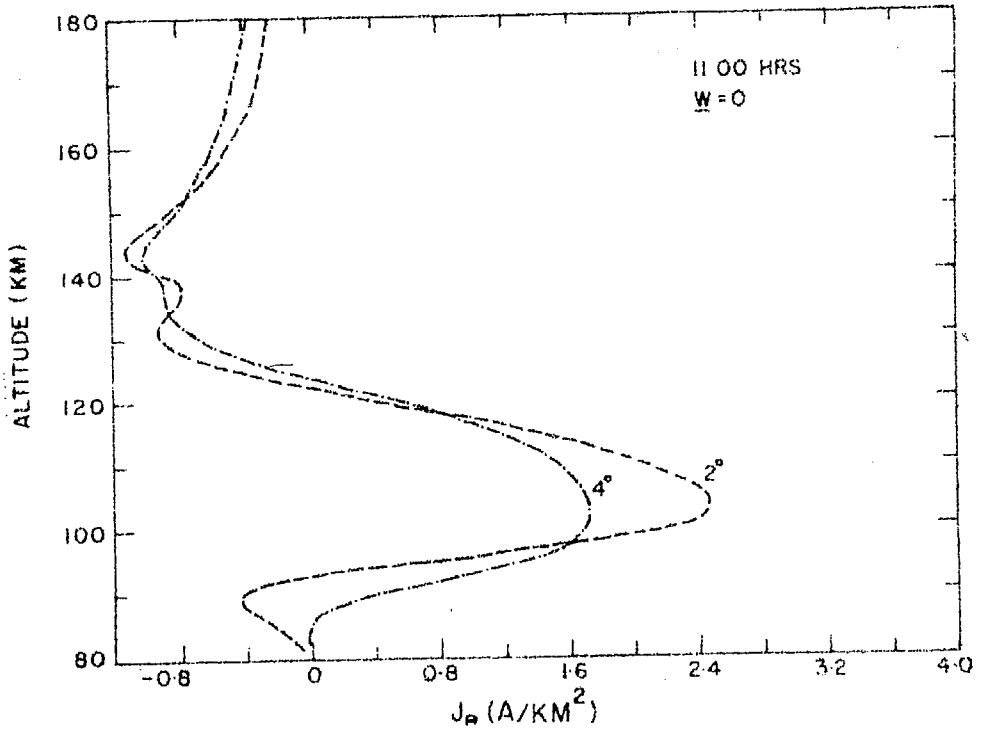

Fig.VI.11:- Vertical profiles of meridional current density Jθ (+ve southward) at 0°, 2° and 4° magnetic latitude. The profiles are for 1100 hrs LT and for no-wind case.

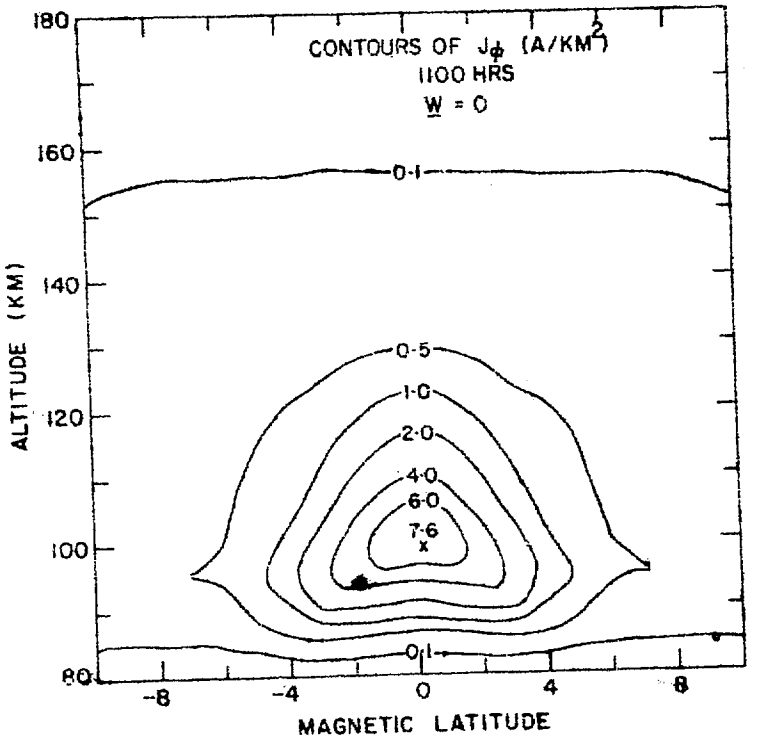

Fig.VI.12:- Distribution of the eastward current density Jø, in the r-θ at 1100 hrs LT and for no-wind case.

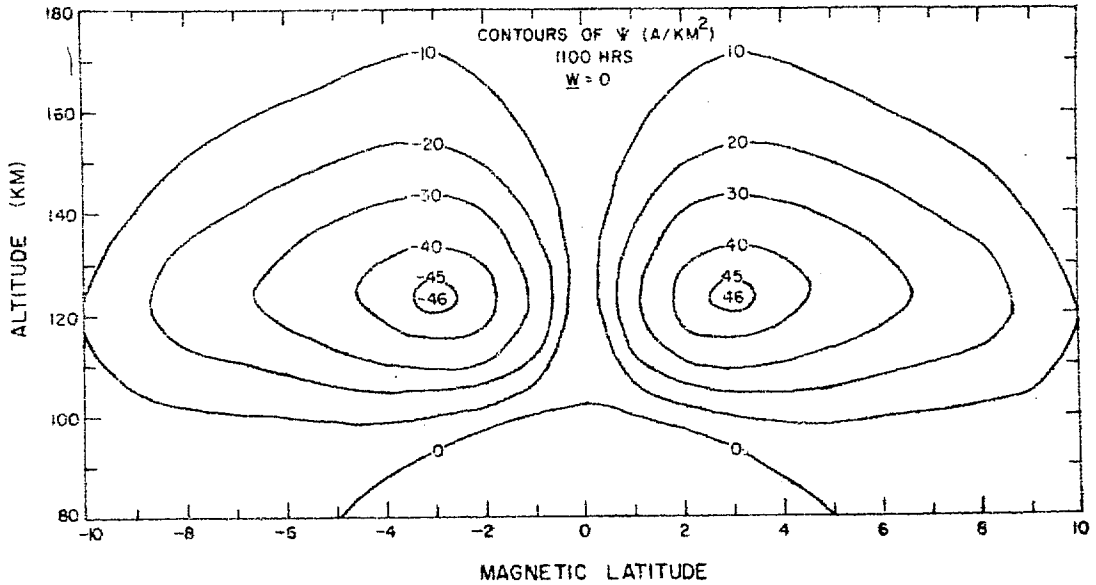

Fig.VI.13:- Distribution of the meridional current function Ψ (in Amperes/km) in the r-θ plane at 1100 hrs LT for no-wind case.

distribution of the electrojet current strength J_ϕ and the meridional current function ψ at 1100 hrs LT in the r-θ plane. The maximum J_ϕ of 7.6A/km^2 is shown to be present at 100 km and at 0°. The electrojet current J_ϕ is fairly symmetric about the dip equator in no-wind case. This plot of J_ϕ can be compared with the observed plot (DAVIS ET AL, 1967) shown in the Fig.I.14 in Chapter I. The observed contours are distorted in shape unlike the smooth curves in the Fig.VI.12. The meridional current function ψ shows two cells centered at about 3° of different polarities on either side of the dip equator. ψ is very small at the equator compared to the values at other latitudes.

The profiles of J_ϕ, E_r, J_r and J_θ at 1420 hrs LT are shown in Figs.VI.14, VI.15, VI.16 and VI.17 respectively. It can be seen that while the currents and fields became weaker at this time than at 1100 hrs (as is expected to happen due to the reduction in electron density), the shapes of these profiles are almost the same as those at 1100 hrs.

The profiles of J_ϕ obtained by the rocket-borne proton precession magnetometer at different local times are shown in Fig.VI.18 (reproduced from SASTRY, 1970). In the figure, the profiles at local times 1108 hrs and 1415 hrs can be compared with the profiles in the Figs. VI.8 and VI.14. For a primary eastward electric field of 0.5 mV/m, the maximum value of J_ϕ computed for 1100 LT is 7.6 A/km^2 while the

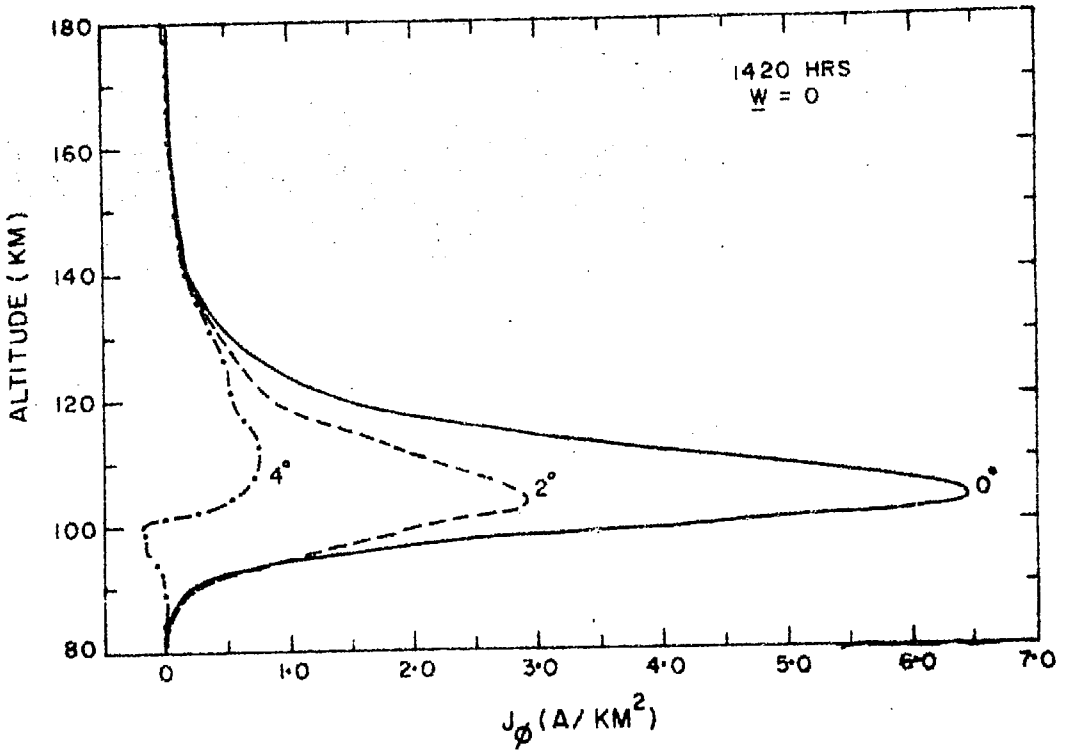

Fig.VI.14:- Vertical profiles of eastward current density J_ϕ at 0^o, 2^o and 4^o magnetic latitude. The profiles are 1420 hrs LT and for no-wind case.

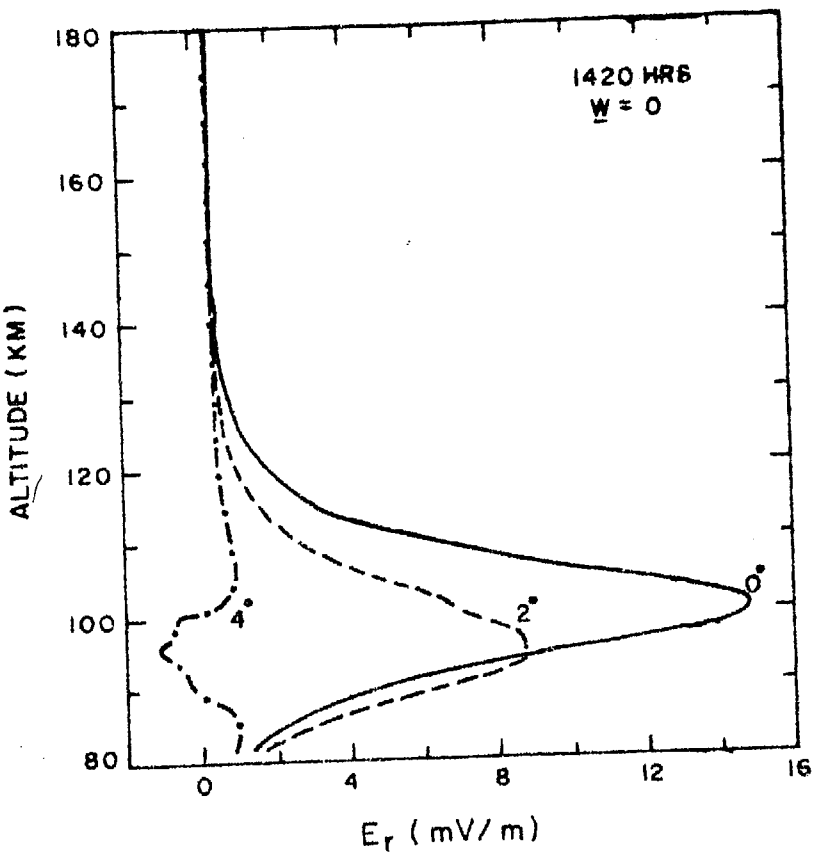

Fig.VI.15:- Vertical profiles of vertical electric field E_r at 0^o, 2^o and 4^o magnetic latitude. The profiles are for 1420 hrs LT and for no-wind case.

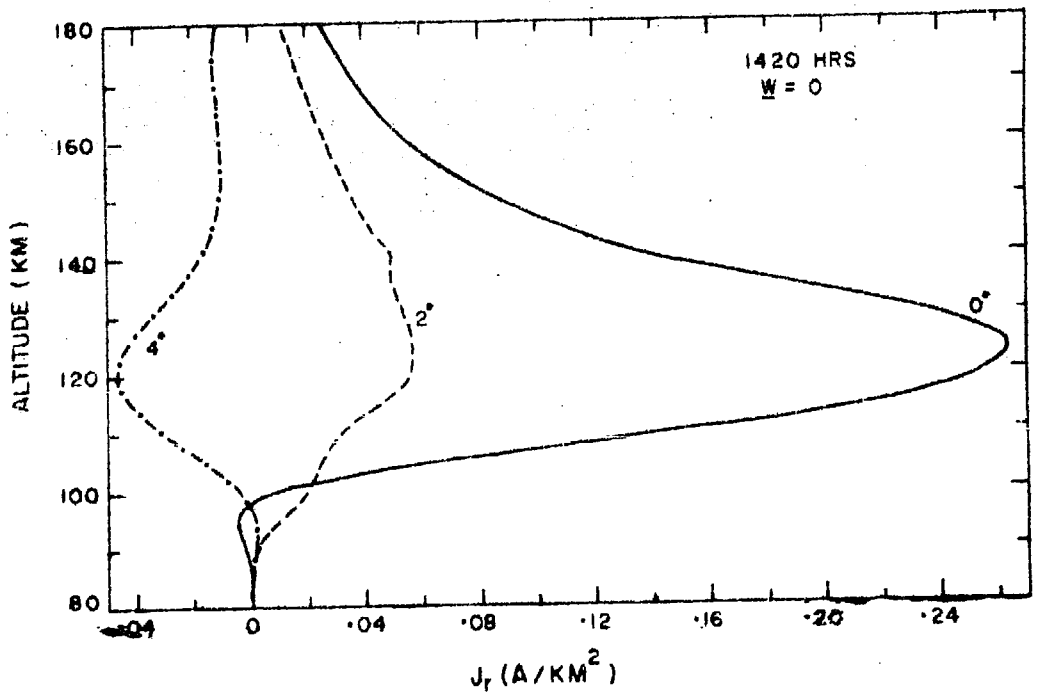

Fig.VI.16:- Vertical profiles of vertical current density J_r at 0^0, 2^0 and 4^0 magnetic latitude. The profiles are for 1420 hrs LT and for no-wind case.

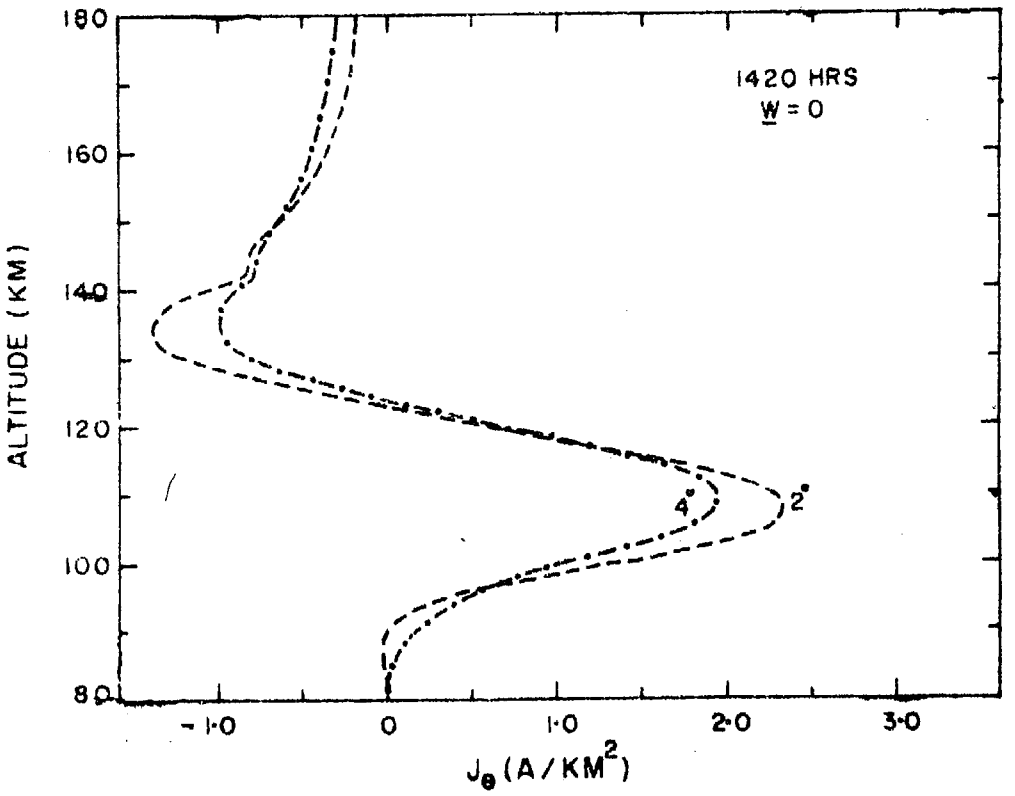

Fig.VI.17:- Vertical profiles of meridional current density J_θ at 0^0, 2^0 and 4^0 magnetic latitude. The profiles are for 1420 hrs LT and for no-wind case.

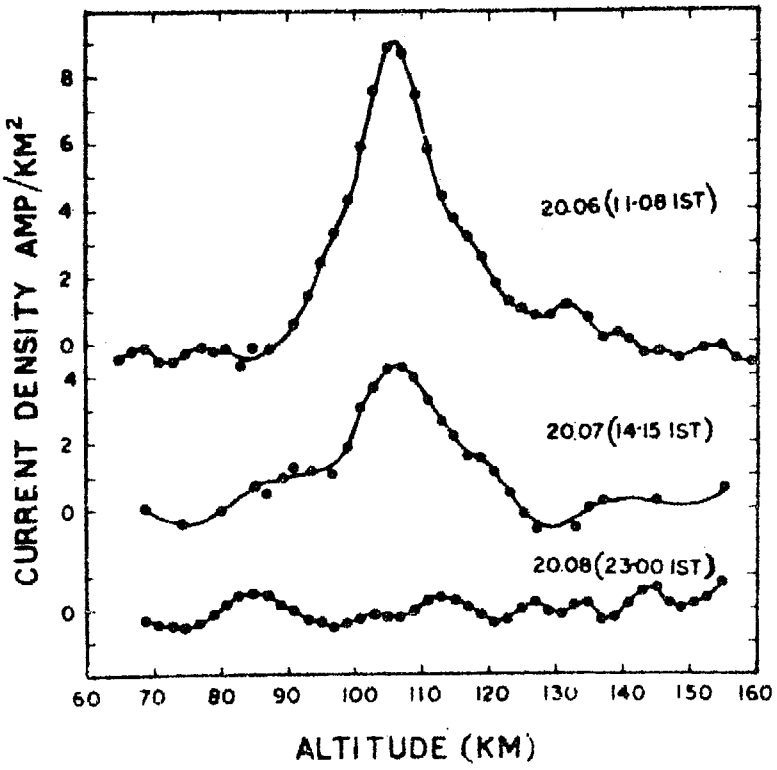

Fig.VI.18:- Vertical profiles of the eastward current density (JØ) obtained by rocket-borne proton precession magnetometers at 1108 hrs, 1415 hrs, 2300 hrs IST, over Thumba, the dip-equator (after SASTRY, 1970).

observed maximum J_ϕ is 9.4 A/km^2 at 1108 LT on 29 Aug. 1968 (SASTRY, 1970) and 7A/km^2 (not shown in the figure) at 1100 hrs LT on 2 Feb. 1972 (BURROWS AND SASTRY, 1976).

BURROWS AND SASTRY (1976) reported that the maximum current density around 1100 hrs (the time of occurrence of maximum increase in H) is found to vary from day to day while the shape of the vertical profile did not reveal any variations. These variations can be attributed primarily to the day-to-day variations in the E_ϕ and hence the choice of 0.5 mV/m in our computations is only a representative value. Besides these arguments, the electric field derived from the horizontal drift velocities in the electrojet measured at Jicamarca suggests that 0.5 mV/m is the representative value for E_ϕ (BAISLEY AND WOODMAN, 1971).

In our model without winds, the thickness of the jet (corresponding to the half-maximum current density points in altitude) is 17 km at 1100 LT and about the same also at 1420 LT indicating that the model without winds does not show any variation of the thickness with local time. SASTRY (1970) observed a thickness of 15 km at 1108 hrs and it becomes broader in the afternoon hours by a few kilometers (Fig.VI.18). The vertical profile of J_ϕ in the latter case is not a smoothly varying one. Except for this, the measured thicknesses are tallying with those obtained by the present model without winds

The width of the electrojet (the distance in north-south corresponding to half-maximum J_ϕ) is inferred from the ground magnetometer data as 580 km (YACOB AND KHANNA, 1963) in the Indian zone and it is significantly wider (660 km) in the South American zone (FORBUSH AND CASAVERDE, 1961; DAVIS ET AL, 1967). The present model without winds shows a width of 550 km (5° latitude) for the Indian zone (Fig.VI.12). Thus, it tallies well with the mean value obtained from the magnetometer data. The width of the electrojet in the Indian zone as obtained by SUGIURA AND POROS (1969) is only about 4° (in latitude). The difference between the present result and that of SUGIURA AND POROS seems to be due to the closer grid-points for the integration in the present model than those chosen by SUGIURA AND POROS. The negative (westward) currents at 7°-8° away from the dip equator obtained by SUGIURA AND POROS (1969) are also found to be due to the larger grid. Thus, these negative currents do not seem to be realistic. RICHMOND (1973 a) and FORBES AND LINDZEN (1976 b) also did not get these negative currents.

The major discrepancy between the observed profile of J_ϕ and that computed by the present model is in the altitude of the maximum J_ϕ. Whereas the observed profiles show the maximum (almost always) at 106 $\pm$ 2 km, the model predicts the maximum J_ϕ at 100 $\pm$ 2 km. This discrepancy seems to be arising due to the uncertainties in the collision frequency models chosen (RICHMOND, 1973 b).

VI.5 Effects of zonal winds and wind shears on the electrojet:

An eastward wind, as discussed earlier in Chapter V, can generate at the dip equator, a non-zero total electric field. This electric field modifies the vertical electric field developed by the primary eastward electric field. Thus, the currents normally driven by the primary field and the associated vertical polarization field in turn get modified. As the cancellation of the wind-induced Lorentz field by the polarization field developed by the wind is less effective away from the dip equator, the effects on the currents due to the winds are expected to be more significant at latitudes away from the equator than at the equator. When an east-west (zonal) wind W_ϕ is introduced, the coefficien f_6 in eqn. (15) is modified as follows

$$f_6 = f_{6o} + f_{6W}$$

with

$$f_{6W} = -\frac{\sin\theta}{a}\left[W_\phi B_r + W_\phi r\frac{\partial B_r}{\partial r} + W_\phi\frac{\partial B_\theta}{\partial\theta} + r B_r\frac{\partial W_\phi}{\partial r}\right] \quad (21)$$

The first three terms in the eqn. (21) represent the effect due to a steady wind. The last term represents the effect of the wind shear. It is found that the contribution of the wind shear term is usually large compared to the other terms. The first and the second terms in the eqn. (21) become comparable with the wind shear term when W_ϕ is large and/or when $(\partial W_\phi/\partial r)$ is small. Among the first

and second terms again, the second term is more significant.

Away from the dip equator, the effect of the steady wind as well as that of the wind shear become more important. The effects of either steady wind or wind shear are symmetric about the dip equator. It is also found that if the vertical gradient (shear) of the zonal wind is positive, the coefficients f_{6o} and f_{6W} are additive (and hence f_6 is enhanced) above 100 km in the northern hemisphere. The southern hemisphere will have the opposite effects. It can easily be seen that although f_{6o} has different polarities in the northern and southern hemispheres, the effect of B_r in the last term of (21) is to make the contribution of the wind identical in both hemispheres.

VI.5.1 Wind shear effect with altitude:

In order to examine the effects of zonal wind shears on the electrojet at different altitudes, two profiles of wind (hypothetical) with λ_z = 10 and 20 km (Fig. VI.19) are used in the model electrojet. The maximum shear strengths corresponding to these two profiles are 64 & 32 m/s/km respectively.

Figs.VI.20 and VI.21 represent the vertical profiles of J_ϕ and E_r respectively for the wind with λ_z = 20 km at 1100 hrs IST. These figures can be compared with the profiles of J_ϕ and E_r without wind (Figs.VI.8 and VI.9). It is clear from the comparison that the effects on J_ϕ and E_r are significant in the region 110-150 km and away from the dip equator.

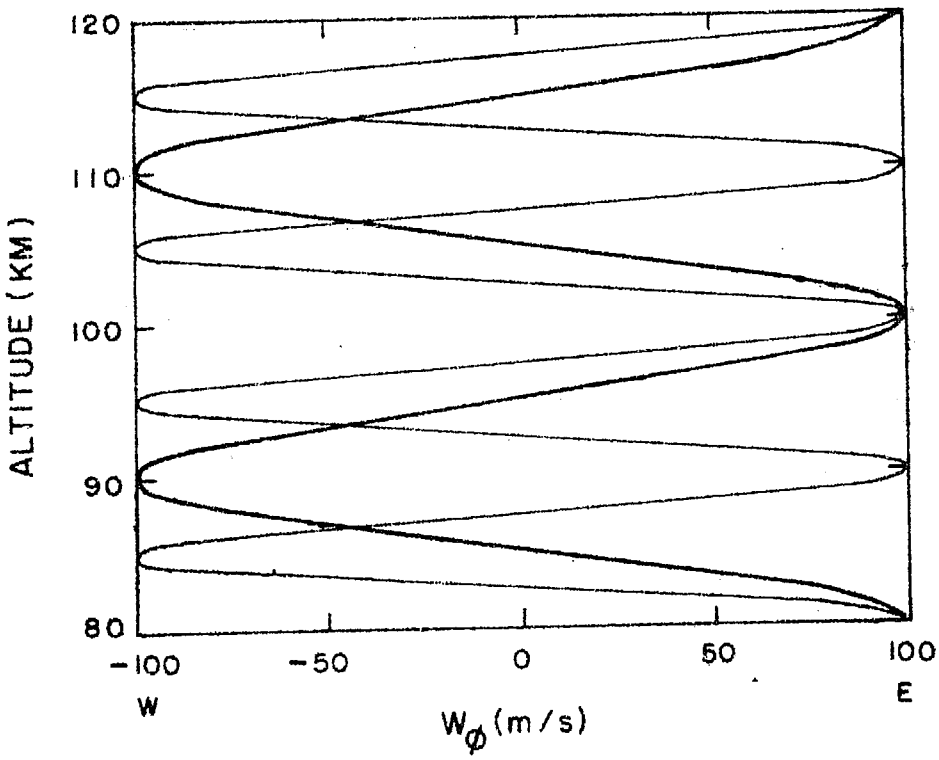

Fig.VI.19:- Hypothetical east-west wind profiles. Thick curve is for a wind of vertical wavelength λ_z = 20 km and thin curve is for λ_z = 10 km. The maximum amplitude of wind is 100 m/s in both cases. These winds are considered to be operative in the entire region 80-200 km.

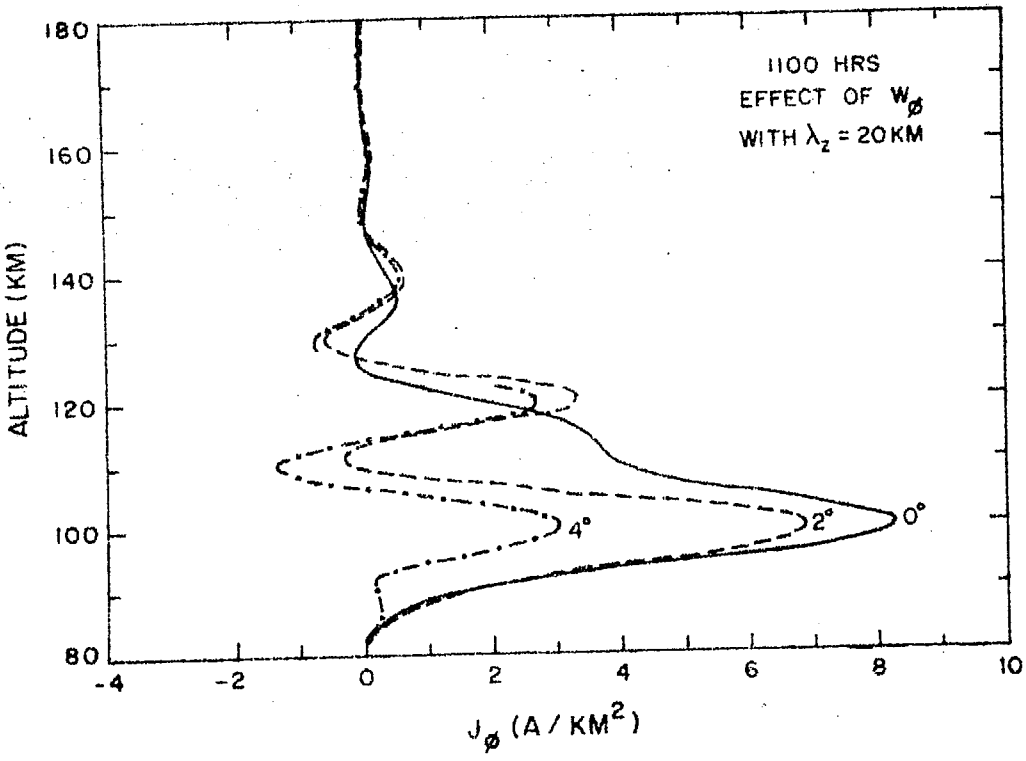

Fig.VI.20:- Vertical profiles of eastward current density Jϕ at 0°, 2° and 4° magnetic latitudes with the hypothetical wind Wϕ of λ_z = 20 km at 1100 hrs LT.

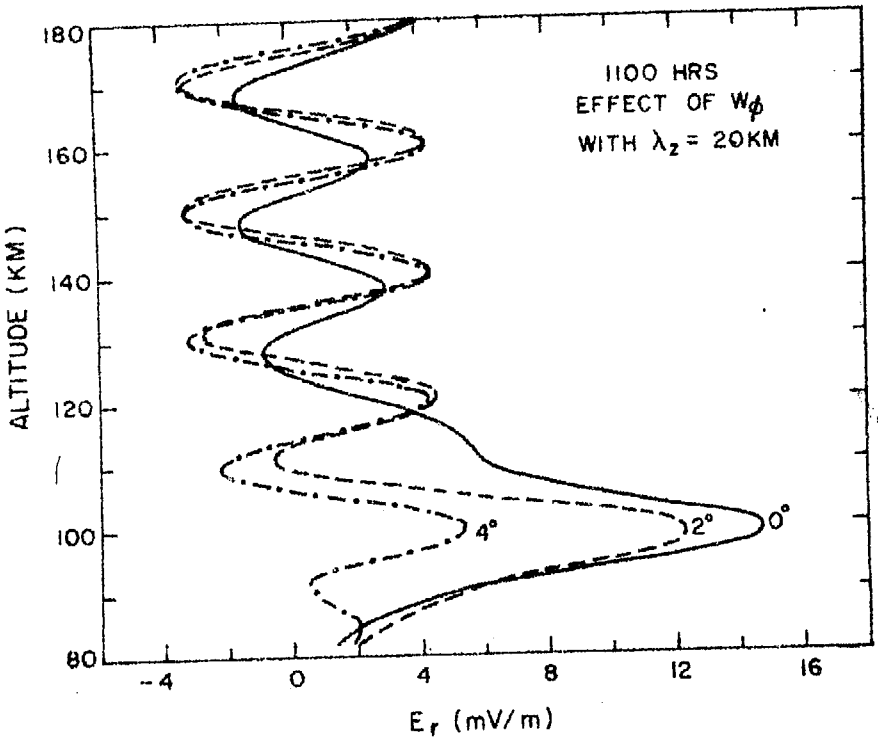

Fig.VI.21:- Vertical profiles of vertical electric field E_r at 0°, 2° and 4° magnetic latitude with the hypothetical wind Wϕ of λ_z = 20 km at 1100 hrs LT.

The percentage changes in the eastward current density J_ϕ computed for the wind with λ_z = 20 km, at different altitudes and latitudes are listed in Table VI.2. It is clear from the table that for a given strength of the shear the effect on J_ϕ is more in the altitude region 110-140 km than in the region 90-110 km which contains the center of the electrojet. In the vicinity of the electrojet (96 km) a shear of 28 m/sec/km produces a deviation of only 15% in J_ϕ at the dip equator. At 116 km, on the other hand, the shear(28 m/s/km) produces a change of 53%.

The magnetic field variations (ΔH and ΔZ) produced on the ground by the electrojet currents are computed from the distribution of the eastward current density J_ϕ using Biot-Savart's law (described in Appendix-II). The effects due to the induced earth currents are not considered. As mentioned earlier in Chapter I, it is not very clearly known as to how much is their contribution. Fig.VI.22 shows the latitudinal distribution of ΔH and ΔZ components of the magnetic field fluctuations at 1100 hrs produced on the ground by the electrojet with no-wind (dashed curves) and the electrojet modified by the wind of λ_z = 20 km (full curves). It is clear from the figure that the magnetic field variations produced by the winds (λ_z = 20 km) are small. This is because the changes in the profile of the current density J_ϕ produced by the sinusoidally varying wind would

TABLE VI. 2

Effect of W_ϕ with λ_z = 20 km on J_ϕ at 1100 hrs

(i) At the dip equator

Altitude (km)	J_{ϕ_o} no wind	J_ϕ with W_ϕ of λ_z = 20 km	Percentage deviation $(\Delta J_\phi / J_{\phi_o}) \times 100$
96	5.667	6.488	15
106*	6.035	5.276	-13
116	2.118	3.234	53
126*	0.702	-0.095	-114
136	0.276	0.539	95
146*	0.182	0.059	-68
156	0.101	0.141	40

(ii) at 2^o magnetic latitude

96	5.324	5.574	5
106*	2.963	2.594	-12
116	1.178	1.489	27
126*	0.549	0.437	-20
136	0.253	0.304	20
146*	0.181	0.162	-11
156	0.101	0.106	5

*indicates the negative wind shear (i.e., W_ϕ decreasing with altitude). The rest are positive wind shears. Magnitude of the wind shear = 28 m/s/km.

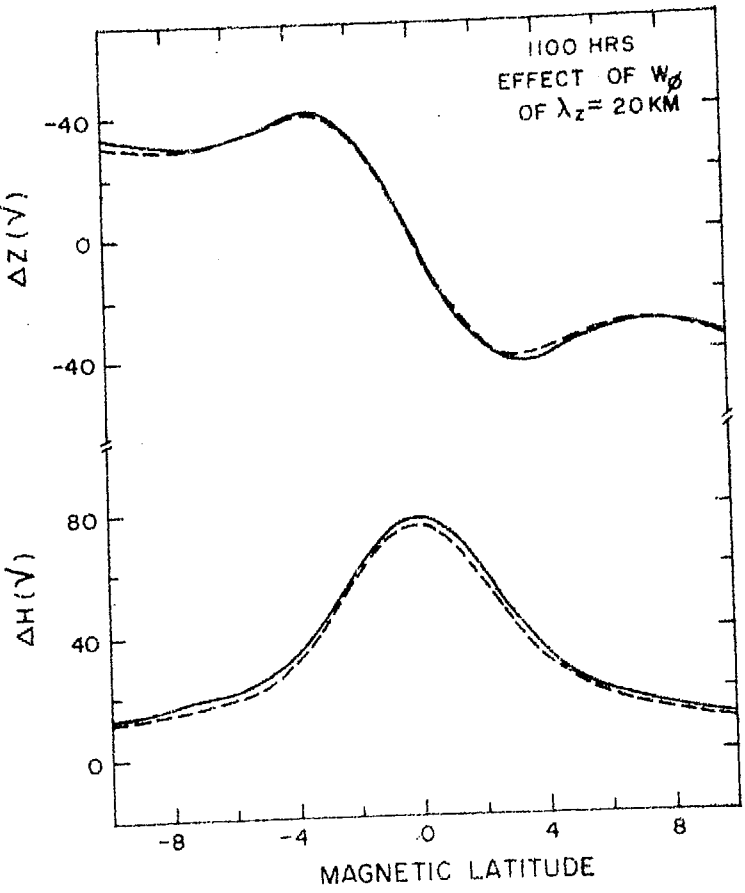

Fig.VI.22:- Latitudinal variation of ΔH (northward) and ΔZ (vertical) components of the magnetic field on the ground produced by electrojet currents at 1100 hrs LT. Full curves represent variations with W_ϕ of λ_z = 20 km and dashed curves are for the no-wind case.

lie in opposing directions and tend to cancel each other. Therefore, the magnetic effects on the ground may not be appreciable (HINES, 1965 b).

It is important to note that the measurements of winds over the dip equator (Chapter II) show that the wind shears usually occur in the 90-110 km region and rarely above it. The strongest shear so far observed at the equator is of intensity 100 m/s/km (NARAYANAN, 1973) at 110 km altitude. Such a shear is found to produce 50% change in J_ϕ at the altitude of the electrojet.

VI.5.2 Effects of observed zonal winds and wind shears:

The zonal wind profiles observed at 1100 and 1420 hrs I (by REES ET AL, 1976) are shown in Fig.VI.23. The effects due to these winds on the electrojet are computed. It is assumed that the wind profiles are latitude-independent in the latitude zone under consideration. The Fig.VI.23 shows the presence of a positive wind shear in the region 100-120 km for both the profiles. In the case of the profile at 1100 hrs (full curve) at 110 km the wind $W_\phi = 0$ and only the wind shear of strength 7 m/s/km exists. At 98 km, on the other hand, wind shear is absent and only a steady wind ($W_\phi = 70$ m/s) exists. Similarly one can identify the altitudes 113 km (where $W_\phi = 130$ m/s and wind shear is absent) and 103 km (where $W_\phi = 0$ and wind-shear of 15 m/s/km exists) on the profile at 1420 hrs. A study of the electrojet parameters

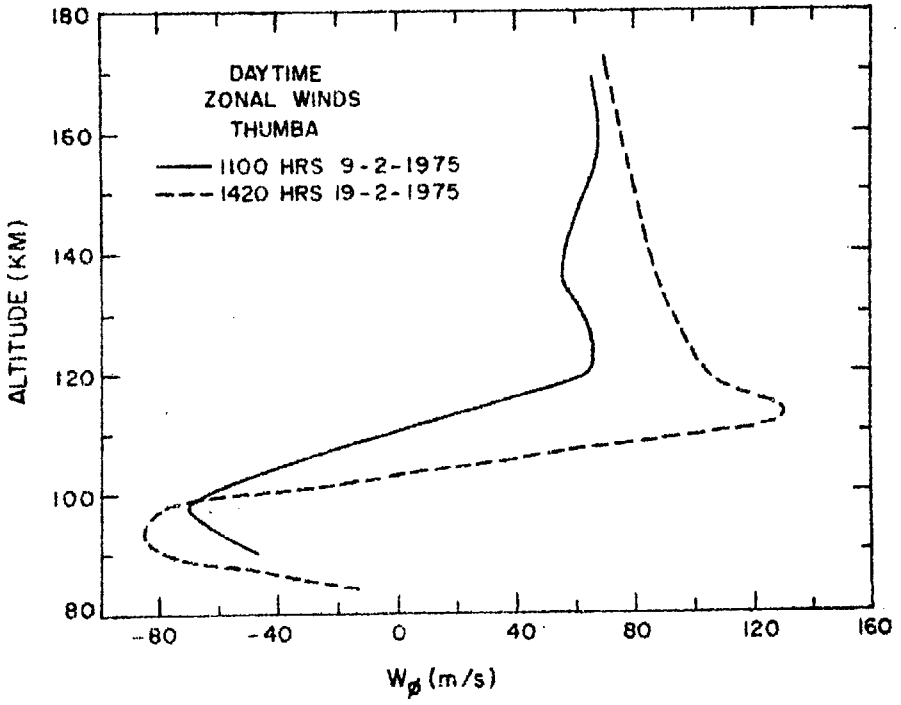

Fig.VI.23:- Profiles of eastward wind velocity Wø observed at 1100 hrs IST (full curve) and 1420 hrs IST (dashed curve). These profiles are taken from REES ET AL(1976).

at these altitudes provides the opportunity to estimate quantitatively the effects of a steady wind and a wind shear. The profiles of J_ϕ, E_r, J_r and J_θ with the wind at 1100 hrs are given in Figs. VI.24, VI.25, VI.26 and VI.27 respectively. The corresponding profiles with the wind at 1420 hrs are given in Figs. VI.28, VI.29, VI.30 andVI.31. A comparison of these profiles with the corresponding profiles with no-wind given earlier, shows that the wind effects are more prominent at latitudes away from the dip equator than at the dip equator. From these plots the percentage deviations in the parameters J_ϕ, E_r, J_r and J_θ are obtained by taking the differences between the two cases viz. with no-wind and with winds. Table VI.3 gives the percentage deviations effected by the wind and wind shear at 1100 hrs and 1420 hrs at different altitudes and at 0° and 2° latitudes.

It is clear from the table that the positive wind shear produces enhancement in all the parameters (save J_θ which is zero) at the dip equator. In both J_ϕ and E_r it is about 20% for the shear of 7 m/s/km at 110 km and about 12% for the shear of 15 m/s/km at 103 km. Thus, at the equator the shear effects are significant well above the altitude of the peak electrojet current strength. In contrast, the steady wind of -70 m/s at 98 km does not have any effect on the electrojet parameters at the dip equator. A zonal

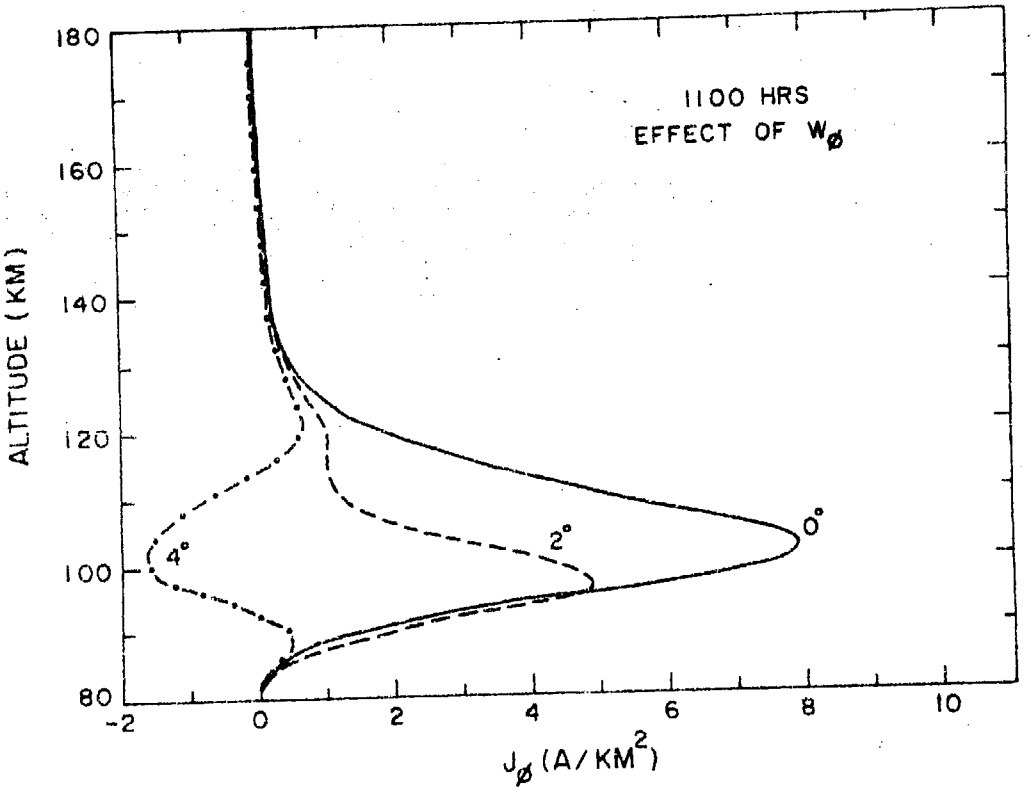

Fig.VI.24:- Vertical profiles of eastward current density J_ϕ at 0°, 2° and 4° magnetic latitudes with the observed east-west wind W_ϕ at 1100 hrs LT.

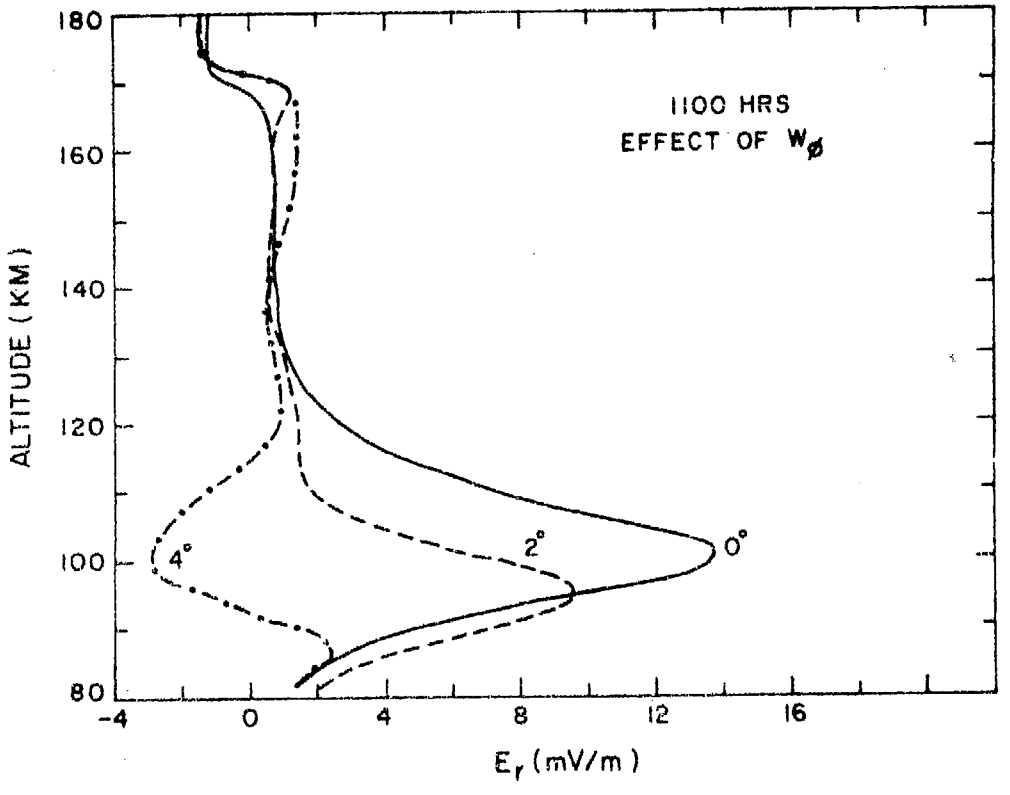

Fig.VI.25:- Vertical profiles of vertical electric field E_r at 0°, 2° and 4° magnetic latitudes with the observed east-west wind W_ϕ at 1100 hrs LT.

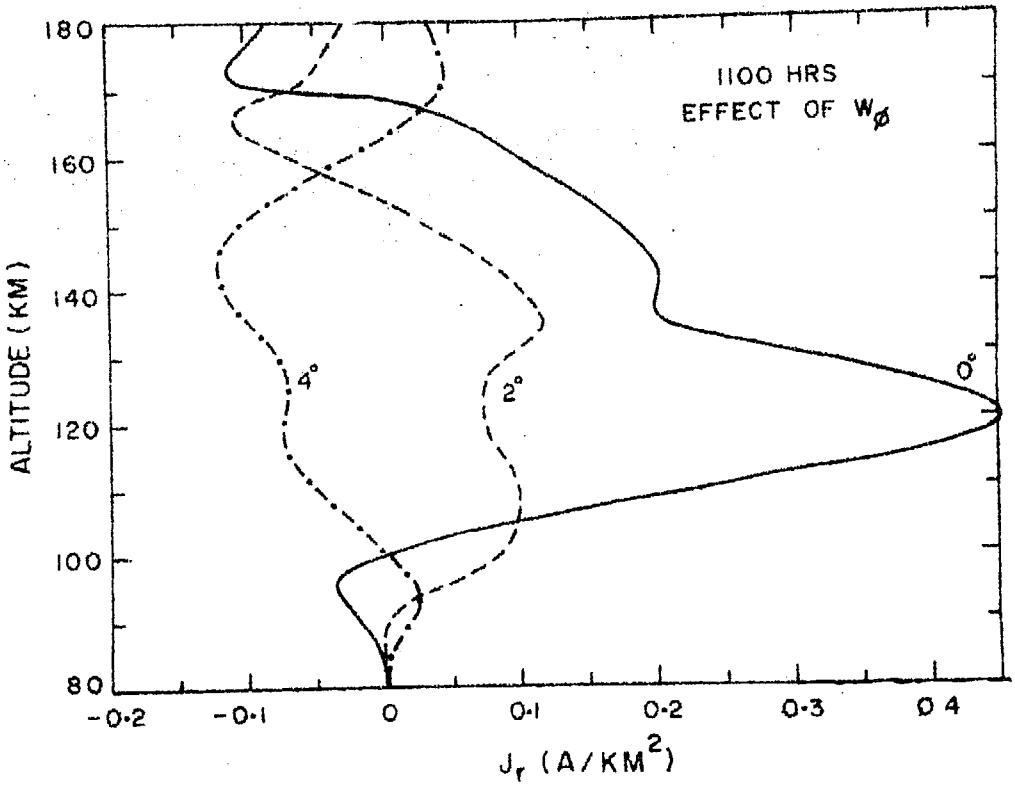

Fig.VI.26:- Vertical profiles of vertical current density J_r at 0°, 2° and 4° magnetic latitudes with the observed east-west wind W_ϕ at 1100 hrs LT.

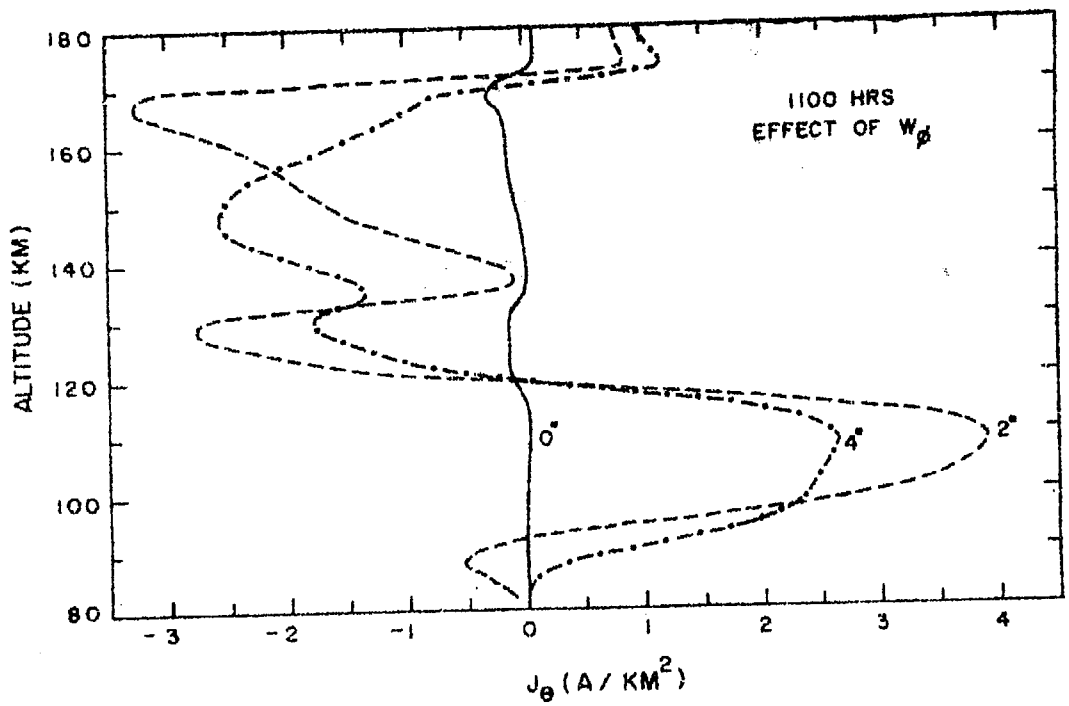

Fig.VI.27:- Vertical profiles of meridional current density J_θ at 0°, 2° and 4° magnetic latitudes with east-west wind W_ϕ at 1100 hrs LT.

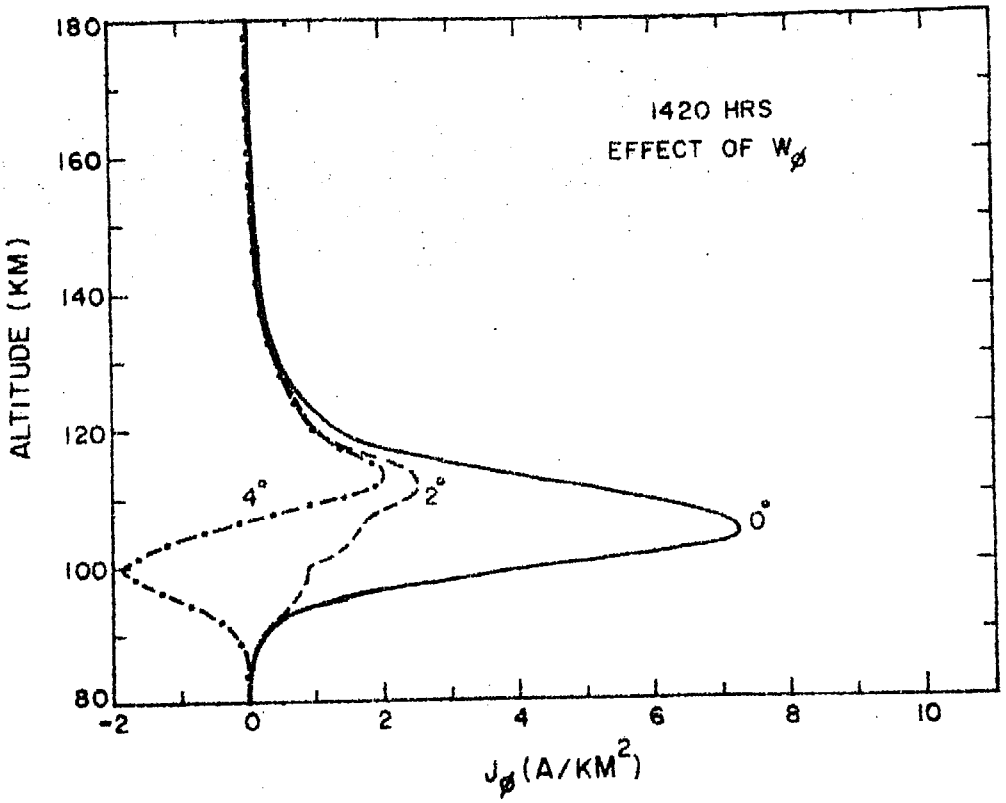

Fig.VI.28:- Vertical profiles of eastward current density J_ϕ at 0°, 2° and 4° magnetic latitudes with the observed east-west wind at 1420 hrs LT.

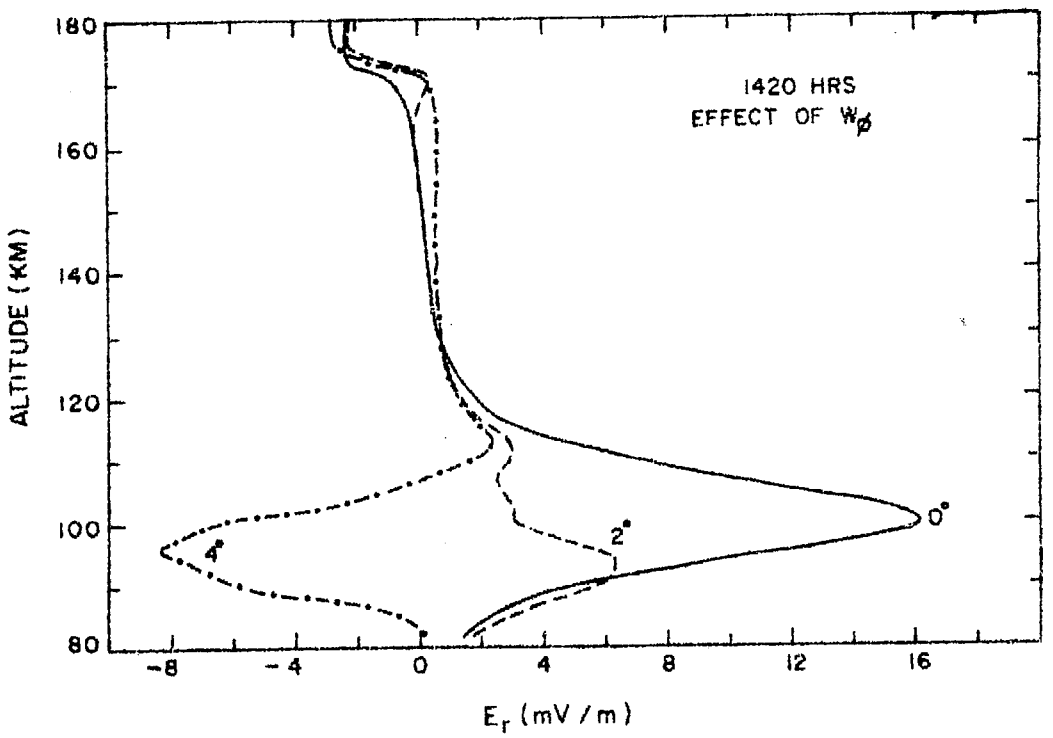

Fig.VI.29:- Vertical profiles of vertical electric field E_r at 0°, 2° and 4° magnetic latitudes with observed east-west wind at 1420 hrs LT.

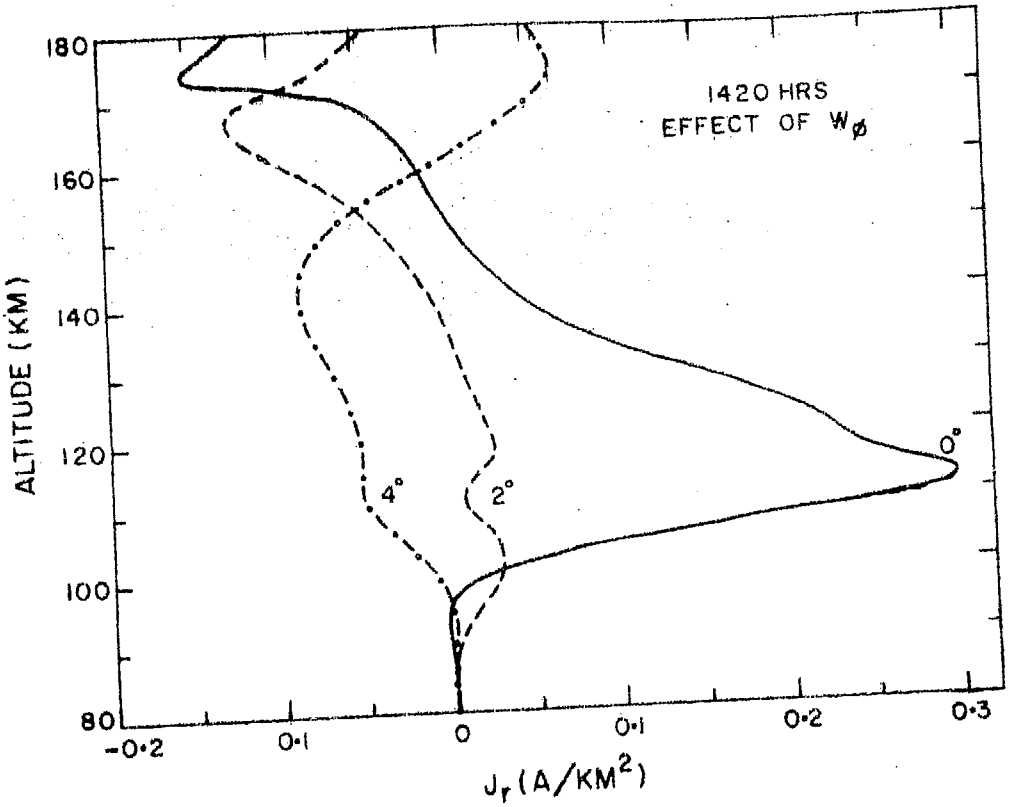

Fig.VI.30:- Vertical profiles of vertical current density J_r at 0°, 2° and 4° magnetic latitudes with the observed east-west wind at 1420 hrs.

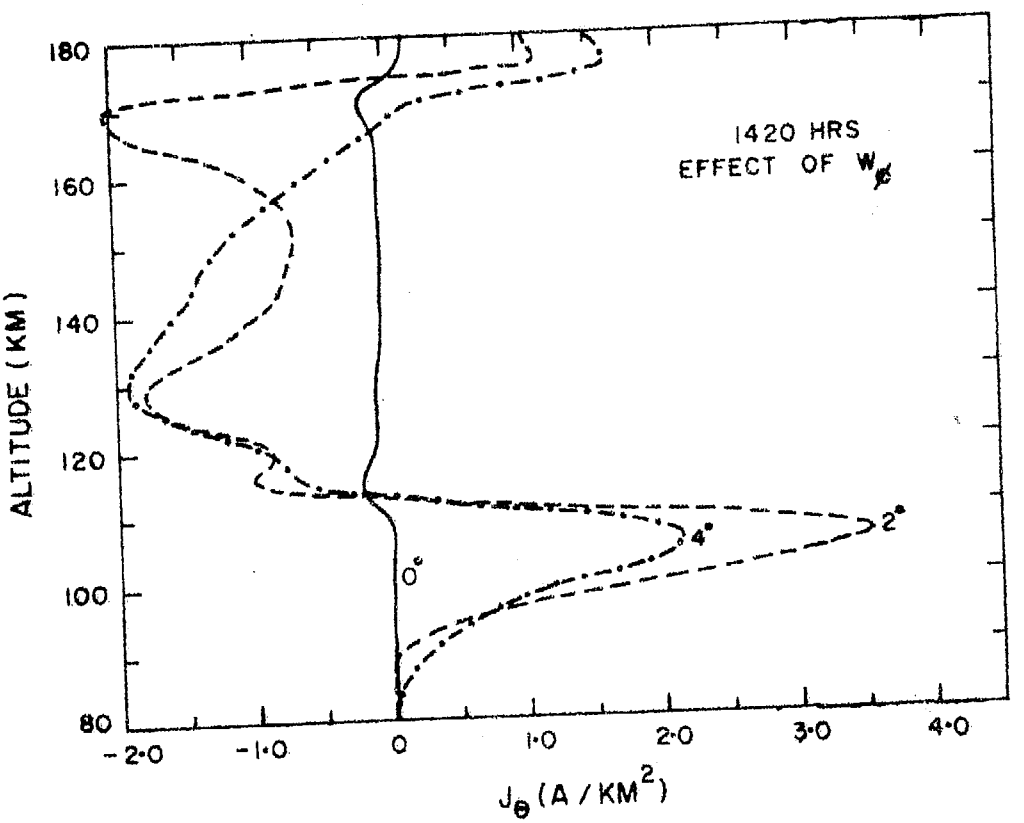

Fig.VI.31:- Vertical profiles of meridional current density J_θ at 0°, 2° and 4° magnetic latitudes with the observed east-west wind at 1420 hrs IT.

TABLE VI. 3

Effects of zonal wind and wind shear on electrojet currents and fields

(i) Steady zonal wind; wind shear = 0

Electrojet parameter	Percentage deviation 1100 hrs W_ϕ = -70 m/s at 98 km		Percentage deviation 1420 hrs W_ϕ = 130 m/s at 113 km	
	0^o	2^o	0^o	2^o
J_ϕ	0	-15	10	30
E_r	0	-15	10	30
J_r	0	40	>100	-75
J_θ	0	40	0	-100

(ii) Wind shear; $W_\phi = 0$

Electrojet parameter	Percentage deviation 1100 hrs $\partial W_\phi/\partial r$ = 7 m/s/km at 110km		Percentage deviation 1420 hrs $\partial W_\phi/\partial r$ = 15m/s/km at 103km	
	0^o	2^o	0^o	2^o
J_ϕ	20	-40	12	-50
E_r	20	-40	12	-50
J_r	50	65	>100	50
J_θ	0	90	0	30

wind as large as 130 m/s can produce only 10% change in J_ϕ at 113 km over the dip equator. Away from the dip equator, however, the deviations produced by the steady winds can be significant. The changes in J_ϕ and E_r at 2° dip latitude are negative for a positive wind shear and are higher (~50%) than those at the equator.

The vertical current, J_r is greatly enhanced (>100%) at the dip equator and is increased by about 50% at 2° dip latitude. The steady wind also produces considerable deviations in J_r at 2° although its effect is negligible at the equator. The meridional current density J_θ away from the equator undergoes deviations in the presence of both steady wind and wind shear. At the equator, J_θ is nearly zero and the zonal wind does not contribute to J_θ.

Fig.VI.32 shows the distribution of the current density J_ϕ in presence of the wind observed at 1100 hrs. A comparison of this with the distribution of J_ϕ without winds (Fig.VI.12) shows that the contours of J_ϕ are compressed by the effect of the wind and wind shear with negative currents at $3^\circ.5$ on either side of the dip equator. Furthermore, the width of the main electrojet is reduced by about 1° in latitude. The thickness of the jet is increased by a few kilometers. As these effects are produced by a positive wind shear centered at 110 km, the opposite effects are expected to be produced by a negative wind shear. Thus, a negative wind shear increases

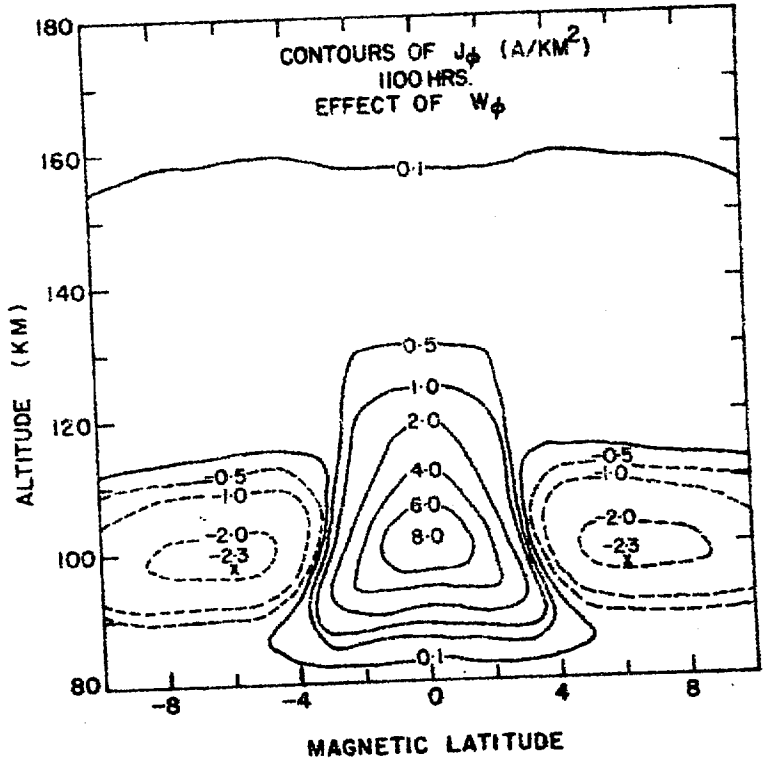

Fig.VI.32:- Distribution of eastward current density Jø in the r-θ plane with the observed east-west w' ıd at 1100 hrs LT.

the width of jet and decreases the thickness. It is possible to interpret the day-to-day variations in width and thickness and also their daily variations as due to such wind shears. Similar changes are found to be effected by the shear at 1420 hrs also.

The latitudinal variations of the northward and the vertical components, ΔH and ΔZ of the geomagnetic field computed from the model electrojet with and without the zonal winds at 1100 hrs LT are shown in Fig.VI.33. The dashed curves represent the variations without wind, while the full curves represent the variations of ΔH and ΔZ when wind (observed) is operative. The observed zonal wind profile at 1100 hrs (Fig.VI.23) represents a +ve wind shear. The effect of such a shear on the latitudinal profile of ΔH is to decrease its width. For this particular case of the wind shear of strength 7 m/s/km with its centre located at 110 km altitude, the width of the ΔH profile is decreased by $1^{\circ}.8$ between the points representing half maximum value. The value of ΔH at the dip equator, however, is unaltered.

The ΔZ profile with winds at 1100 hrs became steeper than the profile with no winds indicating a decrease in the width of the electrojet when a +ve shear is operative. It can be concluded that the scatter in the observational points in the plots of the latitudinal profiles of ΔH and ΔZ (Fig.I.12 and I.13) can possibly be explained by the presence of wind shears of different strengths and polarity.

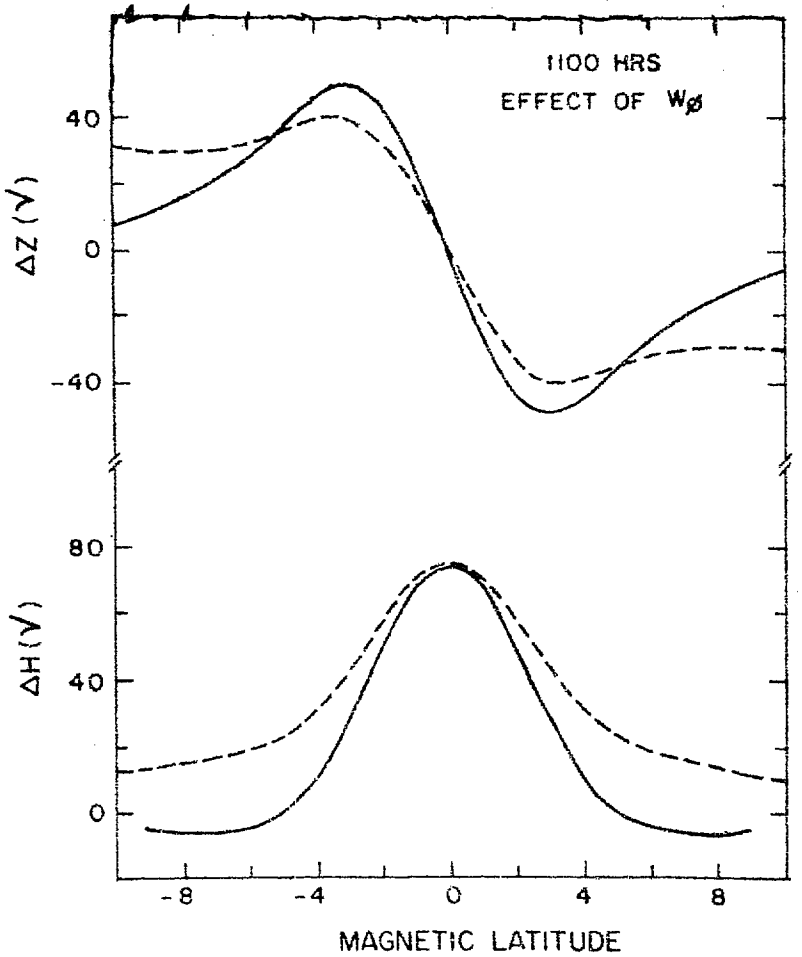

Fig.VI.33:- Latitudinal variation of ΔH (northward) and ΔZ (vertical) components of the magnetic field on the ground produced by electrojet currents at 1100 LT. Full curves represent variations with the observed Wø at 1100 hrs LT and dashed curves are for the no-winds case.

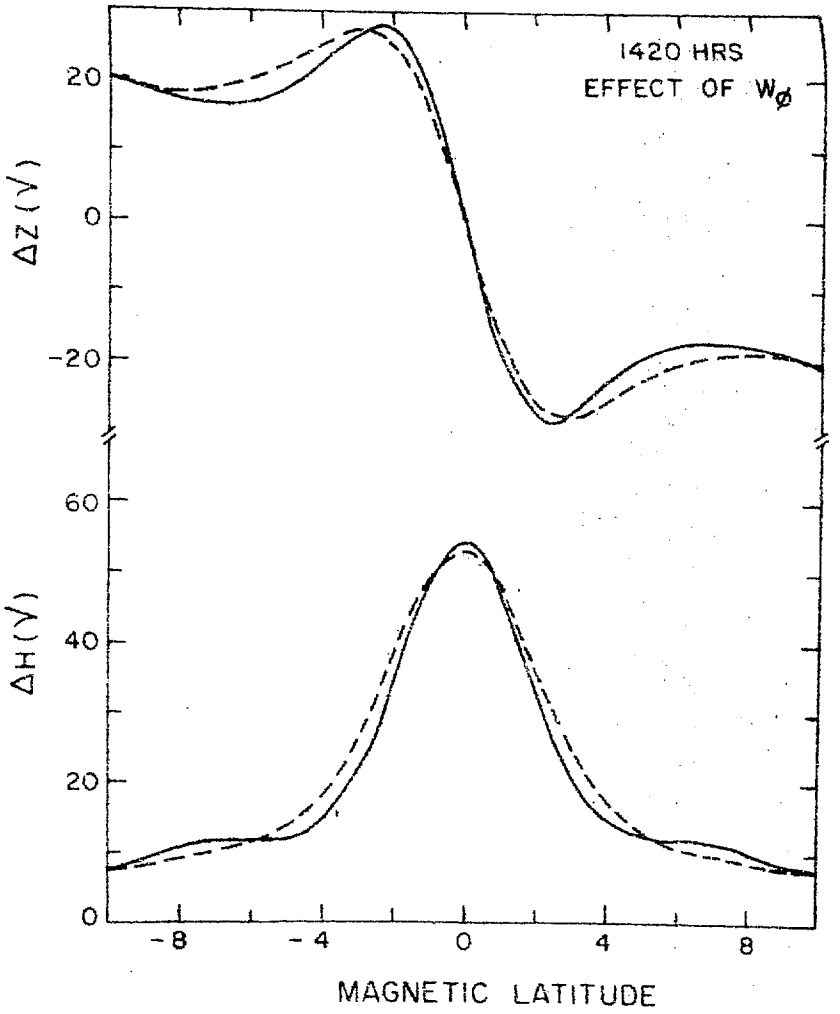

Fig.VI.34:- Latitudinal variation of ΔH (northward) and ΔZ (vertical) components of the magnetic field on the ground produced by electrojet currents at 1420 hrs LT. Full curves represent variations with the observed Wø at 1420 hrs and dashed curves

Fig.VI.34 shows the latitudinal variations of ΔH and ΔZ with the wind at 1420 hrs LT in the model calculations. The center of the wind shear is located at 103 km at 1420hrs (Fig.VI.23) and it has a strength of 15 m/sec/km. The change in the width of ΔH because of the shear is less than a degree. The maximum ΔH value at the dip equator is increased by a small amount by the shear. It is interesting to note that although the shear strength is higher at 1420 hrs than at 1100 hrs, its effect on the width of the ΔH profile is significantly less than that produced by the shear at 1100 hrs. Similar reduction in its effect on ΔZ is observed. The reason is that the extent to which the shear can influence the current density distribution and hence the latitudinal profiles of ΔH and ΔZ depends not only on the strength of the wind shear in the zonal wind but also on the altitude of shear center. It is shown earlier that the effect of the shear (of same magnitude) is greater in the height region of 110-140 km than its effect below 110 km. While comparing the effects of observed wind shears at 1100 hrs and 1420 on the electrojet, it is to be noted that they are located at the altitudes 110 and 103 km respectively. Hence the differences in the computed profiles of ΔH and ΔZ at these two local times.

REES ET AL (1976) estimated the contribution of the observed zonal winds (shown in the Fig. VI.23) to the electrojet current strength under the assumption that the ions are constrained to move with the neutral gas below about 110 km while the electrons are controlled by the electrostatic fields. However, these authors neglected the polarization fields developed as consequence of the charge separation which tend to cancel the wind induced fields to some extent. REES ET AL (1976) thus, over-estimated the contribution due to the winds as pointed out by ANANDARAO (1976). Table VI.4 gives the contributions to J_{ϕ} by the zonal winds at 1100 hrs and 1420 hrs as computed by the present model. Also given in the table are REES ET AL'S results. The table clearly shows that contribution to J_{ϕ} by the winds is far less than that computed by REES ET AL. It is to be noted that in ANANDARAO'S (1976) paper, the signs of values in the columns reading 'our model' in Table 1 (of his paper) are given wrongly. The +ve values should be taken as -ve and vice versa and magnitudes are, however, correct. Similarly in Table 2 (of his paper) the signs of the values in the columns reading "% dev. in J_{ϕ}" have to be reversed.

TABLE VI. 4

Contribution of zonal winds to J_ϕ - A comparison with the results of REES ET AL (1976)

Altitude (km)	1100 hrs		1420 hrs	
	J_ϕ present model	J_ϕ REES ET AL (1976)	J_ϕ present model	J_ϕ REES ET AL (1976)
90	-0.054	0.70	-0.001	1.15
95	-0.107	1.00	0.045	1.32
100	0.126	1.15	0.388	0.70
105	0.515	0.66	0.872	-0.33
110	0.694	0.00	0.936	-1.65
115	0.632	-0.66	0.211	-3.15
120	0.404	-0.80	-0.074	-1.32
130	0.053	-0.16	-0.075	-0.33

VI.6 Effects of meridional winds and wind shears on electrojet:

A meridional wind in the presence of the vertical component of the geomagnetic field produces Lorentz force in the east-west direction. Thus, it can modify the primary eastward electric field which drives the electrojet. At the dip equator, where the magnetic field is entirely northward, the meridional winds can not produce any effect on the eastward currents. However, these winds can produce substantial meridional currents at the equator. At latitudes away from the equator, on the contrary, where the geomagnetic field has a vertical component also, the meridional wind can modify even the east-west currents.

The coefficient f_{6W} in the presence of a meridional wind W_θ is as follows

$$f_{6W} = \left[\left(S + \frac{\partial C}{\partial \theta}\right) W_\theta + \left(\frac{rS}{B_r}\frac{\partial B_r}{\partial r} + \frac{C}{B_r}\frac{\partial B_r}{\partial \theta}\right) W_\theta + \frac{rS}{(\sigma_H/\sigma_P)}\frac{\partial(\sigma_H/\sigma_P)}{\partial r} W_\theta - rS\frac{\partial W_\theta}{\partial r}\right] \frac{\sigma_H}{\sigma_P}\frac{B_r \sin\theta}{a} \quad (22)$$

We assume that $\frac{\partial W_\theta}{\partial \theta} = 0$, because the variation of W_θ in the horizontal direction is much smaller than that in the vertical direction.

Effects of a steady meridional wind:

A steady ($\frac{\partial W_\theta}{\partial r} = 0$) northward ($W_\theta$ is -ve) wind of magnitude 100 m/s is first introduced in the model in order to study its effects on the electrojet. In this special case, the coefficient f_{6W} given in eqn. (22) becomes

$$f_{6W} = \left[\left(S + \frac{\partial C}{\partial \theta}\right) + \frac{rS}{B_r}\frac{\partial B_r}{\partial r} + \frac{C}{B_r}\frac{\partial B_r}{\partial \theta} + \frac{rS}{(\sigma_H/\sigma_P)}\frac{\partial (\sigma_H/\sigma_P)}{\partial r}\right]\frac{\sigma_H}{\sigma_P}\frac{B_r W_\theta \sin\theta}{a} \quad (23)$$

It is found that at the dip equator, the third term inside the brackets in the above equation is the most significant one. At latitudes away from the equator, the fourth term gains more importance.

The profiles of the eastward current density J_ϕ in the presence of the steady northward wind at 1100 hrs LT at magnetic latitudes 0°, 2° and 4° are given in Fig.VI.35. On comparison with the Fig.VI.8 (no-wind case) it is clear that the meridional wind does not alter the current density J_ϕ significantly in the vicinity of the dip equator. However, the effects are rather significant away from the equator. The profiles of the vertical electric field E_r as shown in Fig.VI.36 behave in a way similar to the J_ϕ profiles.

Fig.VI.37 gives the profiles of the vertical current density J_r in the presence of the steady meridional wind. These profiles when compared with those of no-wind case (Fig.VI.10) reveal that the meridional wind does not alter J_r at the equator. However, away from the equator, even at latitudes as close to the equator as 2°, the J_r profiles

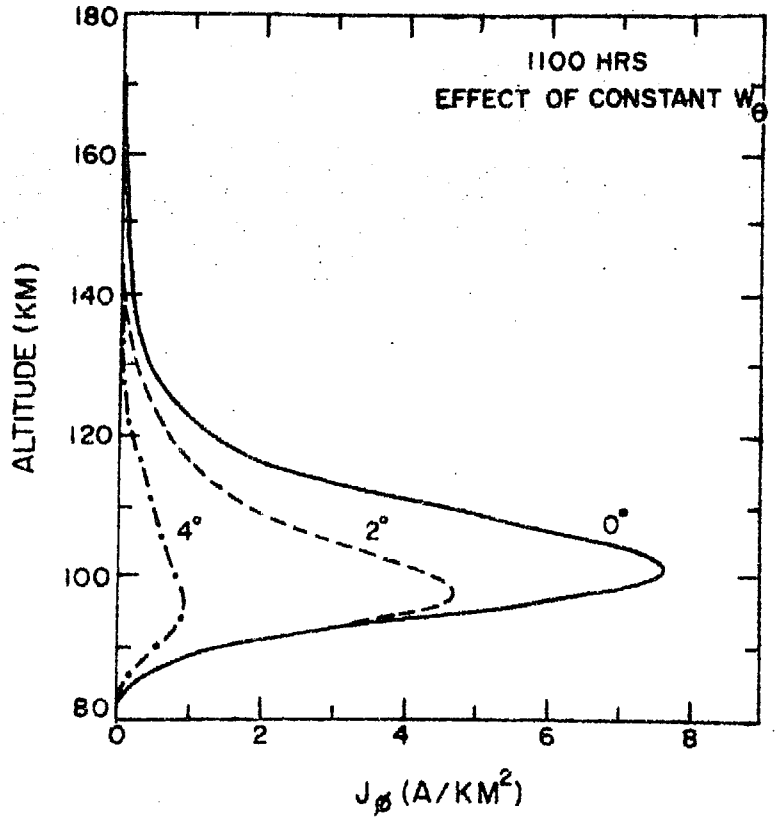

Fig.VI.35:- Vertical profiles of eastward current density J_ϕ at 0°, 2° and 4° magnetic latitudes at 1100 hrs LT with a steady northward wind of 100 m/s.

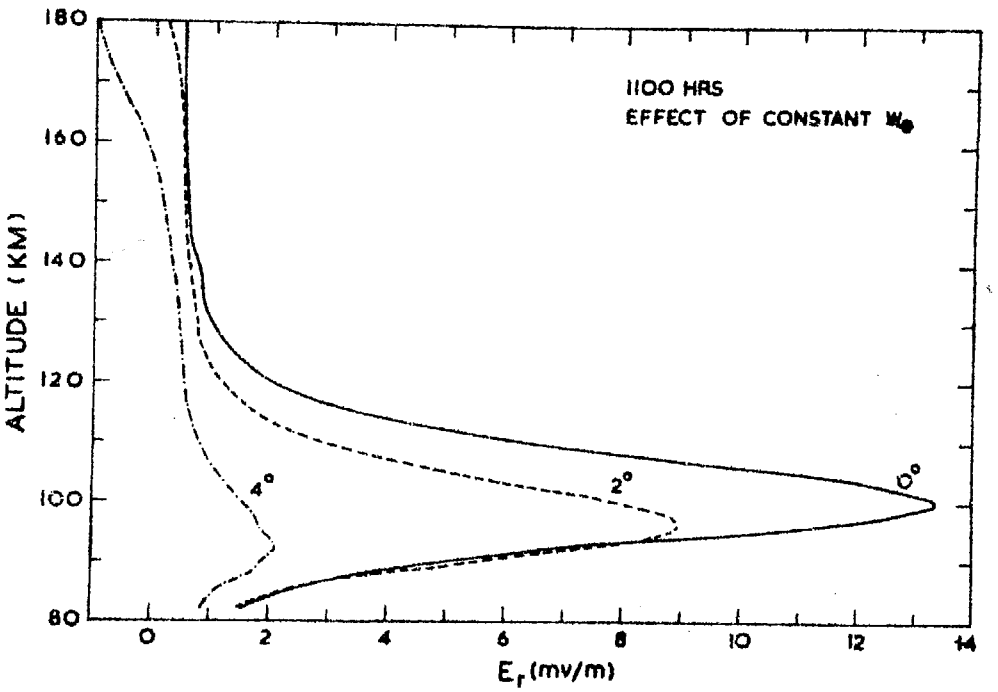

Fig.VI.36:- Vertical profiles of vertical electric field E_r at 0°, 2° and 4° magnetic latitudes at 1100 hrs LT with a steady northward wind of 100 m/s.

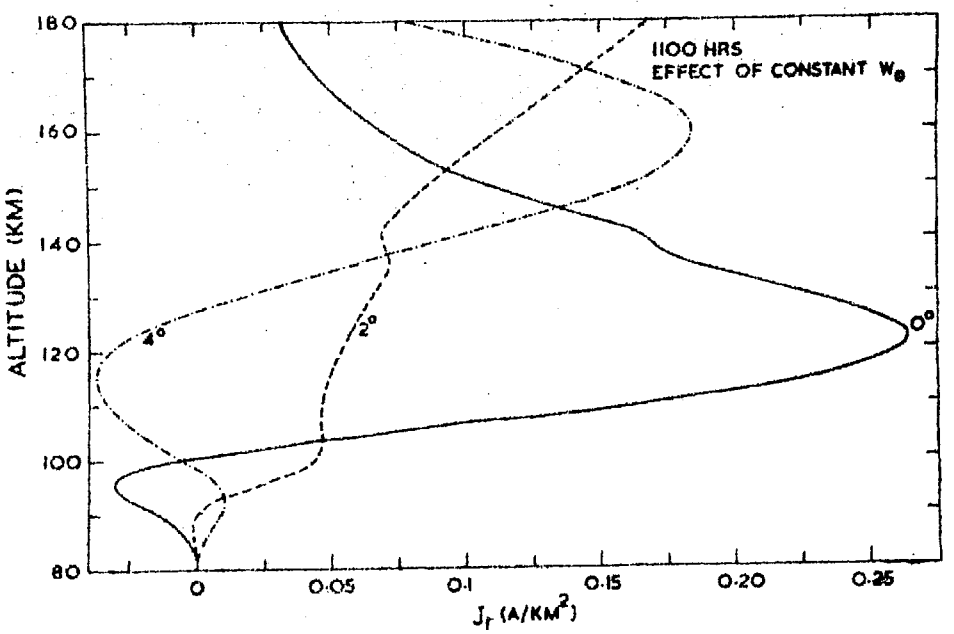

Fig.VI.37:- Vertical profiles of vertical current density J_r at 0°, 2° and 4° magnetic latitudes at 1100 hrs LT with a steady northward wind of 100 m/s.

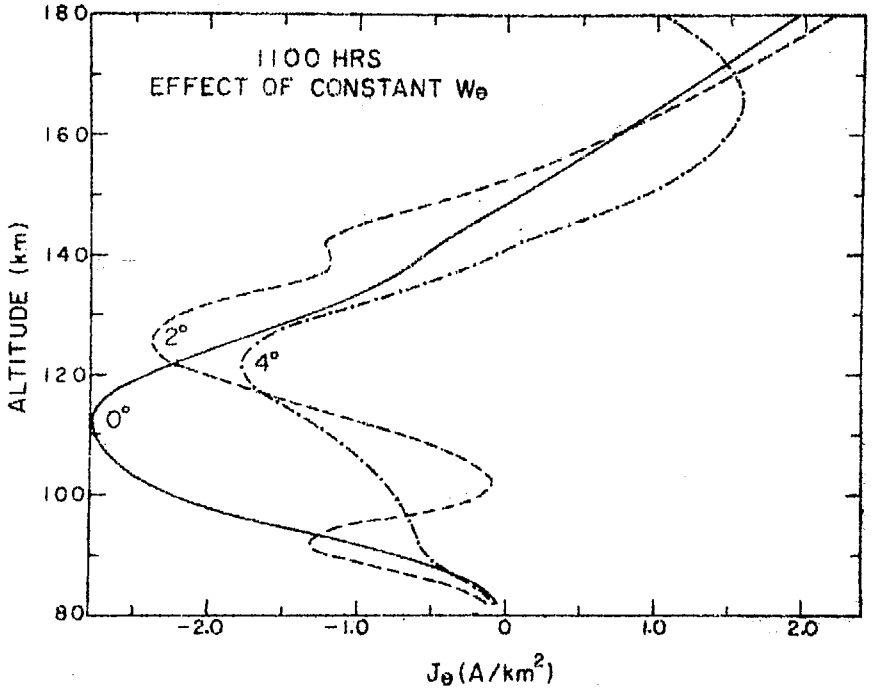

Fig.VI.38:- Vertical profiles of meridional current density J_θ at 0°, 2° and 4° magnetic latitudes at 1100 hrs LT with a steady northward wind of 100 m/s.

show enhancement above a particular altitude which is lower at higher latitudes.

The profiles of the north-south current density J_θ given in Fig.VI.38 when compared with the no-wind case (Fig.VI.11), show that in the northern hemisphere these currents are reversed below 140 km from +ve to -ve values and above 140 km from -ve to +ve values. At the dip equator meridional currents, comparable in magnitude to those at latitudes away from the equator, are produced by the meridional winds. In the no-wind case, the meridional currents at the dip equator are negligibly small.

Fig.VI.39 gives the distribution of the meridional current function ψ in the r-θ plane. When compared with the distribution of ψ without winds (Fig.VI.13), the Fig.VI.39 shows that the northward wind produces negative ψ in the entire region in the r-θ plane, in contrast to the symmetric positive and negative current cells in the northern and southern hemispheres as in the no-wind case. It can be seen from the figure that the variation of ψ with θ is smaller than the variation with r. This indicates that the changes in the meridional current density J_θ which is proportional to the derivative of ψ with r will be much greater than those in the vertical current density J_r which is related to the derivative of ψ with θ.

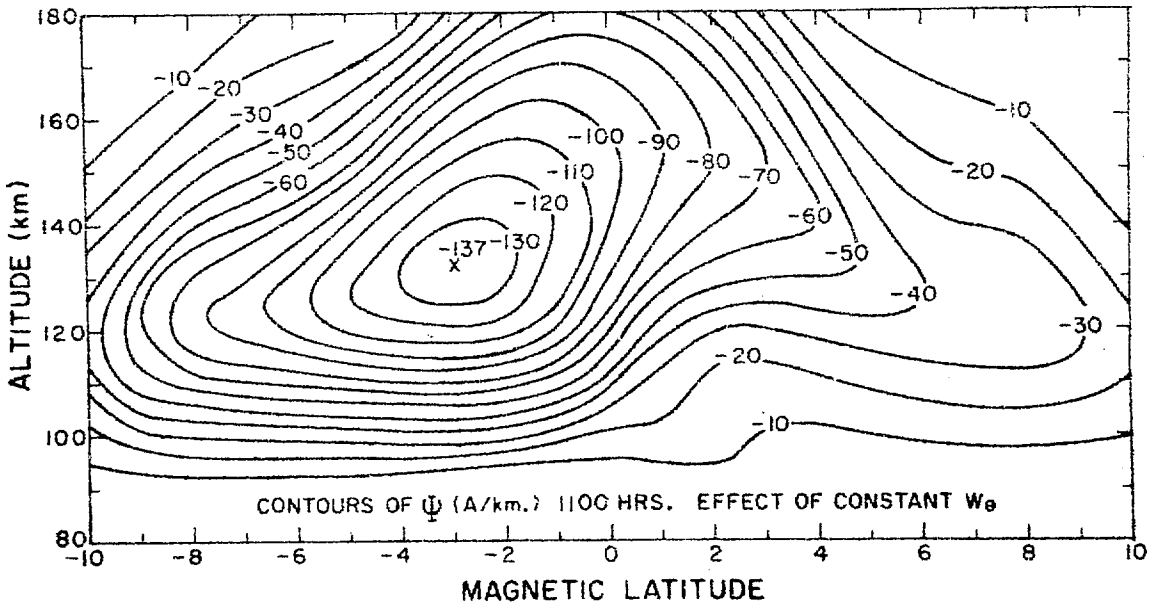

Fig.VI.39:- Distribution of meridional current function ψ in the r - θ plane at 1100 hrs LT with a steady northward wind of 100 m/s.

Table VI.5 gives the percentage changes in the parameters J_ϕ, E_r, J_r and J_θ due to the steady meridional wind at different altitudes. The results are given for the equator and 2° on either side of the equator to represent the behaviour at low latitudes. It is seen from the table that J_ϕ is not altered significantly ($< 10\%$) at any altitude within $\pm 2^\circ$. Correspondingly the change in H on the ground in the electrojet region is not significant. The meridional current density J_θ is affected most. This would produce corresponding significant variations in the declination, D of the geomagnetic field. The effects on J_r are not very significant.

From the study of effects of the steady meridional winds, the following conclusions are in order.

(i) Over the equator, the effects on J_ϕ due to a meridional wind are negligible. A northward wind in the northern hemisphere reduces J_ϕ. It enhances J_ϕ in the southern hemisphere. The effect is more below 100 km than that above 100 km. For example, from the table it can be seen that the percentage change in J_ϕ at 2°N is -30% at 90 km while it is only -10% at and above 100 km. This is because the vertical gradient of (σ_H/σ_P) changes sign from +ve to -ve at about 100 km(which physically means the variation of vertical polarization field with altitude). The coefficient f_{60} (without winds) is mainly governed by the term $S\frac{\partial}{\partial r}(\sigma_H/\sigma_P)$

TABLE VI. 5

Effect of a steady northward wind of 100 m/s on the electrojet parameters at 1100 hrs.

Altitude (km)	Latitude	J_ϕ	E_r	J_r	J_ϕ
90	-2	30	30	Greatly increased	-180
	0	0	0	0	Substantial negative current
	2	-30	-30	Greatly decreased	-180
100	-2	10	10	25	-110
	0	0	0	0	Substantial negative current
	-2	-10	-10	-25	-110
108	-2	10	10	25	-120
	0	0	0	0	Substantial negative current
	2	-10	-10	-25	-120
112	-2	10	10	25	-150
	0	0	0	0	Substantial negative current
	2	-10	-10	-25	-150
120	-2	16	16	20	125
	0	0	0	0	Substantial negative current
	2	-16	-16	-20	-125

and changes its sign at 100 km. For a northward wind in the northern hemisphere below 100 km, f_{6W} is +ve and f_{6o} is -ve; above 100 km, f_{6W} is still +ve but f_{6o} changes sign to +ve. Thus, the reduction in f_{6o} will be more below 100 km, than that above it. Consequently the effects on J_ϕ by the meridional winds will be greater below 100 km.

(ii) A northward wind produces a large northward current (J_θ is -ve) at the dip equator. In the absence of this wind J_θ is negligibly small at the equator.

Finally, it is to be noted that in the electrojet region steady meridional winds in the entire height region of the electrojet are not commonly observed. Winds with shears are common in this region.

From the current density contours of J_ϕ obtained in the presence of a steady wind W_θ at 1100 hrs, the variation of ΔH and ΔZ with latitude are computed using the method described in the Appendix-II and shown in Fig. VI.40. It can be seen from the figure that for a steady northward wind of 100 m/s, the peak of ΔH shifted towards south by about $0^o.5$ in latitude. Similar investigation by RICHMOND (1973 a) shows that a steady southward wind of 10 m/s produces a shift to north of about 0.8 km. Thus, the present result agrees with the direction of shift but differs in its magnitude. The magnetic field fluctuations produced by the steady wind alone vary with latitude. UNTIEDT (1967) also

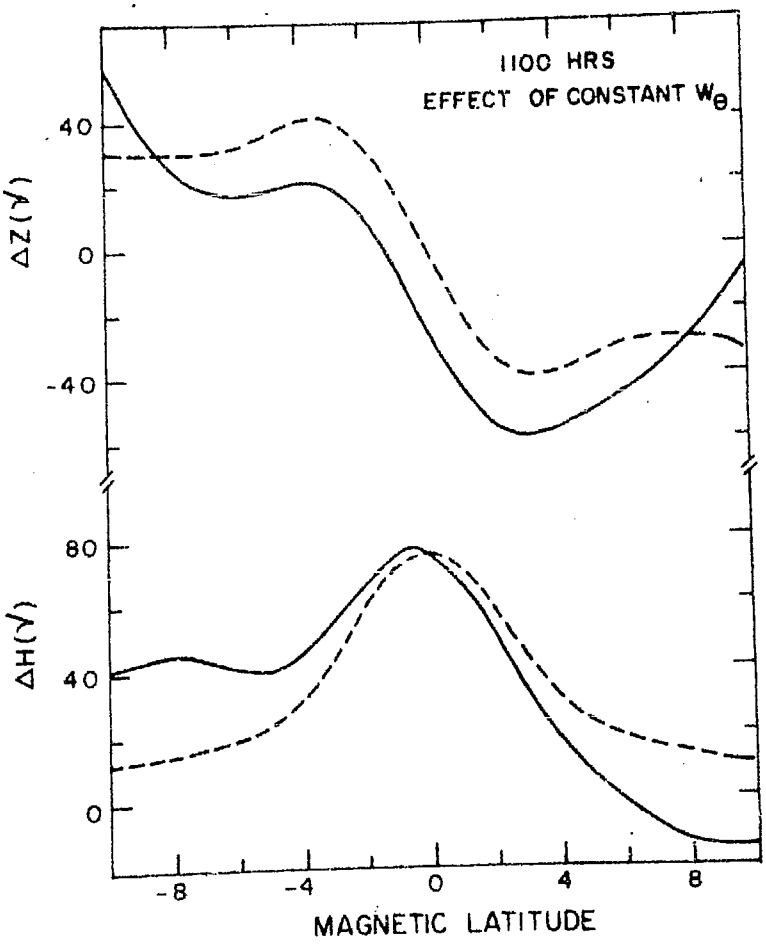

Fig.VI.40:- Latitudinal variation of ΔH (northward) and ΔZ (vertical) components of the magnetic field on the ground produced by electrojet currents at 1100 hrs LT. Full curves represent variations with the steady W_θ and dashed curves are for the no-wind case.

found a similar variation. However, the magnitude of the variation is smaller than what UNTIEDT has predicted.

Effects of the observed meridional winds and shears:

In the coefficient f_{6W} given in eqn. (22), the effect due to a meridional wind shear is represented by the following

$$f_{6W}\ (\text{shear}) = -\frac{rS}{a} B_r \sin\theta \frac{\sigma_H}{\sigma_P} \frac{\partial W_\theta}{\partial r} \qquad (24)$$

It is readily seen from the equation that $f_{6W} = 0$ at the equator where $S = \sin I = 0$. However, at latitudes away from the equator where $S \neq 0$ and the vertical component of the geomagnetic field B_r is substantial, the coefficient may be significant depending upon the strength of the shear.

The electrojet currents and fields are calculated by introducing the meridional winds observed by REES ET AL (1976) in order to study the effects of meridional wind shears. The wind profiles observed at 1100 hrs and 1420 hrs are shown in Fig.VI.41. We present here results obtained from the profile observed at 1100 hrs.

The profiles of J_ϕ shown in Fig.VI.42 indicate that the changes corresponding to the shear occurred at the latitudes outside the dip equator, increasing progressively with latitude. Although the effect of the wind shear is significant at 4°, the modulation on the J_ϕ current profile due to the shear is such as to enhance significantly the current below 100 km than the depletion above it in the

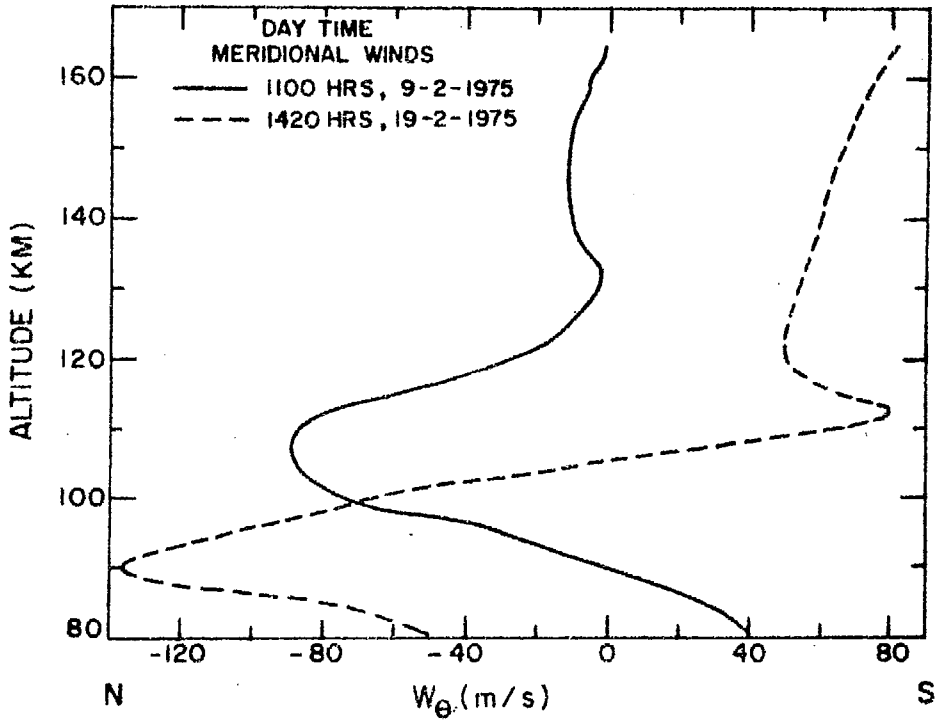

Fig.VI.41:- Profiles of north-south (meridional) wind W_θ observed at 1100 hrs LT (full curve) and 1420 hrs LT (dashed curve). These profiles are taken from REES ET AL (1976).

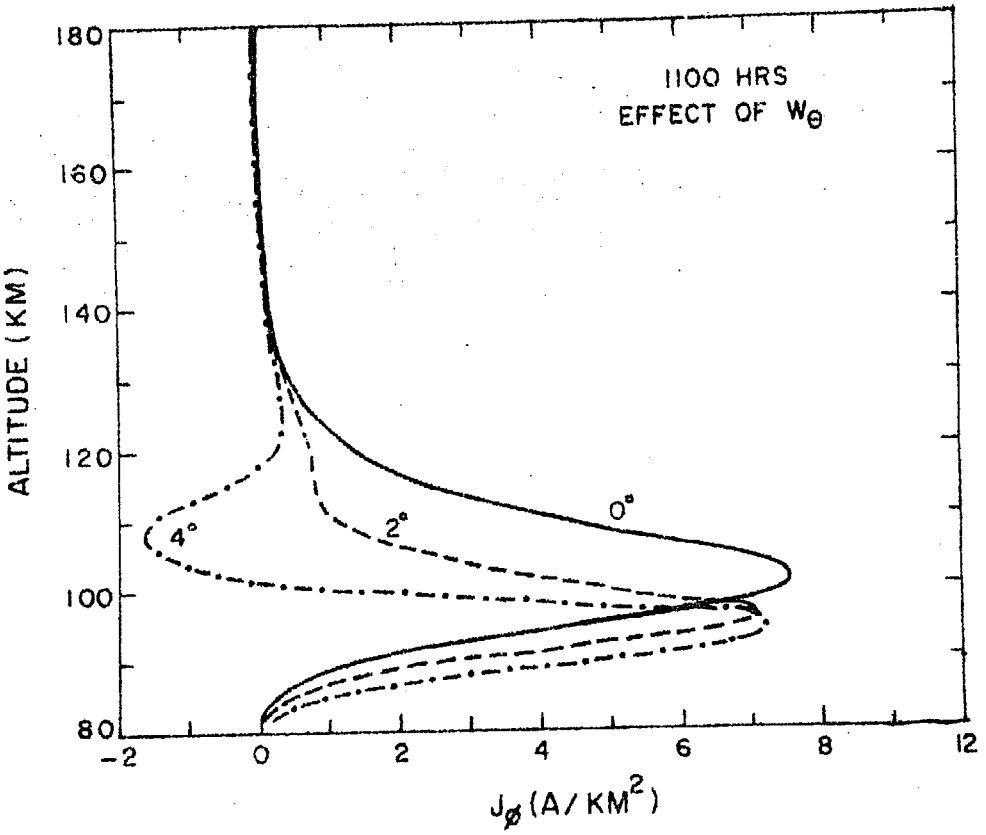

Fig.VI.42:- Vertical profiles of eastward current density $J\phi$ at 0^o, 2^o and 4^o magnetic latitudes with the observed north-south (meridional) wind W_θ at 1100 hrs.

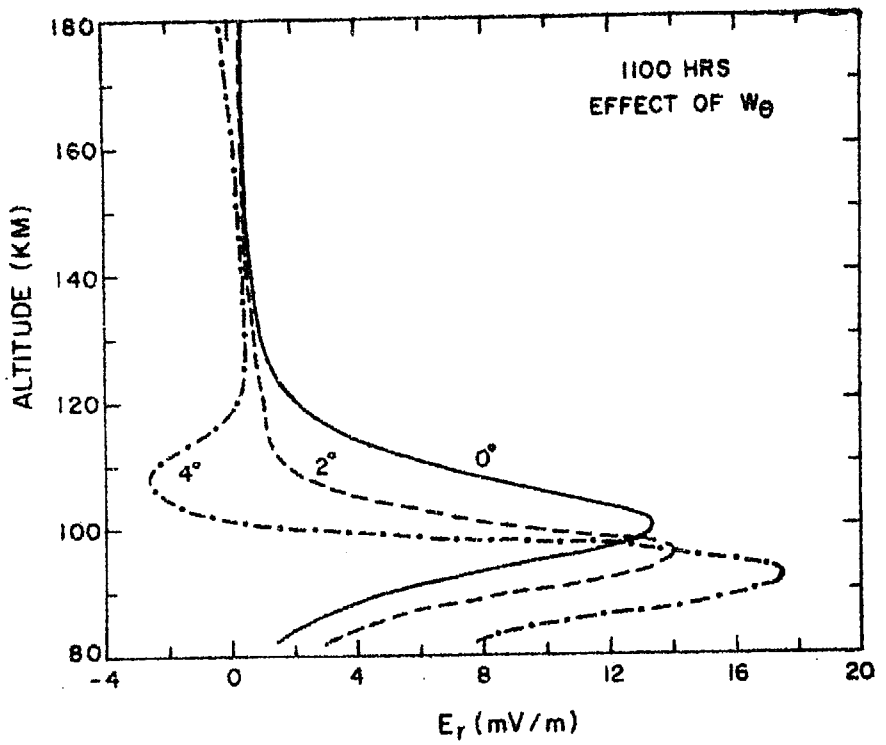

Fig.VI.43:- Vertical profiles of vertical electric field E_r at 0^o, 2^o and 4^o magnetic latitudes with the observed meridional wind W_θ at 1100 hrs LT.

northern hemisphere. It is to be noted that the shear is -ve (-10m/s/km) below and +ve (7m/s/km) above 100 km height. The effects are reversed in the southern hemisphere.

The profiles of E_r are shown in Fig.VI.43. The changes in E_r due to the meridional winds and shears are very much similar to those in J_ϕ.

Fig.VI.44 shows the profiles of the vertical current density J_r. On comparison with the Fig.VI.10 with no-wind, these profiles indicate that J_r is not altered significantly because of the meridional winds and shears.

The profiles of J_θ, the meridional current density are given in Fig.VI.45. These profiles show that at the dip equator the shear causes substantial meridional current J_θ. The profiles at the latitudes 2° and 4° do not seem to be affected greatly except at 90 km where the shear is centered. The profile of J_θ seems to follow the profile of W_θ.

The distribution of the meridional current ψ in the r-θ plane is shown in Fig.VI.46. This figure when compared with the distribution of ψ in the no-wind case (Fig.VI.13), reveals that ψ is greatly distorted due to the meridional wind. Throughout the region of interest, the observed meridional wind at 1100 hrs produced negative ψ.

To study the effects of meridional wind shears on the electrojet, we identify three altitude levels on the wind

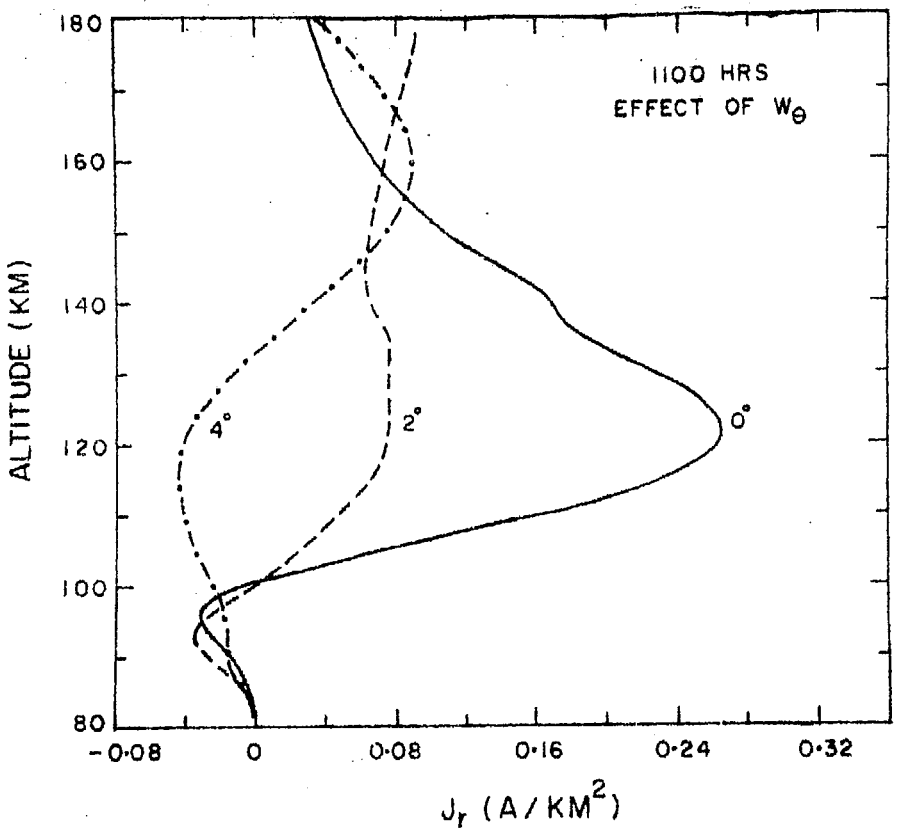

Fig.VI.44:- Vertical profiles of vertical current density J_r at 0°, 2° and 4° magnetic latitudes with the observed meridional wind at 1100 hrs LT.

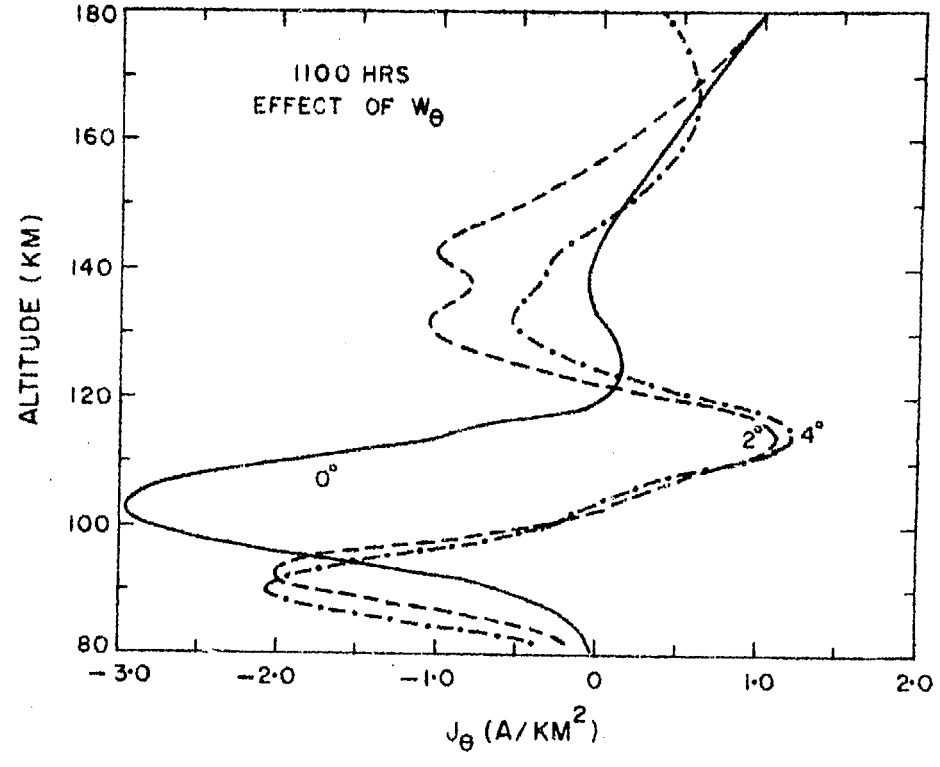

Fig.VI.45:- Vertical profiles of meridional current density J_θ at 0°, 2° and 4° magnetic latitudes with

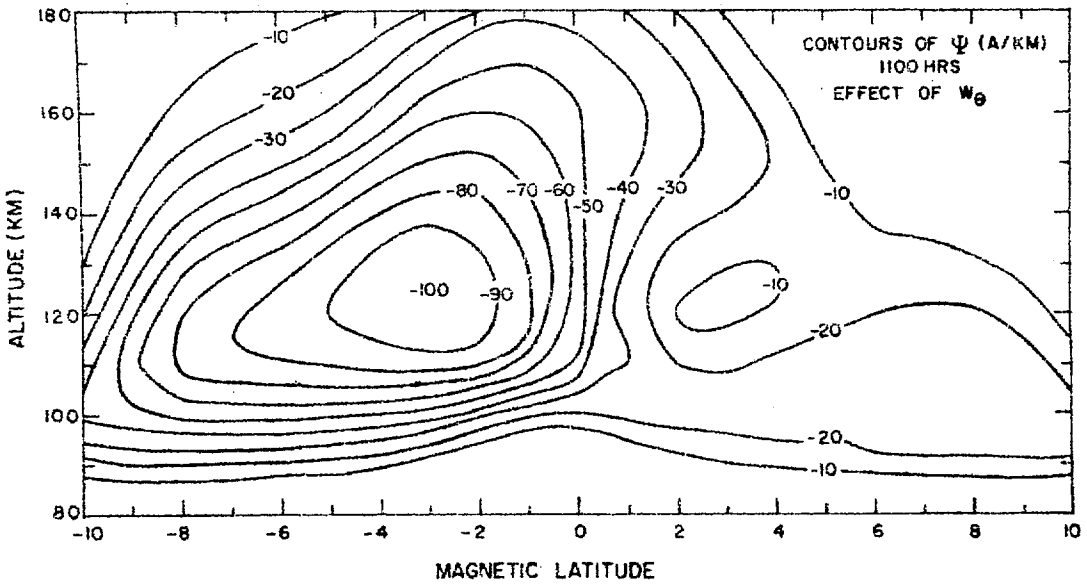

Fig.VI.46:- Distribution of the meridional current function Ψ in the r - θ plane with the observed meridional wind at 1100 hrs LT.

profile at 1100 hrs given in the Fig.VI.41. These are (i) 90 km, where only a shear of strength -6m/s/km is present and the steady wind is absent, (ii) 98 km, where a shear of strength -10m/s/km and a wind of -60m/s (northward) are present and (iii) 114 km, where a shear of strength 7 m/s/km and a wind of -65m/s are present. Case (i) gives us the effects due to the wind shears alone. The wind shears in the cases (ii) and (iii) are of opposite polarity but the wind is almost the same in both cases. Thus, these two cases give a comparative study of the shears of different polarity with slight difference in magnitude at different altitudes.

Table VI.6 gives the percentage deviations in J_ϕ, E_r, J_r and J_θ produced by the shears at the altitudes 90, 98 and 114 km identified on the wind profile. The results are given for magnetic latitudes 0°, 2° and -2°. The table shows that below 100 km, a negative wind shear (i.e., northward wind increasing with altitude or a southward wind decreasing with altitude) enhances the eastward current density J_ϕ in the northern hemisphere (case (i)). In case (ii), the deviation in J_ϕ is +ve but less than that in case (i), eventhough the shear is stronger. This can be explained in the following way. As mentioned earlier in this section, a steady northward wind would reduce the eastward current

TABLE VI. 6

Effects of the observed meridional wind shears at 1100 hrs on the electrojet.

(i) Shear = -6 m/s/km; Wind = 0 at 90 km

Electrojet Parameters	Percentage deviation		
	0^{o}	2^{o}	-2^{o}
J_{ϕ}	0	35	-35
E_{r}	0	35	-35
J_{r}	0	Greatly decreased	Greatly increased
J_{θ}	Substantial -ve current	Greatly decreased	Greatly decreased
	(ii) Shear = -10m/s/km; Wind =-60m/s at 98 km		
J_{ϕ}	0	17	-17
E_{r}	0	17	-17
J_{r}	0	Greatly decreased	Greatly increased
J_{θ}	Substantial -ve current	-150	-150
	(iii) Shear = 7m/s/km; Wind =-65m/s at 114 km		
J_{ϕ}	0	-40	40
E_{r}	0	-40	40
J_{r}	0	0	0
J_{θ}	-ve current	-24	-24

density J_ϕ in the northern hemisphere. The effect is stronger below 100 km than that above 100 km. Thus, at 98 km in case (ii), the negative shear and the northward wind affected the J_ϕ in opposite ways and thus produced net enhancement of 17% in J_ϕ at 2° latitude. If a northward wind of 100 m/s produces a deviation of -10% in J_ϕ, it can safely be assumed that a northward wind of 60 m/s can cause a deviation of -6%. Thus, the -ve shear of 10m/s/km alone at 98 km would have produced 17 + 6 = 23% enhancement in J_ϕ. Similarly a positive wind shear of 7 m/s/km alone at 114 km altitude would have caused a change of -34% instead of -40% in J_ϕ. From these arguments it can be inferred that the effect of the meridional wind shears is more at higher altitudes. Also, the effect of a positive shear in the northern hemisphere and a negative shear in the southern hemisphere is to reduce J_ϕ (and hence the $\triangle$ H) at these regions.

The variation of northward and the vertical components of the earth's magnetic field $\triangle$ H and $\triangle$ Z with latitude due to the electrojet without and with the observed meridional wind at 1100 hrs are plotted in Fig. VI.47. In computing $\triangle$H and $\triangle$Z, the effects of the earth's induction are not considered. A positive wind shear in the meridional wind reduces $\triangle$H in the northern hemisphere and enhances $\triangle$H in the southern hemisphere without altering $\triangle$H value at the dip equator. It is pertinent to note here that during a counter-

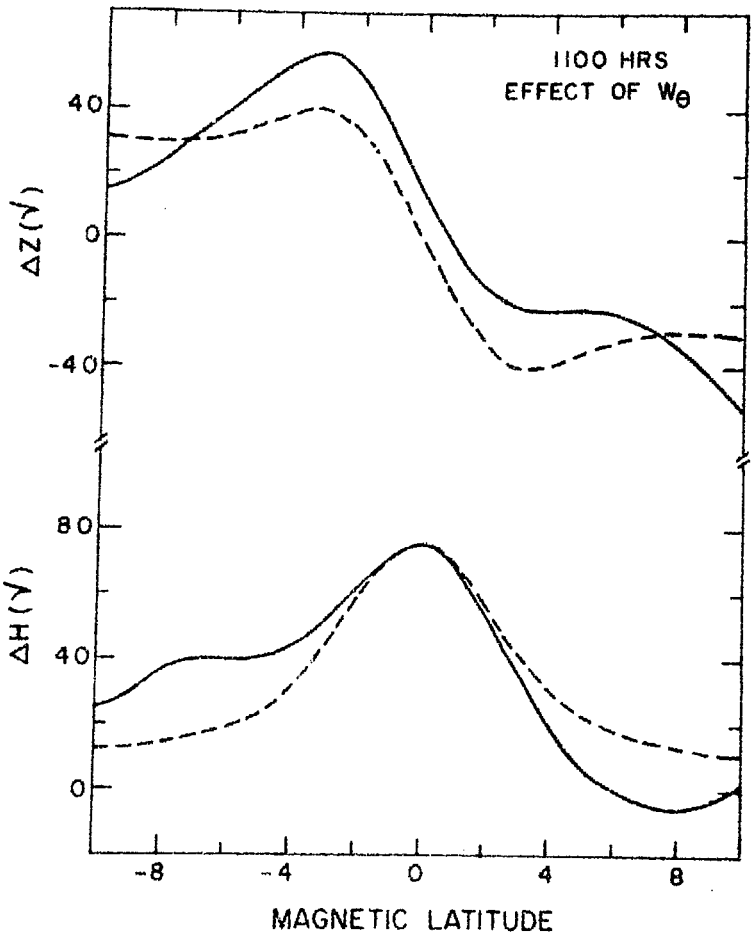

Fig.VI.47:- Latitudinal variation of ΔH (northward) and ΔZ (vertical) components of the magnetic field on the ground produced by electrojet currents at 1100 hrs LT. Full curves represent the variations with the observed W_θ at 1100 hrs LT and dashed curves are for the no-wind case.

electrojet the magnetograms at a station outside the normal electrojet region also show indication of the counter electrojet (RAGHAVARAO, Private communication). In the mechanism proposed by RAGHAVARAO (1976) it is shown that a positive wind shear in the northern hemisphere and a negative wind shear in the southern hemisphere are expected in the meridional winds engendered by the gravity wave of neutral anomaly origin.

The present results of the effects of the shear (in meridional winds) show that the meridional winds proposed by RAGHAVARAO (1976) explain qualitatively the magnetic field variations (ΔH) during C-EJ at latitudes well outside the electrojet.

The variations of ΔZ with latitude obtained in the present investigation without and with the +ve shear in the meridional wind indicate that ΔZ varies appreciably at all latitudes in general. The changes in ΔZ that the present results show at latitudes away from the dip equator can be used in future to test the presence of wind shears expected from the mechanism of RAGHAVARAO (1976) for the signatures of C-EJ in ΔZ at stations outside the electrojet.

VI.7 Effects of vertical winds on the electrojet:

A vertical wind of a few m/s can be as effective as a horizontal wind of a few tens of m/s in driving the ionization (WHITEHEAD AND HOOKE, 1971). Physically it can

be seen how a vertical wind affects the electrojet currents in the following way. A vertically upward wind produces a Lorentz field in the westward direction which opposes the primary eastward electric field. Consequently the upward polarization field and hence the eastward current density also get reduced very effectively.

The coefficient f_{6W} in the presence of a vertical wind is given by

$$f_{6W} = -\frac{B_\theta(\sigma_H/\sigma_P)\sin\theta}{a}\left[\left(\frac{W_r}{r}+\frac{W_r}{(\sigma_H/\sigma_P)}\frac{\partial(\sigma_H/\sigma_P)}{\partial r}+\frac{W_r}{B_\theta}\frac{\partial B_\theta}{\partial r}+\frac{\partial W_r}{\partial r}\right)rS+\left(\frac{W_r}{C}\frac{\partial C}{\partial\theta}+\frac{W_r}{B_\theta}\frac{\partial B_\theta}{\partial\theta}+\frac{\partial W_r}{\partial\theta}\right)C\right] \quad (25)$$

A careful examination of the above equation revealed the following. At the dip equator the second part (i.e., the coefficient of C inside the square brackets) is important. The first part, however, becomes zero because S = Sin I = 0 at the equator. Away from the equator ($\geq 3^\circ$) the two parts are comparable although the first part (the coefficient of rJ inside the square brackets), is greater than the second one. Among the various terms in the first part, the term $\frac{W_r}{(\sigma_H/\sigma_P)}\frac{\partial}{\partial r}(\sigma_H/\sigma_P)$ is the dominant one at latitudes away from the equator. Similarly in the second part, the term $(\partial W_r/\partial\theta)$ is the dominant one in the region of 3° to $4^\circ.5$ dip latitude as per the chosen model of W_r which

is discussed later. As mentioned earlier, the derivative of σ_H/σ_P with altitude i.e., $\frac{\partial(\sigma_H/\sigma_P)}{\partial r}$ changes its sign from +ve to -ve at 100 km. An upward wind (W_r positive) can be shown to reduce the current function ψ at all altitudes.

The vertical wind profile obtained by the barium-strontium cloud releases reported in the Chapter II is reproduced in Fig. VI.48. This profile is taken to be a representative vertical wind over the dip equator at around 1500 hrs during which time the counter electrojet (C-EJ) is most frequently observed. The electron density profile measured at 1532 hrs by PRAKASH ET AL (1976) on a day (17 August, 1972) when the C-EJ is in progress is used to compute the conductivities.

It is known from a study of the characteristic features of the C-EJ, that its effect is maximum in the vicinity of the centre of the normal electrojet. With this in view, a model for the variation of the vertical wind with dip angle is chosen such that the wind decreases on either side of the dip equator. Another argument in favour of such a model is due to RAGHAVARAO (1976) who predicts that vertical winds exist in a narrow region around the dip equator and cause the C-EJ. The variation of vertical wind with dip angle is assumed as

$$W_r = W_r(r,I) = W_r(r) \text{ Cos } 10\,I \qquad (25)$$

This equation shows that the wind reduces to zero at a dip

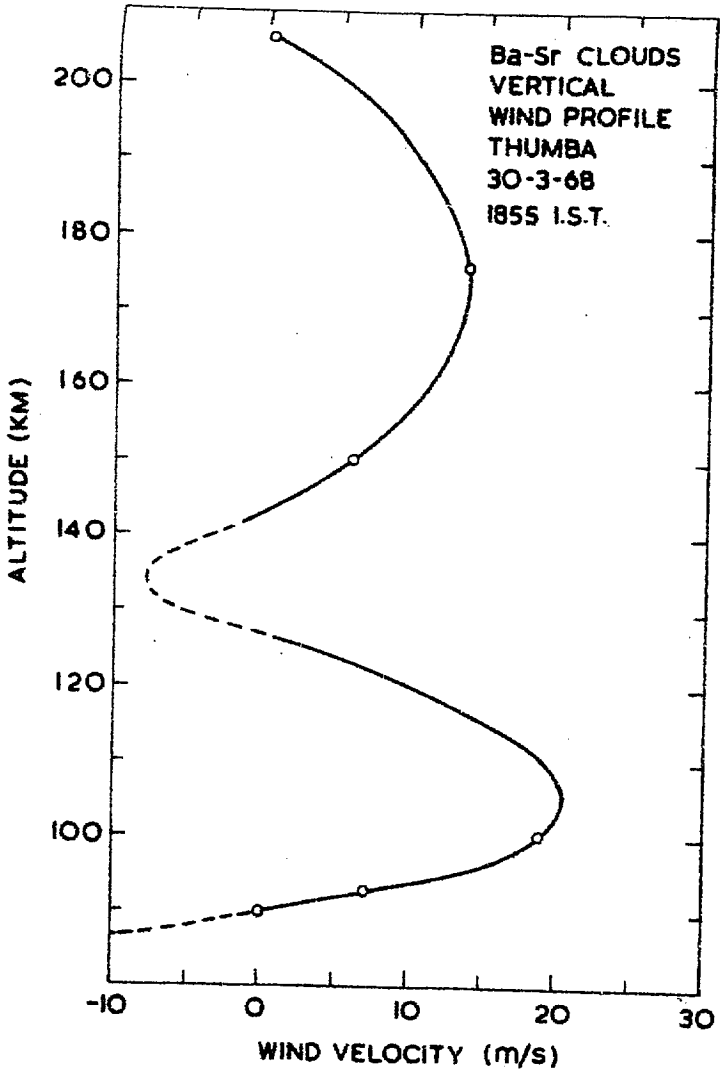

Fig.VI.48:- Profile of vertical wind velocity W_r observed over Thumba at 1855 hrs LT by barium-strontium releases. The dashed portions of the profile indicate the uncertainty in the extrapolation due to lack of experimental points. The circles represent the observations (CHAPTER II).

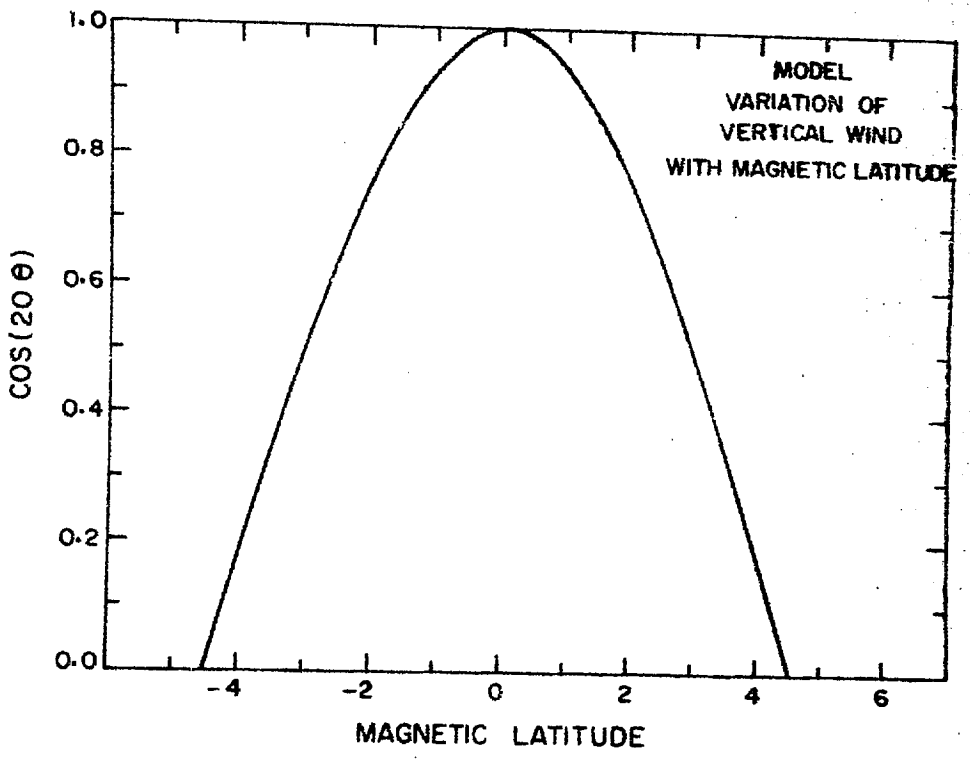

Fig.VI.49:- A model of latitudinal variation of vertical wind velocity W_r. The choice of the function Cos (20 θ) is based on RAGHAVARAO (1976).

angle of 9° (dip latitude $\approx 4^{\circ}.5$) as given in Fig.VI.49. At dip angles greater than 9° on either side of the equator the wind is assumed to be zero. The variation of the vertical wind W_r with latitude chosen above is arbitrary, as the wind can be terminated at any latitude close to the dip equator. However, the choice made here can be justified on the basis of the results obtained. Moreover, it helps gain, for the first time, a physical insight to the problem of C-EJ or to say the least, the knowledge of the effects of vertical winds on the electrojet.

Figs. VI.50 a, b show the profiles of the eastward current density J_{ϕ} at 1532 hrs LT, for no-wind case (a) and for the vertical wind (b) at 0°, 2° and 4° magnetic latitudes. The profiles show a significant deviation of J_{ϕ} in the presence of a vertical wind from the normal profiles. A reversal of J_{ϕ} (westward current density) is seen at the dip equator at the altitude 106 km where the vertical wind is maximum (≈ 20 m/s). Above about 130-140 km, the vertical wind does not show any effect on J_{ϕ}. Thus, the effects are maximum in the electrojet region. It can be seen that a vertically upward wind of 1 m/s can reduce J_{ϕ} by about 7%. At 4° latitude, the current density J_{ϕ} is increased below about 100 km(where W_r is only ≈ 10 m/s)because of the winds. This increase is due to the gradient of W_r with respect to the latitude ($\partial W_r/\partial \theta$) which is maximum at around 4°. The

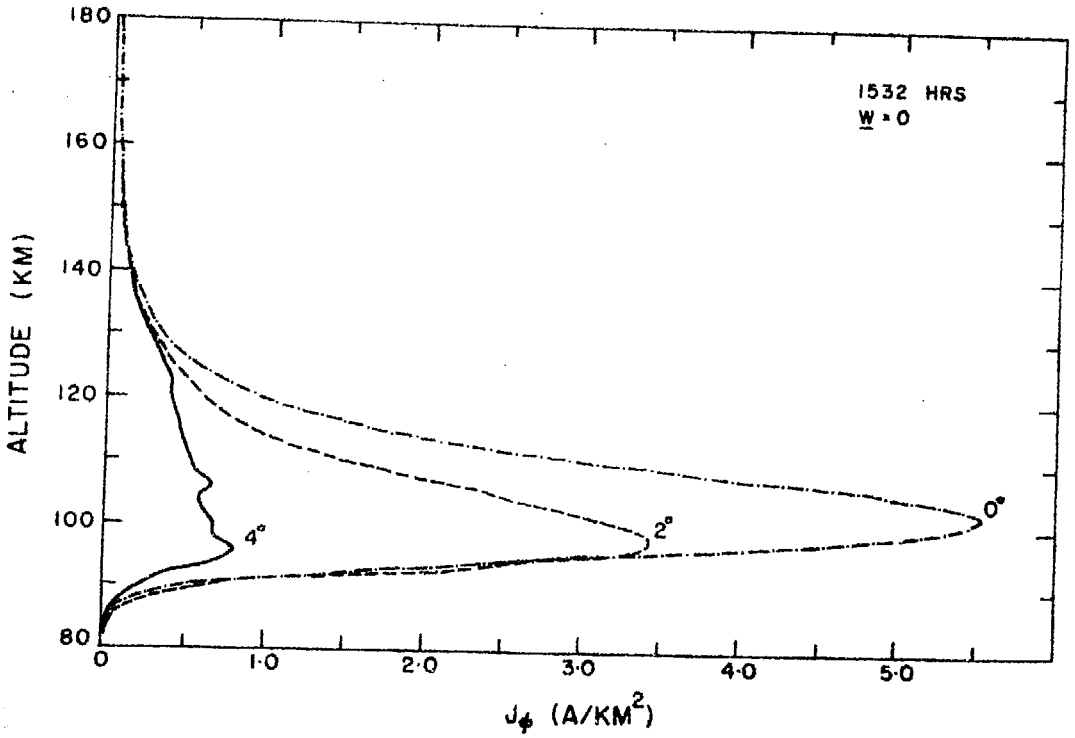

(a)

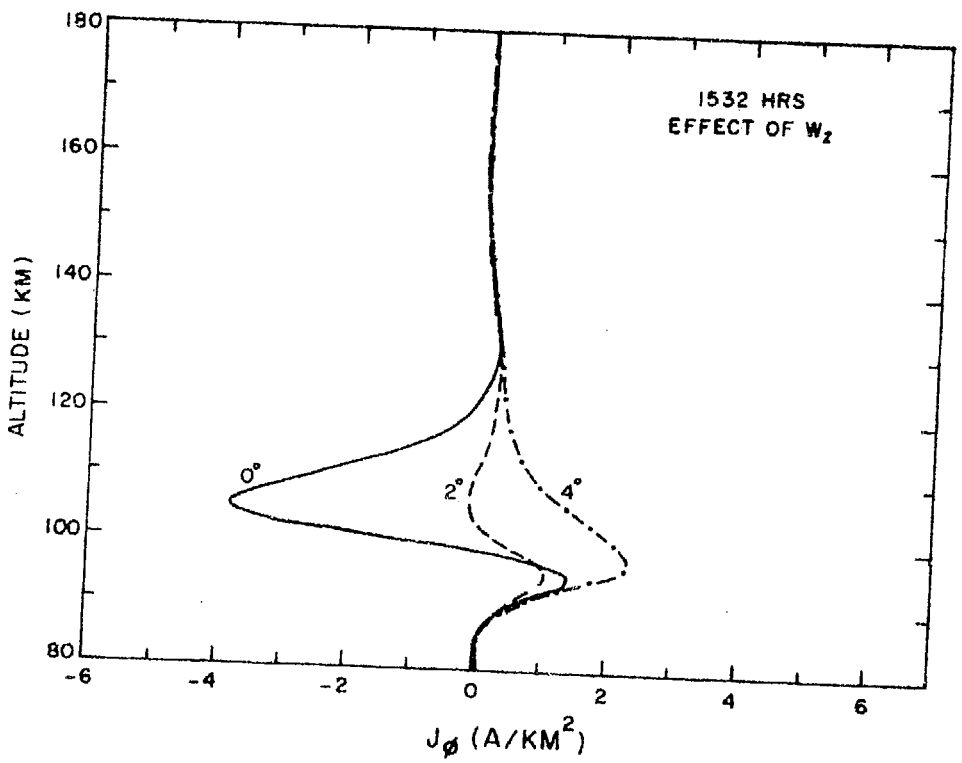

(b)

Fig.VI.50:- Vertical profiles of eastward current density $J\phi$ at 0^o, 2^o and 4^o magnetic latitudes at 1532 hrs LT. (a) No-wind case. (b) With the observed vertical wind W_r.

gradient term ($\partial W_r / \partial \theta$) opposes the other terms and acts to oppose the upward wind effects when the latter is small.

The profiles of the vertical electric field E_r at 0°, 2° and 4° dip latitude without wind (a) and with the vertical wind (b) are shown in Figs. VI.51 a,b. These profiles closely follow the profiles of J_ϕ.

Figs. VI.52 a and b show the profiles of the vertical current density J_r for no-wind case and for the vertical wind respectively. A total reversal of the profiles is seen because of the vertical winds just as in the case of the profiles of J_ϕ. At the dip equator, the peak altitude of J_r is lowered from 120 km to 115 km by the wind. About 180% reduction is obtained at 115 km at the equator. At 2° latitude an enhancement of about 150% is produced by the wind at 115 km. The profile at 4° also is drastically changed though the wind is small. This is because the latitudinal variation of the wind being very rapid at 4°. The effects of the vertical wind on J_r are same in northern and southern hemispheres.

Figs. VI.53 a and b show the profiles of the meridional current density J_θ with no-wind and with the vertical wind respectively. At the equator, the wind does not produce any J_θ, because the vertical wind can not produce a meridional current flow at the equator where the magnetic field

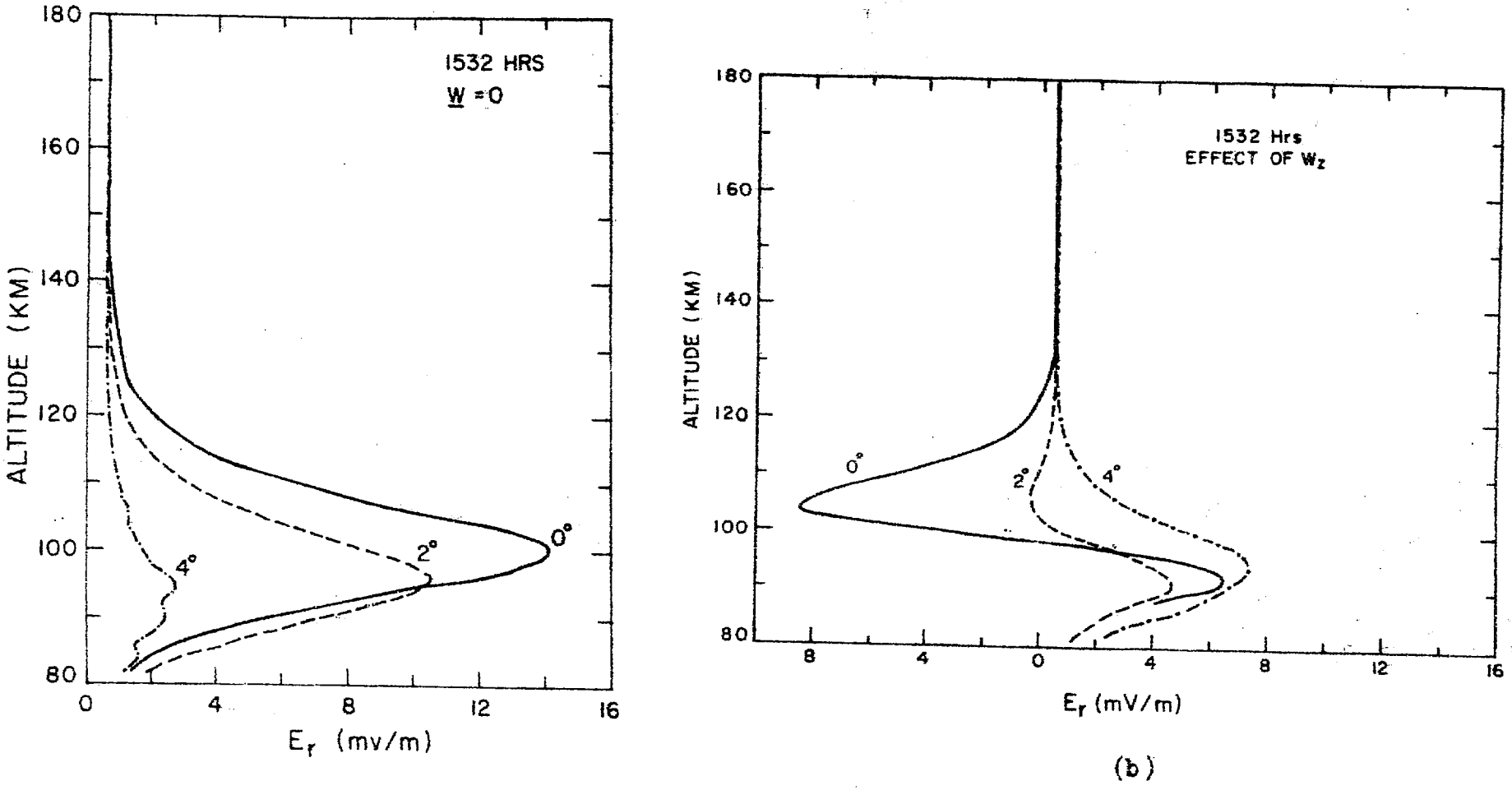

Fig.VI.51:- Vertical profiles of vertical electric field E_r at 0^o, 2^o and 4^o magnetic latitudes at 1532 hrs LT.
(a) No-wind case. (b) with the observed vertical wind W_r.

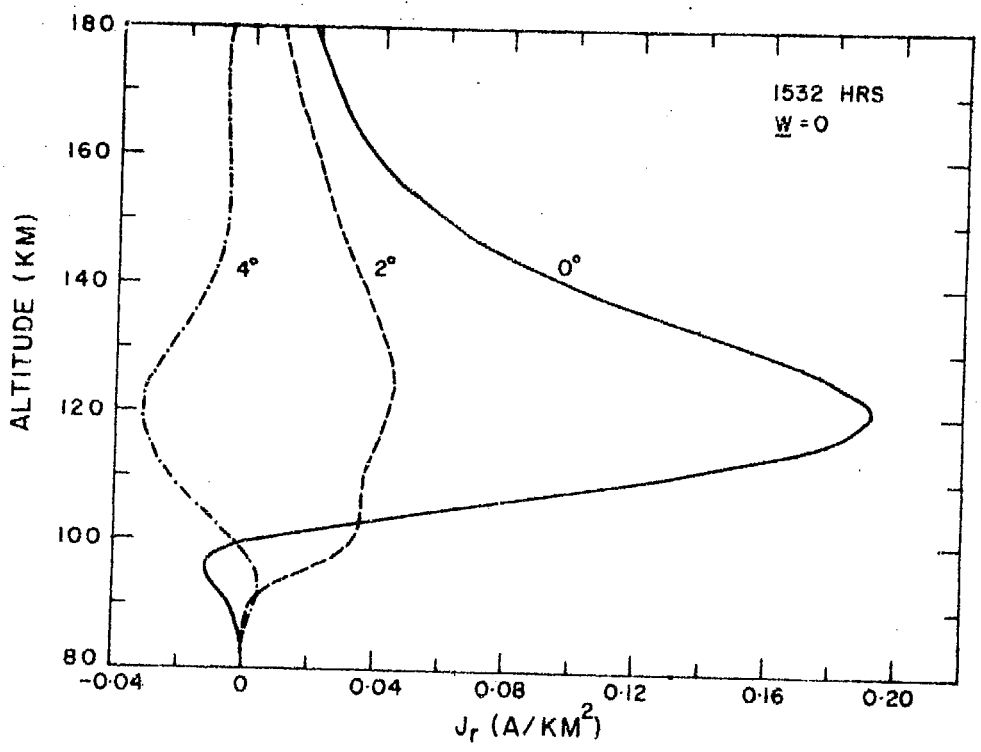

(a)

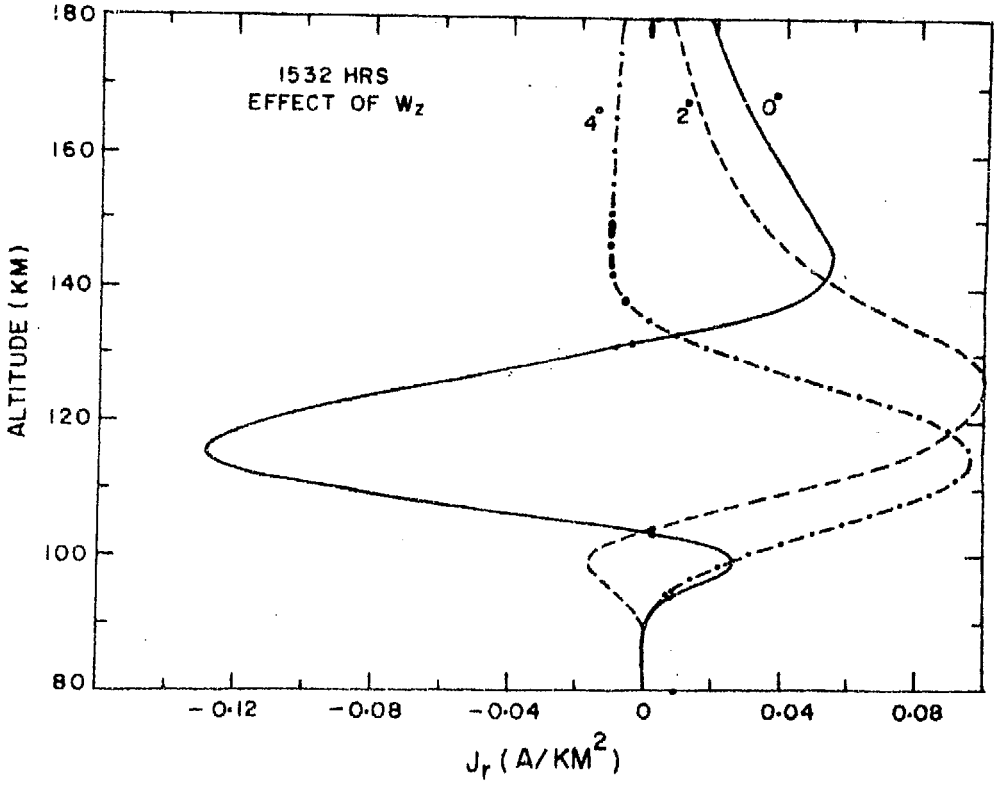

(b)

Fig.VI.52 :- Vertical profiles of vertical current density J_r at 0^o, 2^o and 4^o magnetic latitudes at 1532 hrs LT. (a) No-wind case. (b) With the observed vertical wind W_z.

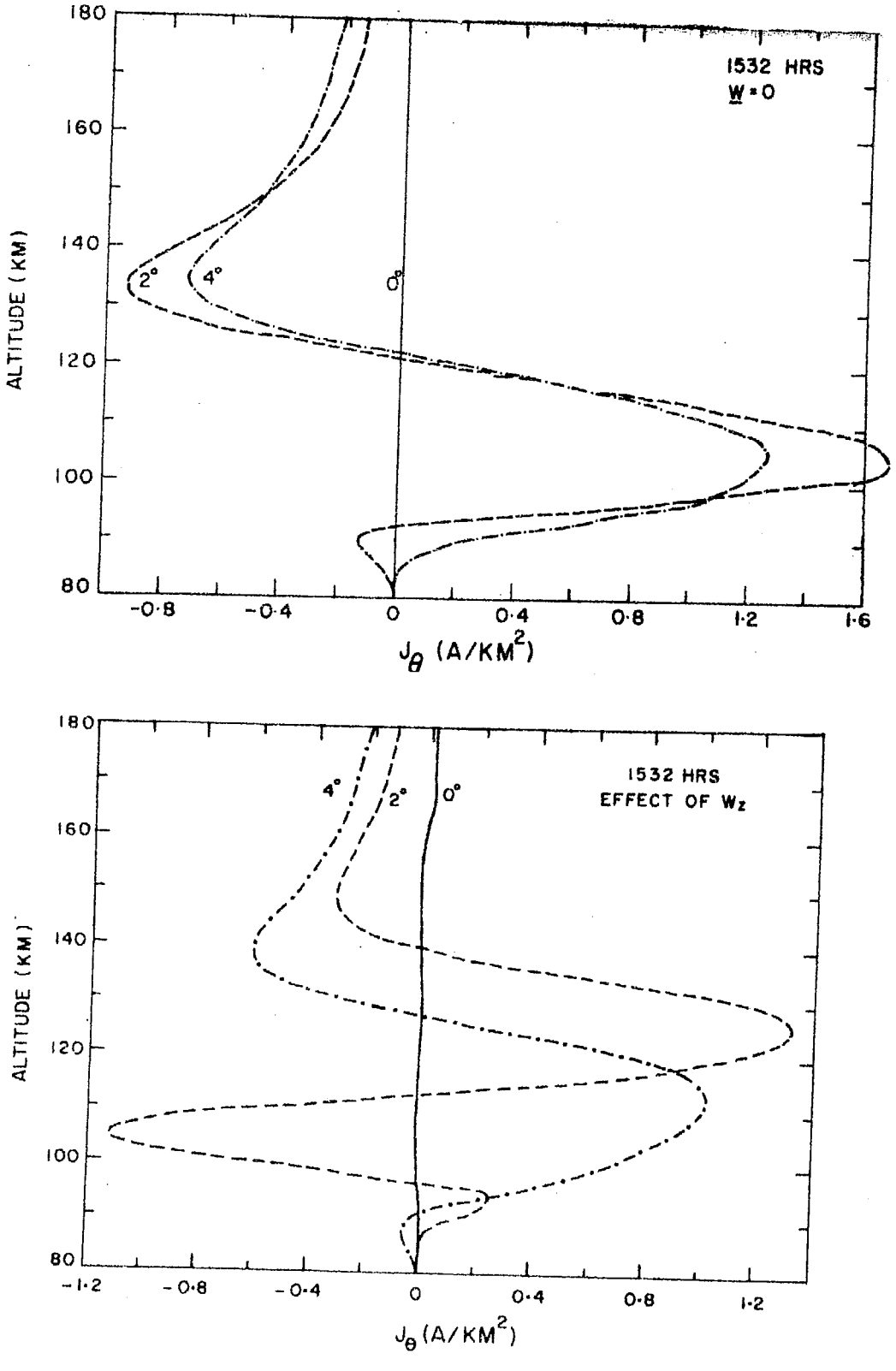

Fig.VI.53:- Vertical profiles of meridional current density J_θ at 0^o, 2^o and 4^o magnetic latitudes at 1532 hrs LT. (a) No-wind case. (b) With the observed vertical wind W_z

is entirely northward. However, at 2^{o} away from the equator, J_{θ} is drastically changed because of the wind. When the wind is upward and maximum at 105 km, J_{θ} reached a negative maximum (i.e., northward current). At 4^{o}, there is no appreciable effect due to the winds. The effects of vertical winds on J_{θ} are opposite in the southern hemisphere to those in the northern hemisphere.

Figs. VI.54 a and b show the distribution of the eastward current density J_{ϕ} in the r-θ plane with no-wind and with the vertical wind respectively. A negative current cell centered at the dip equator and at 105 km, where the wind velocity is maximum is formed because of the wind. The width and thickness of this negative current cell are much smaller than those of the normal electrojet.

The latitudinal variation of the northward component of earth's magnetic field, $\triangle H$, due to the electrojet current density J_{ϕ}, is calculated and plotted in Fig.VI.55 with no-wind (dashed curves) and with the model vertical wind (full curves). In computing the $\triangle H$ and $\triangle Z$, the contribution due to the induced earth currents is ignored. The $\triangle H$ curve with no-wind represents the typical signature on the ground by the normal electrojet. The $\triangle H$ variation with latitude when the vertical wind is present, also shows the characteristic ground signature of the C-EJ as was evidenced in the Fig.VI.2 at 1500 hrs on 31 Jan. 1969.

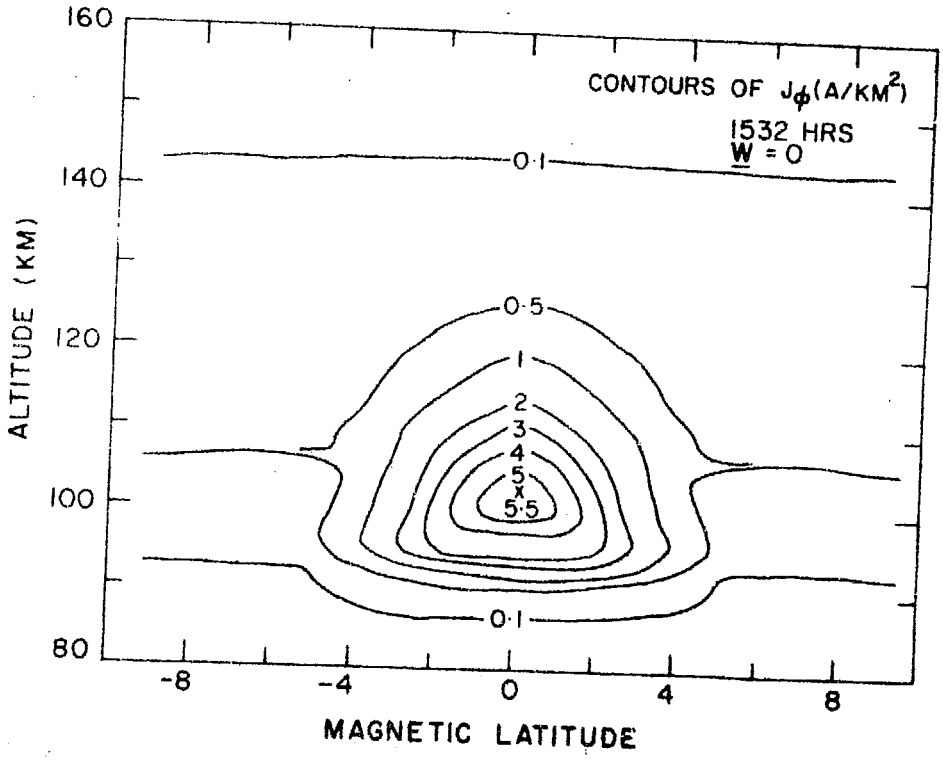

(a)

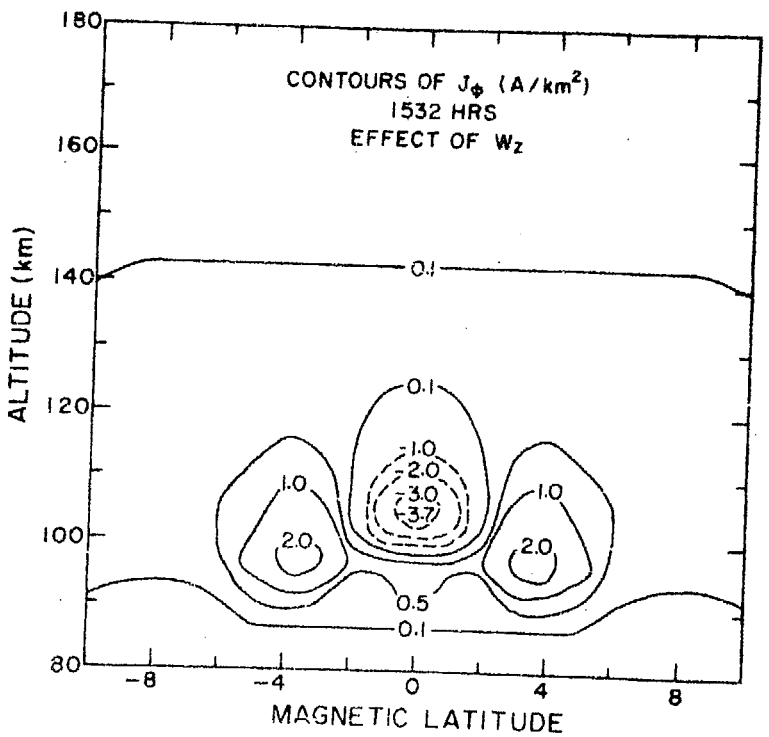

(b)

Fig.VI.54:- Distribution of eastward current density J_ϕ in the r - θ plane at 1532 hrs LT. (a) No-wind case. (b) With the observed vertical wind W_r.

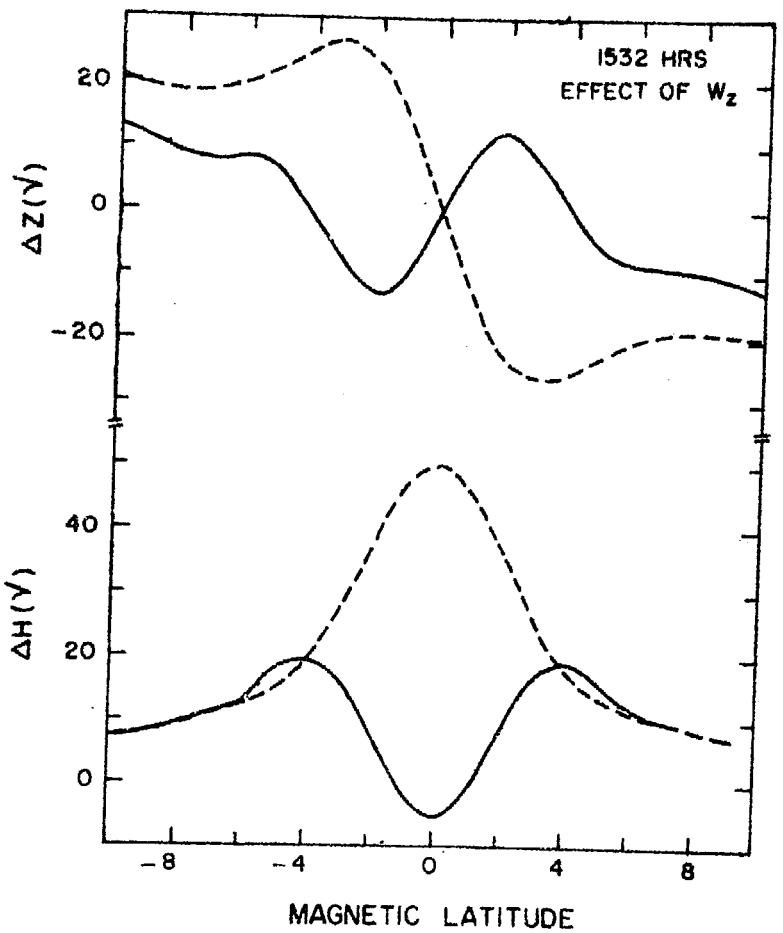

Fig.VI.55:- Latitudinal variation of ΔH (northward) and ΔZ (vertical) components of the magnetic field on the ground produced by electrojet currents at 1532 hrs LT. Full curves represent the variations with the observed vertical wind W_r and dashed curves are for the no-wind case.

The only difference between these profiles is that the magnitude of -ve ΔH is a little higher in the observed profile than the one computed with the model vertical wind. The latitudinal extent of C-EJ, the observed decrease in ΔH, and the reversal in ΔZ can all be reproduced by taking the proper latitudinal extent of the vertical wind and the magnitude of the maximum vertical wind in the present model. In the present case, the maximum vertical wind of 20 m/s has effected a change in ΔH from + 64γ to -5.5γ at the equator i.e., nearly 70γ reduction in ΔH by the electrojet current alone.

The variation of ΔZ with latitude without and with vertical wind is also presented in Fig.VI.55. The change in the ΔZ profile effected by the vertical wind is almost identical with that expected during C-EJ. This can be compared with the ΔZ variation observed at 1500 hrs on 31 January, 1969, shown in the Fig.VI.2.

The most attractive feature of the vertical wind hypothesis for the C-EJ, as compared to any other form of wind in the horizontal direction, is that it explains the maximum reduction in J_ϕ at or in the vicinity of the electrojet. Thus, if such vertical winds were to be present over the dip equator, it is clear from the present computations that the counter electrojet of observed intensity can be effected by a 20 m/s vertical wind.

It is easy to visualize that vertical winds of lesser magnitude than taken in the present model can cause partial counter electrojet. The counter electrojet can be conceived to start soon after the peak value in $\triangle H$ and slowly the depression in $\triangle H$ developing to its lowest value in a period of about 2 to 2.5 hrs (half period) and then again increasing. Thus, the vertical winds, if assumed to be the cause, increase in magnitude and in latitudinal extent with time and decrease to zero in a period of 4 to 5 hours producing different phases of the counter electrojet as revealed by the latitudinal variations of $\triangle H$ and $\triangle Z$ at different local times.

Thus, the mechanism proposed by RAGHAVARAO (1976) with vertical winds as the cause for the C-EJ can explain most of the observed features of the phenomenon. The observed features that require to be explained by the vertical wind mechanismare the following.

(i) Occurrence of blanketing type sporadic E near the dip equator and the associated ledge formation in the electron density profile of the E region (PRAKASH ET AL,1976).

(ii) The changes in F region such as the inhibition of the ionization anomaly associated with the C-EJ (RASTOGI,1974)

Finally it should be noted that in the present computations, we ignored the polarization effects in the horizontal (east-west) direction while introducing the meridional

and vertical winds. The polarization fields generated because of the charge separation in the horizontal direction may cancel the Lorentz (dynamo) field to some extent. While it is quite likely that these polarization fields may not be very significant because of the conductivity being continous in the horizontal direction, we do not have any reason either to neglect these fields. Rigorous computations should include these effects. Furthermore, the effects of the horizontal and vertical winds are considered here separately. It is worthwhile to introduce these winds simultaneously in the model and to see how their individual effects add up or cancel.

CHAPTER VII

CONCLUSIONS

In the foregoing Chapters we discussed results of experimental and theoretical studies on the nature of the neutral wind motions and their effects on the equatorial electrojet. Also, we described how the electric field measurements coupled with simultaneous electron density measurements can be used to verify the theories of the electrojet. Important conclusions and suggestions for future work are summarized in this Chapter.

1. The neutral wind motions obtained by the vapour release experiments performed over the dip equator revealed the presence of vertical shears in the horizontal winds mainly in the altitude region 90-110 km at any time of the day. During the evening hours these shears seem to be prevalent at higher altitudes as well. Internal atmospheric gravity waves are found to be largely responsible for these shears. Gravity waves of amplitudes as large as 80 m/s are sometimes observed, especially during the afternoon hours. The dominant tidal motions at the equator in the altitude region 90-120 km are diurnal with maximum amplitude at an altitude of about 110 km and with vertical scale sizes of the order of 20 km. These are identified with the (1, 1) diurnal propagating mode. More number of artificial vapour release experiments (which

cover a very large range of altitudes) have to be performed at the dip equator, particularly during the daytime to ascertain these results.

2. Vertical winds of amplitude as large as 20 m/s are detected over the dip equator, the maximum amplitude occuring at about 100 km. With this observation coupled with the simultaneous observations of vertical winds at higher altitudes, a wave type profile of vertical winds was obtained. This profile with large vertical wavelength is suggestive of the presence of an internal atmospheric gravity wave in the lower thermosphere. As the trail releases fail to provide the evidence for the presence of vertical winds, experiments with point releases particularly in the daytime are desirable to study the behaviour of these winds. The differential photometric device described in Chapter III is of great value. For, it facilitates the observations of the vapour cloud in the daytime.

3. The ratio of the vertical electric field to the eastward electric field at any altitude over the dip equator is better represented by the ratio of integrated (along a magnetic field line) Hall conductivity to the integrated Pedersen conductivity, than the local ratio of these two conductivities. This supports the model electrojet originally proposed by UNTIEDT (1967) with a non-divergent current system which necessitates the flow of meridional currents.

Measurement of electric fields, in particular during daytime, along with the electron density is necessary to establish the above conclusion. Further, theoretical computations of the latitudinal distribution of the ratio of the integrated conductivities should be carried out. This will be useful in further verification of the theory by making observations on the electric fields at the latitudes close to the dip equator.

4. The wind shear mechanism is found to be operative even at the dip equator if the winds of short scale sizes (compared to tidal winds) such as gravity waves are considered. It is important to take the horizontal wavelength (and hence the vertical motions) of the gravity wave winds into account in computing the electric fields that can be engendered by these winds. The neglect of horizontal wavelength leads (under certain circumstances) to over-estimation of the efficiency of the wind shear mechanism at the dip equator. The occurrence of large-scale stratifications in the profiles of electron density during nighttime over the dip equator can satisfactorily be explained by the wind shear mechanism. We need simultaneous measurements of winds and electron density to prove the validity of the theory. Further, theoretical studies such as solving the continuity equation to estimate quantitatively the intensity of the stratifications when the changes in the photochemical processes and recombination due

to the presence of gravity wave are included.

5. Zonal winds and wind shears are found to be not so effective at the dip equator as at other (low) latitudes in modulating the electrojet currents and fields. The effects of shears are,however, found to be greater in the region 110-140 km than in the region 90-110 km where the shears usually occur. Very strong shears (like, for instance, 100 m/s/km) can cause 50% change in the eastward current density at 100 km over the dip equator. The observed day-to-day and daily variations in the width and thickness of the electrojet can be explained as due to the effects of zonal wind shears.

6. Meridional winds and shears do not affect the electrojet (eastward) current over the dip equator. However, the meridional currents are drastically affected. The observed north-south asymmetry in the distribution of the electrojet currents (and hence in the latitudinal profiles of ΔH and ΔZ) and the shift in the peak of ΔH from the equator can be attributed to the effects of meridional winds and shears.

7. Vertical winds greatly affect the electrojet. A vertical wind of 20 m/s at 100 km can even reverse the electrojet during the afternoon hours. Corresponding profiles of ΔH and ΔZ at the equatorial region are also reversed. It is suggested that the counter-electrojet can be caused by the presence of a vertical wind of 15-20 m/s at 100 km altitude. To verify this theory simultaneous measurements of

currents, winds (both horizontal and vertical) and electron density are suggested. Further theoretical study should be undertaken with more realistic models of winds. Also, the horizontal and vertical winds should be considered together (rather than studying their effects separately). Furthermore, the discrepancy as to the altitude of the maximum current between the models and the observations is yet to be resolved.

APPENDIX I

NUMERICAL SOLUTION OF THE PARTIAL DIFFERENTIAL EQUATION FOR THE CURRENT FUNCTION.

The equation (Eqn. 15, Chapter VI) is technically termed as a second-order elliptic partial differential equation in ψ

$$f_1 \frac{\partial^2 \psi}{\partial r^2} + 2 f_2 \frac{\partial^2 \psi}{\partial r \partial \theta} + f_3 \frac{\partial^2 \psi}{\partial \theta^2} + f_4 \frac{\partial \psi}{\partial r} + f_5 \frac{\partial \psi}{\partial \theta} + f_6 = 0 \qquad (1)$$

f_1 to f_6 are coefficients depending upon parameters which in turn depend upon r and θ. The discriminant $(f_2^2 - f_1 f_3)$ is negative and hence the equation is of elliptic type.

Boundaries and boundary conditions:

The current function is to be computed in the region $80^\circ \leq \theta \leq 100^\circ$ and 80 km $\leq (r - a) \leq 200$. It is assumed that $\psi = 0$ at these boundaries.

Difference equations:

The difference equations for various differential coefficients are written as,

$$\left[\frac{\partial^2 \psi}{\partial r^2}\right]_{i,j} = \left(\psi_{i+1,j} - 2\psi_{i,j} + \psi_{i-1,j}\right) / h_r^2 \qquad (2)$$

$$\left[\frac{\partial^2 \psi}{\partial \theta^2}\right]_{i,j} = \left(\psi_{i,j+1} - 2\psi_{i,j} + \psi_{i,j-1}\right) / h_\theta^2 \qquad (3)$$

$$\left[\frac{\partial^2 \psi}{\partial r \partial \theta}\right]_{i,j} = \left(\psi_{i+1,j+1} - \psi_{i+1,j-1} - \psi_{i-1,j+1} + \psi_{i-1,j-1}\right) / 4 h_r h_\theta (4$$

$$\left[\frac{\partial \psi}{\partial r}\right]_{i,j} = \left(\psi_{i+1,j} - \psi_{i,j}\right) / h_r \text{ or } \left(\psi_{i,j} - \psi_{i-1,j}\right) / h_r \qquad (5)$$

$$\left[\frac{\partial \psi}{\partial \theta}\right]_{i,j} = \left(\psi_{i,j+1} - \psi_{i,j}\right) / h_\theta \text{ or } \left(\psi_{i,j} - \psi_{i,j-1}\right) / h_\theta \qquad (6)$$

where h_r and h_θ are the step sizes in r and θ. $i = 1, 2, \ldots\ldots n+1$ and $j = 1, 2, \ldots\ldots m+1$; n and m being the number of intervals in the ranges for r and θ, i.e., $n = (r_{n+1} - r_1)/h_r$ and $m = (\theta_{m+1} - \theta_1)/h_\theta$. At the outset, the values of $\psi_{i,j}$ are initialized by,

$$\psi_{i,j} = 0, \text{ for } i = 2 \text{ to } n \text{ and } j = 2 \text{ to } m.$$

We then write,

$$F_{i,j} = f_{1i,j}\left(\frac{\partial^2\psi}{\partial r^2}\right)_{i,j} + 2f_{2i,j}\left(\frac{\partial^2\psi}{\partial r\,\partial\theta}\right)_{i,j} + f_{3i,j}\left(\frac{\partial^2\psi}{\partial\theta^2}\right)_{i,j} + f_{4i,j}\left(\frac{\partial\psi}{\partial r}\right)_{i,j} + f_{5i,j}\left(\frac{\partial\psi}{\partial\theta}\right)_{i,j} + f_{6i,j} \qquad (7)$$

The derivatives are replaced by the corresponding difference equations given above.

Method of successive over-relaxation:

In general, if the coefficient of $\psi_{i,j}$ which is determined by the diagonal elements of the coefficient matrix, is predominant over the other coefficients, then the convergence of the equations to a reasonable solution is fast. To ensure the dominance of the diagonal elements we make the right choice of the difference equations for $(\partial\psi/\partial r)$ and $(\partial\psi/\partial\theta)$, so that the coefficient of $\psi_{i,j}$ is maximum. For example, if the coefficient of $\partial\psi/\partial r$ (f_4) is positive, then we choose the first choice for the difference equation of $\partial\psi/\partial r$, $(\psi_{i+1,j} - \psi_{i,j})/h_r$ because the coefficients $\psi_{i,j}$ are negative in the difference equations of higher order differential coefficients.

Now we write,

$$F'_{i,j} - Q_{i,j} \psi_{i,j} = 0 \qquad (8)$$

where $F'_{i,j}$ is the equation $F_{i,j}$ minus the terms containing $\psi_{i,j}$; and $Q_{i,j}$ is the coefficient of $\psi_{i,j}$.

$\therefore \psi_{i,j} = F'_{i,j}/Q_{i,j}$, or

$$\psi_{i,j} = \frac{C F_{i,j}}{Q_{i,j}} + (1 - C) \psi_{i,j} \qquad (9)$$

where C is an arbitrary constant. For the method of successive over-relaxation used to solve the elliptic type of equations, C is generally taken to be greater than 1.

We first substitute the values of $F_{i,j}$, $Q_{i,j}$ and the initial values of $\psi_{i,j}$ and calculate new $\psi_{i,j}$. These new $\psi_{i,j}$ are compared with the initial $\psi_{i,j}$ and it is checked whether the relative error $\{\psi_{i,j}$ (new) $- \psi_{i,j}$ (in$\}/\psi_{ij}$ (i computed/ each time is less than a certain number which determines the accuracy of the numerical results. Till the $\psi_{i,j}$ 'converge' to this accuracy, the 'iteration' is continued.

We achieved fast convergence by choosing C = 1.7 and for accuracy number 0.5×10^{-3}; this number assures that the results are accurate to the first three significant digits.

Furthermore, the physical validity of the numerical results can be verified (i) by changing the boundary conditions, (ii) by changing the boundaries, (iii) by changing the step sizes in r and θ and (iv) by changing the accuracy. It is found that the choice of the boundaries r = 80 and 200 km and $\theta = 80^{\circ}$ to 100° with $\psi = 0$ at all the boundaries and with $h_r = 2$ km and $h_\theta = 0^{\circ}.5$ gives fairly accurate and physically valid results.

APPENDIX - II

MAGNETIC FIELD FLUCTUATIONS ON THE GROUND PRODUCED BY THE ELECTROJET.

The presence of a varying current system in the upper atmosphere, produces magnetic field fluctuations on the ground level. According to Biot-Savart's law the magnetic field potential induced by an infinitely long line of current is given by

$$V = \frac{\mu_0 I}{2\pi} \tan^{-1}\left[\frac{\cos\theta}{(r/a) - \sin\theta}\right] \qquad (1)$$

where, μ_0 is the permeability of free space, I is the line current (in Amperes), θ is magnetic colatitude and r is the radial distance of the location of I from the centre of the earth. a is the radius of the earth.

The magnetic field due to this potential is given by

$$\underline{\Delta B} = -\nabla V \qquad (2)$$

In r, θ, ϕ coordinate system, the components of $\underline{B}$ in θ and r directions are

$$(\Delta B)_\theta = -\Delta H = \frac{1}{r}\frac{\partial V}{\partial \theta}$$
$$(\Delta B)_r = -\Delta Z = \frac{\partial V}{\partial r} \qquad (3)$$

The differentiation of (1) leads to

$$\Delta H = \frac{\mu_0 I}{2\pi r} \frac{(r/a)\sin\theta - 1}{(r/a)^2 + 1 - 2(r/a)\sin\theta} \qquad (4)$$

and $$\Delta Z = -\frac{\mu_0 I}{2\pi r} \frac{(r/a)\cos\theta}{(r/a)^2 + 1 - 2(r/a)\sin\theta} \qquad (5)$$

Here, ΔH and ΔZ are fluctuations in the horizontal (northward) and vertical component of the earth's magnetic field.

The region 80-200 km and 80°-100° in r-θ plane is divided into a number of blocks of width 1°(in θ) and height 4 km (in r). The net current flowing in each of such blocks is computed and the quantities ΔH and ΔZ are calculated using the equations (4) and (5). Finally, the ΔH and ΔZ obtained from the current in each block are added up to give the net ΔH and ΔZ. The results are checked by computing the current in blocks of 1° width and 120 km in hight, i.e., height integrated current at every one degree latitude. The results obtained from these two methods are in good agreement with each other and hence the simpler method of taking the height-integrated blocks is found to be adequate.

REFERENCES

AGGSON, T.L., in Atmospheric Emissions, ed. B.M. MCCORMAC AND A. OMHOLT, Van Nostrand Reinhold, New York, 1969.

AGGSON, T.L., AND HEPPNER, J.P., NASA-GSFC, Rep., 1965.

AMAYENC, P., Radio Sci., 9, 281, 1974.

AMAYENC, P., AND REDDY, C.A., Planet. Space Sci., 20, 1269, 1972.

ANANDARAO, P.G, Geophys. Res. Lett., 3, 545, 1976.

ANANDARAO, B.G., RAGHAVARAO, R., AND REDDI, C.R., J. Geophys. Res., 82, 1510, 1977 a.

ANANDARAO, B.G., RAGHAVARAO, R., DESAI, J.N., AND HAERENDEL, G., J. Atmos. Terr. Phys. (in press), 1977 b.

ANANDARAO, B.G., DESAI, J.N., GILES, M., MARTELLI, G., RAGHAVARAO, R., AND ROTHWELL, P., J. Atmos. Terr. Phys., 39, 927, 1977 c.

APPLETON, E.V., Proc. Roy. Soc., A 126, 542, 1930.

AXFORD, W.I., J. Geophys. Res., 68, 769, 1963.

AXFORD, W.I., J. Geophys. Res., 69, 5093, 1964.

AXFORD, W.I., AND CUNNOLD, D.M., Radio Sci., 1, 191, 1966.

AXFORD, W.I., AND HINES, C.O., Can. J. Phys., 39, 1433, 1961.

AXFORD, W.I., CUNNOLD, D.M., AND GLEESON, L.J., Planet. Space Sci., 14, 909, 1966.

BAKER, W.G., Phil. Trans. Roy. Soc.London, A 246, 295, 1953.

BAKER, W.G., AND MARTYN, D.F., Phil. Trans. Roy. Soc., A 246, 281, 1953.

BAILSLEY, B.B., J. Geophys. Res., 70, 3175, 1965.

BAILSLEY, B.B., J. Atmos. Terr. Phys., 31, 475, 1969 a.

BAILSLEY, B.B., J. Geophys. Res., 74, 2333, 1969 b.

BAILSLEY, B.B., J. Atmos. Terr. Phys. 35, 1035, 1973.

BAILSLEY, B.B., AND WOODMAN, R.F., World Data Center A Rept. UAG-17, 1971.

BANDYOPADHYAY, P., AND MONTES, H., J. Res. NBS, 68D, 1237, 1964.

BANKS, P.M., Planet. Space. Sci., 14, 1085, 1966 a.

BANKS, P.M., Planet. Space.Sci., 14, 1105, 1966 b.

BANKS, P.M. AND KOCKARTS, G., Aeronomy Parts A and B., Academic Press., New York, 1974.

BARTELS, J., AND JOHNSTON, H.F., Terr. Magn. Atmos. Electr., 45, 269, 1940.

BATCHELOR, G.K., The theory of homogeneous turbulence, Cambridge Univ. Press, 1953.

BATES, D.R., J. Geophys. Res., 55, 347, 1950.

BATES, D.R. AND MASSEY, H.S.W., Proc. Roy. Soc.(London) A 192, 1947.

BATTEN, E.S., Report P-2018-NSF, Rand Corp., Santa Monica, Calif., 1960.

BAUER, S.J., Introduction to Planetary ionospheres, Sprenger -Verlag, Berlin, 1973.

BAUER, S.J., AND NAGY, A.F., Proc. I.E.E.E., 63, 230, 1975.

BEDINGER, J.F., Rev. Sci. Instrum., 41, 1234, 1970.

BEDINGER, J.F., J. Atmos. Terr. Phys., 35, 377, 1973.

BEDINGER, J.F., J. Atmos. Terr. Phys., 39, 241, 1977.

BEDINGER, J.F., KNAFLICH, H., MANRING, E., AND LAYZER, D., Planet. Space Sci., 16, 159, 1968.

BEER, T., Atmospheric waves, Adam Hilger, London, 1974.

BEHNKE, R.A., AND HAGFORS, T., Radio Sci., 9, 211, 1974.

BEHNKE, R.A., AND HARPER, R.M., J. Geophys. Res., 78, 8222, 1973.

BEIRMANN, L., Observatory, 77, 109, 1957.

BERNARD, R., Radio Sci., 9, 295, 1974 a.

BERNARD, R., J. Atmos. Terr. Phys., 36, 1105, 1974 b.

BERNARD, R., AND SPIZZICHINO, A., J. Atmos. Terr. Phys. 33, 1345, 1971.

BEST, G.T., Appl. Optics., 9, 2666, 1970 a.

BEST, G.T., J. Atmos. Sci., 27, 979, 1970 b.

BEST, G.T., AND T.N.L. PATTERSON, Planet. Space Sci., 9, 521, 1962

BHAVSAR, P.D., AND RAO, .K.R., Space Res. 8 655, 1968.

BHAVSAR, P.D., NARAYANAN, M.S., AND DESAI, J.N., Space Res., 16, 319, 1976.

BIONDI, M.A., Ann. Geophys ., 20, 34, 1964.

BLAMONT, J.E., Planet. Space Sci., 10, 89, 1963.

BLAMONT, J.E., AND BARAT, J., in Aurora and Airglow, ed. B.M. MCCORMAC, Reinhold, New York, p. 159, 1967.

BLAMONT, J.E., AND BARAT, J., Ann. Geophys. 24, 375, 1968.

BLAMONT, J., AND DONAHUE, T.M., J. Geophys. Res., 66, 1407, 1961.

BLAMONT, J.E., GADSDEN, M., AND DONAHAUE, T.M., J. Geophys. Res., 71, 5047, 1965.

BLIFFORD, J.H., Jr., Appl. Optics., 5, 105, 1966.

BOOKER, H.G., J. Geophys. Res. 61, 673, 1956.

BOOKER, H.G. Proc. I.R.E., 46, 298, 1958.

BOOKER, H.G., AND COHEN., R., J. Geophys. Res., 61, 707, 1956.

BOSTROM, R., J. Geophys. Res., 69, 4983, 1964.

BOWHILL, S.A., J. Res. Natl. Bur. Std., 65D, 275, 1961.

BOWLES, K.L., J. Geophys. Res., 65, 1853, 1960.

BOWLES, K.L., AND COHEN, R., in Ionospheric Sporadic E, eds. E.K. SMITH AND S. MATSUSHITA, 51, Pergamon Press, New York, 1962.

BOWLES, K.L., BAILSLEY, B.B., AND COHEN, R., J. Geophys. Res., 68, 2485, 1963.

BOWLES,K.L., COHEN, R., OCHS, G.R., AND BAILSLEY, B.B., J. Geophys. Res., 65, 1853, 1960.

BOYD, R.L.F., Space Sci. Rev., 7, 230, 1967.

BRIGGS, B.H., in Monograph on Ionospheric Radio, ed. W.J.G. BEYNON, 219, Elsevier, Amsterdam, 1962.

BRIGGS, B.H., AND SPENCER, M., Rept. Progr. Phys., 17, 245, 1954.

BRIGGS, B.H., PHILLIPS, G.J., AND SHINN, D.E., Proc. Phys. Soc., B63, 106, 1950.

BROWN, G.M., Geophys. J. Roy. Astron. Soc., 33, 93, 1973.

BURROWS, K., J. Geophys. Res., 75, 1319, 1970.

BURROWS, K., AND SASTRY, T.S.G., J. Atmos. Terr. Phys., 38, 307, 1976.

BUTLER, S.T., AND SMALL K.A., Proc. Roy. Soc. A274, 91, 1963.

CAHILL, L.J., Jr., J. Geophys. Res., 64, 489, 1959.

CAIN, J.C., DANIELS, W.E., HENDRICKS, S.J., AND JENSEN, D.C., J. Geophys. Res., 70, 3647, 1965.

CARRU, H., PETIT,, M., VASSEUR,,P., AND WALDTEUFEL, P., Ann. Geophys., 23, 455, 196

CHAN, K.L. AND VILLARD, O.G., Jr., J. Geophys. Res., 67, 973, 1962.

CHAPMAN, S., Phil. Trans. Roy. Soc. London, A 218, 1, 1919.

CHAPMAN, S., Proc. Phys. Soc. (London), 43, 26, 483, 1931 a,b.

CHAPMAN, S., Terr. Magn. Atmos. Electr., 53, 247, 1948.

CHAPMAN, S., Proc. Phys. Soc. London, B 64, 833, 1951.

CHAPMAN, S., Nuovo Cimento, 4, Suppl. 4, 1385, 1956.

CHAPMAN, S., Smith. Contrib. Astrophys., 2, 1, 1957.

CHAPMAN, S., Solar plasma, Geomagnetism and Aurora, Blackie and Son Ltd., London, 1964.

CHAPMAN, S., AND BARTELS, J., Geomagnetism, Oxford Univ. Press, London, 1940.

CHAPMAN, S., AND LINDZEN, R.S., Atmospheric Tides, D. Riedel Publ. Dordrecht, 1970.

CHAPMAN, S., AND RAJARAO, K.S., J. Atmos. Terr. Phys., 27, 559, 1965.

CLEMMOW, P.C., AND JOHNSON, M.A., J. Atmos. Terr. Phys., 16, 21, 1959.

CLEMMOW, P.C., JOHNSON, M.A., AND WEEKES, K., Proc. Ionosphere Conf., p. 136, Physical Society, London, 1955.

COCKS, A.C., AND PRICE, A.T., Planet. Space Sci., 17, 471, 1969.

COHEN, R., in Physics of Geomagnetic phenomena, ed. S. MATSUSHITA AND W.H. CHAMPBELL, Pergamon Press, New York, 561, 1967.

COHEN, R., AND BOWLES, K.L., J. Geophys. Res., 68, 2503, 1963 a.

COHEN, R., AND BOWLES, K.L., J. Res. NBS, 67D, 459, 1963 b.

COHEN, R., BOWLES, K.L., AND CALVERT, W., J. Geophys. Res., 67, 965, 1962.

CUCHET, L., Radio Sci., 1, 1101, 1966.

DALGARNO, A., Rev. Mod. Phys., 39, 858, 1967.

DANILOV, A.D., Proc. Int. Symp. Solar Terr. Phys.,Leningrad,1970

DAVIS, M.J., J. Atmos. Terr. Phys., 35, 929, 1973.

DAVIS, M.J., AND DA ROSA, A.V., J. Geophys. Res., 74, 5721,1969.

DAVIS, T.N., BURROWS, K., AND STOLARIK, J.D., J. Geophys. Res., 72, 1845, 1967.

DESAI, J.N., BHAVSAR, P.D., RAGHAVARAO, R., AND NARAYANAN,M.S., Space Res., 15, 267, 1975.

DOUGHERTY, J.P., J. Geophys. Res., 64, 2215, 1959.

DUBIN, M., Sounding Rocket Research Techniques, COSPAR Working Group II for the IQSY, 1964.

DUNGEY, J.W., J. Atmos. Terr. Phys., 9, 90, 1956.

DUNGEY, J.W., Cosmic Electrodynamics, Cambridge Univ. Press., New York and London, 1958.

DUNGEY, J.W., J. Geophys. Res., 64, 2188, 1959.

EGAN, R.D., J. Geophys. Res., 65, 2343, 1960.

EGEDAL, J., Terr. Magn. Atmos. Electr., 52, 449, 1947.

EGEDAL, J., Nature, 161, 443, 1948.

EINAUDI, F., AND HINES, C.O., Can. J. Phys., 48, 1458, 1971.

ELFORD, W.G., IAGA, Rept. to Com. VIII, 1973.

ELFORD, W.G., AND ROBERTSON, D.S., J. Atmos. Terr. Phys., 4, 271, 1953.

ELFORD, W.C., AND ROPER, R.G., Space Res., 7, 42, 1967.

EVANS, J.V., J. Atmos. Terr. Phys., 34, 173, 1972.

EVANS, J.V., The dynamics of upper atmosphere and ionosphere (to be published), 1976

EVANS, J.V., AND SALAH, J.E., Trans. Am. Geophys. Union, EOS, 56, 412, 1975.

FAMBITAKOYE, O., Ann. Geophys. 29, 149, 1973.

FARLEY, D.T., Jr., J. Geophys. Res., 68, 6083, 1963.

FARLEY, D.T., Jr., AND BAISELY, B.B., Trans. Am. Geophys. Union 52, 289, 1971.

FEDOR, L.S., AND PLYWASKI, W., J. Atmos. Terr. Phys., 34, 1285, 1972.

FEJER, J.A., J. Atmos. Terr. Phys., 4, 184, 1953.

FEJER, J.A., in Physics of the Earth's Upper Atmosphere, eds. C.O. HINES, I. PAGHIS, HARTZ, T.R., AND FEJER, J.A., Prentice-Hall, Englewood Cliffs, N.J., p. 157, 1965.

FELLOUS, J.L., These de zeme cycle, Paris, 1972.

FELLOUS, J.L., BERNARD, R., GLASS, M., MASSEBEUF, M., AND SPIZZICHINO, A., J. Atmos. Terr. Phys., 37, 1511, 1975.

FOPPL, H., HAERENDEL, G., LOIDL, J., LUST, R., MELZNER, F., MEYER, B., NEUSS, H., AND RIEGER, E., Planet. Space Sci., 13, 95, 1965.

FOPPL, H., HAERENDEL, G., HASER, L., LOIDL, J., LUTJENS, P., LUST, R., MELZNER, F., MEYER, B., NEUSS, H., AND RIEGER, E., Planet. Space Sci., 15, 357, 1967.

FORBES, J.M., AND LINDZEN, R.S., J. Atmos. Terr. Phys. 38, 897, 1976 a.

FORBES, J.M., AND LINDZEN, R.S., J. Atmos. Terr. Phys., 38, 911, 1976 b.

FORBUSH, S.E., AND CASAVERDE, M., Carnegie Inst. Wash. Publ. 620, 1961.

FRANCIS, S.H., J. Geophys. Res., 78, 2278, 1973.

FRIEDMAN, J.P., J. Geophys. Res., 71, 1033, 1966.

FUKUSHIMA, N., Rep. Ionos. Space Res. Japan, 22, 173, 1968.

GDALEVICH, G.L., Space Res., 4, 452, 1964.

GEORGES, T.M., J. Geophys. Res., 72, 422, 1967.

GEORGES, T.M., J. Atmos. Terr. Phys., 30, 735, 1968.

GIESECKE, A.A., Trans. Brussels Meeting 1951, IATME Bull. No. 14, 288, 1954.

GILES, M., AND MARTELLI, G., Planet. Space Sci., 19, 1, 1971.

GILES, M., HUNTER, J., MARTELLI, G., ROTHWELL, P., AND RUSSEL, R., Proc. Sheffield Symp. S.R.C. Publ. 1970.

GLASS, M., AND SPIZZINCHINO, A., J. Atmos. Terr. Phys., 36, 1825, 1974.

GORDON, W.E., Proc. I.R.E., 46, 1824, 1958.

GOSSARD, E.E., AND HOOKE, W.H., Waves in Upper Atmosphere, Elsevier, Amsterdam, 1975.

GOUIN, P., Nature, 193, 1145, 1962.

GOUIN, P., Bull. Geophys. Obs. Addis Ababa, 3, 81, 1963.

GOUIN, P., AND MAYAUD, P.N., Ann. Geophys., 23, 41, 1967.

GREENHOW, J.S., AND NEUFELD, E.L., Phil. Mag., 1, 1157, 1956.

GREENHOW, J.S., AND NEUFELD, E.L., Proc. Phys. Soc., 74,1,195

GREENHOW, J.S., AND NEUFELD, E.L., J. Atmos. Terr. Phys., 16, 384, 1959 b.

GREENHOW, J.S., AND NEUFELD, E.L., Quart. J. R. Met. Soc., 87, 472, 1961.

GROVES, G.V., J. Geophys. Res., 68, 3033, 1963.

GULATEE, B.L., Survey Ind. Tech. Rep. Pt. 3, 1950.

GUREVICH, A.V. AND TSEDILINA, YE. YE., Geomagn. & Aeronomy, 6, 200, 1966.

GUREVICH, A.V., AND TSEDILINA, YE. YE., Geomagn. & Aeronomy, 7, 527, 1967.

HALL, S.H., MCDONALD, D.G., MCGRATTEN, G.J., AND MACKENZIE, E.(
Planet. Space Sci., 19, 1319, 1971.

HARANG, O., Planet. Space Sci., 12, 567, 1964.

HASER, L., in Aurora and Airglow, ed. B.M. MCCORMAC, p. 391, Reinhold, New York, 1967.

HEARENDEL, G., LUST, R., AND RIEGER, E., Planet. Space Sci., 15, 1, 1967.

HEDIN, A.E., AND MAYR, H.G., J. Geophys. Res., 78, 1688, 1973.

HIND, A.D., AND LLOYD, K.H., WRE-Tech. Memorandum - 1021 (WR & D), 1973.

HINES, C.O., Can. J. Phys. 38, 1441, 1960.

HINES, C.O., Quart. J. Roy. Meteorol. Soc., 89, 1, 1963.

HINES, C.O., J. Geophys. Res., 69, 2847, 1964 a.

HINES, C.O., J. Geophys. Res., 69, 1018, 1964 b.

HINES, C.O., J. Geophys. Res., 70, 177, 1965 a.

HINES, C.O., J. Geophys. Res., 70, 1758, 1965 b.

HINES, C.O., J. Geophys. Res., 71, 1453, 1966.

HINES, C.O., Quart. J. R. Met. Soc., 97, 429, 1971.

HINES, C.O., Upper Atmosphere in Motion, American Geophysical Union, Washington, D.C., 1974.

HINES, C.O., J. Atmos. Terr. Phys., 38, 561, 1976.

HINES, C.O., AND HOOKE, W.H., J. Geophys. Res. 75, 2563, 1970.

HINES, C.O., AND RAGHAVARAO, R., J. Atmos. Terr. Phys. 30, 979, 1968.

HINES, C.O., AND REDDY, C.A., J. Geophys. Res., 72, 1015, 1967

HIRONO, M., J. Geomagn. Geoelec., 2, 1, 1950 a.

HIRONO, M., J. Geomagn. Geoelec., 2, 113, 1950 b.

HIRONO, M., J. Geomagn. Geoelec., 4, 7, 1952.

HIRONO, M., AND KITAMURA, T., J. Geomagn. Geoelec., 8, 9, 195

HONG, S.S., AND LINDZEN, R.S., J. Atmos. Sci., 33, 135, 1976.

HOOKE, W.H., J. Atmos. Terr. Phys., 30, 795, 1968.

HOOKE, W.H., Planet. Space Sci., 17, 749, 1969.

HUTTON, R., J. Atmos. Terr. Phys., 29, 1411, 1967.

HUTTON, R., AND OYINLOYE, O., Ann. Geophys., 26, 921, 1970.

IMYANITOV, I.M., GDALEVICH, G.L., AND SHVARTS, YA.M., Artificial Earth Satellites, 17, 66, 1964.

IVANOV-KHOLODNY, G.S., Space Res., 5, 19, 1965.

JACCHIA, L.G., Smith. Astrophys. Obs. Rep. No. 313, Cambridge, Mass., USA, 1970.

JACHHIA, L.G., Smith. Astrophys.Obs. Rep. No. 332, Cambridge, Maas., USA, 1971.

JACKSON, J.E., AND KANE, J.A., J. Geophys. Res., 64, 1074, 1959.

JUSTUS, C.G., J. Geophys. Res., 72, 1035, 1967.

KANE, R.P., J. Atmos. Terr. Phys., 33, 319, 1971.

KANE, R.P., J. Atmos. Terr. Phys., 35, 1565, 1973.

KANE, R.P., Space Sci. Rev., 18, 413, 1976.

KATO, S., J. Geomagn. Geoelec., 8, 24, 1956.

KATO, S., J. Geomagn. Geoelec., 9, 107, 1957.

KATO, S., Planet. Space Sci., 11, 823, 1963.

KATO, S., Planet. Space Sci., 12, 1, 1964.

KATO, S., Space Sci., Rev., 4, 223, 1965.

KATO, S., J. Geophys. Res., 71, 3201, 1966 a.

KATO, S., J. Geophys. Res., 71, 3211, 1966 b.

KATO, S., Space Sci. Rev., 12, 421, 1971.

KATO, S., Radio Sci., 7, 417, 1972.

KATO, S., J. Geophys. Res., 78, 757, 1973 a.

KATO, S., J. Atmos. Terr. Phys., 35, 1073, 1973 b.

KATO, S., REDDY, C.A., AND MATSUSHITA, S., in Proc. Second Semin. Cause and structure of Temperate Lat. Sporadic E, Vail, Colorado, 1968.

KAVADAS, A., AND JOHNSON, D.W., Space Res., 4, 365, 1964.

KING, J.W., SMITH, P.A., ECCLES, D., FOOKS, G.F., AND HELM,H., Proc. Roy. Soc., A 281, 464, 1964.

KIRCHHOFF, V.W.J.H., AND CARPENTER, L.A., J. Atmos. Terr. Phys., 37, 419, 1975.

KLOSTERMEYER, J., J. Atmos. Terr. Phys., 31, 25, 1969.

KNECHT, R.W., AND MCDUFFIE, R.E., in Ionospheric Sporadic E, ed. E.K. SMITH AND S. MATSUSHITA, 215, 1962.

KOCHANSKI, A., J. Met., 12, 95, 1955.

KOCHANSKI, A., J. Geophys. Res., 69, 3651, 1964.

KOCHANSKI, A., Mon. Weath. Rev., 94, 199, 1966.

KOCHANSKI, A., Ann. de Geophys., 29, 77, 1973.

KOLMOGOROFF, A.N., Dokl. Akad. Nauk. SSSR, Moscow, 30, 301, 1941.

KRISHNAMURTHY, B.V. AND SENGUPTA, K., Proc. Symp. Ionosphere and Magnetosphere, New Delhi, India, 1971.

KRISHNAMURTHY, B.V., AND SENGUPTA, K., Planet. Space Sci., 20, 371, 1972.

LAYZER, D., J. Geophys. Res., 69, 1853, 1964 a.

LAYZER, D., J. Geophys. Res., 69, 5098, 1964 b.

LILLER, W., AND WHIPPLE, F.L., J. Atmos. Terr. Phys., 1, 112, 1954.

LINDZEN, R.S., Mon. Weath. Rev., 94, 295, 1966.

LINDZEN, R.S., J. Geophys. Res., 72, 1791, 1967.

LINDZEN, R.S., Proc. Roy. Soc., A 303, 299, 1968.

LINDZEN, R.S., Geophys. Fl. Dyn., 1, 303, 1970

LINDZEN, R.S., Geophys. Fluid Dynamics, 2, 89, 1971.

LINDZEN, R.S., AND BLAKE, D., Geophys. Fluid Dynamics 2, 3, 1971.

MACLEOD, M.A., J. Atmospheric Sci., 23, 96, 1966.

MADWAR, M.R., Bull. Inst. Egypt., 36, 5, 1953.

MAEDA, H., J. Geomagn. Geoelec., 7, 121, 1955.

MAEDA, H., J. Geomagn. Geoelect., 9, 86, 1957.
MAEDA, H., Inst. Phys. Soc. London, 187, 1963.
MAEDA, H., J. Geomagn. Geoelect., 18, 173, 1966.

MAEDA, H., Space Sci., Rev., 8, 555, 1968.

MAEDA, K., J. Geomagn. Geoelect., 23, 133, 1971.

MAEDA, K., Space Res. 12, 1229, 1972.

MAEDA, K., AND MURATA, H., Rept. Ionos. Space Res., Japan, 19, 272, 1965.

MANNING, L.A., AND ESHLEMAN, V.R., Proc. I.R.E., 47, 186, 1959.

MANNING, L.A., VILLARD, O.G., AND PETERSON, A.M., Proc. I.R.E., 38, 877, 1950.

MANNING, L.A., PETERSON, A.M., AND VILLARD, O.G., JR., J. Geophys. Res. 59, 47, 1954.

MANRING, E, BEDINGER, J.F., AND KNAPLICH, H., Space Res., 2, 1107, 1961.

MARTYN, D.F., Phil. Trans. Roy. Soc., A 246, 306, 1953.

MARTYN, D.F., Proc. I.R.E., 47, 147, 1959.

MASON, E.A., Planet. Space Sci. 18, 137, 1970.
MATSUSHITA, S., J. Geomagn. Geoelec., 3, 44, 1951.
MATSUSHITA, S., in Physics of Geomagnetic Phenomena, ed. S. MATSUSHITA AND W.H. CAMPBELL, Academic Press, New York, p. 301, 1967.

MATSUSHITA, S., Geophys. J. Roy. Astron. Soc., 15, 109, 1968.

MATSUSHITA, S., Radio Sci., 6, 279, 1971.

MATSUSHITA, S., Space Res. 12, 1087, 1972.

MATSUSHITA, S., J. Atmos. Terr. Phys., 35, 1027, 1973.

MATSUSHITA, S., Phys. Earth Planet. Interiors, 10, 299, 1975.

MAYAUD, P.N., Ann. Geophys., 23, 387, 1967.

MAYAUD, P.N., J. Atmos. Terr. Phys., 36, 1367, 1974.

MAYNARD, N.C., J. Geophys. Res., 72, 1863, 1967.

MAYNARD, N.C. AND CAHILL, L.J.,JR., J. Geophys. Res. 70, 5823, 1965.

MAYNARD, N.C., CAHILL, L.J., JR., AND SASTRY, T.S.G., J. Geophys. Res., 70, 1241, 1965.

MIDGLEY, J.E., AND LIEMOHN, H.B., J. Geophys. Res., 71, 3729, 1966.

MISRA, R.K., AND RASTOGI, R.G., J. Inst. Telecomm. Engrs., 17, 406, 1971.

MITRA, A.P., J. Atmos. Terr. Phys., 30, 1065, 1968.

MITRA, A.P., AND BANERJEE, P., Space Res., 11, 1019, 1971.

MITRA, S.N., Proc. Inst. Elec. Eng., 96-III, 441, 1949.

MOZER, F.S., Electric fields, Rept. of Univ.California, Berkeley, 1971.

MOZER, F.S., AND BRUSTON, P., J. Geophys. Res., 72, 1109,1967.

MUNROE, G.H., Proc. Roy. Soc., A 202, 208, 1950.

MUNROE, G.H., Austr. J. Phys., 11, 91, 1958.

MURATA, H., Space Sci. Rev., 16, 461, 1974.

MURGATROYD, R.J., Quart. J. Roy. Meteorol. Soc., 83, 417, 1957.

NAKAMURA, J., J. Atmos. Terr. Phys., 36, 1877, 1974.

NARAYANAN, M.S., Ph.D. Thesis, Gujarat University, Ahmedabad, India, 1973.

ONWUMECHILLI, A., J. Atmos. Terr. Phys., 13, 222, 1959.

ONWUMECHILLI, A., J. Atmos. Terr. Phys., 25, 55, 1963.

ONWUMECHILLI, A., J. Geophys. Res., 69, 5063, 1964.

ONWUMECHILLI, A., in Physics of Geomagnetic Phenomena, eds. S. MATSUSHITA AND W.H. CAMPBELL, Pergamon Press, New York, p. 425, 1967.

ONWUMECHILLI, A., AND AKASOFU, S.I., J. Geomagn. Geoelect., 24, 161, 1972.

OOMMEN, K.M., PADMANABHAN, G., KARTHA, C.B., AND BABU, V.V., PED-PYL-PL-02, VSSC, Trivandrum, India, 1976.

OSBORNE, D.G., J. Atmos. Terr. Phys., 24, 491, 1962

OSBORNE, D.S., J. Atmos. Terr. Phys., 26, 1097, 1964.

PACK, J.L., AND PHELPS, A.V., Phys. Rev., 121, 798, 1961.

PHILLIPS, G.J., AND SPENCER, M., Proc. Phys. Soc., B68, 481, 1955.

PIDDINGTON, J.H., Planet. Space Sci., 12, 127, 1964.

PIGGOTT, W.R., AND RAWER, K., URSI Handbook of Ionogram Interpretation and Reduction, Elsevier, Amsterdam, 1961.

PITTEWAY, M.L.V., AND HINES, C.O., Can. J. Phys., 41, 1935, 1963

PONTIER, L., Ann. Geophys., 6, 238, 1950.

PRAKASH, S., GUPTA, S.P., AND SUBBARAYA, B.H., Planet. Space Sci., 18, 1307, 1970.

PRAKASH, S., GUPTA, S.P., AND SUBBARAYA, B.H., Nature, 230, 170, 1971 a.

PRAKASH, S., GUPTA, S.P., SINHA, H.S.S., AND RAO, T.R., Space Res., 17, 401, 1976.

PRAKASH, S., GUPTA, S.P., SUBBARAYA, B.H., AND JAIN C.L., Nature, 233, 56, 1971 b.

PRAMANIK, S.K., AND HARIHARAN, P.S., Indian J. Meteorol. Geophys., 4, 353, 1953.

PRAMANIK, S.K. AND YEGNANARAYANAN, S., Indian J. Meteorol. Geophys., 3, 212, 1952.

PRICE, A.T., Space Sci. Rev., 9, 151, 1969.

RAGHAVARAO, R., Proc. Solar Planet. Phys. Symp., Vol.I, Reviews, Ahmedabad, India, 1976.

RAGHAVARAO, R., AND RAMACHANDRARAO, B., Nature, 185, 27, 1960.

RAGHAVARAO, R., AND SIVARAMAN, M.R., Nature, 249, 331, 1974.

RAGHAVARAO, R., AND SIVARAMAN, M.R., Space Res., 15, 385, 1975.

RAGHAVARAO, R., SHARMA, P., AND JAIN, A.R., Space Res., 17, 417,

RAGHAVARAO, R., SHARMA, P., AND SIVARAMAN, M.R., Space Res., 17, 1977 b.

RAO, K.N., AND RAJARAO, K.S., Nature, 200, 460, 1963.

RAO, K.R., Ph.D. Thesis, Gujarat University, Ahmedabad, India, 1966.

RASTOGI, P.K., AND BOWHILL, S.A., Aeronomy Rep. No. 68, Univ. Illinois, Urbana, USA, 1975.

RASTOGI, R.G., J. Atmos. Terr. Phys., 24, 1031, 1962.

RASTOGI, R.G., J. Inst. Telecomm. Engrs., 12, 245, 1966.

RASTOGI, R.G., J. Geophys. Res., 79, 1503, 1974.

RASTOGI, R.G., & WOODMAN, R.F., Ann. Geophys. (in Press), 1977.

RATCLIFFE, J.A., (Ed.) Physics of the Uppter Atmosphere, Academic Press, New York, 1960.

RATCLIFFE, J.A., An introduction to the ionosphere and magnetosphere, Cambridge University Press, 1972.

RAWER, K., Proc. Intern. Conf. Ionosphere, 239, Inst. Physics and Physical Society, London, 1963.

REDDY, C.A., AND DEVASIA, C.V., Planet. Space Sci., 21,811,197

REDDY, C.A., AND MATSUSHITA, S., J. Geophys. Res., 74,824,1969

REES, D., J. Brit. Interplan. Soc., 22, 275, 1969.

REES, D., ROPER, R.G., LLOYD, K.H., AND LOW, C.H., Phil. Trans. Roy. Soc. London, 271, 631, 1972 a.

REES, D., BHAVSAR, P.D., DESAI, J.N., GUPTA, S.P., FARMER, A.D. AND ROUNCE, P., Space Res., 16, 407, 1976.

REES, D., NEAL, M.P., LOW, C.H., HIND, A.D., BURROWS, K., AND FITCHEW, R.S., Nature, 240, 32, 1972 b.

REVAH, I., Ann. de Geophys., 25, 1, 1969.

RICHMOND, A.D., J. Atmos. Terr. Phys., 35, 1083, 1973 a.

RICHMOND, A.D., J. Atmos. Terr. Phys., 35, 1105, 1973 b.

RICHMOND, A.D., MATSUSHITA, S., AND TARPLEY, J.D., J. Geophys. Res., 81, 547, 1976.

RIEGER, E., Gerlands Beitr. Geophysik, Leipzig, 80,243,1971.

RIEGER, E., J. Atmos. Terr. Phys., 36, 1377, 1974.

RISHBETH, H., Planet. Space Sci., 19, 357, 1971.

RISHBETH, H., J. Atmos. Terr. Phys., 34, 1, 1972.

RISHBETH, H., AND GARRIOTT, O.K., Introduction to ionospheri Physics, Academic Press, New York, 1969.

ROBINSON, B.J., Rept. Progr. Phys., 22, 241, 1959.

ROBLE, R.G., AND DICKINSON, R.E., Planet. Space. Sci., 18, 1489, 1970.

ROGISTER, A., J. Geophys. Res., 76, 7754, 1971.

ROGISTER, A., J. Geophys. Res., 77, 2975, 1972.

ROGNLIEN, T.D., AND WEINSTOCK, J., J. Geophys. Res. 79, 4733, 1974.

ROPER, R.G., J. Geophys. Res., 71, 5785, 1966.

ROSENBERG, N.W., Space Res., 8, 673, 1968 a.

ROSENBERG, N.W., J. Atmos. Terr. Phys., 30, 907, 1968 b.

ROSENBERG, N.W., AND EDWARDS, H.D., J. Geophys. Res., 69, 2819, 1964.

ROSENBERG, N.W., GOLOMB, D., AND ALLEN, E.F.,JR., J. Geophys. Res., 68, 3328, 1963 a.

ROSENBERG, N.W., GOLOMB, D., AND ALLEN, E.F., JR., J. Geophys. Res. 68, 5895, 1963 b.

ROSENBERG, N.W., GOLOMB, D., AND ALLEN, E.F., JR., J. Geophys. Res., 69, 1451, 1964.

SALAH, J.E., AND WAND, R.H., J. Geophys. Res., 79, 4295, 1974

SALAH, J.E., EVANS, J.V., AND WAND, R.H., J. Atmos. Terr. Phys., 37, 461, 1975 a.

SALAH, J.E., WAND, R.H., AND EVANS, J.V., Radio Sci., 10, 347, 1975 b.

SARTIEL, J., Service d' Aeronomie, C.N.R.S. (France), Internal Report No. 30 G., 1972.

SASTRI, N.S., AND JAYAKAR, R.W., Ann. Geophys., 28, 589, 197

SASTRY, T.S.G., J. Geophys. Res., 73, 1789, 1968.

SASTRY, T.S.G., Space Res., 10, 778, 1970.

SATO, T., Phys. Fluids, 14, 2426, 1971.

SATO, T., Phys. Rev. Lett., 28, 732, 1972.

SCHIELDGE, J.P., VENKATESWARAN, S.V., AND RICHMOND, A.D., J. Atmos. Terr. Phys., 35, 1045, 1973.

SCHUSTER, A., Phil. Trans. Roy. Soc., London, A 208, 163,190

SHARMA, P., Ph.D. Thesis, Guj. Univ., Ahmedabad, 1976.

SHIMAZAKI, T., Rep. Ionos. Res. Japan, 13, 21, 1959.

SIMON, A., Phys. Fluids, 6, 382, 1963.

SINGER, S.F., MAPLE, E., AND BOWEN, W.A., J. Geophys. Res. 56, 265, 1951.

SMITH, E.K., NBS Circ. 582, 1957.

SMITH, E.K., Radio Sci., 1, 129, 1966.

SMITH, E.K., in Physics of Geomagnetic Phenomena, Vol. I, 615, 1967.

SMITH, F.J., Planet. Space Sci., 11, 1311, 1963.

SPIZZICHINO, A., Ann. Geophys., 25, 693, 1969 a.

SPIZZICHINO, A., Ann. Geophys., 25, 755, 1969 b.

SPIZZICHINO, A., Ann. Geophys., 25, 773, 1969 c.

SPIZZICHINO, A., Ann. Geophys., 26, 9, 1970 a.

SPIZZICHINO, A., Ann. Geophys., 26, 25, 1970 b.

STENING, R.J., Planet. Space Sci., 16, 717, 1968.

STENING, R.J., Planet. Space Sci., 17, 889, 1969.

STENING, R.J., Planet. Space Sci., 18, 121, 1970.

STENING, R.J., Radio Sci., 6, 133, 1971.

STENING, R.J., Planet. Space Sci., 21, 1877, 1973.

STEWART, B., Encyclopedia Britannica, 9th Ed., 16, p. 159, 1882.

STOREY, L.R.O., AND HERSE, M., Sci. Rept. 1, Serv. Aeronomie C.N.R.S., Obs. Mendon, 1963.

STUBBE, P., J. Atmos. Terr. Phys., 30, 1965, 1968.

STUBBS, T.J., J. Atmos. Terr. Phys., 35, 909, 1973.

SUBBARAYA, B.H., MURALIKRISHNA, P., SASTRY, T.S.G., AND PRAKASH, S., Planet. Space Sci., 20, 47, 1972.

SUDAN, R.N., AKINRIMISI, J., AND FARLEY, D.T., JR., J. Geophys. Res., 78, 240, 1973.

SUGIURA, M., AND CAIN, J.C., J. Geophys. Res., 71, 1869, 1966.

SUGIURA, M., AND POROS, D.J., J. Geophys. Res., 74, 4025, 1969.

SWIDER, W., J. Geophys. Res., 70, 4859, 1965.

SWIDER, W., Proc. of Conf. on Ground-based Radio wave propagation studies of the Lower Ionosphere (Ottawa, 1966),. p. 29, Def. Res. Board, Canada, 1967.

SWIDER, W., J. Atmos. Terr. Phys., 34, 1615, 1972.

SWIDER, W., in Atmospheres of Earth and the Planets, D. Reidel, Dordecht, ed. B.M. MCCORMAC, p. 259, 1975.

TARPLEY, J.D., Ph. D. Thesis, University of Colorado, USA, 1969.

TARPLEY, J.D., Planet. Space Sci., 18, 1075, 1970 a.

TARPLEY, J.D., Planet. Space Sci., 18, 1091, 1970 b.

TAYLOR, G.N., J. Atmos. Terr. Phys., 36, 267, 1974.

TCHEN, C.M., Research paper, P-595, Inst. for Defence Analysis, Arlinpton, 1970.

TESTUD, J., AND VASSEUR, G., Ann. Geophys., 25, 525, 1969.

THOME, G.D., J. Geophys. Res., 69, 4047, 1964.

THOME, G., J. Geophys. Res., 73, 6319, 1968.

THRANE, E.V., AND PIGGOTT, W.R., J. Atmos. Terr. Phys., 28, 721, 1966.

TIETELBAUM, H., AND BLAMONT, J.E., Planet. Space Sci., 25, 723, 1977.

TITHERIDGE, T.E., J. Geophys. Res. 68, 3399, 1963.

TOLSTOY, I., Rev. Mod. Phys., 35, 207, 1963.

TSUDA, T., SATO, T., AND MAEDA, K., Radio Sci., 1, 212, 1966

UNTIEDT, J., J. Geophys. Res., 72, 5799, 1967.

VAN SABBEN, D., J. Atmos. Terr. Phys., 28, 965, 1966.

VAN ZANDT, T.E., in Physics of Geomagnetic Phenomena, Eds. MATSUSHITA, S. AND CAMPBELL, W.H., p. 509, Academic Press, New York, 1967.

WOODRUM, A., AND JUSTUS, C.G., J. Geophys. Res., 73, 467, 1968.

YACOB, A., J. Atmos. Terr. Phys.,28, 581, 1966.

YACOB, A., J. Atmos. Terr. Phys.,39, 601, 1977.

YACOB, A., AND KHANNA, K.B., Indian J. Meteorol. Geophys., 14, 470, 1963.